VHEE Dosimetry in a FLASH:
Ultrahigh Dose Rate Dosimetry and Real-time Beam Monitoring for Very High Energy Electron FLASH Radiotherapy

Joseph J. Bateman
Oriel College

University of Oxford

A thesis presented for the degree of
Doctor of Philosophy

July 2024

I dedicate this to mum and dad, my two biggest supporters.

Acknowledgements

First and foremost, I would like to thank my supervisory team for guiding me through this DPhil: Roberto Corsini, for allowing me to work as part of the CLEAR team and for making all of the experimental aspects of my DPhil possible, along with his much appreciated contributions to the experiments themselves; Iñaki Ortega Ruiz, for providing the opportunity to work as part of his team on the development of fibre monitors, for sharing his expertise on fibre detectors, as well as his much appreciated support in the development and testing of the fibre monitor, as well as sparking an interest which I am pursuing as I continue my research career; Alex Gerbershagen, for his continual encouragement, technical guidance, and insightful suggestions. His vast knowledge and thoughtful feedback have been instrumental in advancing my work; lastly and by no means least, Manjit Dosanjh, whom I would like to express my deepest gratitude to. Her exceptional mentorship, profound knowledge, and inspirational leadership have greatly influenced my academic journey. It has been an absolute pleasure to work under her guidance. Her overall support and encouragement, both academically and personally, have been invaluable.

I extend my sincere thanks to the CLEAR operation team for their support throughout my research. Additionally, I would like to extend my heartfelt thanks to my colleagues and friends who have provided me with support and experiences that have made this journey immensely more enjoyable and fulfilling. Whilst I won't thank them all individually, there are number who a special thanks is required who left a lasting impact on this journey.

Firstly to my wonderful group of friends: Victoria, Charlotte, Alina, Nathan and Lorenzo who I made such incredible memories with during my time in Geneva, and since then our friendships have flourished. To Vilde, with whom I had the pleasure to work closely with on dosimetry projects at CLEAR and kept me both sane and entertained all the while. To Emily, who I had the pleasure of living with in Oxford for this past year for her companionship and support.

Most notably, I would like to express my admiration to my partner in crime, Cameron. Throughout this DPhil journey we have been inseparable and his unwavering support and companionship has been second to none. I have truly made a friend for life.

I am deeply grateful to my family for their encouragement. Their faith in me has been a source of motivation throughout this process. Lastly, to my dearest partner, Chris, who continually inspires me to be the best possible version of myself. Without his constant love, support and encouragement, none of this would have been possible.

Abstract

Very High Energy Electrons (VHEE) are a promising radiotherapy modality due to their increased penetration, reduced sensitivity to inhomogeneities, and delivery via scanning or focusing. VHEE beams at ultrahigh dose rates (UHDR) could be beneficial for treating deep-seated tumours using the FLASH effect, which selectively spares healthy tissues while maintaining effective tumour control. One of the main challenges in making VHEE FLASH treatment clinically viable is real-time dosimetry and beam monitoring, as ionisation chambers exhibit non-linear responses at UHDR due to recombination effects. This research addresses this challenge through the characterisation of VHEE interactions using Monte Carlo (MC) simulations, film dosimetry at the CLEAR Facility, and by developing a novel fibre array beam monitor.

Using TOPAS MC simulations, the interactions of VHEE beams were characterised. The dose distributions and resulting secondary particles generated from these interactions were evaluated to determine feasible *in vivo* dose verification methods for VHEE UHDR beams.

A radiochromic film dosimetry protocol was developed for VHEE FLASH experiments at the CLEAR Facility to ensure accurate dose measurements. Various Gaussian beam size determination methods were compared. Charge measurements using an integrated current transformer were correlated with dose-area-product measurements on radiochromic films for both UHDR and conventional irradiations. Radiochromic film measurements were also compared to those made with other passive dosimeters to ensure accuracy and reliability.

A novel optical fibre beam monitor was developed for real-time beam profile and dose monitoring at UHDR with VHEE beams. Consisting of silica fibres and a CMOS camera, the monitor was tested and characterised at the CLEAR Facility. A linear response with dose rate was demonstrated alongside accurate beam profile measurements for Gaussian and uniform beams. This shows real potential as a solution to address the critical need for accurate beam monitoring with VHEE FLASH radiotherapy.

List of Publications

Joseph J. Bateman, Emma Buchanan, Roberto Corsini, Wilfrid Farabolini, Pierre Korysko, Robert Garbrecht Larsen, Alexander Malyzhenkov, Iñaki Ortega Ruiz, Vilde Rieker, Alexander Gerbershagen, Manjit Dosanjh. **"Development of a novel fibre optic beam profile and dose monitor for very high energy electron radiotherapy at ultrahigh dose rates."** *Physics in Medicine & Biology* (2024), 69(8), 085006. DOI:10.1088/1361-6560/ad33a0

Alexander Hart, Cloé Giguère, Joseph J. Bateman, Pierre Korysko, Wilfrid Farabolini, Vilde Rieker, Nolan Esplen, Roberto Corsini, Manjit Dosanjh, Luc Beaulieu, Magdalena Bazalova-Carter. **"Plastic scintillator dosimetry of ultrahigh dose-rate 200 MeV electrons at CLEAR"**. *IEEE Sensors* (2024). DOI: 10.1109/jsen.2024.3353190

Nathan Clements, Nolan Matthew Esplen, Joseph J. Bateman, Cameron Robertson, Manjit Dosanjh, Pierre Korysko, Wilfrid Farabolini, Roberto Corsini and Magdalena Bazalova-Carter. **"Mini-GRID radiotherapy on the CLEAR very-high-energy electron beamline: collimator optimization, film dosimetry, and Monte Carlo simulations"**. *Physics in Medicine and Biology* (2024). DOI: 10.1088/1361-6560/ad247d

Hannah C. Wanstall, Pierre Korysko, Wilfrid Farabolini, Roberto Corsini, Joseph J. Bateman, Vilde Rieker, Abigail Hemming, Nicholas T. Henthorn, Michael J. Merchant, Elham Santina, Amy L. Chadwick, Cameron Robertson, Alexander Malyzhenkov & Roger M. Jones **"VHEE FLASH sparing effect measured at CLEAR, CERN with DNA damage of pBR322 plasmid as a biological endpoint"**. *Scientific Reports* (2024). DOI: 110.1038/s41598-024-65055-8

Contents

1 Introduction **2**

1.1 Introduction to Radiotherapy and its Current State 2

1.1.1 The Challenge Posed by Cancer 2

1.1.2 Early History of Radiotherapy 3

1.1.3 Evolution of External Beam Radiotherapy Treatment Modalities 4

1.1.3.1 Photon Radiotherapy 4

1.1.3.2 Electron Radiotherapy 6

1.1.3.3 Hadron Therapy 8

1.1.4 Tissue Response to Radiation and the Therapeutic Window 9

1.2 Ultrahigh Dose-rate Radiotherapy and the FLASH Effect 14

1.2.1 First Evidence of the Differential FLASH Effect 14

1.2.2 Determining the Optimal Parameter Space for FLASH-RT 17

1.2.3 Technological Challenges of UHDR RT 19

1.2.3.1 Dosimetry and Beam Monitoring 19

1.2.3.2 Beam Generation and Dose Delivery 21

1.3 Very High Energy Electron Radiotherapy 23

1.3.1 The Case for Very High Energy Electrons in RT 23

1.3.2 Characteristics of VHEE Beams 24

1.3.3 Dosimetry of VHEE Beams 27

1.4 Research Objective: Challenge of Dosimetry for VHEE UHDR Beams 29

1.5 Thesis Outline 30

2 Theory and Fundamental Concepts 32

2.1 Radiotherapy Physics 32

2.1.1 Interactions of Particles with Matter 33

2.1.1.1 Electron Interactions 33

2.1.1.2 Photon Interactions 35

2.1.2 Introduction to Dosimetric Principles and Quantities 43

2.1.3 Absolute, Reference and Relative Dosimetry 46

2.1.4 Radiotherapy Beam Monitoring 48

2.1.5 *In vivo* Dosimetry 50

2.2 Detectors for Radiotherapy Dosimetry 50

2.2.1 Ionisation Chambers 50

2.2.2 Radiochromic Film 52

2.2.3 Alanine 55

2.2.4 TLDs and OSLDs 55

2.2.5 Semiconductor Detectors 56

2.2.6 Scintillation and Cherenkov Dosimetry 57

2.2.6.1 Scintillation 57

2.2.6.2 Cherenkov Radiation 58

2.2.6.3 Optical Fibres 61

2.2.6.4 Photodetectors 62

2.3 Relevant Principles in Accelerator Physics 64

2.3.1 Transverse Beam Dynamics 66

2.3.2 Charged Particle Acceleration in Linear Accelerators 69

2.3.2.1 Velocity Bunching 70

2.4 Concluding Remarks 71

3 Monte Carlo Characterisation of VHEE Interactions for Dose Monitoring 73

3.1 Introduction 73

3.1.1 *In vivo* Dosimetry Methods 73
3.2 TOPAS Monte Carlo Simulation Setup 75
3.3 Dose Distribution Characteristics 77
3.4 Secondary Particle Production Comparison 78
3.5 Bremsstrahlung 81
3.6 Positron Annihilation Gammas 84
3.7 Cherenkov Radiation 89
3.8 Concluding Remarks and Future Considerations 93

4 Very High Energy Electron Ultrahigh Dose Rate Radiotherapy Dosimetry Studies at the CERN Linear Electron Accelerator for Research (CLEAR) 97

4.1 Introduction 97
4.2 The CLEAR Facility 98
4.2.1 Beam Position and Profile Monitors 102
4.2.2 Charge Measurements 102
4.2.3 Energy Measurements 103
4.3 Radiochromic Film Dosimetry at the CLEAR Facility 103
4.3.1 Film and Scanner Preparation 104
4.3.2 Film Calibration 104
4.3.3 Radiochromic Film Dosimetric Analysis 106
4.3.4 Gaussian Beam Dose Targeting 108
4.3.4.1 Gaussian Beam Size Determination 108
4.3.5 Correlating Charge Measurements to Dose 112
4.4 VHEE Radiochromic Film and Passive Dosimetry Comparisons 115
4.4.1 Alanine 116
4.4.2 TLD and Radiochromic Film Phantom 119
4.5 Concluding Remarks 121

5 **A Novel Fibre Optic Monitor for Beam Profile and Dose Monitoring at Ultrahigh Dose Rates** **124**
5.1 Introduction 124
5.2 Single Fibre Photodetector Evaluation Measurements 128
5.2.1 SiPM and PMT Photodetectors 130
5.2.1.1 SiPM Measurements 131
5.2.1.2 PMT Measurements 133
5.2.2 CCD Camera Photodetector 134
5.2.2.1 Profile Measurements 136
5.2.2.2 Response Linearity 137
5.2.3 Single Fibre Measurement Conclusions 139
5.3 Fibre Array Monitor Assembly 140
5.3.1 Initial Design 140
5.3.1.1 Silica Fibres 140
5.3.1.2 CMOS Camera 142
5.3.2 Improved Design 143
5.4 Experiment Setup 145
5.4.1 Signal Processing 147
5.4.2 Fibre Response Variation and Calibration 148
5.5 VHEE Gaussian Pencil Beam Measurements 150
5.5.1 Response Linearity 151
5.5.1.1 Energy Dependence 153
5.5.1.2 Instantaneous Dose Rate Dependence 154
5.5.1.3 Response Linearity of Upgraded Prototype 155
5.5.2 Profile Measurements 158
5.6 VHEE Uniform Beam Measurements 163
5.6.1 Response Linearity 165

5.6.2 Dose Monitoring 166
5.6.3 Profile Measurements 168
5.7 Beam Perturbation Measurements 172
5.8 Temporal Resolution 175
5.9 Comparison to VHEE-FLASH Treatment Planning Dose Rate Requirements 176
5.10 Performance Comparison to Other UHDR Beam Monitors Under Development . . 176
5.11 Concluding Remarks and Future Directions Towards the Next Generation FOFM and Clinical Implementation 178
5.11.1 A Hybrid Detector 181

6 Conclusions and Future Work **182**
6.1 Discussion and Conclusions 182
6.2 Future Work 188
6.3 Final Concluding Remarks 190

List of Figures

1.1 Worldwide age-standardized cancer mortality rate per 100 000, in 2022 [1]. 3

1.2 Schematic layout of a clinical radiotherapy linac [16]. From: Handbook of Radiotherapy Physics, Set, 2nd Edition by Philip Mayles, Alan E. Nahum, J.C. Rosenwald, Copyright ©2021 by CRC Press. Reproduced by permission of Taylor & Francis Group. 5

1.3 Energy spectra in air for the 6 MV therapeutic X-ray beam for $3 \times 3\,\text{cm}^2$ and a $10 \times 10\,\text{cm}^2$ beam. Reproduced from [19], with permission from Elsevier. 6

1.4 Percentage depth dose (PDD) curves of normalised dose against water equivalent depth for 2 MeV photons (green), 6 MeV electrons (red), 200 MeV protons (blue), and 200 MeV electrons (black). 7

1.5 The relative dose plotted against depth for a range of proton beam energies to demonstrate the superposition of individual proton Bragg peaks of different energies, and hence ranges, in water to form a Spread-Out Bragg Peak, from [28]. From: Proton Therapy Physics, 1st Edition by Harald Paganetti, Copyright ©2012 by CRC Press. Reproduced by permission of Taylor & Francis Group. 9

1.6 Image demonstrating DNA damage mechanisms from ionisation and resultant effect on DNA. DNA damage and indirect damage of the cell occurs from ionising radiation through the radiolysis of water. This damage is either repaired within the cell as a mutation by DNA repair processes and survives and either proliferates passing on the legacy of radiation to its descendant cells (A), or aptosis (programmed cell death) may occur. The irradiated cell (blue) may also communicate with other non-irradiated neighbouring cells (cyan) by cell-to-cell gap junction communication and/or secretion of soluble factors eliciting non-targeted apoptosis (black) or micro-nucleation (red) in cells that have not been exposed to radiation (B), from [29].Copyright (2005) National Academy of Sciences, U.S.A. 11

1.7 Dose response curves of the tumour control probability (TCP) and normal tissue complication probability (NTCP), from [16]. From: Handbook of Radiotherapy Physics, Set, 2nd Edition by Philip Mayles, Alan E. Nahum, J.C. Rosenwald, Copyright ©2021 by CRC Press. Reproduced by permission of Taylor & Francis Group. 12

1.8 Schematic demonstration of how FLASH-RT "widens the therapeutic window" by shifting the NTCP curve to the right due to healthy tissue sparing, from [48]. Reproduced with permission from Springer Nature. 15

1.9 36 weeks post-RT comparisons in CONV-irradiated spots and FLASH-irradiated spots on a mini-pig. Reproduced from Clinical Cancer Research, Copyright 2019, Vol. 25 Issue 1, Vozenin *et al*, The Advantage of FLASH Radiotherapy Confirmed in Mini-pig and Cat-cancer Patients, with permission from AACR [50]. 16

1.10 Demonstration of how instantaneous dose rates for delivering 100 /s vary depending on pulse repetition frequency (PRF), from [58]. 18

1.11 The PTW Advanced Markus ionisation chamber's ion collection efficiency plotted as a function of the dose-per-pulse according to water phantom (open symbols) and simultaneous film and chamber measurements (filled symbols), as well as the logistic function (lines) fitted to the data points, for a polarizing voltage of 50 (cross signs), 150 (circles), and 300 V (squares). Reproduced from [71] ©2017 American Association of Physicists in Medicine. 20

1.12 Percentage depth dose of single very high-energy electrons (VHEE) beams and MV photon beams (dotted lines) for field sizes of $10 \times 10\,\text{cm}^2$ (left) and $3 \times 3\,\text{cm}^2$ (right). VHEE beams for different energies are shown for parallel beams (solid lines) and for beams with an SSD of 50 cm (dashed-dotted lines). Reproduced from [100] ©2021 American Association of Physicists in Medicine. 24

1.13 Lateral penumbrae (the distance between the 90% and 10% of the maximum dose) for VHEE beams with different SSD (solid, dashed, and dashed-dotted lines) and MV photon beams (dotted lines) as a function of depth in water for field sizes of $10 \times 10\,\text{cm}^2$ (left) and $3 \times 3\,\text{cm}^2$ (right). Reproduced from [100] ©2021 American Association of Physicists in Medicine. 25

1.14 Example treatment plan comparison for a lung cancer patient. Axial images of the clinical reference plan using photon VMAT (a) and VHEE plan using a 7×200 MeV configuration (b), from [108]. 26

1.15 Ion collection efficiency values of the PTW Advanced Markus ionisation chamber response to 200 MeV electrons at the CLEAR facility for different DPP values. Squared symbols indicate 3.5 mm FWHM beam, circle symbols indicate 7.0 mm FWHM beam, from [73]. 29

2.1 Collision, radiative and total mass stopping powers for electrons in water, with values from NIST ESTAR database [120] 35

2.2 The dominant photon interaction mechanisms for photons of energies between 0.01 - 100 MeV. Graph reproduced from [15], with permission from the IAEA. 37

2.3 Theoretical and experimental photo-absorption cross-sections of ^{16}O. Reproduced from [127], with permission from Elsevier. 41

2.4 Image of an ionisation monitor chamber (left). An example schematic of the quadrant design monitor chamber, where A, B, E and F monitor the radial flatness and symmetry as well as summed together to measure the first integral dose, and C, D, G and H monitor the transverse flatness and symmetry as well as the second integral dose. Images from [16]. From: Handbook of Radiotherapy Physics, Set, 2nd Edition by Philip Mayles, Alan E. Nahum, J.C. Rosenwald, Copyright ©2021 by CRC Press. Reproduced by permission of Taylor & Francis Group. 49

2.5 A schematic of a parallel-plate ionisation chamber, whereby upon interactions from ionising radiation, positive ions (orange) and electrons (blue) are formed and drift to the respective electrode under the influence of the applied electric field. 51

2.6 The structutre of the constituent layers of Gafchromic EBT3 (left) and EBT-XD (right) radiochromic films. Reproduced from [152], with permission from Elsevier. 53

2.7 Film absorbance spectra across the relevant photon wavelengths for EBT3 and EBT-XD radiochromic films for different doses. Reproduced from [154], ©2019 American Association of Physicists in Medicine. 54

2.8 Angle of emission of Cherenkov photons from incident electrons of energies up to 250 MeV in silica, polymethyl methacrylate (PMMA) and water 59

2.9 Threshold energy of emission of Cherenkov radiation as a function of the refractive index of the medium for protons (blue) and electrons (red). Specific values are highlighted for water, silica and PMMA. 60

2.10 Schematic of emission Cherenkov photons (γ) at an angle θ_c from an incident electron traversing an optical fibre at an energy above the threshold of E'. The total internal reflection condition has been met, showing the trapping of optical Cherenkov photons. Image from [180] 62

2.11 Graphical depiction of the Frenet-Serret coordinate system for describing the motion of a charge particle in a magnetic field. Image from [191] 65

2.12 The Twiss ellipse in horizontal xx' phase, showing the relation of the Twiss parameters to x and x', where ϵ is equivalent to J_x. Image from [192] 67

2.13 Plot of accelerating potential $V(t)$ against time or phase, t or ϕ, showing two particles, A (on the synchronous phase, ϕ_s, and B (off phase) (top). Along with a plot of energy offset, ΔE against phase, ϕ showing the oscillation of the off-phase particle, B, around the synchronous particle, A, in longitudinal phase space as they are accelerated (bottom). Image from [188] 71

3.1 Schematic of the TOPAS Monte Carlo simulation setup, whereby a 200 MeV electron or proton beam with a transverse Gaussian distribution with a FWHM of 1 cm is targeted towards a $30 \times 30 \times 30\,\mathrm{cm}^2$ water or PMMA phantom, with a source to surface distance (SSD) of 100 cm. 75

3.2 200 MeV VHEE (left) and proton (right) 2D dose distributions within a water phantom, scored with a bin size of 0.2 mm in the z and y direction. 77

3.3 Bar chart showing the number of bremsstrahlung, positron annihilation gammas, prompt gammas, secondary neutrons and Cherenkov photons scored leaving the water or PMMA phantom, following the irradiation of 200 MeV VHEE and proton beam, normalised to the dose deposited by the beam in the phantom. 79

3.4 Energy spectra of the scored secondary photons leaving the water and PMMA phantoms following irradiation of 200 MeV VHEE beam (left) and proton beam (right), up to a photon energy of 10 MeV, with bin sizes of 10 keV. 81

3.5 The 2D distribution in the z-y plane of the generation of bremsstrahlung radiation in a water phantom following the irradiation of a 200 MeV VHEE beam (left) and proton beam, (right). 83

3.6 The relative dose distribution contribution of the bremsstrahlung radiation in the water phantom following irradiation of the 200 MeV VHEE beam (left), and the corresponding energy spectra of the bremsstrahlung radiation (right) scored in bins of 100 keV produced from VHEE beam irradiation of a water and PMMA phantom. 84
3.7 The 2D distribution in the z-y plane of the generation of positron annihilation (PA) gamma rays radiation in a water phantom following the irradiation of a 200 MeV VHEE beam (top left) and proton beam, (top right), as well as those with a final energy of 511 keV (bottom left for VHEE and bottom right for protons). 86
3.8 The 2D distribution in the z-y plane of the β^+ activity in a water phantom following the irradiation of a 200 MeV VHEE beam (top left) and proton beam (top right), along with a bar plot showing the contributions of PA gamma rays resulting from β^+ emitters to the total signal of PA gamma rays resulting from both the VHEE and proton beam irradiation (bottom). 88
3.9 The 2D distribution in the z-y plane of the relative Cherenkov radiation emission in a water phantom following the irradiation of a 200 MeV VHEE beam (top), along with the direct comparisons between the relative percentage depth light (PDL) emission from the Cherenkov and percentage depth dose (PDD) from the VHEE beam (bottom left) by averaging over transverse widths of 0.4 cm (solid line), 2 cm (dashed line) and 30 cm (dotted line), and a comparison between the relative dose and Cherenkov emission transverse profiles (bottom right) at depths of 1 cm (solid line), 15 cm (dashed line) and 29 cm (dotted line). 91

4.1 Photo of the CLEAR facility beam line. 98
4.2 The CERN Accelerator Complex, from [248] 99
4.3 The time structure of the electron pulses at CLEAR, adapted from [249]. 100
4.4 Layout of the CLEAR experimental beam line (the electron beam runs from right to left) [251]. 101

4.5 Calibration curve for EBT3 (left) and EBT-XD (right) radiochromic film irradiated to 5.5 MeV electrons at the eRT6 machine at CHUV, Lausanne. 105

4.6 Scanned TIFF image of an irradiated EBT3 radiochromic film (left) and processed dose map in the green channel (right) 107

4.7 EBT3 Film Beam Size measurements of a 10 Gy target VHEE pulse, showing the raw film dose map (top left), 2D Gaussian fit (top centre), 2D Gaussian fit residuals (top right), 1D Gaussian fit to 2 mm wide strips in x and y (bottom left) and 1D Gaussian fit to the x and y projection of the profile (bottom right). 110

4.8 YAG Screen Beam Size measurements of an 10 Gy target VHEE pulse, showing the raw YAG screen intensity map (top left), 2D Gaussian fit (top centre), 2D Gaussian fit residuals (top right), 1D Gaussian fit to 2 mm wide strips in x and y (bottom left) and 1D Gaussian fit to the x and y projection of the profile (bottom right). 111

4.9 Beam size measurements on EBT3 radiochromic film and a scintillating YAG screen for 8 Gy and 10 Gy and UHDR (left) and CONV (right) dose rates. Beam sizes are calculated from σ of the Gaussian fit for three different methods: 2D Gaussian fit, 1D Gaussian fit applied to x and y strips of 2 mm width, and 1D Gaussian fit of the projection of the beam distribution along the x and y axes. 112

4.10 Correlation between the ICT charge measurement and the dose-area product measured on MDV3 radiochromic film with a CONV delivery of 300pC/pulse at 0.833 Hz (left). Correlation between the ICT charge measurement and the dose-area product measured on EBT-XD radiochromic film with a CONV delivery of 10pC/pulse 10 Hz (right). 114

4.11 TIFF image of example radiochromic film, with area of alanine pellets outlined to define the AOI for determining corresponding dose to the pellets (left), dose map of one of EBT-XD films irradiated targeting 20 Gy showing the AOI overlaid (right). . 116

4.12 Alanine and EBT-XD Radiochromic Film Dose Measurement Comparisons for 50, 100, 150 and 200 MeV VHEE beams at target doses of between 10 and 20 Gy delivered at CONV dose rates. 118

4.13 Photo of radiochromic film holder, with area of TLD phantom visible behind the film (left), dose map of one of EBT-XD films irradiated targeting 10 Gy showing the AOI overlaid (right). 120

4.14 TLD/Film Phantom and Radiochromic Film Dose Measurement Comparisons for 200 MeV VHEE beams with a target dose of 10 Gy delivered at UHDR and CONV dose rates. 121

5.1 Signal per pulse of built-in transmission ionisation monitor chamber, 1 mm electrode separation (a) and 0.6 mm (b) at operating voltages of −320 V and −1200 V, plotted against the DPP for a 10 MeV electron beam with a 3.5 µs pulse width delivered a pulse repetition frequency of 200 Hz. Reproduced from [78], ©2025 Radiation Research Society. 125

5.2 Cross-section of the 0.50 NA Step-Index Multi-modal Fibre from ThorLabs. 129

5.3 Photographs of the single optical fibre measurements setup in the CLEAR in-air test stand, with black box which houses the silica fibre and SiPM/PMT photodetector (left) and the setup showing the alignment of the optical fibre in the beam path (right). 130

5.4 Digitiser signal trace for the silica fibre and SiPM photodetector response to a single bunch for charges of between 30 pC and 150 pC (left) and the corresponding response plot of the integrated area under the signal for each bunch charge ($R^2 = 0.973$) (right). 132

5.5 Digitiser signal trace for the silica fibre and SiPM photodetector response to each charge per pulse, for pulse widths of between 10 and 200 bunches (left) and the corresponding response plot of the integrated area under the signal for each pulse charge ($R^2 = 0.994$) (right). 132

5.6 Analogue signal trace for the silica fibre and PMT photodetector response to a single bunch for charges of between 20 pC and 400 pC (left) and the corresponding response plot of the integrated area under the signal for each bunch charge ($R^2 = 0.989$) (right). 133

5.7 Analogue signal trace for the silica fibre and SiPM photodetector response to each charge per pulse, for pulse widths of between 1 and 100 bunches (left) and the corresponding response plot of the integrated area under the signal for each pulse charge ($R^2 = 0.984$) (right). 135

5.8 Photographs of the single optical fibre measurements setup in the CLEAR in-air test stand, with the sensitive region of the fibre oriented at 46° (left). The setup with the transport fibre and CCD photodetector which was positioned behind the beam dump and hence not visible in this image (right). 135

5.9 Vertical beam profile measurement of 200 MeV electron pulses with a Gaussian fit applied (red line), and with the vertical error bars corresponding to 1σ of the mean value measured from the 20 repeated measurements for each position for a 1 nC pulse (left) and a 10 nC pulse (right). 137

5.10 The response of the single optical fibre and CCD camera photodetector by summing the pixel value at each vertical position ($R^2 = 0.985$) (left), and where the response is calculated from the integral of the Gaussian fit ($R^2 = 0.998$) (right). 138

5.11 A chart showing the scored optical photons from different TOPAS MC simulations of 5 different fibre setups, following the irradiation of a 200 MeV electron beam. **1.** 0.2 mm diameter core multi-modal fibre (0°) 20 cm length, **2.** 0.2 mm diameter core multi-modal fibre (0°) 120 cm length, **3.** 0.2 mm diameter core multi-modal fibre (45°) 120 cm length, **4.** 0.2 mm diameter core fused silica fibre (0°) 30 cm length, **5.** 0.4 mm diameter core fused silica fibre (0°) 30 cm length. 141

5.12 Spectral response of the SONY IMX249 CMOS chip, used within the 2.3 MP Basler ace CMOS camera that reads out the signal from the fibres in the FOFM. From [288].142

5.13 a) Schematic of the FOFM assembly with the CMOS cameras and silica fibre array, where the working distance (WD) between the edge of the lens and the fibres is 105 mm. b) Schematic of 3D printed fibre support displaying the vertical arrangement of the silica fibres. c) Photograph of the fibre array of the FOFM, consisting of 24 fused silica fibres, installed in the in-air test stand at the CLEAR facility. . . . 144
5.14 a) Schematic of the FOFM assembly with the CMOS cameras and silica fibre array, where the working distance (WD) between the edge of the lens and the fibres is 105 mm. b) Schematic of 3D printed fibre support displaying the vertical arrangement of the silica fibres. c) Photograph of the fibre array of the FOFM, consisting of 24 fused silica fibres, installed in the in-air test stand at the CLEAR facility. 145
5.15 Schematic of the plan view of the experimental setup of the first FOFM prototype installed in the in-air test stand at the CLEAR facility. 146
5.16 Schematic of the plan view of the experimental setup of the second FOFM prototype installed in the in-air test stand at the CLEAR facility. 147
5.17 An example image of the fibre signal measured by the CMOS camera (after noise removal) following a 30 nC pulse. 148
5.18 Relative normalised response of each of the fibres in the first FOFM prototype. . . 149
5.19 Relative normalised response of each of the fibres in the updated FOFM prototype. 150
5.20 The dose-per-pulse (DPP) response of the first FOFM prototype between 4.3 and 39.0 /pulse, with the same gain settings on the CMOS camera for all measurements ($R^2 = 0.996$). 152
5.21 Plot showing the dose-per-pulse (DPP) response of the first FOFM prototype between 0.9 /pulse and 6.1 /pulse in low intensity DAQ Mode ($R^2 = 0.996$) and 3.1 /pulse and 57.4 /pulse in high intensity DAQ ($R^2 = 0.999$) mode (left). The same plots but with the low intensity DAQ Mode values scaled by the ratio between the 3.1 /pulse measurements made with low intensity and high intensity DAQ mode ($R^2 = 0.999$) (right). 153

5.22 The dose-per-pulse (DPP) response of the first FOFM prototype between 0.9 /pulse and 38.8 /pulse for a 200 MeV electron beam ($R^2 = 0.997$) and a 160 MeV ($R^2 = 0.999$) electron beam at 400 pC/bunch. 154
5.23 The DPP response of the first FOFM prototype for a 200 MeV ($R^2 = 0.998$) and a 200 MeV ($R^2 = 0.981$) electron beam at 75 pC/bunch (with the fits from the 400 pC/bunch measurements shown for comparison). 155
5.24 The dose-per-pulse (DPP) response of the upgraded FOFM prototype between 0.9 /pulse and 76.2 /pulse for a 200 MeV electron beam (with $R^2 = 0.999$) and a 160 MeV electron beam (with $R^2 = 0.999$), both at 400 pC/bunch. 157
5.25 Pre-calibration vertical profile measurements made by the first FOFM prototype for a 1 nC (left); and a 10 nC (right) electron pulse at 200 MeV with a Gaussian fit applied (black line). 159
5.26 Post-calibration vertical profile measurements made by the first FOFM prototype for a 1 nC (left); and a 10 nC (right) electron pulse at 200 MeV with a Gaussian fit applied (black line), comparing the Gaussian fits from the radiochromic film measurement (green line), and YAG screen measurement (yellow line). 160
5.27 Vertical beam profile measurements using the upgraded FOFM prototype of a uniform dual-scattered 200 MeV electron beam for a 0.5 nC (top left), 1 nC (top right) (using a CMOS camera normalised gain of 1), 5 nC (centre left), 10 nC (centre right), 20 nC (bottom left) and 40 nC (bottom right) (using a CMOS camera normalised gain of 0.3) pulses. The applied Gaussian fit is shown with the black line. . 162
5.28 Gaussian beam profile measurements for the upgraded FOFM prototype 200 MeV electrons with a 1 nC pulse (top left) and 10 nC (top right) and for 160 MeV electrons with a 1 nC pulse (bottom) with a Gaussian fit applied (black line), comparing the Gaussian fits from the radiochromic film measurement (green line), and YAG screen measurement (yellow line). 163

5.29 The dose-per-pulse (DPP) response of the upgraded FOFM prototype between 0.6 Gy/pulse and 12.2 Gy/pulse for a 200 MeV dual-scattered electron beam at 66.6 pC/bunch performed before, (with $R^2 = 0.999$), and after, (with $R^2 = 0.994$), accumulating a total dose of approximately 17.5 kGy in 24 hours. 165

5.30 The predicted DPP determined from the FOFM output using Eq. 5.5 plotted against the measured DPP with EBT-XD films at 25 mm depth in water. The dashed line with slope 1 is plotted to evaluate the deviation from linearity of the FOFM response. The percentage residual from this slope is plotted below. 167

5.31 Vertical beam profile measurements using the upgraded FOFM prototype of a uniform dual-scattered 200 MeV electron beam for a 0.5 nC (top left), 1 nC (top right), 3 nC (bottom left) and 5 nC (bottom right) pulse. 169

5.32 Plot showing the comparison of the normalised vertical beam profile measurements for a 1 nC pulse using the FOFM (orange), EBT-XD film (blue), and YAG screens positioned before (green) and after (red) the FOFM for a uniform dual-scattered 200 MeV electron beam. 171

5.33 Vertical profiles taken with a 2 mm strip width of 200 MeV VHEE Gaussian pencil beams with a pulse charge of 1 nC both in air (200 mm behind the FOFM) (left), and at a depth of 100 mm in a water phantom (positioned 200 mm behind the FOFM) (right) with the FOFM inserted and extracted from the beam path. 172

5.34 Vertical profiles taken with a 2 mm strip width of 200 MeV VHEE uniform beams with a pulse charge of 1 nC in air (200 mm behind the FOFM) (left), and 5 nC at a depth of 25 mm in a water phantom (positioned 200 mm behind the FOFM) (right) with the FOFM inserted and extracted from the beam line. 174

List of Tables

3.1 Measurements of the transverse dose and Cherenkov emission distribution measurements obtained from the standard deviation Gaussian fit applied to the vertical projection of the beam profile. The uncertainty of the beam size measurement is expressed as the error on the standard deviation of the 1D Gaussian fit. 93

4.1 List of CLEAR Beam Parameters as per 2023 [249] 99

4.2 The depth in water each alanine pellet and radiochromic film was irradiated at for each energy. 117

5.1 Vertical beam size measurements made with the single fibre and CCD camera photodetector, and scintillating YAG screen obtained from the standard deviation Gaussian fit applied to the vertical projection of the beam profile. The uncertainty of the beam size measurement is expressed as the error on the standard deviation of the 1D Gaussian fit. 137

5.2 The gradient values of the linear fit and their corresponding standard error for the measurements shown in Fig. 5.22 and 5.23. 156

5.3 The gradient values of the linear fit and their corresponding standard error for the measurements shown in Fig. 5.24. 157

5.4 Vertical beam size measurements made with the FOFM, radiochromic film (with the type of film stated in brackets), and scintillating YAG screen obtained from the standard deviation Gaussian fit applied to the vertical projection of the beam profile. The uncertainty of the beam size measurement is expressed as the error on the standard deviation of the 1D Gaussian fit. 160

5.5 Vertical beam size measurements made with the updated FOFM prototype with an improved spatial resolution, radiochromic film (with the type of film stated in brackets), and scintillating YAG screen obtained from the standard deviation Gaussian fit applied to the vertical projection of the beam profile. The uncertainty of the beam size measurement is expressed as the error on the standard deviation of the 1D Gaussian fit. 164

5.6 Vertical uniform beam size measurements made withthe upgraded FOFM prototype, radiochromic film (with the type of film stated in brackets), and scintillating YAG screen obtained from the full-width half maximum (FWHM) of the vertical projection of the beam profile. 170

5.7 Measurements in air (25 mm behind the FOFM) and in water (25 mm depth for uniform beams and 100 mm depth for Gaussian beams) of the beam profile and maximum dose using radiochromic film for both uniform and Gaussian 200 MeV electron beams with the FOFM inserted and removed in the beam path. 173

5.8 Comparison of the characteristics of current UHDR beam monitors that are under development. 177

List of Abbreviations

BCT	Beam Current Transformer
CCD	Charge Coupled Device
CLEAR	CERN Linear Electron Accelerator for Research
CMOS	Complementary Metal Oxide Semiconductor
CONV	Conventional Dose rate
DAP	Dose Area Product
DAQ	Data Acquisition
DPP	Dose Per Pulse
EPID	Electronic Portal Imaging Device
FOFM	Fibre Optic FLASH Monitor
FWHM	Full Width Half Maximum
IC	Ionisation Chamber
ICT	Integrating Current Transformer
kV	Kilovoltage
linac	Linear Accelerator
LWFA	Laser-Wakefield Accelerator
MV	Megavoltage

OD	Optical Density
OSLD	Optically-stimulated Luminescent Dosimeter
PA	Positron Annihilation
PET	Positron Emission Tomography
PDD	Percentage Depth Dose
PG	Prompt Gamma
PMMA	Polymethyl Methacrylate
PMT	Photomultiplier Tube
p.r.f	Pulse repetition Frequency
PV	Pixel Value
RGB	Red, Green, Blue
RF	Radiofrequency
RT	Radiotherapy/Radiation Therapy
SiPM	Silicon Photomultiplier
TLD	Thermoluminescent Dosimeter
UHDPP	Ultrahigh Dose Per Pulse
UHDR	Ultrahigh Dose Rate
VHEE	Very High Energy Electron(s)
YAG	Yttrium Aluminium Garnet

1 Introduction

1.1 Introduction to Radiotherapy and its Current State

1.1.1 The Challenge Posed by Cancer

Cancer is a major global health challenge, as demonstrated by the fact that in 2022, there were almost 20 million newly diagnosed incidences of cancer, as well an estimated 10 million deaths (with the global distribution shown in Fig. 1.1), making it among the leading cause of mortality worldwide. Current projections anticipate a projected 32 million newly diagnosed patients and 17 million deaths in 2045 [1, 2]. In the UK, Macmillan Cancer estimate that as of 2022, 3 million people are living with cancer, and this number is expected to rise to 5.3 million by 2040 [3], with the most commonly diagnosed cancers being lung, breast, prostate and colorectal [4]. Radiation therapy (often referred to as radiotherapy, or simply RT) is an essential part of cancer care and is used for the treatment of around half of all cancer patients worldwide, as well as being effective for 40% of all cancer cures (either wholly or in combination with other cancer treatment methods) [5]. In the UK, however, RT was only used to treat between 24-27% of cancer patients in 2019 [6]. Furthermore, RT is by far one of the most cost effective methods for treating cancer, and only contributes to a fraction of overall cancer care costs in comparison to other treatment methods such as chemotherapy and immunotherapy [7]: the ESTRO-HERO report published in May 2024 showed that in England, radiotherapy accounted for only 7% of the total cancer spend.

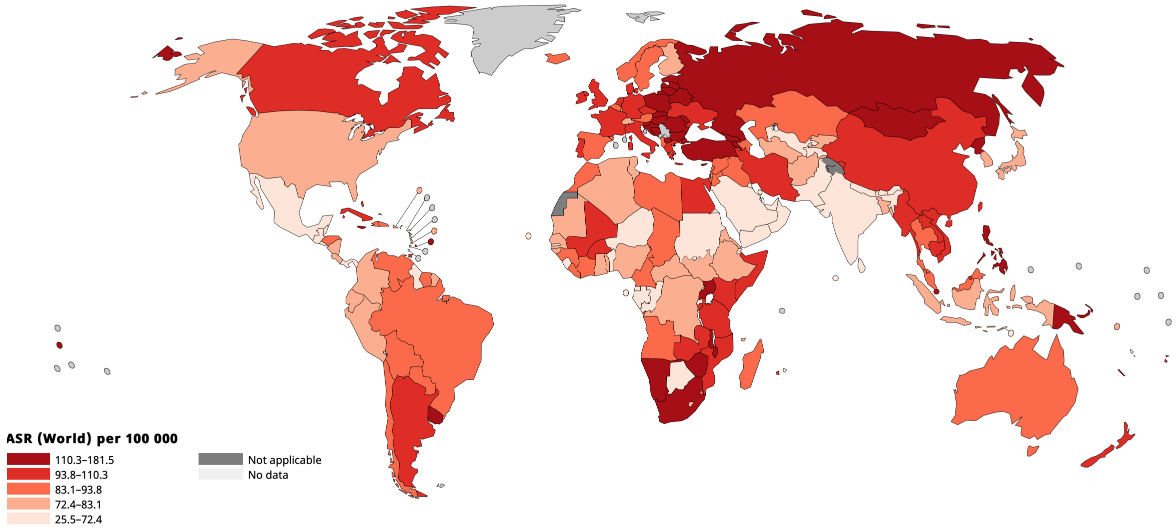

Figure 1.1: Worldwide age-standardized cancer mortality rate per 100 000, in 2022 [1].

1.1.2 Early History of Radiotherapy

Following the discovery of the X-ray by Röntgen in 1895, for which he was awarded the first Nobel Prize in Physics [8], the application of this form of radiation for medical imaging and diagnosis was promptly realised. Within a year of Röntgen's announcement, the use of X-rays for therapeutic benefit had already been employed on at least two separate attempts. One by Grubbé on two patients in Chicago, and another by Despeignes in Lyon, however neither of these attempted treatments proved to be successful [9]. The first successful treatment of a patient using X-rays was carried out in 1896 by Freund [10]. Following this, the Nobel Prize winning discovery and development of the theory of radioactivity by Becquerel and the Curies was made. This eventually led to the discovery by Marie Skłodowska-Curie that tumour-forming cells were killed faster than healthy cells when exposed to radium [11] - paving the way for modern radiation oncology. During this period of initial realisation of the therapeutic benefits of radiation, much was learnt about the potential side effects of radiation on the patients being treated. Hence, an accurate way of quantifying exactly what the delivered dose of radiation was necessary. From this, the field of dosimetry was born, where one of the first reliable methods of determining the delivered dose of X-ray radiation was from measuring the ionisation of gases within a chamber - the ionisation chamber. On this basis the first unit of delivered dose was defined at the Second International Congress of Radiology at Stockholm in 1928 - the Röntgen [12].

1.1.3 Evolution of External Beam Radiotherapy Treatment Modalities

1.1.3.1 Photon Radiotherapy

Kilovoltage X-rays played an important role in the very early development of external beam radiotherapy in the early 20th Century, and were historically the first modality to be used for treatment. Kilovoltage X-rays are produced in an X-ray tube where electrons are accelerated across a potential difference between a cathode and an anode where they are stopped. Their use however is limited to the treatment of superficial tumours due to limitations on their penetration and dose deposition at the skin surface [13]. In order to initially overcome this issue of limited penetration depths of kV X-rays, Cobalt-60 sources were introduced as a "high energy" replacement (> 1 MeV), and provided penetrating γ-ray beams capable of reaching deeper into the patient. Despite the fact that methods of generating megavoltage (MV) X-rays using accelerators had been in development. These Cobalt-60 machines were however phased out due to security concerns and the lack of ability to provide sharper radiation beams compared to MV beams from linear accelerators (linacs), as well as their slowly decaying output power [14].

Presently, the vast majority of cancer patients who are prescribed RT treatment undergo external beam radiotherapy using predominantly MV X-ray photons [15]. These X-rays are in the form of bremsstrahlung that are produced from electrons that have been accelerated in a linac and guided towards a tungsten target, a schematic of which is shown in Fig. 1.2. The mass stopping power, S_{tot}, governs the rate of total electron energy loss:

$$S_{tot} = \frac{1}{\rho}\frac{dE}{dx} \tag{1.1}$$

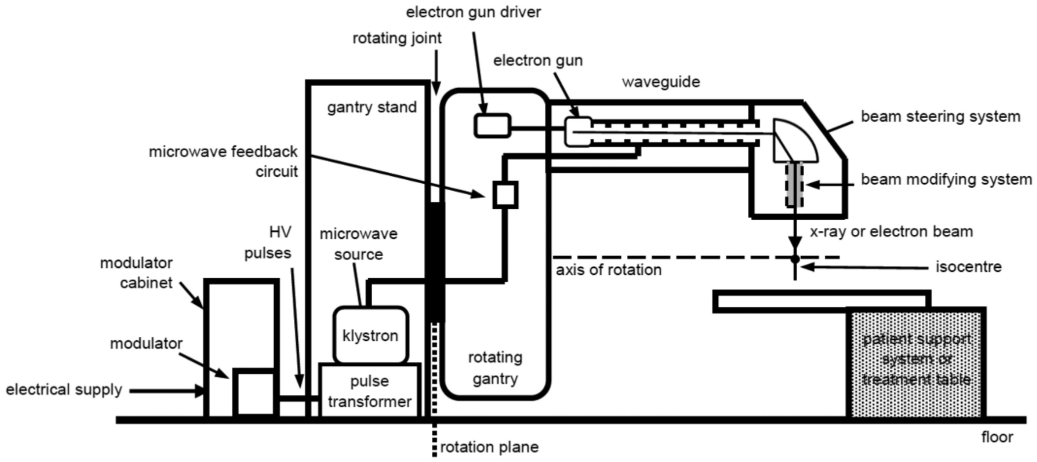

Figure 1.2: Schematic layout of a clinical radiotherapy linac [16]. From: Handbook of Radiotherapy Physics, Set, 2nd Edition by Philip Mayles, Alan E. Nahum, J.C. Rosenwald, Copyright ©2021 by CRC Press. Reproduced by permission of Taylor & Francis Group.

where dE is the kinetic energy of the electron which is lost over a distance dx, in a medium of density ρ [15]. This loss of energy from the incident electrons on the X-ray target is then mainly split between bremsstrahlung generation and heat deposition in the target. For a 10 MeV beam interacting with a tungsten target approximately equal amounts of energy are used for X-ray production as they are lost to heat deposition. At electron energies used for MV photon radiotherapy, the X-ray yield from incident electron energies is between 10 - 40$\%$, however following subsequent beam collimation and modification, the final yield that is used therapeutically is approximately 5$\%$.

MV X-rays are used to treat deep-seated tumours because of their improved penetrating properties as well as the advantage of having a lower skin dose than for kV X-rays. The first cancer patient to receive linac-based RT was in 1953 at Hammersmith Hospital (London, UK) [17], shortly followed by treatments at the Stanford Medical Linear Accelerator (Stanford, USA) in 1956 [18] - manufactured by Varian (Palo Alto, USA), which remain the global leaders in manufacturing RT linear accelerators. The penetration quality of the MV photon beam depends on energy at which the electrons are accelerated to and the quality of the filtration of the bremsstrahlung photons. The characteristic shape of an MV X-ray depth dose curve is shown in Fig 1.4, and has a dose build-up region within the first few centimetres up until the point of max dose deposition, followed by an exponential dose fall-off, allowing for a large range of tumours to be treated with this modality. The energy for an MV photon beam is typically 6 - 15 MV, meaning that the electrons are accelerated to 6 - 15 MeV within the linear accelerator and are then aimed at the X-ray target where they produce a bremsstrahlung spectrum as shown in Fig. 1.3. The beam is then further modified using a flattening filter to make the forward peaked bremsstrahlung transverse distribution more uniform and applicable for clinical use. The beam is then further shaped transversely using large collimator jaws and eventually multi-leaf collimators (MLCs) in order to achieve the desired transverse photon beam distribution.

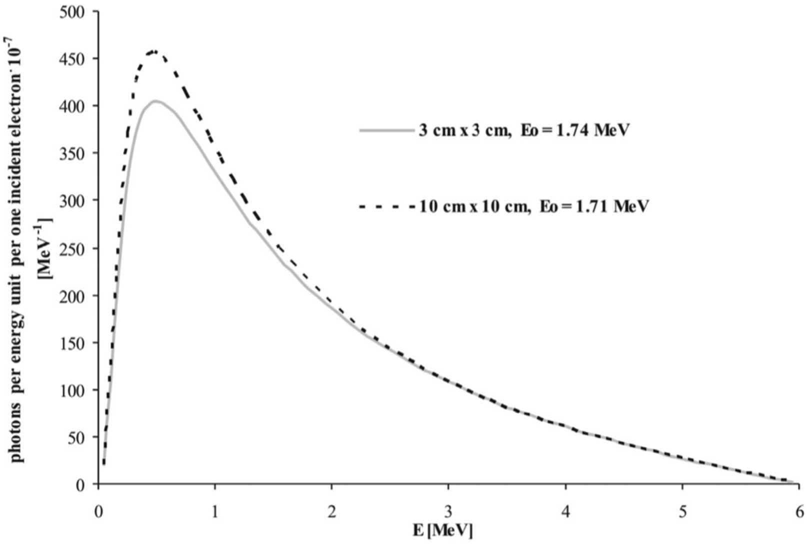

Figure 1.3: Energy spectra in air for the 6 MV therapeutic X-ray beam for 3 × 3 cm^2 and a 10 × 10 cm^2 beam. Reproduced from [19], with permission from Elsevier.

1.1.3.2 Electron Radiotherapy

The first uses of electron beams for radiotherapy dates back to the 1930s where Van de Graaff accelerators and betatrons were used to deliver beams of approximately 5 - 20 MeV, and were predominately used for the treatment of chest wall and breast tumours [20]. Following the development

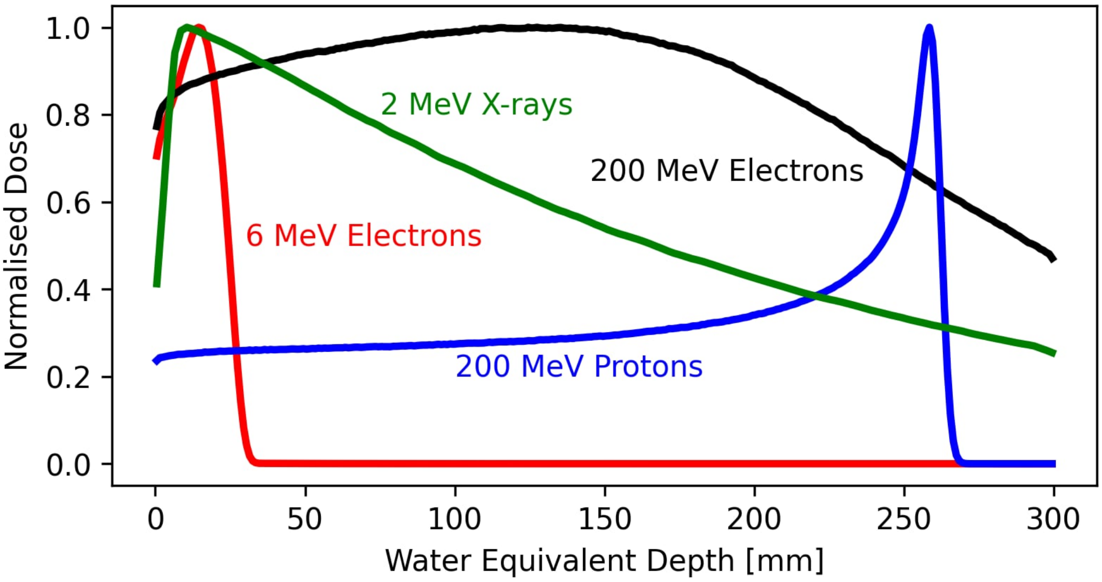

Figure 1.4: Percentage depth dose (PDD) curves of normalised dose against water equivalent depth for 2 MeV photons (green), 6 MeV electrons (red), 200 MeV protons (blue), and 200 MeV electrons (black).

of linacs for X-ray radiotherapy, a variety of approaches were investigated for producing large and uniformly distributed electron beam fields. These linac-based electron beams (most commonly between energies of 4 MeV to 25 MeV) are delivered from a standard clinical MV linac without the use of a tungsten target. The electrons are magnified and flattened using dual-scattering systems [21], and are primarily used for the treatment of skin and superficial tumours. This is because of the characteristics of electron beams in this energy range, in that they deliver uniform dose distributions, have a well-defined region at which the dose is delivered and have a limited penetration depth with a sharp dose fall off, as shown in Fig. 1.4. This makes them a preferable choice for the treatment of skin or shallow tumours [16]. The electrons experience significant scattering between being accelerated and reaching the patient, through interactions with the vacuum window, beam monitoring devices, collimators, and air. Therefore, because of these properties, clinical electron beams in this low energy range are modified using electron applicators or cones as opposed to MLCs, these applicators prevent the lateral scattering of the electron beam from causing irradiation to outside of the desired treatment volume.

One further use for low energy electron beams in radiotherapy is intra-operative electron radiotherapy (IOERT), whereby these electrons are delivered directly to the tumour site in an open-wound immediately following surgery and thus exposure to surrounding healthy tissue is minimised [22]. IOERT is carried out with miniaturised, mobile linear accelerators which can be used within the operating room. IOERT can provide improved penetration depth and dose homogeneity in the region of the tumour bed compared to other intra-operative radiotherapy (IORT) modalities such as high dose rate sealed sources or kVp IORT [23].

1.1.3.3 Hadron Therapy

In 1946, Wilson first proposed the use of proton beams for medical applications, due to their uniquely advantageous stopping power properties for cancer treatment. The main appeal for the use of protons and hadrons in cancer treatment is that the majority of their dose is deposited in a small region called the Bragg peak [24]. The energy of the hadron beams can be selected so to position the depth of this peak over the tumour and thereby minimise the dose to the healthy tissue, as shown in Fig. 1.4. Following the development of the cyclotron for the acceleration of hadrons by Lawrence in 1932, in 1954 the first patient was treated with protons at Lawrence Berkeley National Laboratory (Berkeley, California, USA) [25]. However, production of protons and other hadrons (namely carbon and oxygen ions) at the energies required for treatment of deep-seated tumours requires large and costly facilities - evident in the fact there are currently only 134 hadron therapy facilities in the world as of January 2024 [26]. The majority of proton therapy centres use isochronous cyclotrons which accelerate the protons up to their maximum energy (typically 230 - 250 MeV), and then use degraders to reduce this energy. For heavy ion therapy, the ions are typically accelerated within a synchrotron instead, whereby the energy is modulated within the accelerator itself. In hadron therapy the beams are either transversely modulated through passive scattering, or pencil beam scanning (PBS). In passive scattering, the beam passes through two-sets of scattering foils which magnify and homogenise the transverse distribution of the beam, which is then collimated before it reaches the patient. In PBS , which is the most commonly used method of delivering hadron therapy currently, a small Gaussian distributed pencil beam with full width half maximum (FWHM) of < 1 cm is transversely scanned using dipole magnets across the tumour area, and the energy is altered to "paint" the Bragg peak over the volume of the tumour [27]. Both of these methods require the use of some form of energy degrader or range modulator, in order create a spread out Bragg Peak (SOBP), from superimposed Bragg peaks of a range of energies that cover the entire longitudinal range of the tumour, demonstrated in Fig 1.5.

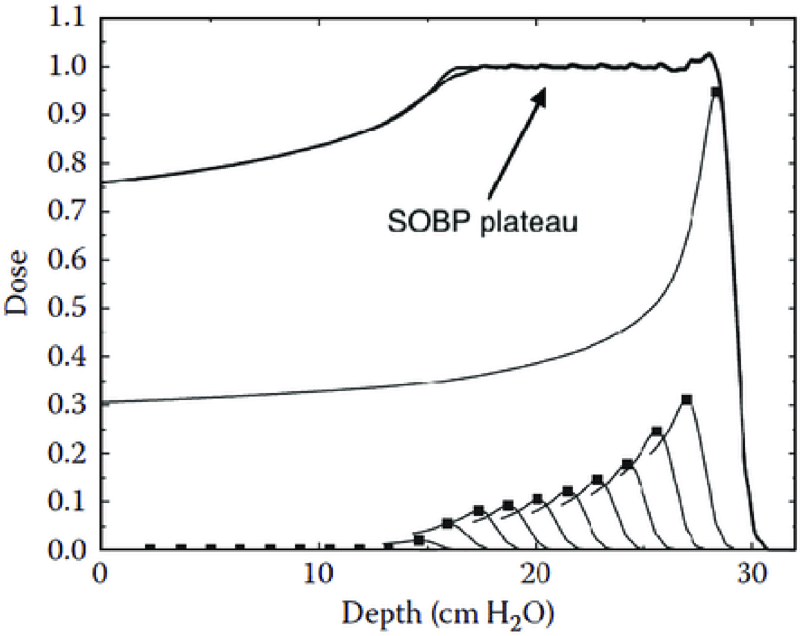

Figure 1.5: The relative dose plotted against depth for a range of proton beam energies to demonstrate the superposition of individual proton Bragg peaks of different energies, and hence ranges, in water to form a Spread-Out Bragg Peak, from [28]. From: Proton Therapy Physics, 1st Edition by Harald Paganetti, Copyright ©2012 by CRC Press. Reproduced by permission of Taylor & Francis Group.

1.1.4 Tissue Response to Radiation and the Therapeutic Window

Ionising radiation is inherently toxic to all biological matter through its ability to damage cellular molecules by ionisation interactions with the constituent atoms. However the damage to the DNA of the cells is the most critical, since most other cellular constituents are able to regenerate. This DNA damage is either direct damage by the incident radiation itself, or through indirect damage that is caused by the creation of short-lived and very unstable radicals, which are produced by the radiolysis of water. Examples of these radicals are: hydroxyl radicals (*OH*), ionised water (H_2O+) or reactive oxygen species (*ROS*) [16]. These radicals react with nearby molecules and thus transfer chemical damage to these too, which causes damage to all components of the cell, shown in Fig. 1.6. Following this radiation damage the cells either die from or repair the damage, but if these cells misrepair so that they are non-identical to how they were prior to radiation damage, they can mutate into malignant tumour cells. The probability of each of these outcomes occurring depends on several variables such as the volume of tissue being irradiated, the oxygen concentration, the type of cell, and the stage of cell life cycle [29, 30]. Since it is not possible to precisely predict the effects of exposure to ionising radiation to a specific cell, models are used to estimate the expected cell survival on a macroscopic scale. The linear-quadratic (LQ) model is often used to describe the survival of cells (survival fraction $S(D)$) following irradiation [31]:

$$S(D) = e^{-\alpha D - \beta D^2} \tag{1.2}$$

Where D is the dose delivered to the cells, and α and β are fitting parameters. Here, the linear component is associated with single-hit mechanisms of damage, and the quadratic component with double-hit mechanisms. However, large variations from the LQ model are observed from cell survival experiments at low dose and high dose fractions, as well as a large number fractions [32]. From this model the probability at which no tumour cell survives - the tumour control probability (TCP) - can be derived based on Poisson statistics (by assuming an ideal model situation where there is no variation in the response between tumours or patients) [33].

$$TCP = e^{-nS(D)} \tag{1.3}$$

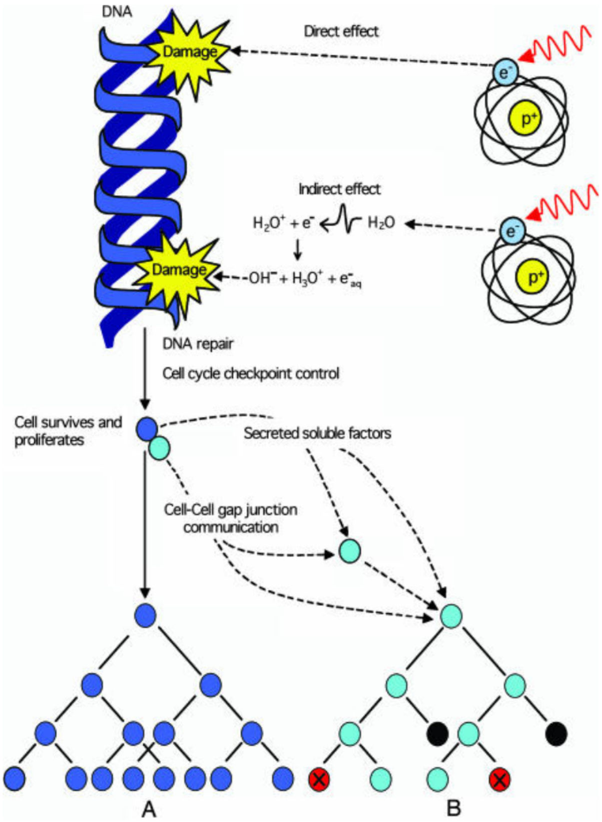

Figure 1.6: Image demonstrating DNA damage mechanisms from ionisation and resultant effect on DNA. DNA damage and indirect damage of the cell occurs from ionising radiation through the radiolysis of water. This damage is either repaired within the cell as a mutation by DNA repair processes and survives and either proliferates passing on the legacy of radiation to its descendant cells (A), or aptosis (programmed cell death) may occur. The irradiated cell (blue) may also communicate with other non-irradiated neighbouring cells (cyan) by cell-to-cell gap junction communication and/or secretion of soluble factors eliciting non-targeted apoptosis (black) or micro-nucleation (red) in cells that have not been exposed to radiation (B), from [29].Copyright (2005) National Academy of Sciences, U.S.A.

where n is the number of live cells before irradiation. Conversely, the probability in which complications arise in normal healthy tissue is called the normal tissue complication probability (NTCP). However, modelling the NTCP is non-trivial due to the complexity and number of radiobiological mechanisms to consider [34]. In general, both the TCP and NTCP increase in a sigmoidal relation with dose (seen in Fig. 1.7), and from these dose response curves the probability of complication-free tumour control, P, can be calculated as originally proposed by Holthusen in 1936 [33, 35]:

$$P = TCP(1 - NTCP) \tag{1.4}$$

In RT the ultimate goal is to maximise this value thus producing a so-called therapeutic window, where such doses cause the highest possible differential response between the cancerous and normal tissue. The most common method through which a sufficiently wide enough therapeutic window is maintained in present-day radiotherapy is through the use of dose fractionation, by delivering the dose over a series of weeks as opposed to in a single fraction. This was first established by early radiation oncologists in the 1920s after noticing the same tumour control as a single-dose treatment but with less severe side effects following dose fractionation over a period of weeks [36]. It was

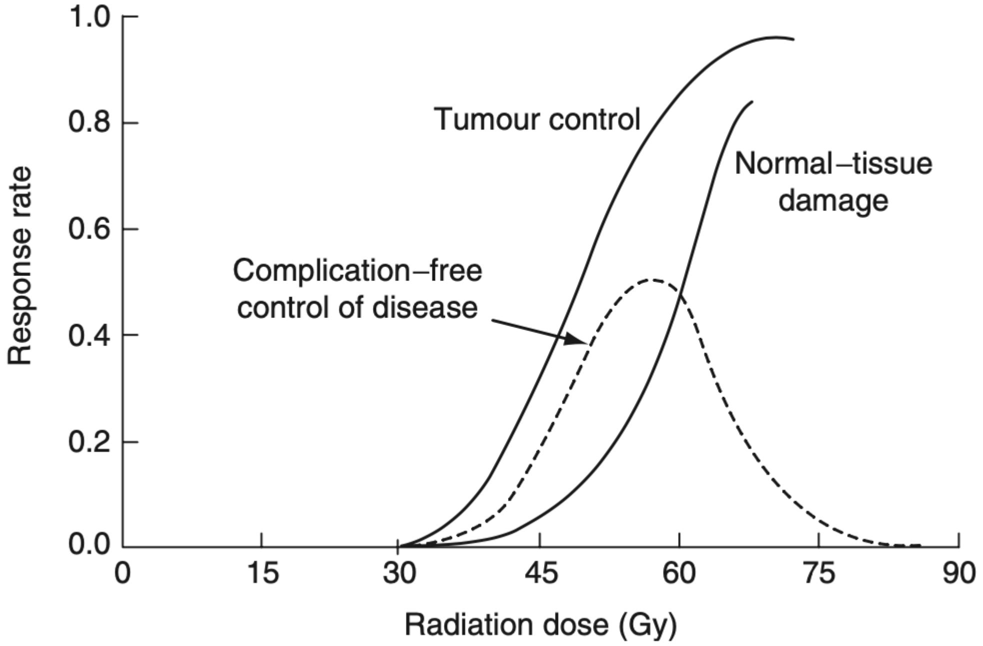

Figure 1.7: Dose response curves of the tumour control probability (TCP) and normal tissue complication probability (NTCP), from [16]. From: Handbook of Radiotherapy Physics, Set, 2nd Edition by Philip Mayles, Alan E. Nahum, J.C. Rosenwald, Copyright ©2021 by CRC Press. Reproduced by permission of Taylor & Francis Group.

concluded that normal-tissue reactions limit the maximum deliverable dose when treating with a single-dose fraction, however, these reactions have a greater capacity for repair than most cancerous tumours [37]. Since then, extensive clinical and radiobiological research has been conducted to further understand the mechanisms which benefit from dose fractionation in order to optimise time-dose relationships and ensure positive clinical outcomes [38]. Currently most conventional RT treatments are delivered in around 30 fractions, five days a week, with 1.5 Gy - 2 Gy per fraction [16]. Recent research suggests that it may be possible to widen the therapeutic window through the delivering the prescribed dose at ultrahigh dose rates of $> 40\,\mathrm{Gy/s}$. This topic will be explored in greater detail in Section. 1.2.

The majority of other advances in widening the therapeutic window have focused on optimising dose delivery in the spatial domain (with the exception of fractionation as mentioned above) through improving the conformality of the delivered dose distribution to the target tumour region, in order to maximise dose to the tumour volume and minimise that to the healthy tissue. The first of these was the progression from uniquely manufactured patient-specific cut-out collimators for each patient to the use of MLCs for 2D-conformal and eventually 3D- conformal radiotherapy (CRT), the radiation beams are delivered from multiple gantry angles with the MLCs shaping the transverse distribution of the beam to match that of the tumour profile from each angle of delivery. Following this development came intensity modulated radiotherapy (IMRT), where not only is the transverse dose distribution modified but also the intensity of each segment of the transverse distribution is modified. This allows for an even sharper dose conformality to the tumour [39, 40]. IMRT can be delivered in two possible ways: step-and-shoot mode where the radiation is delivered for each MLC configuration and the MLCs remain static, and dynamic mode where the MLCs move between their configurations whilst the radiation is continually delivered [41]. A further advancement of IMRT came in the form of volumetric-modulated arc therapy (VMAT), where the dose is delivered continuously whilst both the gantry rotates and the MLCs move simultaneously, further aiding in the sparing of healthy tissue [42]. Even more precise therapies such as stereotactic body RT (SBRT) and radiosurgery (SRS) take advantage of small field sizes and hypo-fractionation (high dose fractions) to further prevent the exposure of healthy tissue, particularly in sensitive regions e.g. head and neck tumours [43]. As the complexity of the dose delivery in these radiotherapy treatments increases and becomes much more precise, so has the need for more complex dosimetry methods and detectors to measure and quantify the dose. This also necessitates the need to verify both the patient position and the dose delivered through utilising advanced image guidance techniques. The ultimate goal is the implementation of real-time adaptive RT using both *in vivo* imaging and dosimetry techniques.

1.2 Ultrahigh Dose-rate Radiotherapy and the FLASH Effect

Numerous experiments were conducted on a range of cancerous cells to investigate the effect of ultrahigh dose-rate (UHDR) irradiations on typical cell and DNA damage mechanisms and the role of oxygen, to see whether these differ in ultrahigh dose rate irradiations. A large proportion of the studies were conducted on HeLa cervical cancer cell lines, and the majority of the results would conclude that under UHDR irradiations, the cancerous cells investigated either had the same or less damage when compared those exposed to conventional dose rates [44, 45, 46].

1.2.1 First Evidence of the Differential FLASH Effect

A groundbreaking study was published in 2014 by Favaudon *et al* [47] performing an irradiation of mice lungs with 17 Gy at a mean dose rate of 40 Gy/s with 4.5 MeV electrons, and comparing to an irradiation of the same prescribed dose at conventional dose rates of 0.03 Gy/s with both 4.5 MeV electrons and ^{137}Cs γ-rays The study showed that radiation-induced lung fibrosis is reduced in mice whilst still maintaining the same damage to tumorous tissue within the mice following the UHDR irradiation. This was coined the FLASH effect, whereby it appears possible to effectively widen the therapeutic window due to the apparent sparing of healthy tissues with UHDR delivery whilst providing the same level of tumour control, as shown in Fig. 1.8. A follow-up study conducted by Montay-Gruel *et al* in 2017 [49] using a "Novel Object Recognition Test" on mice to determine whether the FLASH effect could be observed outside the lung. By delivering a 10 Gy dose of

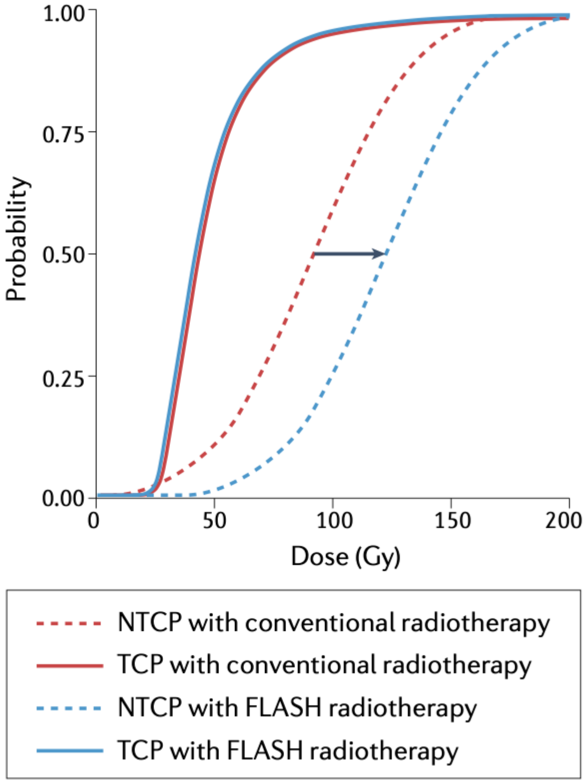

Figure 1.8: Schematic demonstration of how FLASH-RT "widens the therapeutic window" by shifting the NTCP curve to the right due to healthy tissue sparing, from [48]. Reproduced with permission from Springer Nature.

4.5 MeV and 6 MeV electrons at mean dose rates of between 0.1 Gy/s - 500 Gy/s as well as with a single pulse of 1.8 µs (with a dose rate of 5.6×10^6 Gy/s) the investigators showed that at 2 months post-irradiation the memory of the mice was preserved for mean dose rates of 100 Gy/s and above to levels similar to that of unirradiated mice. A further study by Vozenin *et al* in 2019 [50] went on to demonstrate a skin-sparing FLASH effect using electrons at dose rates of 300 Gy/s compared to conventional dose rates of 0.083 Gy/s at doses of 28 Gy, 31 Gy, and 34 Gy, shown in Fig. 1.9. This study also involved a phase 1 clinical trial for the treatment of cats with squamous cell carcinomas using electrons doses of 25 Gy to 41 Gy delivered at FLASH dose rates. Five out of the six cats in the trial showed complete responses 16 months post-irradiation and no evidence of late toxicity a year post-irradiation. However, a follow-up phase 3 trial conducted in cats using FLASH doses of 30 Gy in a single fraction compared to standard CONV doses had to be prematurely ended due to late toxicities showing in 3 out of the 7 cats treated with FLASH [51]. This demonstrated that particular caution should be taken in regards to late-toxicities from UHDR RT at these higher doses.

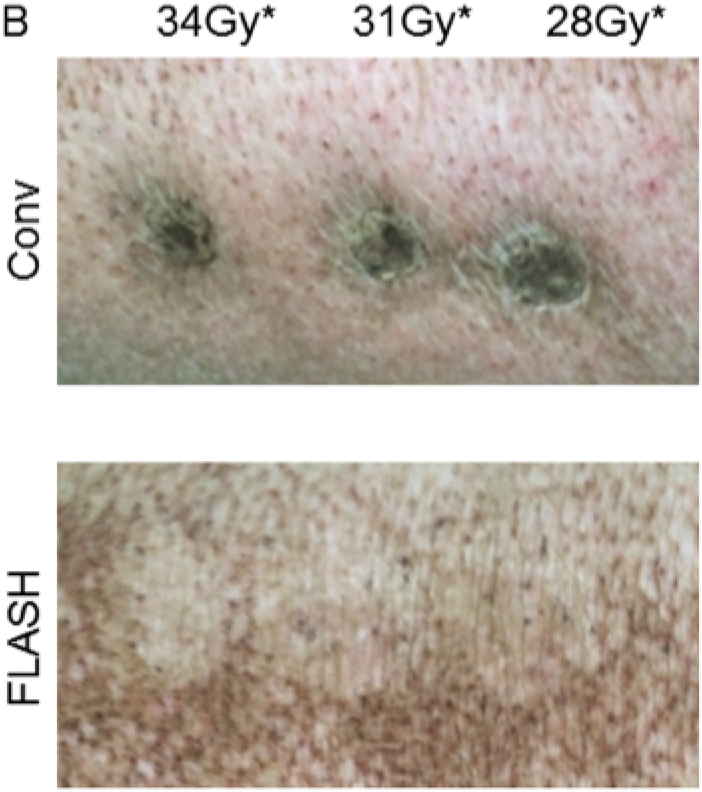

Figure 1.9: 36 weeks post-RT comparisons in CONV-irradiated spots and FLASH-irradiated spots on a mini-pig. Reproduced from Clinical Cancer Research, Copyright 2019, Vol. 25 Issue 1, Vozenin *et al*, The Advantage of FLASH Radiotherapy Confirmed in Mini-pig and Cat-cancer Patients, with permission from AACR [50].

There have so far been two human trials for testing the efficacy of FLASH-RT. The first at Centre Hospitalier Universitaire Vaudois (CHUV), Lausanne, Switzerland where a patient was treated for skin lymphoma with a dose of 15 Gy using 5.6 MeV electrons [52]. The tumour responded completely 36 days post-irradiation and showed that FLASH-RT treatment was feasible and safe with a favorable outcome both on normal skin and the tumour. The second trial was at Cincinnati Children's Hospital, Cincinnati, USA for dosimetry and pain relief purposes for bone metastases with 250 MeV transmission protons (shoot-through, i.e. not using the Bragg peak) with doses of 8 Gy single-fraction delivered at $\geq$40 Gy/s [53]. The trial demonstrated that FLASH-RT with UHDR protons was clinically feasible and that the treatment efficacy and side-effects were comparable with those of standard-of-care radiotherapy treatments with photons.

1.2.2 Determining the Optimal Parameter Space for FLASH-RT

Since these landmark studies, a vast array of pre-clinical mechanistic studies have been carried out to investigate the reproducibility of the observed differential response between healthy tissue and cancerous tissue at UHDR. Such experiments have been performed both with electrons, and with other modalities including protons, photons, and heavy ions; and have attempted to define the parameter space in which this observed effect is most prominent and reproducible. Determining the dose delivery parameters at which the FLASH effect is present at is still a very active area of research, current pre-clinical data seems to suggest that the optimal parameter space for eliciting the FLASH effect is described by the delivery of doses. of above 10 Gy within a total delivery time of <500 ms at mean dose rates of $\approx$ 40 Gy/s [48, 54, 55, 56]. Research is ongoing to determine the precise beam parameters required to induce the FLASH effect. Presently, the average dose rate of the beam delivered to the patient is considered to be one of the key physical requirements to induce the FLASH effect. A wide variety of beam time structures can however be used to achieve the same average dose rate, by varying characteristics such as the dose per pulse, pulse repetition frequency and pulse duration, all of which will vary depending on which type of accelerator is used. For example, an isochronous cyclotron for delivering proton therapy delivers a quasi-continuous beam of protons with pulse widths in the order of nanoseconds at a pulse repetition frequency of around 100 MHz [57]. In comparison electron clinical linacs deliver electron beams with pulse widths in the order of microseconds with pulse repetition frequencies of around 10 - 250 Hz [58]. Therefore, delivering the same average dose rate with each delivery method would constitute in vastly different instantaneous dose rates, as demonstrated in Fig 1.10. Such parameters have been investigated to

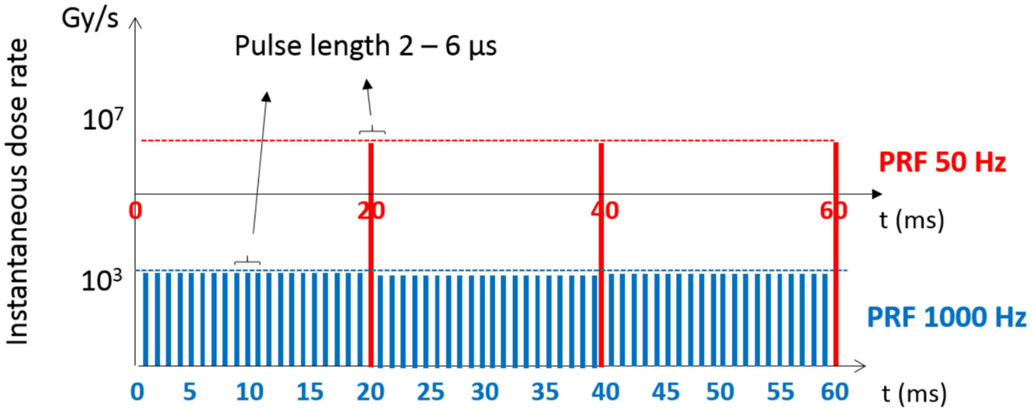

Figure 1.10: Demonstration of how instantaneous dose rates for delivering 100 Gy/s vary depending on pulse repetition frequency (PRF), from [58].

determine whether any of these play a more important role in inducing the FLASH effect as opposed to the average dose rate and total treatment time. Initial studies showed that the largest amount of healthy tissue sparing was observed when the entire dose was delivered in one electron pulse, i.e. at the maximum mean dose rate and in the minimum treatment time [59]. Further studies have also concluded that the main driving-factor for eliciting the FLASH effect is the mean dose rate and irradiation time, however the effect of the dose rate within each bunch or pulse should not be excluded [60, 61].

Whilst a full understanding of the mechanisms is not vital before translation into the clinic, a more in-depth understanding of the FLASH effect and being able to control how and where it is elicited will allow for a more meaningful clinical implementation [48]. Currently,the underlying mechanism is still not fully understood, however exploring which biological effects are fundamental to this phenomena is still a very active area of research. One of the most popular initial hypotheses was that the delivery if radiation at UHDR induces rapid oxygen consumption which leads to transient local oxygen depletion which protects normal healthy tissue but still damages tumours [48, 55, 56, 62, 63]. However the accuracy of this hypothesis is doubted since the level of depletion required for the healthy tissue-sparing to be observed is well above 100 Gy and hence above clinically usable doses, as well as the consumption of oxygen at high dose rates being lower due to radical recombination [64, 65]. There is still a consensus within the radiation oncology community that oxygen plays a key role in the FLASH effect, particularly since *in vivo* experiments have shown that high oxygen levels negate the FLASH effect [66], and *in vitro* experiments have shown protection of healthy cells only at intermediate oxygen levels [67]. Other popular hypotheses include potential sparing of the circulating blood cells and immune cells lymphocytes [68, 69] and peroxyl radical recombination [70].

1.2.3 Technological Challenges of UHDR RT

1.2.3.1 Dosimetry and Beam Monitoring

Perhaps one of the most important technological challenges for the clinical translation of FLASH radiotherapy is related to the difficulty of real-time dosimetry and beam monitoring at UHDR. The necessity to be able to perform accurate and reliable dosimetry at UHDR in both pre-clinical studies and clinical trials is twofold: the first is to ensure that a safe dose is delivered to test subject, or is within the desired parameter range. The second being that it is vital for UHDR mechanistic investigations to ensure that the same dose is delivered and hence verified either through beam monitoring or *in vivo* dosimetry in order to confirm that any differential response observed is in fact due to the dose rate and not a difference in absorbed dose.

For UHDR beams, ionisation chambers - which are the gold standard detector for both reference dosimetry and beam monitoring - exhibit large non-linearities in the UHDR regime. These non-linearities in the response are due to the recombination effect, which is caused by the high charge density in each pulse of radiation that causes anions and cations to recombine with each other before they drift to the electrodes. This means that the response of the ionisation chamber is no longer linear with the dose deposited within its volume [71]. This effect has been observed for both ionisation chambers for reference dosimetry [71, 72, 73, 74, 75, 76], as well as for large area transmission ionisation chambers in the linac head used for beam monitoring [77, 78]. The initial study by Petersson *et al* in 2017 [71] looked to devise an empirical model using a logistic fit to model the ion collection efficiency, $\frac{1}{k_s}$ (where k_s is the ion combination correction factor for ionisation chambers) in order to correct the response of the PTW Advanced Markus chamber to 6 MeV electron beams up to 10 Gy/pulse (with pulse widths of between 0.5 - 1.8 µs) from the Oriatron eRT6 linac, CHUV, Lausanne, Switzerland, shown in Fig 1.11. The results showed the model was able to accurately correct for the absorbed dose measurements in the ionisation chamber with an uncertainty estimate of 2.8% - 4.0%. Additionally, in 2017, Gotz *et al* [79] proposed a numerical

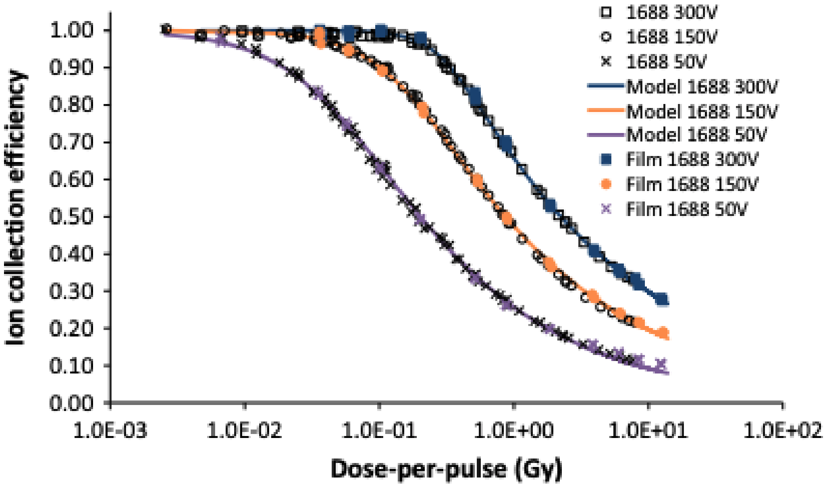

Figure 1.11: The PTW Advanced Markus ionisation chamber's ion collection efficiency plotted as a function of the dose-per-pulse according to water phantom (open symbols) and simultaneous film and chamber measurements (filled symbols), as well as the logistic function (lines) fitted to the data points, for a polarizing voltage of 50 (cross signs), 150 (circles), and 300 V (squares). Reproduced from [71] ©2017 American Association of Physicists in Medicine.

solution to a 1D transport model of the liberated charges in a plane-parallel ionisation chamber to model the recombination factor, k_s within a PTW Advanced Markus Chamber to 20 MeV electrons up to 1 Gy/pulse at the ELBE accelerator, Dresden, Germany. The numerical model was found to successfully replicate the experimental measurements of the ionisation chamber response. Furthermore, these studies on the ion recombination model have consequently been used to determine the optimal design parameter for novel ultra-thin plane-parallel ionisation chambers (UTIC) that can operate within the UHDR regime without significant recombination effects. The first of these developments was done by Gomez *et al* in 2022 [80], and used a chamber which had an electrode separation of 0.25 mm and was reported to achieve a linear response up to 10 Gy/pulse with a 4 μs pulse width using a 9 MeV electron beam on the ElectronFlash Linac, SIT. Liu et al in 2024 [81] developed a range of UTIC prototypes with varying electrode separation and found that the model with an electrode separation of 0.3 mm had linear response up to 5 Gy/pulse with a charge collection efficiency of $\geq 95\%$ and no observable dependence on the pulse width. A new proposed design of ionisation chambers for UHDPP beams is under development by Di Martino *et al* [82] called the ALLS gas chamber, which uses a sensitive volume filled with a noble gas, such as argon, with an adjustable pressure, rather than being vented and air-filled, to prevent the electron capture by gas molecules and therefore effectively eliminate ion recombination effects. The ALLS chamber is being designed to be able to operate in conditions of up to 40 Gy/ pulse.

1.2.3.2 Beam Generation and Dose Delivery

Whilst FLASH-RT offers the promise of normal tissue sparing along with the other benefits of UHDR radiation delivery, there are still many technological challenges associated with the delivery of radiation at ultrahigh dose rates that need to be addressed in order to facilitate the clinical translation of FLASH-RT. The first of these challenges is the ability to generate these radiation beams and deliver the dose to the patient at UHDR. Most of the pre-clinical experiments for FLASH to date have been conducted using low energy electrons (typically of energies 4 - 18 MeV): the main reason for this being that these beams are the easiest to produce at UHDR. It is even possible to use clinical MV photon linacs with minor modifications to deliver UHDR low energy electron beams [83, 84, 85]. This is because the intensity of electrons which are accelerated and aimed at tungsten targets for MV X-ray RT is already sufficient for FLASH. However, the use of electrons at these energies within the clinic is limited to the treatment of skin or superficial tumours, or IOERT, due to the limited penetration depth of these electrons. Given that MV photons are the most widely used modality for delivering RT, they would be the obvious choice to adopt for FLASH. They are however particularly difficult to generate at UHDR due to the inefficiency of the electron to X-ray beam conversion process from heat deposition in the target [86, 87]. In order to generate MV X-rays at the UHDR conditions required for the FLASH effect modifications are required to both the power of the electrons impinging on the target, as well as modifications to the X-ray target itself in order to minimise the effects of the heat deposition [88, 89].

The production and delivery of hadrons for UHDR-RT faces a different challenge. The most common accelerators for the delivery of proton beam therapy are isochronous cyclotrons, however the degrader reduces the beam intensity to below what is required for FLASH. For pencil beam scanning (PBS), the Bragg peak is "painted" over the tumour both transversely (using dipole scanning magnets) and longitudinally, through degrading the energy of the proton beam: as such a scanning speed of 75 cm/ms for step-and-shoot or 43 cm/ms for continuous scanning would be required to meet the the FLASH dose rate and treatment time requirements for treating a 125 mL volume [57]. Presently the current fastest scanning speed available is 2 cm/ms at PSI, Switzerland [90]. Instead,“shoot-through” protons are used at the maximum energy (typically 250 MeV) to maintain an intensity high enough for FLASH dose-rates. Whilst these higher energy protons have some advantages, such as a flat dose-depth profile which is less susceptible to uncertainties, and a sharper lateral profile capable of producing plans that are superior to state-of-the-art photon methods [91], the advantage of the Bragg peak is lost using this delivery method. One method that is under investigation and development is the use of patient specific ridge filters to enable the utilisation of the Bragg peak by modulating the energy sufficiently for each spot to position the spread-out Bragg Peak in the correct position [92].

Therefore, with the currently available technology, the delivery of UHDR beams to elicit the FLASH effect for deep-seated tumours is a major challenge. One potentially promising solution is to use electrons in the energy range of 50 - 250 MeV, the case for which is described in the following section.

1.3 Very High Energy Electron Radiotherapy

1.3.1 The Case for Very High Energy Electrons in RT

A conundrum that the radiation oncology community has faced over the recent decades is whether there exists a radiation modality that matches the precision of proton and heavy ion beams, is as easily applicable in the clinical environment as conventional radiotherapy from MV clinical linacs, and possesses lower normal tissue toxicity compared to the latter [93]. The case for a possible answer to this question was first put forward in the early part of this century by DesRosiers *et al* [94] and Papiez *et al* [95] through the use of electrons at energies of 50 - 250 MeV, being termed Very High Energy Electron (VHEE) radiotherapy. This was the first such work to explore the use of electron beams in this energy range for RT, which was done through the use of PENELOPE Monte Carlo (MC) simulation code, in addition to radiochromic film dose measurements in a water phantom. The main attraction of this modality highlighted in these works is the increased penetrating ability, and hence practical range, associated with the increased electron energy. For electron energies above 150 MeV the practical range exceeds 40 cm and hence that of the typical patient body, meaning that electrons in the VHEE energy range can be used to treat deep-seated tumours, as shown in Fig. 1.12.

Interest in the use of VHEE beams for radiotherapy has grown exponentially in recent years for two main reasons. Firstly, there have been recent advances in high gradient electron accelerator technology such as X-band radiofrequency (RF) cavities developed as part of the CLIC study at CERN [96], novel compact C-band RF cavities [97], and laser-driven plasma wakefield accelerators [98, 99]. This means that the higher electron energies that are required to reach deep-seated tumours are possible with machines that could feasibly fit inside a hospital campus. Secondly, delivery of FLASH-RT to deep-seated tumours with the currently available technology is a major technological challenge, as previously discussed in Section. 1.2.3.2. Therefore, since it is technologically easier to generate high intensity electron beams for a higher dose to be delivered over larger areas of tumorous tissue regions, VHEE is a promising candidate for eliciting the FLASH effect in deep-seated tumours [100].

1.3.2 Characteristics of VHEE Beams

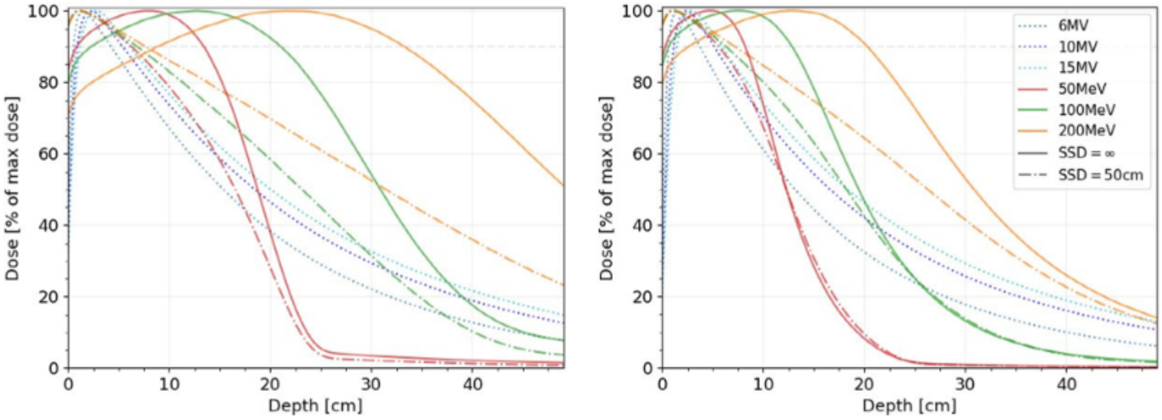

Figure 1.12: Percentage depth dose of single very high-energy electrons (VHEE) beams and MV photon beams (dotted lines) for field sizes of 10 × 10 cm^2 (left) and 3 × 3 cm^2 (right). VHEE beams for different energies are shown for parallel beams (solid lines) and for beams with an SSD of 50 cm (dashed-dotted lines). Reproduced from [100] ©2021 American Association of Physicists in Medicine.

In addition to the previously mentioned advantages of increased penetration and range of VHEE beams within the patient in comparison to clinical electron beams [94], these initial studies showed that VHEE beams produce lateral dose distributions with much sharper penumbrae than current clinical energy electron beams. At depths shallower than 10 cm, 150 MeV electrons show a penumbra similar to that of MV photon beams. Furthermore, it was demonstrated that the scattering properties of electron beams in the VHEE energy range allows for the possibility of intensity modulation via the electromagnetic scanning of a VHEE pencil beam [95]. Doing so requires much lower magnet strengths to achieve the same scanning angles as protons - due to the lower magnetic rigidity of VHEE beams. A more rigorous Monte Carlo simulations study of the characterisations of VHEE beams - particularly on their applicability to the treatment of deep-seated tumours - were performed by Böhlen *et al* [100] in 2021 using the RayStation treatment planning system. This study investigated the effect of varying important treatment parameters such as the beam energy, source-to-surface distance (SSD) and beam divergence. One such result, demonstrating the evolution of the lateral penumbra (the distance between the 90% and 10% of the maximum dose) of VHEE beams of different energies in water is shown in Fig. 1.13. The electromagnetic and ballistic

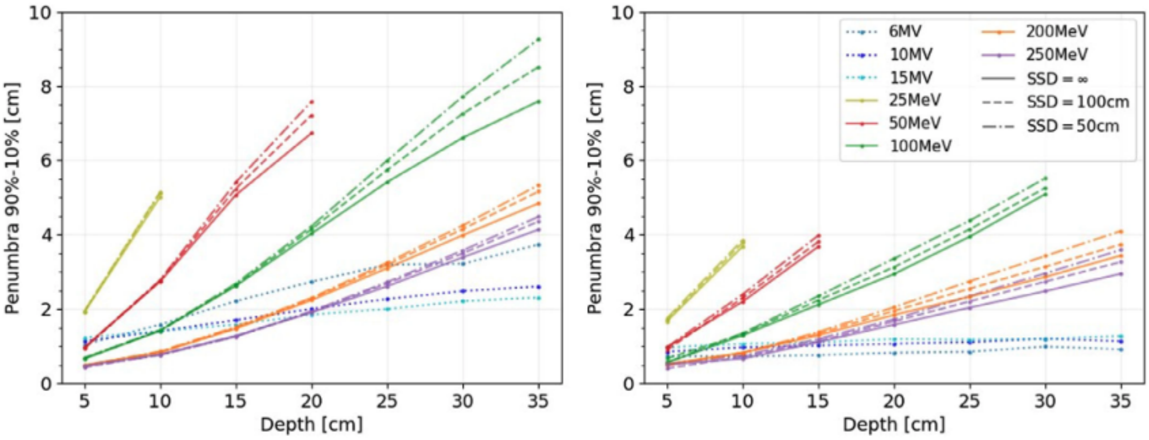

Figure 1.13: Lateral penumbrae (the distance between the 90% and 10% of the maximum dose) for VHEE beams with different SSD (solid, dashed, and dashed-dotted lines) and MV photon beams (dotted lines) as a function of depth in water for field sizes of 10 × 10 cm^2 (left) and 3 × 3 cm^2 (right). Reproduced from [100] ©2021 American Association of Physicists in Medicine.

properties of VHEE beams allow the possibility of a novel delivery of the dose through the use of strong focusing. Here a quadrupole is used to focus the VHEE beam to a “waist”, or a so-called “electron peak”, analogous to that of the proton Bragg peak, at the location of the tumour. The dose is thus maximised at a depth which is dictated by the quadrupole strength [101, 102]. From utilising this technique it is then possible to create a "spread-out electron peak" over the entire depth of the tumour by superimposing focused VHEE beams using different quadrupole strengths [103]. It has been demonstrated experimentally that VHEE beams also have reduced scattering within the inhomogeneous tissues in the patient due to the high relativistic inertia of the electrons at these energies, and thus reducing the sensitivity of the dose distribution to unaccounted uncertainties within the patient compared to proton and photon beams [104]. A number of treatment planning studies have been conducted using VHEE beams to investigate the aforementioned advantages this modality provide, compared with other radiation modalities. The majority of these studies have been performed with VHEE pencil beam scanning and show that VHEE beams can produce superior treatment plans to state-of-the-art intensity modulated photon treatment plans [105, 106, 107]. This has even been shown to be the case for 3D-conformal delivery of VHEE beams, when compared to intensity modulated photon beams [108], with an example shown in Fig. 1.14. Furthermore, in some cases (certain head and neck treatments) these treatment plans have been shown to be comparable to proton treatment plans [106, 107]. Additionally, other VHEE treatment planning studies have shown VHEE treatments to be dosimetrically comparable to shoot-through proton beams, when considering treatment planning for FLASH-RT treatments [91]. Currently, pre-clinical studies suggest that the FLASH effect requires the entire irradiation time to be in less than 500 ms. Therefore, this puts technological restrictions on the delivery of VHEE for FLASH-RT. The proposed methods are currently either the delivery of broad VHEE beams (limited to approximately 15 cm along each axis due to dose-rate limitations on larger beams) through a number of fixed beam-limes using 3D-CRT or utilising intensity modulation through the use of pencil beam scanning [91, 108, 109, 110, 111].

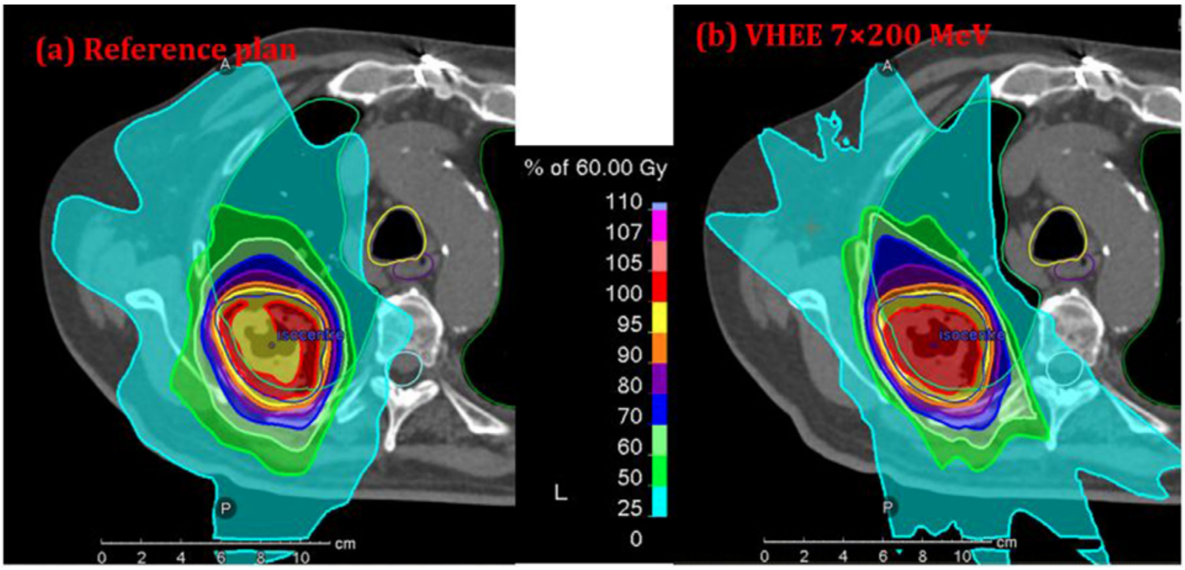

Figure 1.14: Example treatment plan comparison for a lung cancer patient. Axial images of the clinical reference plan using photon VMAT (a) and VHEE plan using a 7×200 MeV configuration (b), from [108].

1.3.3 Dosimetry of VHEE Beams

The first attempt at dosimetrically characterising electron beams within the VHEE energy range was reported in the seminal VHEE paper by DesRosiers *et al* [94], whereby radiochromic film measurements of a 150 MeV beam with 2 cm radius were performed at the Oak Ridge electron linear accelerator (ORELA), Oak Ridge National Laboratory, Tennessee, USA. Gafchromic radiochromic film measurements were performed at a range of depths within a solid water phantom along the central axis of the beam, and were used to benchmark the PENELOPE MC code. The radiochromic film measurements were found to be within relatively close agreement to the MC simulations, with discrepancies between the two being attributed to the lack of stability of the ORELA, an unaccounted for energy spread and potential contamination of the primary beam with backscattered electrons. The first dosimetric characterisation of laser-plasma accelerated VHEE beams was performed by Lundh *et al* in 2012 [112], using a 120 MeV beam at the Laboratoire d'Optique Apliquée facility, Paris, France. Photosensitive films were used to calculate the electron fluence at different depths within a polystyrene phantom, which were compared to GEANT4 MC simulation results. A more thorough comparison of radiochromic film measurements using Gafchromic EBT2 film [113], with MC simulation using EGSnrc/BEAMnrc and DOSXYZnrc codes, was conducted by Bazalova-Carter *et al* [114], also in 2012, with 50 MeV and 70 MeV electron beams at the Next Linear Collider Test Accelerator (NLCTA), SLAC National Accelerator Laboratory, Stanford, USA. This study compared the PDD curves, relative beam size measurements, and absolute dose measurements made with radiochromic films at different depths within a polystyrene phantom with MC simulations. Good agreement between the experimental measurements and MC simulation for the relative PDD and beam size measurements was reported, however differences of between 10% - 40% were reported for the absolute dose measurements. These differences were deemed to be due to imperfect beam steering and subsequent loss of charge. An in-depth dosimetric characterisation of both a 135 MeV laser-plasma accelerated VHEE beam from the Alpha-X laser wakefield accelerator at the University of Strathclyde, UK and a 165 MeV electron beam from the INFN

SPARC linac, Frascati National Laboratory, Italy, was carried out in 2014 by Subiel *et al* [115], also using Gafchromic EBT2 films. This study involved extensive film measurements of the depth dose distributions for VHEE beams in a water phantom compared with FLUKA MC simulations. These radiochromic film measurements showed extremely close agreement with MC simulations for dose determination and beam size measurement across the entire depth dose profile, and was the first such study to confirm the reliability of radiochromic film calibrated to clinical energy electron beams (20 MeV). The first dosimetric characterisations of the VHEE beam at the CERN Linear Electron Accelerator for Research (CLEAR), CERN, Switzerland were performed by Lagzda *et al* in 2020 [104], measuring a 156 MeV electron beam using EBT-XD radiochromic film [113] and comparing it to TOPAS GEANT4 MC simulations. Once more the film measurements showed close agreement with MC simulated values, further confirming the validity of radiochromic films calibrated to low energy electron clinical beams (15 MeV). These experimental data points were more recently validated by extensive MC simulation characterisations of VHEE beams by Böhlen *et al* [100].

The first dosimetry measurements of VHEE beams using an active dosimeter, namely an IBA CC04 ionisation chamber, were performed by Subiel *et al* [116] to 165 MeV VHEE beams at the SPARC linac with ultra-short pulses on the order of femtoseconds. The response of the ionisation chamber showed that VHEE beams with ultra-short pulse lengths induce a significantly large recombination effect, and that the application of conventional correction factors are not suitable for measuring beams of this type. Two separate studies measuring the response of two models of ionisation chamber to 200 MeV electron beams at UHDR were conducted at the CLEAR facility. The first, by McManus *et al* [72] using a PTW Roos Chamber, which was bench-marked against a primary standard graphite calorimeter, showed a strong dependence of the recombination correction factor on the dose-per-pulse, with a measured charge collection efficiency of only 4$\%$ at 5.26 Gy/pulse . The second experiment was using a PTW Advanced Markus Chamber by Poppinga *et al* [73], an ionisation chamber in which the response to clinical electron beams at high dose rates has previously been characterised and bench-marked against radiochromic film and FLUKA MC simulations. These results showed a measured collection efficiency reduced to approximately 30% at roughly 12 Gy/pulse, as shown in Fig. 1.15. The findings of both of these experiments showed that it may be possible to perform ionisation chamber dosimetry of VHEE beams at UHDR if the correction of saturation effects can be applied to the readings. However, the relative uncertainties of the values with low efficiencies in the UHDR regime are significant.

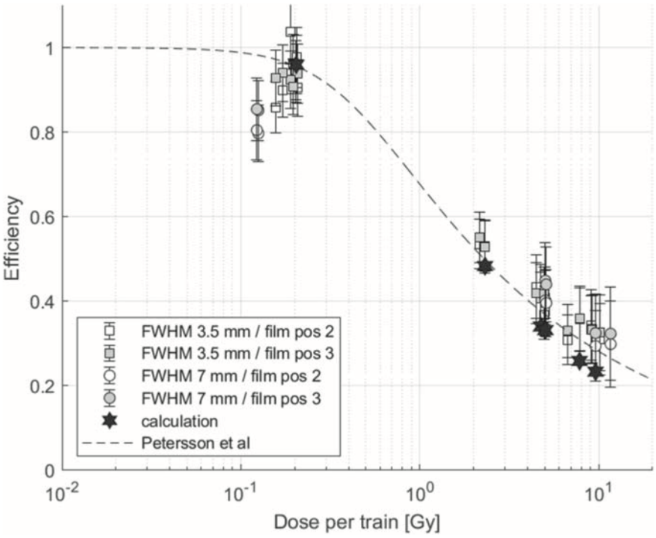

Figure 1.15: Ion collection efficiency values of the PTW Advanced Markus ionisation chamber response to 200 MeV electrons at the CLEAR facility for different DPP values. Squared symbols indicate 3.5 mm FWHM beam, circle symbols indicate 7.0 mm FWHM beam, from [73].

1.4 Research Objective: Challenge of Dosimetry for VHEE UHDR Beams

In order to facilitate accurate and reproducible results in UHDR VHEE pre-clinical studies as well as to enable a reliable translation of FLASH RT with VHEE beams to the clinic, accurate dosimetry and real-time beam monitoring needs to be carried out for these UHDR beams. Subsequently, reliable and precise dosimetry of UHDR beams is a pre-requisite for clinical implementation. The recombination effect which occurs in ionisation chambers in the UHDR regime - or more specifically the ultrahigh dose-per-pulse regime - is much more prominent for VHEE beams where the delivery of the radiation is in the form of ultra-short pulses from a linac (or LWFA). The typical delivery of these beams is with pulse repetition frequencies on the order of 10 - 250 Hz. This recombination effect is much more prevalent for these pulsed beam deliveries because the instantaneous dose rate within each pulse is extremely high in order to be able to obtain the average dose rates that are required to elicit the FLASH effect. Hence for these modalities alternative detector technologies for real-time dosimetry and beam monitoring at UHDR requires investigation. **Therefore, the purpose of the research presented in this thesis is to investigate both existing dosimetry methods and novel detector technologies and their feasibility for the purpose of dosimetry and real-time beam monitoring at the UHDR conditions that would be required for the delivery of FLASH-RT with VHEE beams.**

1.5 Thesis Outline

The research presented within this thesis aims to contribute to the rapidly advancing field of dosimetry and detectors for UHDR and UHDPP beams - in particular with pulsed VHEE beams - intended for use in FLASH-RT, through three main contributions:

1. The contribution presented in **Chapter 3** outlines a TOPAS MC simulation-based feasibility evaluation of a range of potential *in vivo* dose verification methods for use with VHEE RT, particularly at UHDR. This chapter first presents a comparison of the yield of particular types of secondary particles produced following the irradiation of a water phantom with a VHEE beam and proton beam to determine whether methods such as transit dosimetry and in-beam positron emission tomography (PET) techniques already being in use for photon radiotherapy and hadron therapy could be feasible for VHEE RT. Then, a more thorough comparison between the simulated VHEE dose distribution within a water phantom compared to the distribution of the generation of such secondary particles is performed, in order to evaluate which methods are most promising for reconstructing the delivered VHEE dose.

2. The contribution presented in **Chapter 4** involves the development, optimisation and validation of a radiochromic film dosimetry protocol intended for use in a wide range of VHEE-FLASH experiments at the CLEAR facility at CERN. The work in this chapter outlines the preparation, calibration and analysis procedures using radiochromic film that have been developed in order to provide dosimetry for UHDR experiments at CLEAR, as well as how these methods are used to deliver the correct doses in the experiments. This chapter then also provides a comparison of the dose measurements determined from radiochromic films with other passive dosimetry measurements.

3. The contribution presented in **Chapter 5** involves the development, optimisation and characterisation of a novel fibre optic monitor for real-time beam profile and dose monitor for VHEE beams at UHDR. The detector consists of an array of silica fibre-based Cherenkov sensors which are then read out using a complementary metal oxide semiconductor (CMOS) camera, called the Fibre Optic FLASH Monitor (FOFM). The chapter first outlines the initial tests of a single silica fibre with different photodetectors at the CLEAR facility to 200 MeV electrons, from which the first prototype is designed and developed. Subsequently the measurements performed with the first FOFM prototype to VHEE beams at the CLEAR facility are presented, namely that of the dose-per-pulse response linearity, beam profile measurements as well investigations into the response dependent on energy and instantaneous dose rate. Further optimisations of the design of the FOFM are described with more measurements at the CLEAR facility repeating the previous measurements with both VHEE Gaussian pencil beams and dual-scattered uniform beams to investigate the detector's ability to provide real-time dose monitoring using a uniform beam and beam perturbation measurements. Finally, a brief comparison with other UHDR beam monitors under development is performed and the next steps in the development of the detector are outlined.

2 Theory and Fundamental Concepts

In this chapter, the theoretical foundations and general methods that support the work in the three subsequent chapters of this thesis are described, beginning with the physical principles of radiation dose delivery in matter. The use of radiation therapy to treat malignant tumour tissue, relies on the ability of medical physicists' to understand and estimate the absorbed dose that is deposited within the human body. The accurate and precise delivery of RT modalities are all based on the principles of how radiation interacts with biological tissue and being able to quantify this effect and precisely characterise and monitor the radiation beam through dosimetry techniques. The first section will discuss the relevant beam-matter interactions for electron-based radiotherapy techniques, particularly those within the VHEE energy range and the resulting secondary particles produced. Then an introduction to the basic principles of the quantity of dose and how dosimetry standards are defined within the field of radiotherapy. This is followed by an overview of the types of detectors that used for both dosimetry and beam monitoring for radiotherapy. Finally, this chapter describes some of the relevant principles in accelerator physics to provide the reader with background on how the beams described in this thesis are transported through accelerators.

2.1 Radiotherapy Physics

The work presented in this section is first focused on the fundamental physics behind interactions with photons and electrons with matter, which is paramount to understanding how the quantity of dose is defined. The interactions introduced within this section are also key to providing a background for the results and data presented on characterising VHEE interactions with Monte Carlo simulations. Following this, the basic dosimetric quantities and principles are described, as well as their methods of implementation within radiotherapy centres. The theory of this section was taken principally from the published works of a few key textbooks [15, 16, 117].

2.1.1 Interactions of Particles with Matter

2.1.1.1 Electron Interactions

Electrons interact directly with matter via three primary mechanisms: electronic losses, or collisions, through interactions with atomic electrons; radiative losses through bremsstrahlung generation; and elastic scattering with heavy atomic nuclei. The principal mechanism of electronic losses is through Coulomb interactions with bound atomic electrons, whereby electrons create a path of ionisations and excitations along its trajectory. These inelastic collisions can be categorised by the impact parameter, b, which is distance from the central atom at which the incident electron interacts. Soft collisions occur when $b >>$ atomic radius, and involve small losses in kinetic energy from the incident electrons from interactions between the incident electrons and outer shell valence electrons in the form of ionisations and excitations. Ionisations occur when there's an inelastic collision between an incident electron and a bound atomic electron, in which the incident electron imparts an energy greater than the binding energy of the atomic electron, and hence leads to the emission of this previously bound electron. If the energy imparted is large enough for this secondary electron to have a significant range and cause ionisations of its own, then it is called a delta-ray. Excitations occur when the incident electron interacts with valence electrons and imparts an energy that is not large enough to release the electron, but instead excited the electron to higher orbit, which releases a characteristic photon of a given quantised energy upon de-excitation. Hard collisions, which occur when $b \approx$ atomic radius, result in the liberation of inner-shell electrons. The collision contribution to the mass stopping power can be described by a contribution of the soft and hard collisional stopping powers, as derived by Bethe [118] using the Born approximation (assuming that kinetic energy is a lot larger than the electrons orbital energy of an atom). The total mass collisional stopping power is described by the equation:

$$\left(\frac{dE}{\rho dx}\right)_c = 4\pi r_0^2 m_e c^2 \left(\frac{N_A Z}{A}\right)\left(\frac{z^2}{\beta^2}\right)\left[\ln\left(\frac{2m_e c^2\beta^2}{I^2(1-\beta^2)}\right) - \beta^2\right] \tag{2.1}$$

where r_0 i the classical electron radius, m_e is the electron mass, and c the speed of light in a vacuum. The $\left(\frac{N_A Z}{A}\right)$ term consisting of Avogadro's number, N_A, atomic number, Z, and mass number of the atomic medium, M, is the number of electrons per unit mass. The $\left(\frac{z^2}{\beta^2}\right)$ term describes the ratio of the of the charge of the incident particle, z, to the Lorentz factor $\beta = \frac{v}{c}$, with v being the velocity of the incident projectile particle. $I(\propto Z)$ is the mean excitation potential. The radiative contribution to the mass stopping power concerns the loss of kinetic energy from the incident electrons via the production of bremsstrahlung photons. This occurs through nuclear electric field interactions when the incident electron is within the nuclear radius of the atom, $b <<$ atomic radius, and causes the emission of photons in the form "breaking radiation" from the electron. These photons, typically of high energy, leave the interaction region and will proceed to transfer their energy and deposit dose elsewhere. The equation, according to Podgorsak [119], for the mass radiative stopping power is:

$$\left(\frac{dE}{\rho dx}\right)_r = \frac{1}{137} r_0^2 \frac{N_A Z^2}{A}(E_{K_0} + m_e c^2) B_{\text{rad}} \tag{2.2}$$

where E_{K_0} is the initial kinetic energy of the electron, and B_{rad} is a function of Z. The total mass stopping power for electrons is then the combination of these two:

$$\frac{dE}{\rho dx} = \left(\frac{dE}{\rho dx}\right)_c + \left(\frac{dE}{\rho dx}\right)_r \tag{2.3}$$

and Fig. 2.1 shows the total, collision and radiative stopping powers for electrons in water, with values taken from the NIST ESTAR database [120]. Of particular interest in Fig 2.1 is the radiative contribution to the mass stopping power in the VHEE energy range of 50 - 250 MeV, which becomes increasingly significant, and ends up being the dominant contribution beyond 100 MeV. This means that VHEE beams produce a much larger amount of bremsstrahlung within the patient in comparison to clinical electron beams, and therefore the interaction of these photons within the media of the patient become increasingly important for this energy. Such interactions are discussed in the following section.

2.1.1.2 Photon Interactions

In radiotherapy physics, understanding of high energy photon interactions is of particular importance since the majority of radiotherapy treatments are delivered using MV photons. Furthermore, the majority of standardised dosimetry protocols involve calibration for absolute dose from radioactive γ-ray sources such as ^{60}Co, so an understanding of how these particles deposit dose is paramount to characterising the response of such detectors. Electron beams within the VHEE energy range produce a significantly large amount of bremsstrahlung radiation when interacting with matter, and therefore understanding how these interactions contribute to dose deposition within

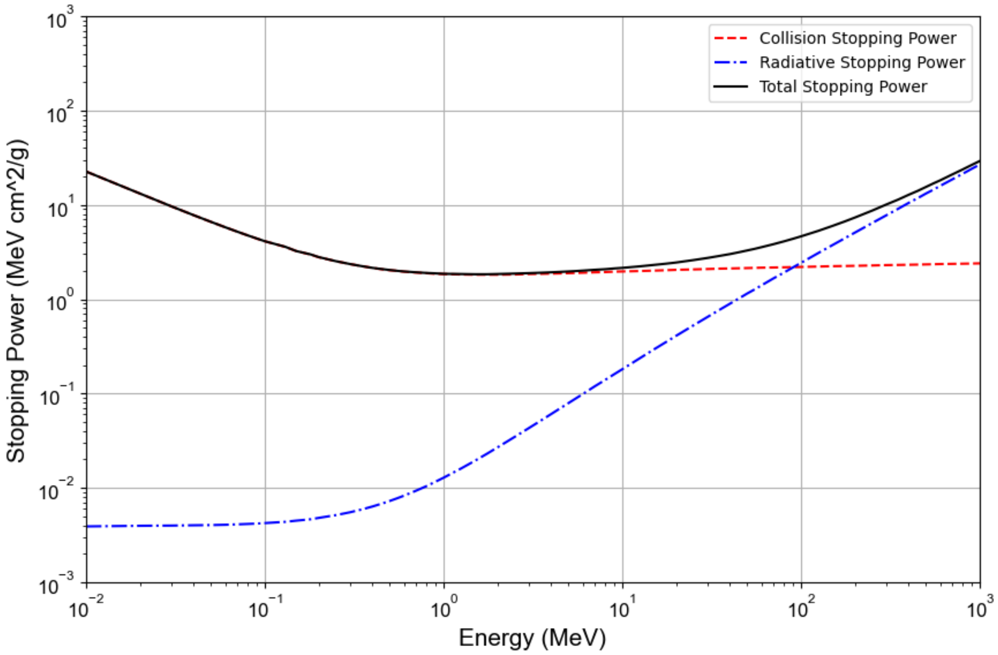

Figure 2.1: Collision, radiative and total mass stopping powers for electrons in water, with values from NIST ESTAR database [120]

the patient as well as secondary particle production is very important. High energy photons, produced either through bremsstrahlung or radioactive decay, are non-ionising particles that deposit their dose indirectly, mostly through interactions with valence electrons resulting in the liberation of these secondary electrons which then go on to deposit their dose a small distance away from the interaction site. This concept is the reason why the dose buildup region is present in MV photon percentage-dose deposition (PDD) curves. The secondary electron and charged particle fluence increases up until the depth of maximum dose deposition, at this point transient charged particle equilibrium (TCPE) is established [121]. From this depth the exponential dose fall-off is observed due to photon scattering and attenuation, which for a monoenergetic photon beam, can be described by:

$$I = I_0 e^{-\mu x} \tag{2.4}$$

where I is the intensity at a given depth x, with initial intensity I_0 and interaction probability μ. This attenuation of photons is primarily through the transfer of energy to secondary particles, mostly electrons, is due to a number of different interactions between the photons and the media of attenuation. The main modes of these interactions, namely: *Rayleigh scattering*, *photoelectric effect*, *Compton scattering*, *pair (and triplet) production* and *photonuclear interactions*. The dominant modes of photon interactions for a range of photon energies are shown in Fig. 2.2.

Rayleigh (or coherent) scattering is when a photon of sufficiently low enough energy interacts with the entire atom and is collectively scattered by all of the atomic electrons. In this interaction no energy is transferred from the photon, but is scattered through a given angle θ whilst transferring momentum, x. The differential cross-section for Rayleigh scattering is directly proportional to the square of the form factor $F(x, Z)(\propto \left(\frac{Z}{E}\right)^2)$. Therefore, F takes its maximum when $\theta = 0$ and no momentum is transferred, and then $F \to 0$ as x increases.

The *photoelectric effect* is the dominant interactions for incident photon energies of up to 26 keV in water. This interaction occurs when an incident photon is absorbed by an atom resulting in the emission of an orbital electron from one of the atomic shells with a kinetic energy: $E = h\nu - E_B$, where $h\nu$ is the energy of the photon and E_B is the binding energy of the electron. The cross section for the photoelectric exhibits discontinuities called absorption edges, which occur when $h\nu = E_B$. This cross section is strongly dependent on atomic number Z, and is proportional to $\left(\frac{Z^4}{E^3}\right)$ [122].

Compton scattering is dominant mode of interaction in soft tissues above 30 keV and below 30 MeV. The interaction is an inelastic scattering process between the incident photon and an orbital electron which results in the scattering of the photon at an oblique angle, θ, and resulting energy, E_γ as well as the liberation of a recoil electron at energy E_{e-} at an angle of ϕ. This process

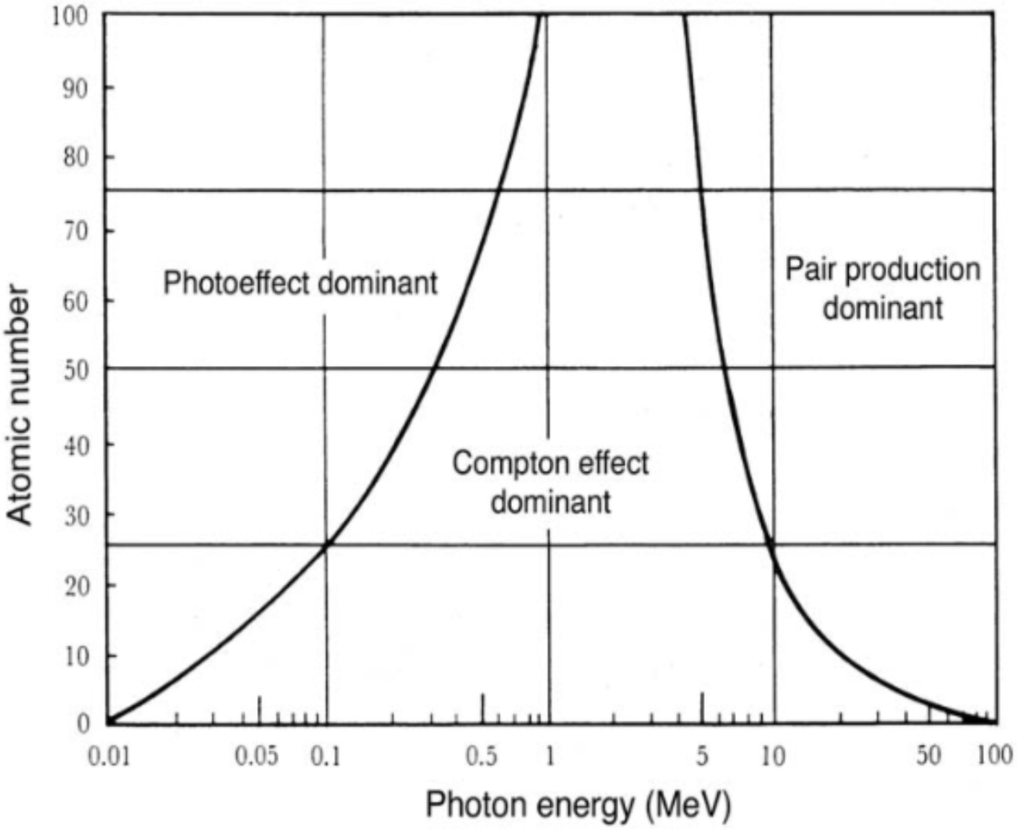

Figure 2.2: The dominant photon interaction mechanisms for photons of energies between 0.01 - 100 MeV. Graph reproduced from [15], with permission from the IAEA.

can be described by the equation:

$$E_\gamma = h\nu' = \frac{h\nu}{1 + \alpha(1 - \cos\theta)} \tag{2.5}$$

where $\alpha = \frac{h\nu}{m_e c^2}$. The energy of the recoil electron is described by $E_{e-} = h\nu - h\nu'$ and its scatter angle can be determined from the relation:

$$\cot\phi = (1 + \alpha)\tan\frac{\theta}{2} \tag{2.6}$$

at high incident photon energies, almost all of the energy is transferred to the electron and the photon is back-scattered. The differential cross-section for Compton scattering per electron can be described by the Klein and Nishina formula [123]:

$$\frac{d_e\sigma_{KN}(\theta)}{d\Omega} = \frac{r_e^2}{2}\left(\frac{h\nu'}{h\nu}\right)^2\left[\frac{h\nu'}{h\nu} + \frac{h\nu}{h\nu'} - \sin^2\theta\right] \tag{2.7}$$

where Ω is the solid angle, and r_e is the classical electron radius given by $r_e = \frac{1}{4\pi\epsilon_0}\frac{e^2}{m_e c^2} \approx$ 2.8179×10^{-15} m. In the low energy limit of $h\nu \rightarrow 0$ the scattering is known as classical Thomson scattering and the cross-section simplifies to:

$$\frac{d_e\sigma_{KN}(\theta)}{d\Omega} = \frac{r_e^2}{2}(1 + \cos^2\theta) \tag{2.8}$$

If the recoil electron produced in Compton scattering is from an incident photon of high energy, this electron may become energetic enough to create further ionisations in the surrounding matter, these secondary electrons are referred to as delta-rays.

Pair production occurs at energies above a threshold of 1.02 MeV ($= 2m_e c^2$). This interaction takes place when a the incident photon is absorbed in the nuclear electric field resulting in the emission of an electron-positron pair in the forward direction. The sum of the kinetic energies of the electron-positron pair is $E^- + E^+ = h\nu - 2m_e c^2$. At incident photon energies of $h\nu >>$

1.02 MeV the average angle of departure from the incident photon direction, $\bar{\theta}$ is:

$$\bar{\theta} \approx \frac{m_e c^2}{\bar{E}} \tag{2.9}$$

where $\bar{E}$ is residual; energy above the threshold energy with $\bar{E} \approx \frac{1}{2}(h\nu - 1.02\,\mathrm{MeV})$. *Triplet production*, is a similar interaction to pair production, but occurs when the incident photon interacts within electric field of an atomic electron, which causes the atomic electron to recoil with energy that is sufficient to be ejected from its orbital shell. This interaction has a threshold energy of 2.04 MeV $(= 4m_e c^2)$, and results in the production of three electrons. The differential cross sections for pair production and triplet production are zero below their threshold energies and then above this energy vary approximately with the square of atomic charge for pair production, ${}_a\sigma_{pair} \propto Z^2$, and approximately with atomic charge for triplet production, ${}_a\sigma_{trip} \propto Z$ [124].

Photon interactions with inner-shell electrons via the photoelectric effect, Compton scattering or triplet production which lead to the ejection of said electron result in inner-shell vacancies. These can lead to either the emission of characteristic x-rays or Auger electrons where the energy is released from the of an outer-shell electron to an inner shell either as a photon or through internal energy transfer to another orbital electron, respectively.

Photonuclear interactions can occur at high photon energies, typically above 10 MeV [125]. These photon interactions are usually of less relevance for conventional MV photon radiotherapy due to the high energy threshold reaction to induce these reactions. However for VHEE radiotherapy, these interactions require consideration due to the high energy bremsstrahlung that is produced following the interaction with the electron beam within the patient. Photonuclear interactions from these bremsstrahlung photons can lead to neutron production and induced radioactivity through the process of photo division. For photon energies in the range of 10 - 200 MeV photonuclear interaction cross-sections are evaluated using the compound nucleus reaction hypothesis - which assumes that the decay of the compound nucleus is independent of how it is formed yet the energy, spin and parity are conserved. In this energy range a photon is absorbed by a nucleus through two main mechanisms, the giant dipole resonance (GDR) and quasi-deuteron photo-absorption process (QD). The cross-section for the photo-absorption process within this entire photon energy range can be described by:

$$\sigma_{abs}(E_\gamma) = \sigma_{GDR}(E_\gamma) + \sigma_{QD}(E_\gamma) \tag{2.10}$$

with $\sigma_{GDR}(E_\gamma)$ and $\sigma_{QD}(E_\gamma)$ being the cross-sections for GDR and QD, respectively. The main channels for these reactions is mostly through (γ, n), (γ, p), $(\gamma, 2n)$, and (γ, pn) reactions. At photon energies of $E_\gamma \lesssim 30\,\text{MeV}$, more specifically at energies of $\approx 25\,\text{MeV}$ for light nuclei and ≈ 12 - $16\,\text{MeV}$ for heavy nuclei, the GDR phenomena occurs. The threshold for a (γ, n) interaction is approximately the binding energy (E_B) for a neutron within a given nucleon, and the giant dipole resonance begins above this threshold. This reaction occurs due to the fact that a photon that has an energy of less than 30 MeV, has a wavelength that is larger than the size of the nucleus and therefore interacts with the nucleus as a whole. This photonuclear interaction excites the nuclear, and is then followed by de-excitation via decay with the production of a neutron. Several models can be used to describe the measured GDR photo-absorption cross-section, $\sigma_{GDR}(E_\gamma)$, but the most suitable which has been confirmed by experimental data is a Lorentzian with the shape of:

$$\sigma_{GDR}(E_\gamma) = \sigma_R \frac{E_\gamma^2 \Gamma_R^2}{((E_R^2 - E_\gamma^2)^2 + E_\gamma^2)\Gamma_R^2} \tag{2.11}$$

where σ_R is the GDR peak cross-section, E_R is the resonance energy and Γ_R is the width of the Lorentzian [126]. The photo-absorption cross-section resonance form in this energy range can be seen from Fig. 2.3. Within the energy range of the GDR the QD component can be assumed to be negligible and therefore $\sigma_{abs}(E_\gamma) \simeq \sigma_{GDR}(E_\gamma)$. Photo-disintegration of the nuclei is the main mechanism for secondary particle production within the GDR energy range, and the main mechanism for neutron production here is the evaporation of neutrons from the excited nucleus [128]. For photo-absorption interactions at photon energies of $E_\gamma \gtrsim 30\,\text{MeV}$, the cross-section can be described reasonably well by the modified Levinger equation [129]:

$$\sigma_{QD}(E_\gamma) = L\frac{NZ}{A}\sigma_d(E_\gamma)p_b \tag{2.12}$$

where L is a constant ≈ 10 for heavy nuclei, σ_d is the cross section for the photo disintegration of the free deuteron, and p_b is the Pauli blocking factor. This cross-section is approximately an order of magnitude lower than that for the GDR. In this energy range, the wavelength of the photons are such that they interact with a neutron-proton pair within a nucleus, a quasi-deuteron, as opposed to the entire nucleus [127]. This process for neutron production is important for high Z materials, and therefore an important consideration for secondary particle generation within the VHEE machine treatment head from bremsstrahlung interactions. During this reaction process, energies greater the

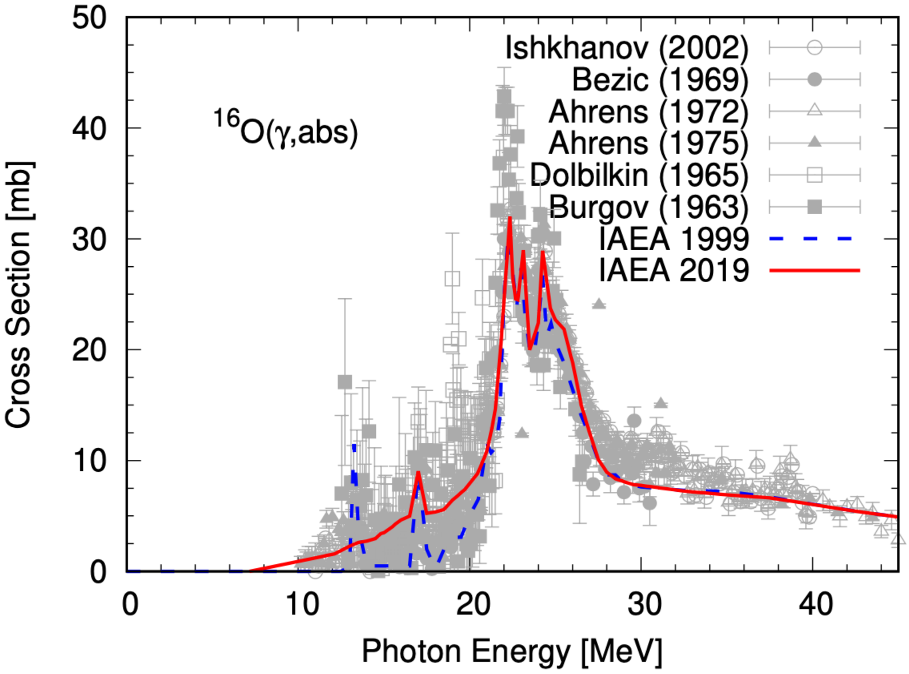

Figure 2.3: Theoretical and experimental photo-absorption cross-sections of ^{16}O. Reproduced from [127], with permission from Elsevier.

nuclear potential are reached by some parts of the nuclei and are hence expelled from the atom. At even higher energies of photons, above approximately 140 MeV, the photonuclear cross-section begins to increase again due to photo-pion production. For electron beams within the VHEE energy range, photonuclear interactions are important to consider due the production of secondary neutrons and induced radioactivity that occur within the patient following a treatment with VHEE beams, and how these contribute to dose deposition and relative biological effectiveness (RBE) of VHEE beams. The neutron yield, Y, resulting from a VHEE beam interacting with matter can be determined from a theory of cascade processes [130, 131] as:

$$Y = 0.572 \frac{E_0 X_0 N_0}{A} \int_{E_{\text{th}}}^{E_0} \frac{\sigma(E_\gamma)}{E_\gamma^2} dE_\gamma \tag{2.13}$$

In which E_0 is the energy of the incident electron, X_0 is the radiation length (= 37.1 g/cm^2), N_0 is Avogadro's number, A is the atomic number of the material, $\sigma(E_\gamma)$ is the cross section for a photonuclear interaction where the energy of the incident photon is between E_γ and $E_\gamma + dE_\gamma$, and E_{th} is the threshold of the photoabsorption by the target hadron. The integral can then be evaluated as:

$$\int_{E_{\text{th}}}^{E_0} \frac{\sigma(E_\gamma)}{E_\gamma^2} dE_\gamma = \frac{A^{\frac{5}{3}}}{444} \text{mbarn MeV}^{-1} \tag{2.14}$$

Initial studies on the use of VHEE beam for radiotherapy used equations 2.13 and 2.14 to evaluate the neutron yield for 150 MeV and 200 MeV electron beams, which gives yields of 0.027 and 0.037 neutrons per incident electron [94]. From this, using flux to dose conversions from [132], DesRosiers *et al* [94] determined that at the position of maximum dose deposition, neutrons can contribute to a approximately 0.2% increase in the dose. Furthermore, the calculation in the increased dose within the patient from induced radioactivity of carbon, oxygen and nitrogen inside the human body was calculated as roughly 0.01%. Consequently, it was determined that the RBE for VHEE beams taking into account secondary neutron production and induced radioactivity following photonuclear interactions from the bremsstrahlung is 1.02 - 1.025 [94]. Conversely, further MC simulation experimental VHEE dosimetry studies performed by Subiel *et al* [115] in 2014 showed a calculated neutron flux for 165 MeV VHEEs in water phantom on the order of 10^{-5} neutrons/cm^2 per primary electron, which is three orders of magnitude lower than previously calculated semi-empirically by DesRosiers *et al* [94]. These results are also consistent with recent VHEE dosimetry and radioprotection simulation studies by Masilela *et al* [133]. It was also concluded by Subiel *et al* [115] that the induced radioactivity within the water phantom was found to be small and therefore only has a negligible impact on the total dose deposited. Once again, this was further confirmed by the first theoretical determination of RBE for VHEE by Delorme *et al* [134] which concluded that VHEE beams are not expected to have a higher biological efficacy than clinical MV or electron beams, and that there are no significant consequences in terms of the biologically-relevant calculated quantities due to the higher probability of nuclear interactions at electrons of this energy.

The secondary particles produced from interactions between the incident electrons, and the bremsstrahlung photons, could be used as a potential tool for indirectly verifying and mapping the dose deposited by VHEE beams within the patient, similar to what is currently used for dose and verification methods in proton and carbon ion therapy such as prompt gamma imaging and in-beam Positron Emission Tomography (PET). The possible application of such methods with VHEE beams is discussed in more detail in Chapter 3.

2.1.2 Introduction to Dosimetric Principles and Quantities

Arguably the most important quantity in the field of radiotherapy physics is absorbed dose, since this is the quantity through which is prescribed by radiation oncologists to treat cancerous tumours as well as being used in the field of radiobiology as a reference for biological irradiation studies. Theoretically, the point quantity of dose, D, refers to the energy that is deposited within an infinitesimally small amount of International Commission on Radiation Units and Measurements (ICRU) [135] as:

$$D = \frac{dE}{dm} \rightarrow \frac{\Delta E}{\Delta m}, \left[\frac{\mathrm{J}}{\mathrm{kg}}\right] = \frac{d\bar{\varepsilon}}{dm} \tag{2.15}$$

where $d\bar{\varepsilon}$ is the mean energy imparted by ionising radiation to matter of mass dm. However, the definition of dose is better represented as an average over a defined region as opposed to an infinitesimally small point since the energy deposition from atomic and subatomic events is discrete with respect to this volume. The unit of the Gray (Gy) is used to describe dose and is defined as: $1\,\mathrm{Gy} = 1\,\mathrm{J/kg}$. It is important to define exactly which medium in which the dose is being referred to since there are differences, for example between dose to water and dose to air since the amount of energy deposited in each of these mediums differs. The understanding of these differences is paramount to the characterisation of detector response for absorbed dose measurements. Considering Eq. 2.15 further, this equation arises from the transfer of energy, ΔE resulting from the kinetic energy loss of the incident charged particle, to a volume of matter of mass m. By assuming that this kinetic energy is lost in discrete steps of straight lines with length Δx, then the stopping power of the incident charged particle can be defined as the kinetic energy lost by the charged particle over a total path length travelled, s, within the volume of matter, $\frac{\Delta E}{\Delta x}$. This value is then related to the force acted on by the medium to cause the incident charged particle to lose energy. This loss of energy is related to the dose, D, by:

$$D = \frac{s}{m} \cdot \left(\frac{\Delta E}{\Delta x}\right) = \frac{s}{V} \cdot \left(\frac{\Delta E}{\rho \Delta x}\right) \rightarrow D = \frac{1}{A} \cdot \left(\frac{\Delta E}{\rho \Delta x}\right) = \phi \cdot \left(\frac{\Delta E}{\rho \Delta x}\right) \tag{2.16}$$

for a many-particle scenario. Here, the normalisation of the particle's stopping power to density, ρ, of the medium is known as the mass stopping power. ϕ is the fluence of incident charged particles upon an area, A, and volume, V, of medium. This equation assumes that rate of energy loss of the charged particle is constant as it traverses the medium and is known as the thin-film approximation. To be able to describe the loss of energy of the charged particles within the medium, a more general equation to describe the deposited dose is used:

$$D = \int_0^{E_{max}} \phi'(E) \left(\frac{dE}{\rho dx}\right)_c dE \tag{2.17}$$

Here, $\phi'(E)$, is the differential charged particle fluence with respect to the charged particle energy, and $\left(\frac{dE}{\rho dx}\right)_c$ is the collision, or electronic, contribution to the mass stopping power, which has been described in Section. 2.1.1.1. One further assumption which is made when calculating the dose within a given volume of interest, is that charged particle fluence remains constant throughout this region and at the point whereby the dose is defined at. This is called charged particle equilibrium (CPE), and requires that the charged particle fluence which enters the region of interest also leaves the region of interest. This therefore requires a limitation on the energy spectrum of the charged particle fluence, in order to exclude energetic delta-rays which produced within this region but deposit their energy through interactions elsewhere. The measurement of absorbed dose to water from a medical linear accelerator (or cyclotron or synchrotron in the case of hadron therapy) underpins almost all practices within radiotherapy physics, from the values used for patient treatment planning to reference values used for machine quality assurance (QA) and commissioning. This quantity is so pertinent since direct measurements of the dose to different mediums are exceedingly difficult and susceptible to large uncertainties as well as requiring many assumption for the measurements. Therefore, it is much more practical to instead maintain one reference quantity which is measured by a standard device. This standard is then easily propagated across all clinical centres using a precise instrument which is calibrated to the standard. Ionisation chambers are the most widely used device for the measurement of of absorbed dose to water from medical linear accelerators. Currently, the primary quantity used to calibrate ionisation chambers is the absorbed dose to water from a ^{60}Co γ-ray source with a near mono-energetic energy spectrum that has a mean energy of 1.25 MeV (although this was previously determined for air kerma measurements from an in air calibration). The calculation of absorbed dose to water is defined by the International Atomic Energy Agency Technical Report Series (IAEA TRS) 398 [136], and the calibration of reference dosimeters for radiotherapy is defined in IAEA TRS 469 [137].

2.1.3 Absolute, Reference and Relative Dosimetry

Absolute Dosimetry refers to the measurement of a ionising radiation quantity using an instrument that has the highest level of metrological quality and is performed in Primary Standards Laboratories, such as the National Physical Laboratory (NPL) in the UK [138]. For the determination of absorbed dose to water, as per the IAEA TRS 398 [136], a water or graphite calorimeter is used, which measures this quantity from the corresponding increase in temperature of either water or graphite from the energy deposited within that medium by the ionising radiation. The reference conditions involve the the calorimeter as placed at the reference depth of 5 cm within a 30 × 30 × 30 cm^3 water phantom, which is positioned with a source to surface distance (SSD) of 100 cm. A 10 × 10 cm^2 collimated ^{60}Co γ-ray beam is used. For example, the absorbed dose to water quantity, D_w, measured by a water calorimeter at a point in water with a distance r away from the thermistor corresponds to a temperature increase at that point, ΔT and is quantified through the relationship:

$$D_w = \Delta T_w c_w k \tag{2.18}$$

where c_w is the specific heat capacity of water and k is a correction which takes into account a variety of defects and disturbances to the temperature increase and dose deposition measurement. Another method for the determination of absorbed dose to water, also as per IAEA TRS 398 [136], involves using a known volume ionisation chamber on a graphite phantom, whereby the measurement is carried out using the same reference conditions as the water calorimeter.

Reference Dosimetry refers to the measurement of absorbed dose to water with an ionisation chamber using the beam of a RT machine in the hospital or institution. The dosimetry procedure is carried out by reproducing the reference conditions that are used by the calibration laboratory for the absolute dosimetry measurement, and is defined by the IAEA TRS 469 [137]. This ionisation chamber is first calibrated to an absolute dosimetry measurement at a calibration laboratory using their standard instrument, which determines a calibration factor, $ND_{w,Q}$ for the ionisation chamber:

$$N_{D,w,Q} = \frac{^{lab}D_{w,Q}}{^{lab}M_{w,Q}} \tag{2.19}$$

where $^{lab}D_{w,Q}$ is the absorbed dose measurement at the calibration laboratory and $^{lab}M_{w,Q}$ is the reading of the ionisation chamber under these reference conditions. Measurements of absorbed dose to water with this reference chamber, $D_{w,Q}$, are then performed using a reference beam of the same quality as that at the calibration laboratory using the RT treatment machine at the hospital. The equation used to determine the absorbed dose to water is:

$$D_{w,Q} = M_{w,Q}N_{D,w,Q}k_Q \tag{2.20}$$

where $M_{w,Q}$ is the average reading of the reference chamber using the reference beam on the RT machine, and k_Q is a beam quality factor to adjust for the quality of the RT machine beam (which is usually using 6, 10, 15 MV photons from a linac) to that of the calibration laboratory (^{60}Co γ-ray beam).

Relative Dosimetry refers to almost every dose measurement performed on the RT machine and are performed mostly under non-reference conditions, Therefore the calibration factor determined from the primary standards laboratory is not necessary [139]. A variety of different detectors can be used for this purpose as opposed to just a specific reference ionisation chamber. These devices are calibrated to the absorbed dose to water measurements made by the reference chamber. The use of such devices include regular machine quality assurance (QA) (for measuring field sizes, percentage depth dose distributions etc.) and for patient-specific QA for comparing measured 2D dose distributions, or the point dose at a specific location within a phantom, to the predicted dose generated by the treatment planning software.

2.1.4 Radiotherapy Beam Monitoring

Within the treatment head of MV linac, or within the nozzle of a proton/ion therapy treatment machine, a beam monitor is located. These devices are used to monitor the "intermediate beam", i.e. the radiation beam prior to any beam shaping and modification, with their positioning within MV linacs, and hadron therapy nozzles [16]. The purpose of this device is to monitor the crucial beam parameters such as the integrated dose, the dose rate, the beam flatness and symmetry (for photon beams, electron beams and passively scattered proton beams) or the beam spot position (for PBS proton and ion beams). Any variations in these parameters detected by the beam monitor outside of pre-defined tolerances is then relayed back to the machine control system to activate the interlock and terminate the beam delivery, or any small detected deviations related to the steering of the beam can be corrected using beam steering corrections. In all external beam radiation and particle therapy treatment machines, large area parallel-plate transmission ionisation chambers are used for this purpose. Since the beam monitor is critical for patient safety when delivering RT from the treatment machine, the International Electrotechnical Commission (IEC) and additional international standards require that there must be at least two independent sealed monitor chambers with independent power supplies and electrometers [140]. In MV linacs, the monitor chamber typically consists of a quadrant design, shown in Fig.2.4, which allow the ionisation chamber to monitor the beam flatness and symmetry along with two separate measurements of the dose and dose rate. In hadron therapy nozzles, the monitoring system consists of two or three transmission ionisation chambers for integrated dose measurements and a spot position monitor, which is either a segmented ionisation chamber or a multi-wire proportional chamber (MWPC). In some cases, mostly for heavy ion therapy synchrotrons, there will be a beam profile monitor prior to the nozzle also.

The integrated dose and dose rates measured by the beam monitoring system are quantified by monitor units (MU). This is defined such that:

$$1\,\mathrm{MU} = 1\,\mathrm{cGy} \tag{2.21}$$

for specified reference conditions measured by the reference ionisation chamber. For MV photons, this is 1 cGy measured at the depth of maximum dose deposition, D_{max}, for a $10 \times 10\,\mathrm{cm}^2$ beam with an SSD of 100 cm [16]. The definition is difficult for proton PBS treatments, but is commonly defined as the same field size as photons (which the proton beam is scanned over) at a pre-defined reference depth. When a treatment beam is delivered, a set number of MU are pre-defined for the treatment, once the measured number of MU is equal to the prescribed MU, a dosimetry interlock terminates the beam.

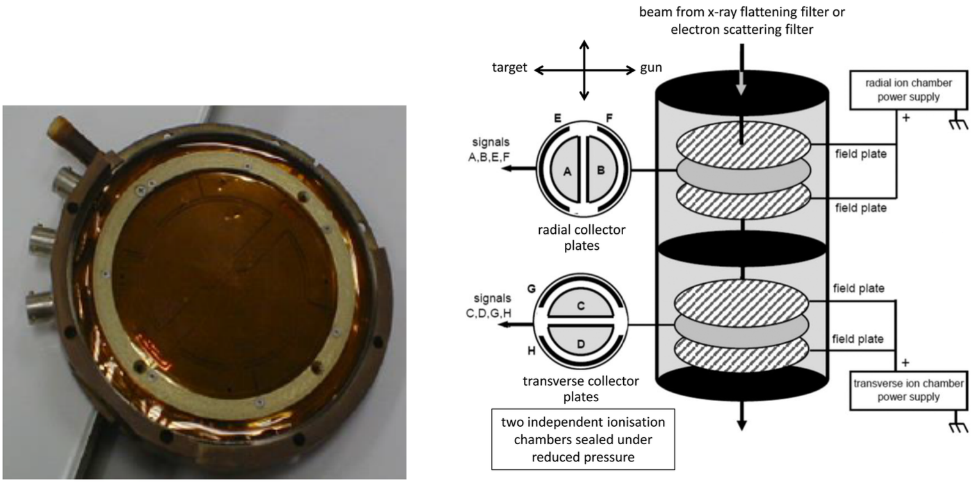

Figure 2.4: Image of an ionisation monitor chamber (left). An example schematic of the quadrant design monitor chamber, where A, B, E and F monitor the radial flatness and symmetry as well as summed together to measure the first integral dose, and C, D, G and H monitor the transverse flatness and symmetry as well as the second integral dose. Images from [16]. From: Handbook of Radiotherapy Physics, Set, 2nd Edition by Philip Mayles, Alan E. Nahum, J.C. Rosenwald, Copyright ©2021 by CRC Press. Reproduced by permission of Taylor & Francis Group.

2.1.5 *In vivo* Dosimetry

In vivo dosimetry (IVD) is a form of quality assurance (QA) which verifies the accuracy of the dose delivery during the treatment of a patient. A dosimeter is placed at a point of interest (usually at a particular point on the patients surface), and the measured dose can be validated against the expected dose (within some tolerance level) [141]. With the ever-increasing complexity of radiotherapy treatments, IVD is becoming more essential in order to detect treatment delivery errors and verify the dose delivered to the patient. IVD is also a key element of the strive towards online adaptive radiotherapy, whereby the dose measured by an IVD detector during treatment can provide feedback to dose delivery in order to make any adaptations for the next treatment fraction in order to minimise delivery errors. However, most of these devices are often limited to providing point dose measurements at a specific location, or a 2D planar measurement of the dose over a certain area. It also necessary to understand the abilities and limitations of the detectors used for IVD in order to obtain an accurate measurement of the dose.

2.2 Detectors for Radiotherapy Dosimetry

2.2.1 Ionisation Chambers

Ionisation chambers (ICs) are by-far the most widely used radiation detector within the field of medical physics. These detectors were also the first of which to be utilised for the measurement of radiation exposure. ICs are a part of the gaseous ionisation group of detectors (which also include proportional counters and Geiger-Müller tubes). They are operated within the voltage range such that the initial charges released through ionisations are collected by the electrodes with an almost 100% efficiency. A schematic of a parallel-plate ionisation chamber is shown in Fig. 2.5 where the chamber consist of a gas-filled cavity with two electrodes, between which a voltage is applied ($\approx$180 V). Following the interaction between the radiation and the gas volume, the electric field causes the electrons and positive ions (formed from ionisations) to drift to the respective positive and

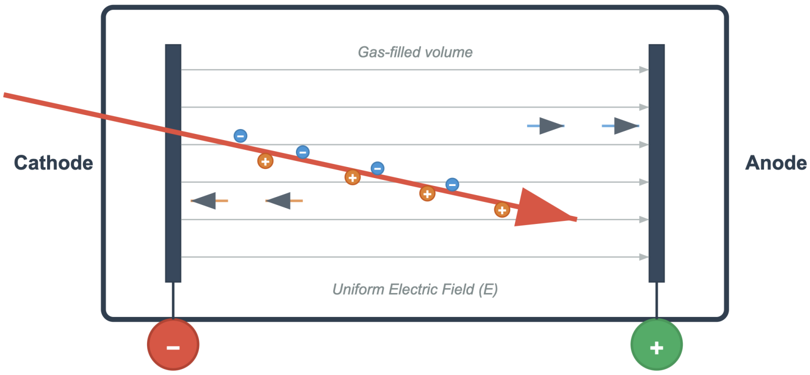

Figure 2.5: A schematic of a parallel-plate ionisation chamber, whereby upon interactions from ionising radiation, positive ions (orange) and electrons (blue) are formed and drift to the respective electrode under the influence of the applied electric field.

negative electrodes, creating a current which is measured by an electrometer [138]. There are three main types of IC: the thimble (or Farmer) chamber, parallel-plate chamber, and spherical chamber. The ICs used clinically are cavity chambers which have walls enclosing the air volume and are characterised by Bragg-Gray Cavity/Spencer-Attix theory which provides a comprehensive method for calculating the dose of ionising radiation absorbed by a medium, through the measurement of a small volume of dose.

The TRS 398 [136] formula for the calculation of absorbed dose to water from an ionisation reading has already been stated in Eq. 2.20, however the value of M consists of many corrections factors:

$$M = M_{raw} P_{T,P} P_{ion} P_{pol} P_{elec} P_{leak} P_{rP} \tag{2.22}$$

where M_{raw} is the raw reading of the chamber, $P_{T,P}$ is the temperature-pressure correction factor, P_{ion} is the ion recombination correction factor, P_{pol} is the polarity correction factor, P_{elec} is the electrometer correction factor, P_{leak} is correction factors for any other contribution not related to ionisation within the cavity and P_{rP} is the correction factor for any off-axis variation in the intensity profile.

Ion recombination effects occur in ionisation chambers when the generated ions of opposite charge recombine before they are collected by the electrodes, resulting in a reduced charge collection efficiency. There are three main mechanisms for ion recombination within the IC cavity volume [142]:

- Initial recombination - recombination of ions from the same charged particle track. Typically only important for high LET radiation [143],
- Ionic diffusion - ions diffuse to electrodes against the direction of the electric field [144].
- General recombination - recombination of ions from different charged particle tracks .

General recombination has a strong dependence on the dose rate, or dose-per-pulse and increases with increasing dose rate. A number of both theoretical and semi-empirical models exist for calculating correction factors for this effect, such as the work by Boag *et al* [145] to correct for the recombination effect in pulsed electron beams. However, as the dose rate, and dose-per-pulse, reach the levels required for the FLASH effect, even these models are not able to sufficiently correct for the extreme recombination that occurs within the IC cavity, and further models and methods to correct the response are required [71].

2.2.2 Radiochromic Film

Film dosimetry is capable of providing 2D measurements of the dose distribution over a large area with a high spatial resolution. Historically, radiographic films were widely used for radiological imaging and radiotherapy dosimetry, this is however widely been phased out due to the long chemical processes required for developing the film along with its energy dependence and non-tissue equivalency. 2D flat panel imagers have replaced radiographic film for radiological imaging and radiochromic film is now widely used in radiotherapy dosimetry. Radiochromic films have the advantageous properties of water (and hence tissue equivalency) [146], ease of handling (i.e. they are self-developing), and have no noticeable dose rate dependence [147, 148, 149] or energy dependence in the MV range [149, 150, 151]. Such characteristics means they are particularly useful for providing comparisons of planar dose distributions for QA purposes, as well for dosimetry of small fields and non-uniform films that have steep dose gradients. The most widely used range of films are those manufactured by Gafchromic, of which there are various models depending on the intended dose range: EBT1-4 (for doses up to 10 Gy), EBT-XD (for doses up to 40 Gy), MD-V3 (for doses between 1 Gy and 100 Gy) and HD-V2 (for doses between 10 Gy and 1000 Gy). The films comprise of an active sensitive layer sandwiched between two protective polyester layers, an example of the composition of EBT3 and EBT-XD film is shown in Fig. 2.6. The main difference between the composition of the different film types is the thickness of the active layer and its chemical composition.

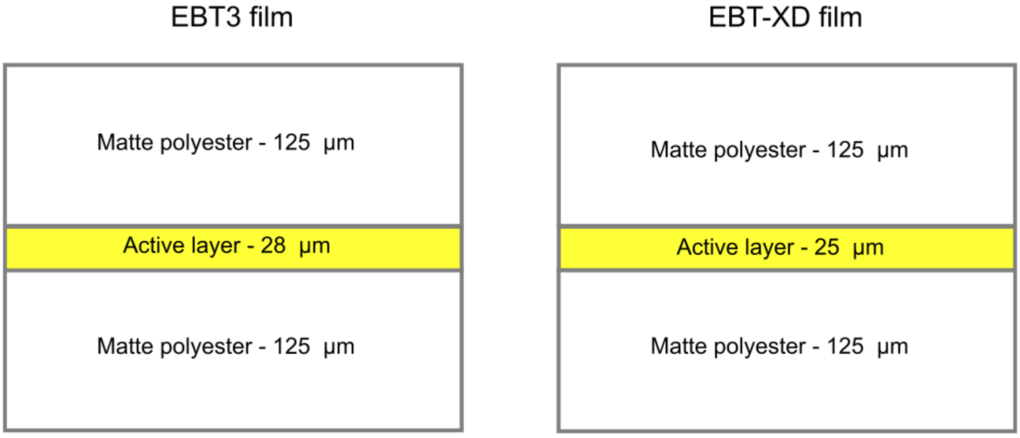

Figure 2.6: The structutre of the constituent layers of Gafchromic EBT3 (left) and EBT-XD (right) radiochromic films. Reproduced from [152], with permission from Elsevier.

The mechanism behind radiochromic film dosimetry is that following interactions with ionising radiation, the constituent monomers within the active layer of the film form into polymers which leads to a visible darkening of the film. This can be quantified by the optical density (OD) of the film. The film is then scanned using a flatbed scanner, from which a broad-band light source and CCD array can provide a transmitted light intensity information using the red, green and blue colour channels. A convolution between the emission spectra of the flatbed scanner light source, the absorption spectra of the film and the spectral sensitivity of the CCD array within the flatbed scanner constitutes the measured OD by the scanner. An example of the absorption spectra of EBT3 and

EBT-XD radiochromic film following irradiation to different doses with 6 MeV photons is shown in Fig. 2.7, where the larger dynamic range of the EBT-XD film can be clearly observed. The primary absorption band for the EBT3 film can be observed to saturate at a lower dose (i.e. when the red channel is most sensitive) and then at a higher dose the secondary absorption bands (i.e. the green channel) becomes more usable [153]. A calibration curve is then established to quantify the relationship between the measured OD and the corresponding dose. The procedure for calibration and analysing the films to obtain the dose is explained in greater detail in Chapter 4.

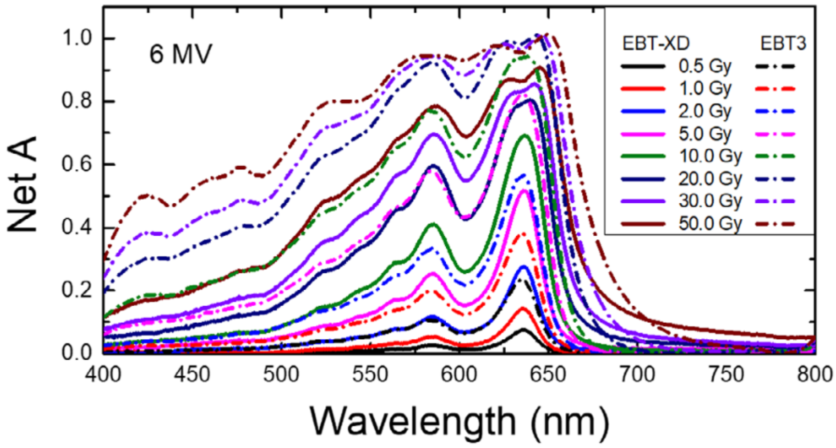

Figure 2.7: Film absorbance spectra across the relevant photon wavelengths for EBT3 and EBT-XD radiochromic films for different doses. Reproduced from [154], ©2019 American Association of Physicists in Medicine.

Whilst radiochromic films have many advantages, there are a number of factors that can affect the response of the films to ionising radiation, this includes the type of radiation, the LET of the radiation, the energy, and dose rate; as well as environmental factors such as temperature, humidity and exposure to ambient visible and UV light [155]. Further considerations for radiochromic film dosimetry when dealing with radiochromic films include film handling, the orientation in which the films are scanned, post-irradiation darkening of the films and the requirement of individual calibration factors for each batch of film. Due to all of these factors, and the numerous procedures and causes of potential uncertainty that radiochromic film dosimetry entails, several studies have concluded that radiochromic films can result in overall uncertainties of 2-5% [154, 156, 157]. The negligible dose rate dependence of EBT3 and EBT-XD films means that they are particularly useful for relative dosimetry for UHDR beams - especially for pre-clinical FLASH studies. Uncertainties of 5% have been reported in the literature for pulsed UHDR electron beams [148, 158].

2.2.3 Alanine

Alanine electron spin resonance (ESR) dosimetry is a passive dosimetry technique for point dose measurements which measures the concentration of unpaired electron radicals caused by interactions between ionising radiation and the alanine pellet [159]. Alanine itself is a amino acid which forms stable radicals following irradiation. The presence of the unpaired electron within the chemical causes paramagnetic properties within the compound. This type of dosimeter is often used for industrial applications with high doses [160]. However at low doses its use is limited due to a low signal-to-noise ratio. Another property of this dosimeter is that it has been shown to be independent of dose rate at delivered doses of less than 5 kGy, and is suitable for measuring instantaneous dose rates of up to 10^{10} Gy/s and mean dose rates of greater than 10^3 Gy/s [75]. This making them ideal for relative dosimetry of UHDR beams [161]. Their small size also means they are very useful for *in vivo* dosimetry and were used for this on the first patient treated with FLASH-RT [52].

2.2.4 TLDs and OSLDs

Thermoluminescent and optically stimulated luminescence dosimeters (TLDs and OSLDs) are also small pellet dosimeters used for passive dosimetry. These principles behind the measuring the dose of ionising radiation is through the trapping of electrons and holes in the energy gap between the valence and conduction band of the insulating crystal material [162]. The interaction of the ionising radiation can generate free electrons and holes (electron vacancies) from the valence band into the conduction band where the electrons would normally recombine with the opposite charge and return to the valence band. However, TLD and OSLD materials are doped with impurities such that there lattice defects in the energy gap which traps free electrons and holes. For determine the dose measured by the TLD or OSLD, the recombination of the electron and hole pairs is induced via an external stimulus of either heat or light photons. This results in the emission of a light curve, the analysis of which is used to determine the dose from a pre-defined calibration factor [163]. However, similar to radiochromic film, TLDs have to be read-out at least 24 hours after irradiation, to avoid the release of low energy trapped electrons. OSLDs are typically of a lower sensitivity to TLDs but can be readout sooner, as well as the potential of active readout emerging. TLDs have been widely investigated for use with UHDR beams and have a well-established dose rate independence up to around 10^9 Gy/s [148, 164]. They have also been frequently used in a number of pre-clinical FLASH studies for IVD verification. Some studies have shown that OSLDs are also capable of providing dose measurements at UHDR, although the dose rate response of these detectors for FLASH is yet to be fully explored [148, 165, 166].

2.2.5 Semiconductor Detectors

Semiconductor dosimeters are active detectors that can provide real-time dose measurements either as a standalone device for a point dose measurement, or can be assembled into linear, 2D or 3D arrays. These detectors convert ionising radiation into an electrical signal, which can be precisely measured by an electrometer [117]. The fundamental mechanism by which semiconductor detectors work involves the interaction of ionising radiation with the semiconductor material, which creates electron-hole pairs. These pairs are then separated and collected by an applied electric field, resulting in an electrical signal proportional to the energy deposited by the radiation. When ionising radiation passes through the semiconductor material, it transfers energy to the electrons in the material, creating electron-hole pairs. A reverse-biased electric field applied across the semiconductor separates these electron-hole pairs. Electrons move towards the positive electrode, while holes move towards the negative electrode. The movement of these charges generates a current, which is collected and measured as an electrical signal [167]. The magnitude of this signal is directly proportional to the amount of radiation energy deposited in the detector. The main types of semiconductor detector employed in radiotherapy dosimetry are silicon diode detectors, diamond detectors, and more recently silicon carbide (SiC) detectors due to their superior radiation hardness characteristics. Both diamond [168] and SiC detectors [169, 170] look to be promising options for real-time dosimetry of UHDR and UHDPP beams, with both showing response linearity well into the UHDR regime [75].

2.2.6 Scintillation and Cherenkov Dosimetry

Radioluminescence (RL) based detection is one of the oldest methods for detecting ionising radiation, and the clinical use of scintillation and Cherenkov based dosimetry can be split into two main categories; fibre based dosimetry - using either a scintillator coupled to an optical fibre, or using the fibre itself as the sensitive medium, which is in turn connected to a photodetector; or through optical imaging, where either a screen, surface or volume that generate scintillation or Cherenkov light are directly imaged by a camera. The interest in fibre-coupled scintillating dosimeters have gained significant attention in recent years due to their ability to perform fast real-time measurements with high temporal and spatial resolution, making them particularly useful for *in vivo* and small-field dosimetry [171]. Whereas for surface or volume imaging, optical cameras are operated with gating and can verify 1D point dose measurements, 2D surface dose distributions, or 3D volumetric dose distributions in real-time [172].

2.2.6.1 Scintillation

Scintillation is a form of RL from an insulator with a wide energy gap that produces light upon the interaction of ionising radiation via a complex multi-stage process [173]:

1. conversion of the incident ionising radiation into electrons and holes in the scintillating material;
2. transportation of these electrons and holes towards the luminescence centres;
3. radiatve recombination of electrons and holes at the luminescence centre, or molecular and atomic transitions, which result in the emission of a characteristic spectrum of light from the material - the exact mechanism varies depending on the type of scintillation material used.

Scintillators can either be organic (such as plastic or polystyrene based), or inorganic (such as doped glasses or crystals). Organic scintillators have the advantage of being almost water-equivalent whereas inorganic scintillators are not and therefore require a more complex dose calibration process. Inorganic scintillators also have a higher light production efficiency due to larger photon interaction cross sections within the material. One issue related with scintillation based dosimetry is that under high LET radiation such as protons and heavy ions, the relation between absorbed dose and light yield becomes non-linear due to quenching effects. The outcome of which can lead to underestimation of the dose at the distal edge of the Bragg peak, where the LET is highest, by around 10% [174, 175, 176].

2.2.6.2 Cherenkov Radiation

Cherenkov radiation is the resulting optical photons that have been emitted when a charged particle travels through a dielectric medium at a phase velocity that is greater than the phase velocity of light in that particular medium. This is caused by the asymmetric polarisation in the dielectric medium that can occur along the particle's trajectory at these phase velocities, and the subsequent radiation of energy with a net constructive interference from the relaxing dipoles which is observed as optical photons [177]. For RT modalities where low energy electrons are the primary source of Cherenkov radiation, the angle at which the Cherenkov radiation is emitted, θ_c strongly depends on the energy. The angle of emission for Cherenkov radiation follows the equation:

$$cos\theta_c = \frac{1}{\beta n} \tag{2.23}$$

where $\beta = \sqrt{1 - \frac{mc^2}{E+mc^2}}$ and n is the refractive index of the dielectric medium [24]. This energy dependence is not ideal for real-time dosimetry or beam monitoring of modalities that operate at a range of energies. For the case of VHEE beams, since the electrons are relativistic i.e., $\beta = \frac{v}{c} \to 1$, the relative variation of the angle of emission of Cherenkov radiation reduces at these electron energies, as can be seen in Fig. 2.8 for 0 - 250 MeV electrons. The threshold energy, E', at which the charged particle must be at in order to emit Cherenkov radiation can be defined as:

$$E' \geq mc^2 \left(\frac{1}{\sqrt{1 - \frac{1}{n^2}} - 1} \right) \tag{2.24}$$

and is shown in Fig. 2.9 for electrons and protons with the thresholds for water, silica and polymethyl methacrylate (PMMA) highlighted. Showing that proton beams at clinical energies do not directly emit Cherenkov radiation, but instead it is via liberation of secondary electrons with an energy above the threshold energy, E. This therefore means the use of Cherenkov optical imaging is not applicable to proton beams. The Frank-Tamm formula [178] can be used for charged particles travelling with an energy $E \geq E'$, to give the number of optical photons dN, that are emitted per unit path length travelled by the charged particle, dx, per unit wavelength dλ:

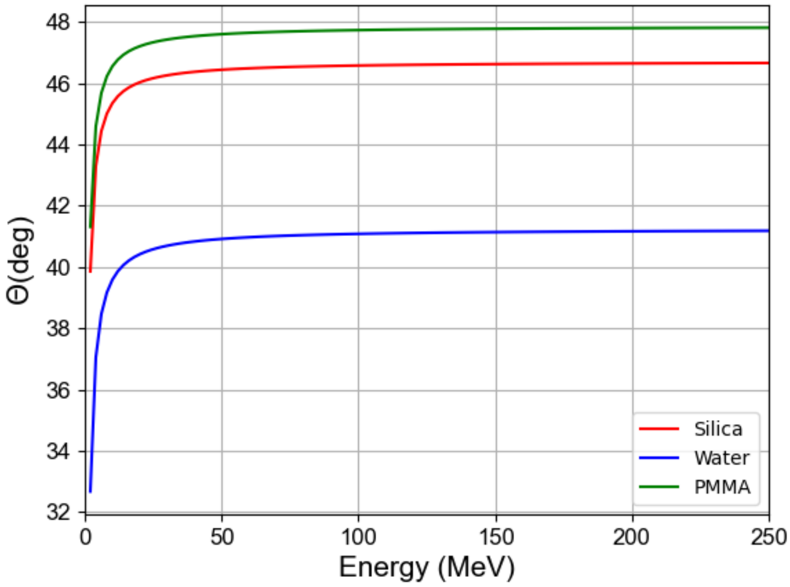

Figure 2.8: Angle of emission of Cherenkov photons from incident electrons of energies up to 250 MeV in silica, polymethyl methacrylate (PMMA) and water

$$\frac{dN}{dx} = \frac{2\pi\alpha z^2}{hc}\left[1 - \frac{1}{\beta^2 n^2}\right]\left(\frac{1}{\lambda_2} - \frac{1}{\lambda_1}\right) \tag{2.25}$$

where h is the Planck constant and λ is the wavelength of the emitted optical photons, α is the fine structure constant ($\approx \frac{1}{137}$), and z is the particle unit charge. From this equation, it becomes clear that the the amount of Cherenkov signal produced within the medium is highly dependent on the amount of the medium exposed as well as its orientation [179]. For this reason Cherenkov radiation, along with its energy dependence, is considered a source of contamination for scintillation fibre optic dosimetry since the amount of Cherenkov radiation produced is not always proportional to the amount dose deposited due to these other factors. However, for applications where the position and orientation of medium are fixed, such as fibres for a beam monitoring detector or the irradiation of a phantom for optical imaging, using Cherenkov radiation as a means for detection has many

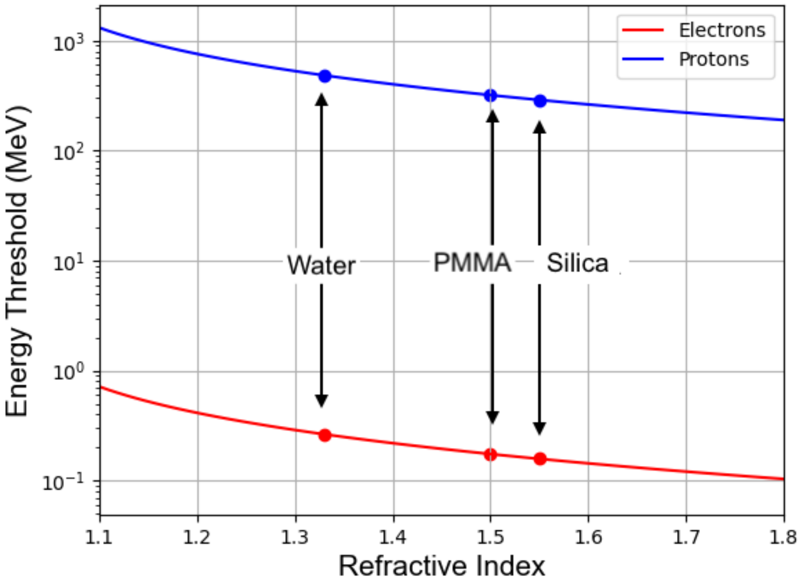

Figure 2.9: Threshold energy of emission of Cherenkov radiation as a function of the refractive index of the medium for protons (blue) and electrons (red). Specific values are highlighted for water, silica and PMMA.

advantages. These include an almost instantaneous emission on the order of 10^{-12} s, as well as no quenching in high LET fields. Cherenkov photons emitted from electron beams within the VHEE energy range, also have the additional benefit of having very little dependence on the angle of emission, as can be seen from Fig. 2.8. It can also be seen from Eq. 2.25 that for a given energy,E, of the incident charged particle, the Cherenkov emission peaks in the ultraviolet region and drops off towards visible light and infrared wavelengths. This is typically the opposite behaviour to what is observed in optical fibres where attenuation is at a minimum for infrared and increases towards visible light and UV, leading to the Cherenkov radiation reaching the photodetector peaking in the visible light wavelength [180].

2.2.6.3 Optical Fibres

In optical fibre-based dosimetry and detector systems, the optical fibres collect the light (in the case of scintillator-coupled optical fibre dosimeters), or generate the light (in the case of Cherenkov detector systems or with scintillating fibres), as well as transport the generated light to the photodetector. The most commonly used type of optical fibre for these applications are solid core fibres. These are commonly made of silicate-based glasses and various plastics such as polymethyl-methacrylate (PMMA) [181]. The structure of the fibre consists usually of a core region surrounded by a cladding region, whereby the core has slightly higher refractive index than the cladding, to allow for total internal reflection to occur. The light is trapped inside the fibre due to the total internal reflection at the boundary of the fibre core. Only photons collected or emitted within the critical angle, θ_{crit} are trapped within the fibre and transported to the photodetector, where critical angle can be derived from Snell's Law as:

$$\theta_{crit} = \sin^{-1}\left(\frac{n_{cladding,air}}{n_{core}}\right) \tag{2.26}$$

where $n_{cladding,air}$ is the refractive index of the optical fibre cladding or air (whichever the optical fibre core is in direct contact with) and n_{core} s the refractive index of the optical fibre core. For fibre detector systems where the light is emitted within the fibre itself, the lights is emitted and transported within both direction, and therefore it is sometimes necessary to use a mirror or reflective surface on on the end of the fibre to maximise light transportation to the photodetector. The loss of signal as the light propagates through the optical fibre is specified in terms of the attenuation length. The main processed contributing to the attenuation of the light being transported through the fibre are absorption and scattering. Self absorption often occurs fibres due to excitations of energy levels within the fibre material resulting in wavelength specific absorption, and is much higher for plastic-based fibres than for glass based fibres. Whereas loss from scattering is caused by Rayleigh scattering at imperfections at the core boundary which means the trajectory of the photon no longer meets the total internal reflection condition and leaves the fibre [182].

2.2.6.4 Photodetectors

A variety of different photodetectors are used for measuring the light output from optical fibre-based and optical imaging based radiation detection. For one 1D measurements of single fibres, photomultiplier tubes (PMTs) and silicon photomultipliers (SiPMs) are commonly employed due to their fast response and high photon collection efficiency. For 2D measurements of fibre arrays or optical imaging of screens and surfaces, multi-channel PMTs, photodiode arrays, charge-coupled

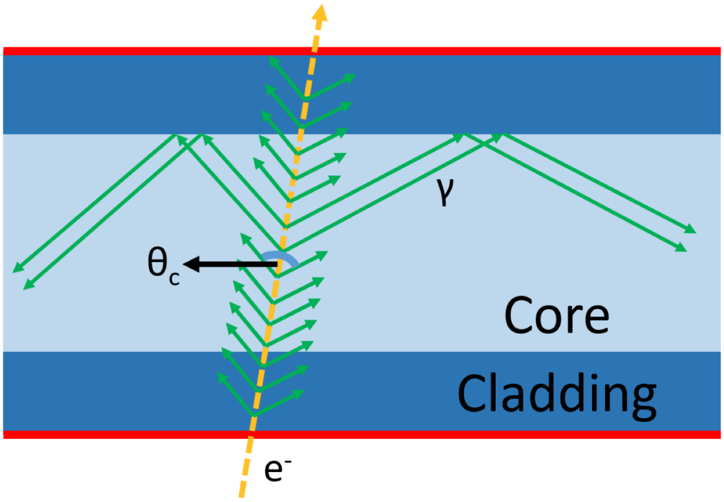

Figure 2.10: Schematic of emission Cherenkov photons (γ) at an angle θ_c from an incident electron traversing an optical fibre at an energy above the threshold of E'. The total internal reflection condition has been met, showing the trapping of optical Cherenkov photons. Image from [180]

device (CCD) cameras and complementary metal oxide semiconductor (CMOS) cameras are popular choices. The basic principles of the operation of a select few of these photodetectors is described in this subsection.

SiPM A Silicon Photomultiplier (SiPM) is solid-state detector consisting of an array of single-photon avalanche diodes (SPADs), called microcells. Upon the interaction of an incident photon with a microcell, an electron-hole pair in the p-n junction is created. This electron is then accelerated by an electric field from a bias voltage that is above the breakdown voltage of the diode, which causes an avalanche of secondary electron-hole pairs. This results in a large pulse of current. The signal output from all of the SPADs is then summed which results in a signal that is proportional to number of incident photons. Due to this process, SiPMs have a high photon detection efficiency, a low operating voltage and fast rise and decay times that are on the order nanoseconds [183].

PMT A Photomultiplier Tube (PMT) is a photodetector that consists of a thin cathode which converts incoming photons to electrons via the photoelectric effect. The electrons ejected from the photocathode are then accelerated towards dynodes whereby secondary electrons are created. These electrons are then accelerated towards towards the next dynode which further increases the number of electrons. This process is repeated several times leading to an exponential increase in the number of electrons, where the electric field between the dynodes increasing successively [184]. This amplified electron signal is then collected at the anode producing a measurable signal. PMTs have the benefit of a high gain and high sensitivity, as well as a fast response time due to the rapid electron multiplication process [185].

CCD Camera A charge-coupled device (CCD) is a camera fitted with a semiconductor chip. The CCD chip is divided up into small pixels. Photons incident on each pixel generate electron-hole pairs in the pixel which is a p-n junction. These pairs are subsequently collected in potential wells with a positive applied voltage at the surface of the pixel. A CCD consists of a large number of pixels arranged in rows and columns. During readout this collected charge is transferred vertically along sensor to readout channels at the bottom of the CCD. The charge is then moved horizontally, one pixel at a time, to the output amplifier, where it is converted to a voltage signal [186]. CCD sensors have the advantage of a low readout noise, however due to the charge transfer process, they are have a limited readout speed.

CMOS Camera A Complementary Metal-Oxide Semiconductor (CMOS) sensor is an active pixel sensory array, whereby each pixel consists of a photodiode that is a p-n junction. Incident photons generate electron-hole pairs and the generated electrons are immediately converted to a voltage within each pixel. Each pixel can be read out independently and in parallel, which allows for faster readout speeds compared to CCD sensors. However since each chip has its own chip has its own circuity, CMOS cameras are more susceptible to electronic noise [187].

2.3 Relevant Principles in Accelerator Physics

This subsection will discuss some of the key concepts in accelerator physics. These concepts are introduced in order to provide a background on the generation and transport of beams for which the use of is described throughout the remainder of this thesis. The accelerator physics theory discussed in this section was taken primarily from the published textbooks and presentation from [188, 189, 190].

The force, F, that a charged particle experiences in the presence of an electromagnetic field is called the Lorentz force:

$$\vec{F} = q(\vec{E} + \vec{v} \times \vec{B}) \tag{2.27}$$

where q is the unit charge of the particle, $\vec{v}$ is the velocity of the particle, $\vec{E}$ is the electric field strength, and $\vec{B}$ is the magnetic field strength. From Eq. 2.27 it can be seen that the magnetic force is perpendicular to the particle movement and therefore contributes to the transverse motion of the particle. By equating the Lorentz force to the centripetal force that causes the circular motion of the charged particle within the magnetic field, its motion can hence be described by:

$$B\rho = \frac{pc}{q} \tag{2.28}$$

where ρ is the bending radius, and p is the momentum of the particle. The quantity $B\rho$ is described as the magnetic rigidity of the particle, and defines the the value of the magnetic field strength to achieve a certain bending radius. In accelerator physics, the Frenet-Serret coordinate system is used to define the motion of each particle relative to a reference particle that travels along an ideal trajectory through the accelerator with a path length, s, with momentum p_0. Within this coordinate system x, y, and z are used to define the horizontal, vertical, and longitudinal displacements, respectively, to the ideal reference trajectory, as can be seen in 2.11. The remaining coordinates within the system x' and y' describe the horizontal and vertical divergence from the ideal trajectory, and δ is the fractional offset in longitudinal momentum, which can be defined as:

$$x' = \frac{dx}{ds} \qquad y' = \frac{dy}{ds} \qquad \delta = \frac{p - p_0}{p_0} \tag{2.29}$$

The x and y are decoupled in first order, but for simplicity, throughout the remainder of this section the treatment x and y can be assumed to be identical, i.e, the equations expressed in terms of x, are equally applicable to the y direction also.

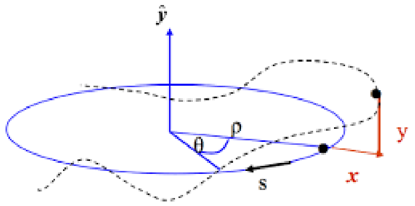

Figure 2.11: Graphical depiction of the Frenet-Serret coordinate system for describing the motion of a charge particle in a magnetic field. Image from [191]

2.3.1 Transverse Beam Dynamics

The transverse motion of particles undergoing betatron oscillations as they pass through magnetic elements can be described by Hill's equation:

$$\frac{d^2x(s)}{ds^2} + K(s)x(s) = 0 \tag{2.30}$$

where $K(s)$ is a non-constant restoring force which depends on the the longitudinal displacement s and is a periodic function, i.e., $K(s+L) = K(s)$ where L is the lattice period. The general solution to the equation is in the form of a quasi-harmonic oscillator whereby the phase and amplitude depend on the position s:

$$x(s) = \sqrt{\beta_x(s)J_x(s)}\cos(\mu_x(s) + \mu_{x,0}) \tag{2.31}$$

where J_x is the action or Courant-Snyder invariant, $\mu_{x,0}$ is an integration constant, μ_x is the betatron phase and $\beta_x(s)$ is the beta function, and is a periodic function given by the properties of dipoles and quadrupole lattices. $\beta_x(s)$ is one of the Twiss parameters along with, $\alpha_x(s)$ and $\gamma_x(s)$ which are defined as:

$$\alpha_x(s) = -\frac{1}{2}\frac{d\beta_x(s)}{ds} \qquad\qquad \gamma_x(s) = \frac{1+\alpha_x^2(s)}{\beta_x(s)} \tag{2.32}$$

From the general solution for the Hill's equation in Eq. 2.30, $x(s)$, in Eq. 2.31 and its derivative, $x'(s)$, this can be solved for J_x:

$$J_x = \gamma_x(s)x^2(s) + 2\alpha_x(s)x(s)x'(s) + \beta_x(s)x'^2(s) \tag{2.33}$$

This equation gives a parametric representation of the motion of the particle in a circular accelerator as it traces out an ellipse in phase space after multiple turns, as demonstrated in Fig.2.12. The shape and orientation of this ellipse is given by the Twiss Parameters. As the particle moves through a linear accelerator the ellipse constantly changes since the Twiss parameters are not constant. Liouville's theorem states that in an ideal accelerator, if there is no beam energy change, then the area of the ellipse in phase space mapped out by the particle along its trajectory must remain constant. This applies under the conditions of Hamiltonian dynamics, meaning there are no non-conservative forces. Non-linear elements, such as sextupoles, as well as collimation and beam losses processes, can alter the phase space area. To illustrate the motion of a beam composed of the phase space of many individual particles, each with its own action, one can select an area in phase space that includes a specific fraction of the beam, whereby this area is defined as the emittance of the beam. Particle distributions within phase space usually have a Gaussian transverse distribution;

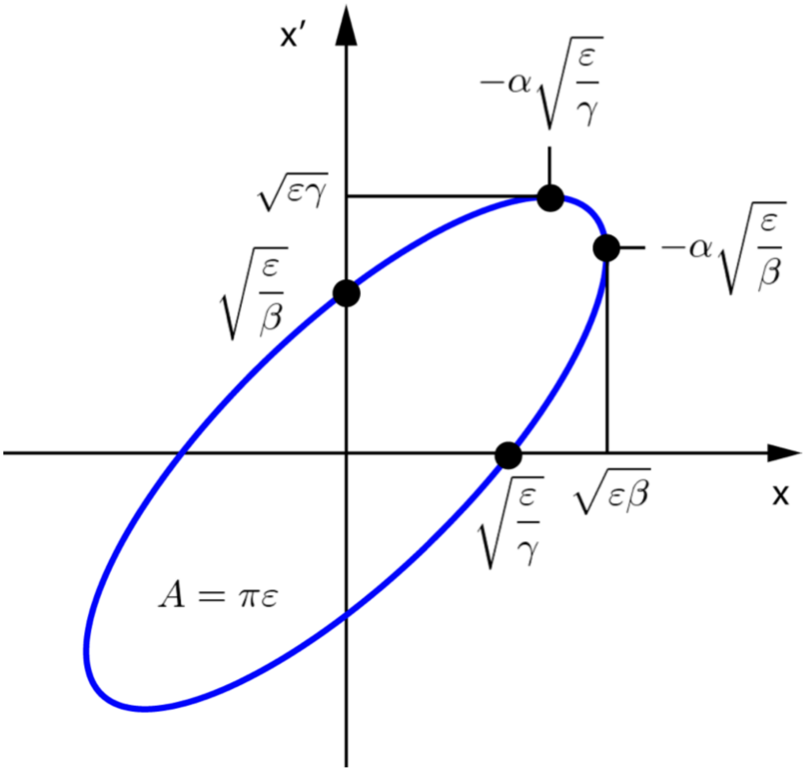

Figure 2.12: The Twiss ellipse in horizontal xx' phase, showing the relation of the Twiss parameters to x and x', where ϵ is equivalent to J_x. Image from [192]

such distributions can be described using a covariance matrix called the beam matrix.

$$\Sigma_x = \begin{pmatrix} \sigma_{11} & \sigma_{12} \\ \sigma_{12} & \sigma_{22} \end{pmatrix} = \begin{pmatrix} \sigma_x^2 & \sigma_{xx'} \\ \sigma_{xx'} & \sigma_{x'}^2 \end{pmatrix} = \begin{pmatrix} \langle x \rangle & \langle xx' \rangle \\ \langle xx' \rangle & \langle x'^2 \rangle \end{pmatrix} \tag{2.34}$$

where $\sigma_{21} = \sigma_{12}$ due to the symmetry of the covariance matrix. The square root of this matrix's determinant is proportional to area of the beam distribution in phase space, which is also defined as the geometric emittance:

$$\epsilon_{geom} = \sqrt{\boldsymbol{det}\Sigma_x} = \sqrt{\sigma_x^2\sigma_{x'}^2 - \sigma_{xx'}^2} \tag{2.35}$$

and is proportional to the area of the beam distribution in phase space. The root mean squared (RMS) emittance, ϵ_{rms}, of the beam distribution is defined using the moments of the distribution:

$$\epsilon_{rms} = \sqrt{\boldsymbol{det}\Sigma} = \sqrt{\langle x^2 \rangle \langle x'^2 \rangle - \langle xx' \rangle^2} \tag{2.36}$$

and does not rely on the transverse distribution of the beam being Gaussian. The beam size, which measured as the standard deviation of the Gaussian distribution, σ_x, and divergence, $\sigma_{x'}$, are related to the RMS emittance through the relations:

$$\sigma_x(s) = \sqrt{\epsilon_{rms}\beta_x(s)} \qquad\qquad \sigma_{x'}(s) = \sqrt{\frac{\epsilon_{rms}}{\beta_x(s)}} \tag{2.37}$$

As the the beam undergoes acceleration, i.e. the momentum of the beam increases, adiabatic damping causes the transverse phase space angles to decrease and hence reduces the area of the ellipse in phase space. It is therefore helpful to normalise the emittance such that this quantity remains constant under acceleration as:

$$\epsilon_n = \beta\gamma\epsilon_{rms} \tag{2.38}$$

where in this case β and γ are the relativistic Lorentz values of the beam (not to be confused with the Twiss parameters). It is possible to obtain a value for the emittance of a beam by deriving the beam matrix from measurements of the beam size. One method to do this is through quadrupole tuning; whereby a quadrupole, a drift space and movable scintillating screen are used to make measurements of the RMS beam size across a range of quadrupole focusing strengths from which the RMS emittance and Twiss parameters of the beam can be deduced.

2.3.2 Charged Particle Acceleration in Linear Accelerators

Linacs, cyclotrons and synchrotrons are all used for accelerating charged particles to the required energies in radiotherapy and particle therapy. However, since this research is based on VHEE radiotherapy, the principle of acceleration of electrons in a radiofrequency (RF) linac are described. In RF linacs, the charged particles are accelerated by electromagnetic fields that are contained within resonant cavities, which are powered by sinusoidal time-varying pulsed RF sources, such as magnetrons or klystrons. The simplest description of the principle of linear accelerators is using the Wideroe scheme, through what is known as a drift-tube linac [188]. Here, a series of cylindrical electrodes called drift tubes are spaced along the accelerating section. The drift tubes shield the charged from decelerating electric fields. The resonant frequency of the alternating electric field is synchronised with the velocity of the particles, ensuring they receive acceleration only when they traverse the gaps between the drift tubes. The distance between the gaps increases along the length to account for the increasing velocity of the particle. For high β particles that are relativistic, drift-tube linacs are less efficient since much higher RF frequencies are required to achieve the higher accelerating gradient. In this frequency range, cylindrical RF cavities are used through establishing a standing wave (SW) in the $\mathrm{TM}_{0,1}$ mode, which is a resonance condition that depends on both the cavity dimensions as well as frequency of the microwave RF source. At resonance, the longitudinal electric field component is at a maximum whilst the radial component is zero, and the magnetic field is only radial with no longitudinal component [16]. Alternatively, travelling wave (TW) structures are used. In TW structures the wave co-propagates through the cavity with the particle, similar to as in a waveguide, whereby the particle velocity is matched to the phase velocity of the wave [193].

Here, the beam absorbs energy from the wave and it is continuously accelerated. TW accelerating structures are commonly used for relativistic electrons since their velocity can be assumed constant along the entire accelerating structure. For non-relativistic particles, such as electrons at injection, or ions, whereby the velocity increases during acceleration; it is difficult to modulate the phase velocity [194]. For high energy electron accelerators, such as those required for VHEE beams: proposed designs include SW cavities for the injector, and TW cavities for the accelerating structure [97].

2.3.2.1 Velocity Bunching

The charged particles must be synchronous with the accelerating wave when in injected into the linac in order to achieve the optimal acceleration. Therefore, they have to enter the linac on a phase that is well-defined with respect to the oscillating sinusoidal field. Subsequently, this phase needs to be maintained during the acceleration process. However, if the phase in which the charged particles are injected aligns to the wave crest, any slight discrepancy in phase will cause an eventual loss of synchronicity. Injecting the beam at a slightly lower phase, a synchronous phase, will cause particles to oscillate around the synchronous phase during the process of acceleration, as shown in Fig. 2.13. This causes any particle that arrives ahead of the central phase to experience a smaller accelerating force, and any particle arriving later will receive a greater accelerating force. This results in the particles bunching together, into what is called an RF bucket, at a frequency through which the RF is applied to the cavities [195]. The off-energy particles oscillate around the synchronous phase, in energy-position space, during acceleration - forming a phase space ellipse. Since this RF bunching relies on particle velocity variations, it works optimally for lower energy electrons [194]. As the energy increases, the rate of compression drops. Therefore it is optimal to perform the bunching before the main acceleration stage.

The most common frequency for radiotherapy electron linacs is S-band (2 - 4 GHz). However, to achieve higher accelerating gradients to reach the necessary energies for VHEE beams within a reasonable space, higher gradient RF cavities that are either C-band (4 - 8 GHz) [97], or X-band

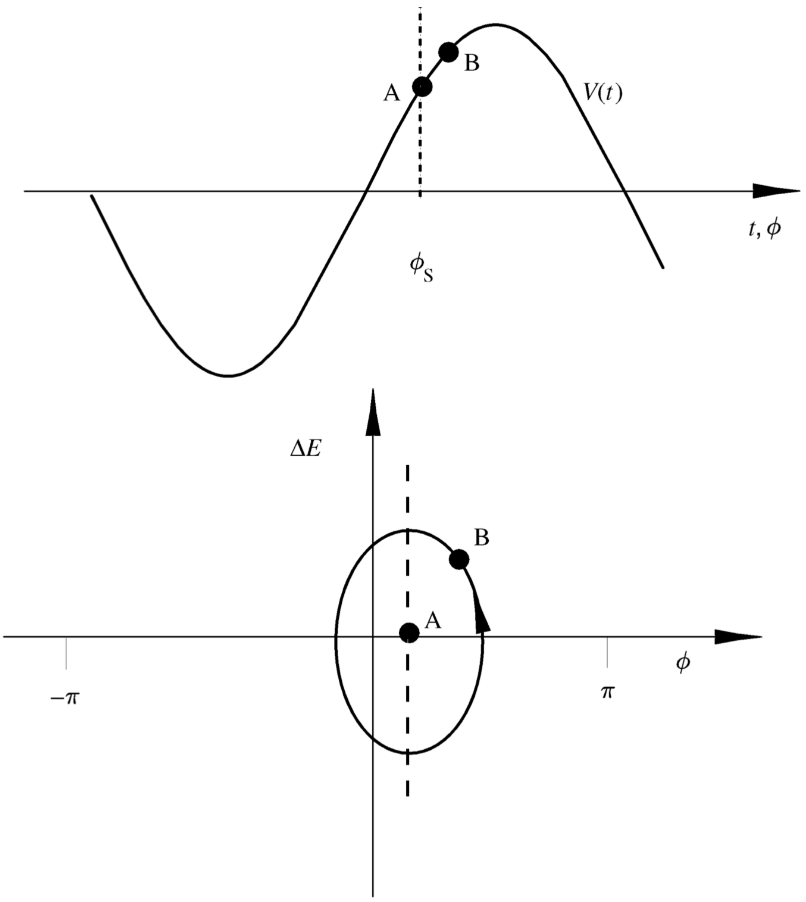

Figure 2.13: Plot of accelerating potential $V(t)$ against time or phase, t or ϕ, showing two particles, A (on the synchronous phase, ϕ_s, and B (off phase) (top). Along with a plot of energy offset, ΔE against phase, ϕ showing the oscillation of the off-phase particle, B, around the synchronous particle, A, in longitudinal phase space as they are accelerated (bottom). Image from [188]

structures, such as those proposed for CLIC, (8 - 12 GHz) [96] are proposed for VHEE linacs.

2.4 Concluding Remarks

The fundamental physics principles, methods, and their underlying concepts that have been outlined in this chapter provide important background and groundwork for the rest of the work presented in this thesis. Much of the work in the subsequent chapters includes the descriptions of more specific theory and methods which is relevant to the results presented. Therefore, the methods introduced here are expanded upon as needed in the sections of each chapter. The theory and concepts of beam-matter interactions, namely for electrons and photons, discussed in Section 2.1.1 is fundamentally important firstly for understanding the transport of these beams through medium and how they deposit energy, and secondly for the resultant secondary particle production, the likes of which will be discussed in greater detail in Chapter 3. The detector and dosimeter concepts outlined in Section 2.2 provide an important introduction and background to a number of detectors which are used in Chapters 4 and 5.

3 Monte Carlo Characterisation of VHEE Interactions for Dose Monitoring

3.1 Introduction

A number of studies have been performed examining the dosimetric characteristics and interactions of VHEE beams, particularly looking at the percentage depth dose distributions, the lateral spread and beam penumbra [94, 95, 100, 131, 196], as well investigating contributions to the dose deposited inside the patient or phantom due to secondary neutrons and induced radioactivity [94, 115, 131, 133, 197]. Whilst the work in this chapter uses a similar setup for the basis of the Monte Carlo simulations of VHEE interactions, the aim of this study is to assess the resulting secondary particles from these interactions that are emitted from the target and evaluate their feasibility for indirect *in vivo* dose verification methods and other radiation detection methods, such as for machine and patient-specific QA applications.

3.1.1 *In vivo* Dosimetry Methods

In vivo Dosimetry (IVD) measurements, as previously introduced in Section 2.1.5, can be divided into a number of different categories. The first of which being direct or indirect measurements. Direct IVD measurements involve those in which a radiation detector is used to measure the radiation beam directly, and are often small detectors which are placed on the patient. Direct IVD methods can be split into two further categories of online and offline measurements. Online measurements are those made with a detector that can provide real-time measurements, such as diode detectors and fibre-coupled scintillator detectors. The other type are offline detectors, and are those that require post processing after irradiation, examples of these include radiochromic film, OSLDs and TLDs. Indirect methods measure signals resulting from interactions between the beam and the patient tissue. The most common method for indirect IVD measurements currently is transit dosimetry using an Electronic Portal Imaging Device (EPID). EPIDs are flat panel amorphous silicon (a-Si) detectors that were intended for MV imaging the patient for verification of the treatment setup, and are positioned parallel to the treatment head on the opposite side of the patient. These detectors also present useful dosimetric characteristics and are now commonly used for IVD verification methods. The EPID detector measures the beam fluence exiting the patient, and then uses either back-projection or forward-projections methods to verify the dose delivered to the target volume [141, 198, 199]. Forward-projection methods involve predicting the dose distribution/image that is measured by the EPID during the treatment, and then compare this to the actual measured values [200, 201]. Back-projection methods are more complex and involve reconstructing the dose delivered to the patient from the measured signal on the EPID using iterative convolution technique, this method can allow for the potential fully reconstructing the 3D dose distribution within the patient [202, 203, 204]. In hadron therapy where the Bragg peak is utilised there is little to no exit dose. Research into indirect verification methods is a particularly active area of research for proton and heavy ion therapy because of this and additionally verifying the longitudinal positioning of the Bragg peak, which is extremely sensitive to variations in tissue density. Therefore, it is important to be able to maximise the therapeutic benefit of proton therapy to ensure the Bragg peak is positioned correctly. Consequently, alternative indirect IVD verification measurements utilise the measurement of secondary radiation resulting from interactions between the primary beam and the patient. Such techniques aim to correlate the measurements of these signals and determine the range of the beam within the patient, as well as attempting to reconstruct the dose distribution within the patient from these signals [205, 206]. One of the first techniques developed for this purpose was the measurement of positron annihilation (PA) gamma rays in order to reconstruct the β^+ activity within the patient using PET detectors, with the initial aim of correlating the measured activity to the range of hadron beam. Although more recent techniques look to reconstruct the dose distribution from the β^+ activity [207, 208, 209]. An alternative novel method to in-beam PET imaging is the detection of prompt gamma (PG) rays. These high energy photons are emitted almost instantaneously at characteristic energies following the de-excitation of target nuclei, from which the location of the peak in the signal can be correlated to that of the distal edge of the Bragg peak [210, 211, 212, 213]. Another such indirect imaging technique is ionising radiation acoustic imaging (iRAI), whereby ultrasound detectors can be used to measure the pressure waves generated from the energy released when the dose is deposited [214, 215].

3.2 TOPAS Monte Carlo Simulation Setup

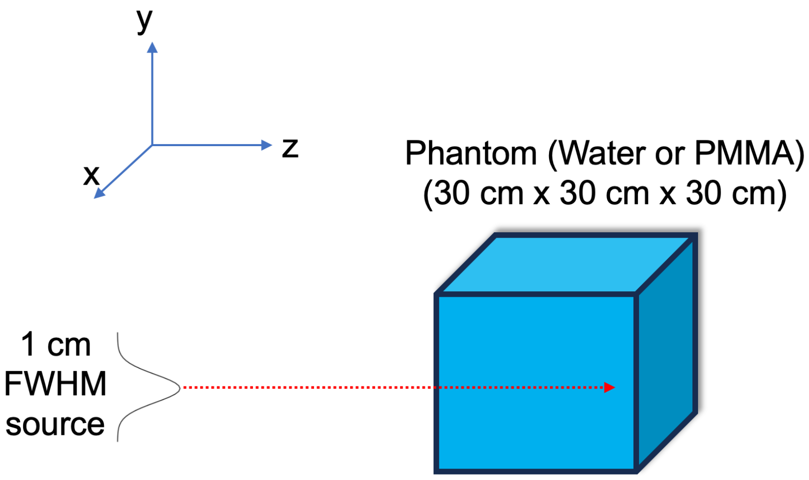

Figure 3.1: Schematic of the TOPAS Monte Carlo simulation setup, whereby a 200 MeV electron or proton beam with a transverse Gaussian distribution with a FWHM of 1 cm is targeted towards a $30 \times 30 \times 30\,\mathrm{cm}^2$ water or PMMA phantom, with a source to surface distance (SSD) of 100 cm.

Monte Carlo (MC) simulations were performed using the TOPAS (Tool for Particle Simulation) Geant4 MC software. TOPAS MC simulation software built on the Geant4 toolkit and is specifically designed to facilitate the modeling of RT modalities. TOPAS uses a parameter control system to provide access to Geant4's functionality [216]. The MC software code was initially validated against proton therapy measurements from the Massachusetts General Hospital (MGH) beamline.

Geant4 has been widely benchmarked in medical physics and is comparable to other MC codes like PENELOPE for radiation shielding applications [217]. For VHEE beams, TOPAS has been validated through comparisons with FLUKA, showing good agreement in dose distributions and beam spread [196]. The MC simulations were performed to evaluate the secondary particle production following the irradiation of a water or PMMA phantom by a mono-energetic 200 MeV VHEE beam. Additionally, a simulation using a 200 MeV proton beam was also performed to compare the magnitude of the secondary particle production for indirect IVD methods that are being researched for proton therapy. In order to ensure that results produced from these MC simulations could be comparable to other published work on VHEE MC simulations, a very similar setup to the used by Masiela *et al* [133] was used for this work. A schematic shows the setup in Fig. 3.1. The setup involved a Gaussian beam source with an full-width half maximum of 1 cm. The $30 \times 30 \times 30\,\text{cm}^3$ phantom was positioned at source-to-surface distance (SSD) of 100 cm. The outer walls of the phantom were defined as the phase space scorer, to score the secondary particles leaving the phantom by applying appropriate filtering methods. For each simulation a total of 10^7 histories were used. The *QGSP_BERT_HP_EMZ* reference physics list was used for all simulations in this chapter. QGSP (Quark Gluon String model with Precompound model) and BERT (Bertini-style Cascade) were applied for hadronic interactions above and below 12 GeV respectively, with the FTF (Fritiof) model handling the transition between them. Geant4 addresses neutron interactions—including radiative capture, elastic and inelastic scattering, and fission—using the High Precision (HP) neutron model. The electromagnetic physics options were specified by the *emstandard_opt4* physics list, that provides high accuracy for electron and photon transport. It is optimised for medical physics and space applications requiring precision between 100 eV and 100 TeV [218]. Additionally, the *g4optical* physics module was also used for investigating the Cherenkov radiation generation.

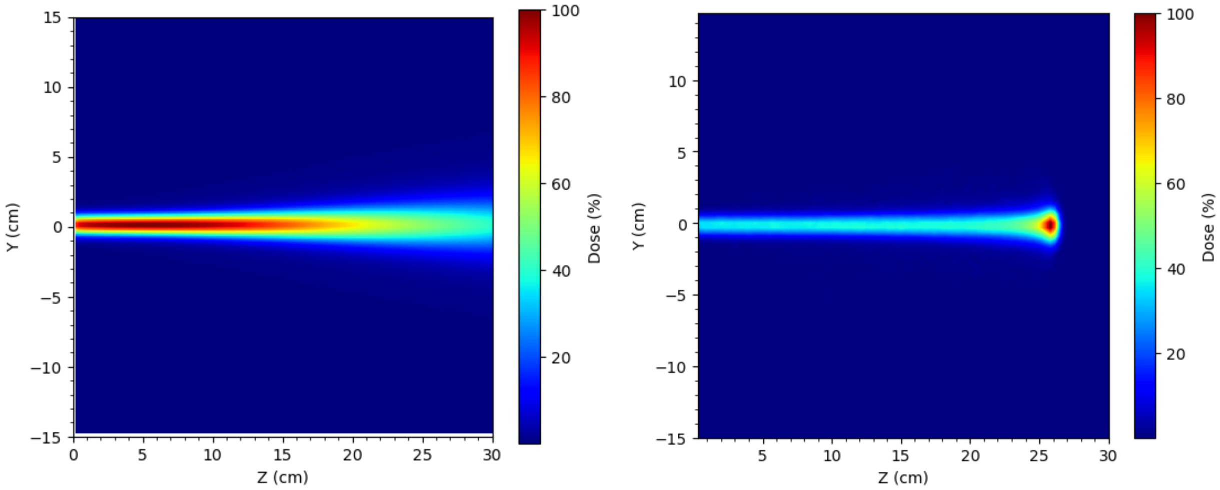

Figure 3.2: 200 MeV VHEE (left) and proton (right) 2D dose distributions within a water phantom, scored with a bin size of 0.2 mm in the z and y direction.

3.3 Dose Distribution Characteristics

The resulting 2D dose distributions for the 200 MeV Gaussian VHEE and proton beam with a FWHM of 1 cm irradiating the water phantom in the $z - y$ plane are shown in Fig. 3.2. Firstly, it can be seen that the VHEE dose distribution is much more continuous than that of the proton beam, whereby most of the dose deposited is concentrated around the Bragg peak region. Therefore, from this information it can be assumed that *in vivo* range verification techniques such as PG imaging, and iRAI, that rely on the detecting the increase in signal from the distal edge of the Bragg peak would not be as useful for VHEE beams. The more continual nature of the VHEE dose distribution does mean that transit dosimetry methods, such as using EPID detectors could be employed for IVD methods however. For this particular simulation, the exit dose of the VHEE beam for a 30 cm water-equivalent thickness phantom was 61.2%, therefore showing that there would be a significant dose absorbed by the EPID detector. Whilst MV photon beams or VHEE beams with an energy other than 200 MeV were not simulated in this study. The work by Böhlen *et al* [100], as shown in Fig. 1.12 showed that for a $10 \times 10\,\text{cm}^2$ flat beam field size, VHEE beams at energies of above 100 MeV have a larger exit dose than that of 6 MV photon beams in a 35 cm water-equivalent thickness phantom. However, for $3 \times 3\,\mathrm{cm}^2$ 100 MeV VHEE beams have an exit dose of less than 5% and are much lower than that of MV photon beams. The Gaussian VHEE beam simulated also showed an increase in transverse beam size (σ) of 147.7% from the position of maximum dose deposition to the exit, and 211.7 % from the entrance beam size to the exit beam size. Furthermore, the study by Böhlen *et al* [100] showed that for all VHEE energies, the lateral spread of the beam penumbra for the uniform beams was higher than that of MV photon beams at the exit of the water phantom with a 35 cm water-equivalent thickness, previously shown in Fig. 1.13. However, the difference between the 200 MeV VHEE beam and 6 MV photon beam can be seen to be less than 1 cm. This demonstrates that the applicability of transit dosimetry methods for IVD for VHEE beams depends on the energy that is used, both in terms of the exit dose and also in terms of the lateral spread of the beam as it passes through the target or patient, since this will dictate the level of complexity of the algorithms for calculating or monitoring the deposited dose. However, EPID-based transit dosimetry methods for IVD verification of VHEE beams appears to be a promising method, mostly due to the fact that the longitudinal dose deposition properties of VHEE beams are similar to those of MV photon beams.

3.4 Secondary Particle Production Comparison

The first aim of the MC simulation evaluations looked to quantify the resulting secondary radiation production between the 200 MeV VHEE and proton beam irradiation. The total number of bremsstrahlung photons, Positron Annihilation (PA) photons, Prompt Gamma (PG) photons, neutrons and Cherenkov photons scored leaving both the water and PMMA phantom were normalised to the maximum dose deposited by the primary radiation beam within the phantom. The resulting comparison between these values for a VHEE and proton beam irradiation is shown in Fig. 3.3. The first observation that can be made from Fig. 3.3 is that the largest source of secondary radiation out of those compared is Cherenkov radiation; with the highest yield being produced by the VHEE beam interacting with the PMMA phantom. The Cherenkov radiation produced by the

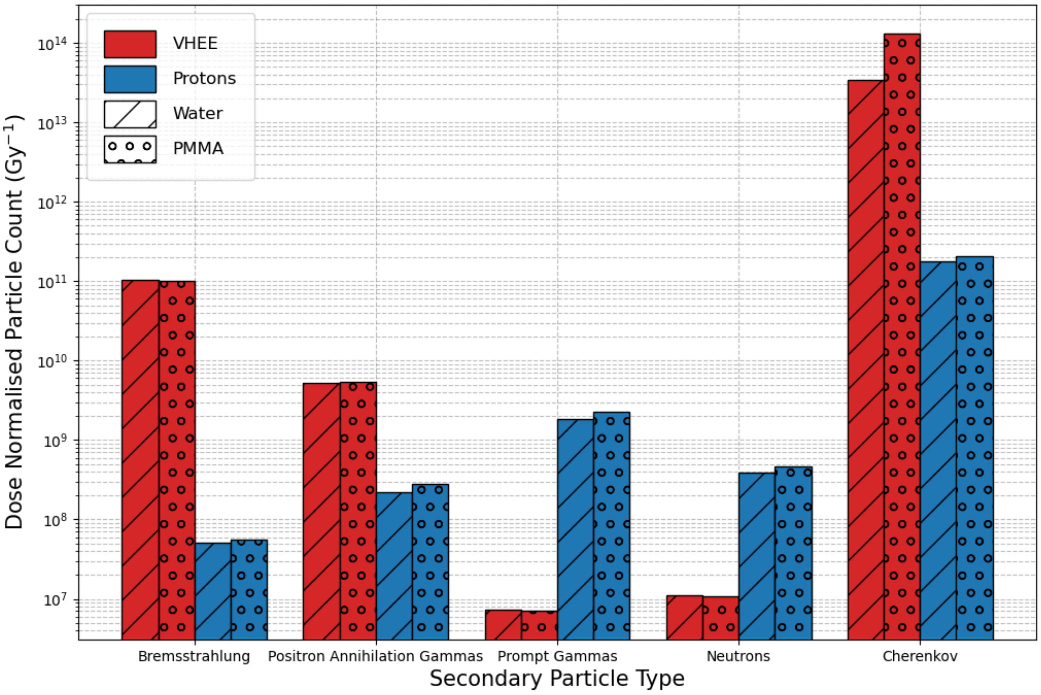

Figure 3.3: Bar chart showing the number of bremsstrahlung, positron annihilation gammas, prompt gammas, secondary neutrons and Cherenkov photons scored leaving the water or PMMA phantom, following the irradiation of 200 MeV VHEE and proton beam, normalised to the dose deposited by the beam in the phantom.

VHEE beam is nearly three orders of magnitude higher than that produced by the proton beam. This is because the VHEE beam is relativistic and at energies much higher than the threshold energy for Cherenkov generation, hence produces Cherenkov radiation directly. On the other hand, the threshold for protons to produce Cherenkov radiation directly in water, according to Eq. 2.24, is 290 MeV and hence above the clinical proton energy range; therefore, the resulting Cherenkov radiation is produced from secondary electrons. It can also be seen from Fig. 3.3 that the VHEE beam produces significantly more bremsstrahlung radiation and PA photons than the proton beam. However, the proton beam produces a larger proportion of PG photons and secondary neutrons. This is also to be expected, since according to Fig. 2.1, for electron beams in the VHEE energy range i.e., above 100 MeV the radiative stopping power dominates the stopping power. However, it is important to note that whilst the radiative stopping power dominates, for VHEE beams the largest contribution to the dose distribution ($\approx 70\%$ of the relative dose) is from ionisations caused by the primary electrons [133]. Proton beams in this energy range instead lose the majority of their energy from direct Coulomb interactions with the nuclei of the target material, hence resulting in a larger proportion of secondaries from nuclear interactions, as opposed to radiative interactions, as is the case with VHEE beams. The PG photons that were scored for the VHEE beam were those resulting from both electro-nuclear interactions between the primary beam, and for protons these were scored as proton inelastic collisions. The yield of secondary neutrons scored leaving the phantom for the VHEE beam irradiations was 9.54×10^{-7} neutrons/cm^2 per primary electron for water and 9.67×10^{-7} neutrons/cm^2 per primary electron for PMMA, approximately two orders of magnitude lower than what is produced following proton irradaiton of the respective phantom materials. These values for the neutron yield from a VHEE beam are consistent with those already published by Subiel *et al* [115, 197] and Masiela *et al* [133]. The yield of PG photons following VHEE irradiaton were also approximately two orders of magnitude lower than those resulting from proton beam irradiation, however these values only take into account PG photons produced following electro-nuclear interactions from the VHEE beam. When also considering PG photons produced following photonuclear interactions 6.92×10^7 photons/Gy and 4.58×10^7 photons/Gy and produced for water and PMMA phantoms respectively. This is still an order of magnitude lower than those produced following the proton beam irradiation.

For each simulation setup, the total secondary gamma radiation (excluding Cherenkov photons) scored leaving the phantom was totalled and plotted as a function of energy. The resulting spectra of these gamma rays, between the energies up to 10 MeV with bin widths of 10 keV is shown in Fig. 3.4. It can clearly be seen that the resulting secondary gamma production from the VHEE irradiation is about magnitude larger than that from a proton irradiation of the same beam energy and fluence. The 511 keV positron annihilation peak can be seen clearly on both spectra, however it is more prominent for the VHEE irradiations, as also confirmed by Fig. 3.3. Furthermore, the secondary gamma ray spectra for the VHEE beam has a more continuous distribution across this energy range, as opposed to the resulting gamma spectra from the proton beam. The reason for this is because of the bremsstrahlung radiation being the dominant form of secondary gamma rays from the VHEE beam. As opposed to the proton beam where there are characteristic spikes from the prompt gamma ray emissions at discrete energies following the relaxation of excited nuclei following proton inelastic interactions.

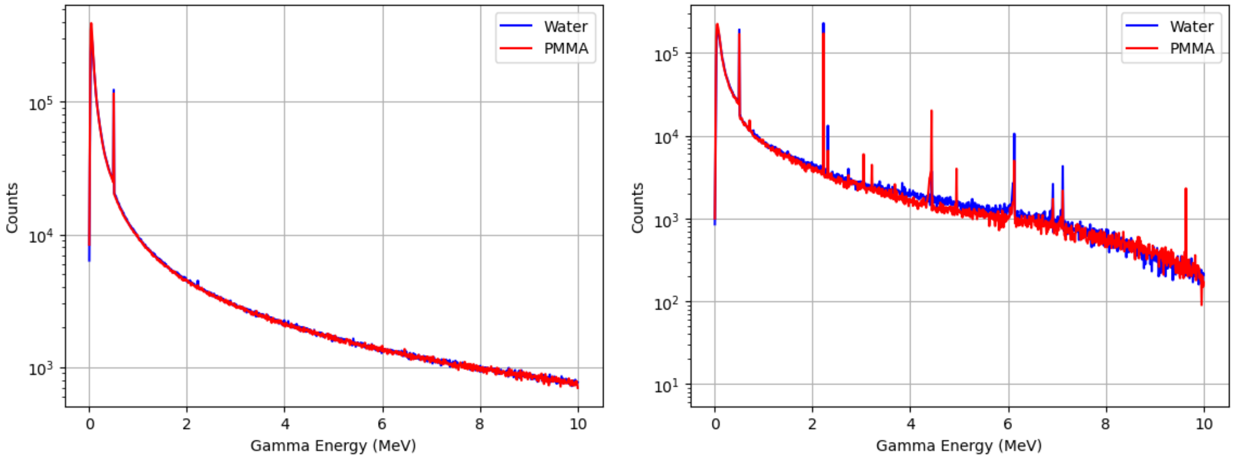

Figure 3.4: Energy spectra of the scored secondary photons leaving the water and PMMA phantoms following irradiation of 200 MeV VHEE beam (left) and proton beam (right), up to a photon energy of 10 MeV, with bin sizes of 10 keV.

The *in vivo* dose verification methods employed for proton therapy range verification, particularly PG imaging and also methods including secondary neutron tracking already face the challenge of low signal [206]. Only the methods in which the yield of secondaries is higher for VHEE beam irradiation is discussed in the following sections.

3.5 Bremsstrahlung

The production of bremsstrahlung radiation is the primary contributor to the loss of energy for electrons that have energies above 100 MeV, as has already been discussed in Section. 2.1.1.1. The stopping power of the electron beam due to this radiative energy loss is described by Eq. 2.2.

Given the higher electron energies of VHEE beams, this means the resulting bremsstrahlung emitted following the interactions between the beam and the medium will be more intense and have a larger energy spread than for clinical MV photon and electron beams. Therefore characterisations of the production of bremsstrahlung from these VHEE beams in water is important in order to understand how it contributes to the VHEE dose deposition, as well as the resulting secondary radiation produced from photon interactions that occur at these higher energies. Previous studies on the dosimetric properties of VHEE beams investigated the impact of bremsstrahlung on the dose deposited within the patient and the resulting secondary neutrons and induced radioactivity induced by photonuclear interactions of the bremsstrahlung, as well as radiation protection considerations [94, 131, 197]. These studies concluded that whilst there was an additional contribution from these interactions, the additional dose received within the patient was negligible compared to existing conventional RT modalities, and was noticeably less than that from proton therapy.

The distributions shown in Fig. 3.5 are of the bremsstrahlung generation within a water phantom following the irradiation of a 200 MeV VHEE and proton beam. The bremsstrahlung generation for a VHEE beam follows a very similar to distribution to the dose distribution which is shown in Fig. 3.2 The exception is at the end of the distribution where there is an increase in bremsstrahlung generation, which caused by electron back-scatter at the boundary between the water phantom and the air. The bremsstrahlung generation distribution for the proton beam irradiation differs noticeably from the proton range in water, due to the fact the bremsstrahlung is emitted from the secondary electrons, therefore it is most prominent near the entrance of the phantom where the secondary electrons are liberated with the highest kinetic energy. Hence a much lower amount of bremsstrahlung radiation is produced, and the distribution of which does not follow the pattern of the proton dose distribution. The dose deposited by the resulting bremsstrahlung radiation from the VHEE beam irradiation, relative to the maximum total dose deposited, is shown in Fig. 3.6. The dose distribution can be seen to have a peak at a greater depth than that of the overall dose distribution in Fig. 3.2; as well as having a much larger lateral spread, particularly at greater depths. Also shown in Fig. 3.6 is the overall energy spectrum for the bremsstrahlung. The spectra ranges from zero to

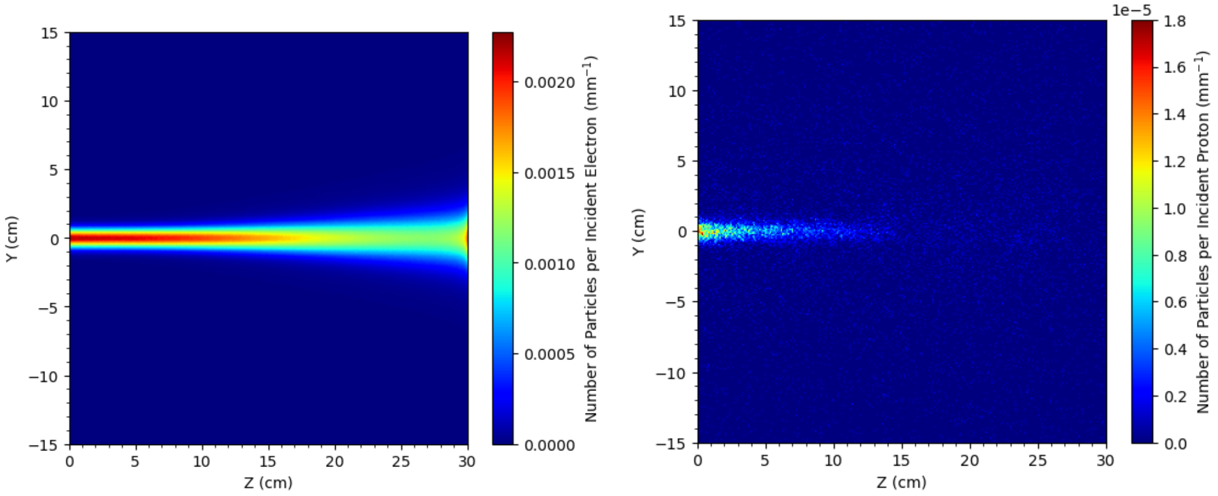

Figure 3.5: The 2D distribution in the z-y plane of the generation of bremsstrahlung radiation in a water phantom following the irradiation of a 200 MeV VHEE beam (left) and proton beam, (right).

the kinetic energy of the incident electron, where the number of emitted photons is a minimum. The resulting spectra presented in Fig. 3.6 is a convolution of all of the bremsstrahlung spectra from all of the primary electrons passing through the water phantom. It can also be clearly seen that it is the bremsstrahlung photons that dominates the secondary gamma spectra for the VHEE beam. The angular distribution at which the bremsstrahlung radiation is emitted is forward peaked for high energy electrons, and then as the electron energy decreases, this angle widens [94]. This can explain why the peak in dose deposited from the bremsstrahlung radiation is at a greater depth than for the overall distribution and why the bremsstrahlung dose distribution has a larger later spread at these depths. Furthermore, this means that the majority of the resulting photon interactions from bremsstrahlung are likely to become more prominent at greater depths.

The large flux of bremsstrahlung radiation at the exit of the water phantom means that if transit dosimetry methods such as EPID were to be used with VHEE beams, the resulting beam exiting the patient would be a mix of electrons and of bremsstrahlung radiation, both with a wide energy spectra. Therefore, considerations of the detector type used for this method would need to take this into account, particularly since one of the disadvantages of currently employed EPID dosimetry

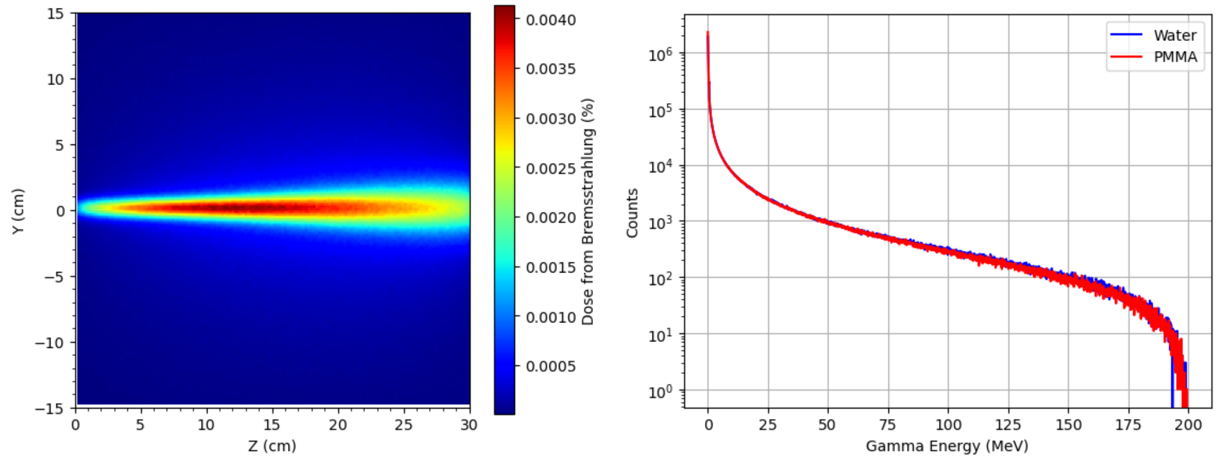

Figure 3.6: The relative dose distribution contribution of the bremsstrahlung radiation in the water phantom following irradiation of the 200 MeV VHEE beam (left), and the corresponding energy spectra of the bremsstrahlung radiation (right) scored in bins of 100 keV produced from VHEE beam irradiation of a water and PMMA phantom.

systems is the energy dependence of the detector [219].

3.6 Positron Annihilation Gammas

The detection of Positron Annihilation (PA) gamma rays is the basis of Positron Emission Tomography (PET) imaging, a well established technique for diagnostic and functional imaging within the field of nuclear medicine. The method entails the use of a radioactive tracer which undergoes β^+ decay, whereby two opposing γ-rays, each with an energy of 511 keV, are emitting following the annihilation of the emitted positron and a nearby free or atomic electron. This technique has also been utilised for *in vivo* range and dose monitoring with proton and ion beam therapy. This technique works on the basis that the hadron beam induces β^+-activation along its path n the traget volume, which subsequently leads to the emission of PA γ-rays [207]. From the deduced β^+-activation within the patient, the range of the proton or ion beam can determined through correlations in the distal fall-off activity and the distal fall off of the Bragg peak, or between comparing the measured β^+-activity and the expected activity from analytical calculations [220, 221, 222] or Monte Carlo simulations [223, 224]. More advanced techniques look to reconstruct the entire dose distribution rather than just the beam range within the patient, and involve using the treatment planning system to predict the induced activity within the patient. From which any discrepancies between the predicted activity distribution and the measured distribution can then be used to quantify any changes in the delivered dose or patient anatomy [225, 226]. A further, more mathematically rigorous approach entails the use of analytical models to describe the relationship between the emitted PA signal and the deposited dose, to allow for a direct reconstruction of the dose distribution from the measured PET signal [227, 228, 229]. Commonly created reaction products within the patient that lead to PA γ-ray emission following the irradiation of a hadron beam include ^{11}C ($T_{1/2} = 20$ min), ^{13}N ($T_{1/2} = 10$ min), and ^{15}O ($T_{1/2} = 2$ min). Due to the differences in half-lives of the β^+ - emitters, PET imaging of the induced activity can either be performed on-line during the treatment using purpose built in-beam PET scanners, in which a larger signal will be detected owing to the shorter half-life of ^{15}O [230], but is more challenging due to logistics of developing a scanner that can be used alongside the treatment beam. Such in-beam PET techniques have been implemented using a partial ring [231], or using 2D planar detectors [232, 233]. The PET imaging can also be performed off-line which can make use of either specialist in-room PET scanners that can be used directly after treatment [234] or commercially available or readily installed PET scanners [235], but the signal is a lot lower due to biological washout causing a loss in the produced activity. The potential of UHDR irradiations promises an almost instantaneous positron yield and hence allows for the possibility of a stronger and quicker PET signal compared to conventional dose rates as well as reducing the effect of the biological washout [236]. However, this increased signal means additional considerations need to be taken into account for the PET detectors in order to avoid saturation and potential radiation damage, as well as for the rate of data acquisition and processing [237]. One recent study suggested that in-beam PET imaging of prompt PA γ-rays could be a promising option for *in vivo* dose monitoring of VHEE beams at UHDR [238]. An investigation into the distribution of PA γ-ray emission and that of induced β^+-activation following the irradiation of a 200 MeV electron beam, compared to that of a proton beam is presented below.

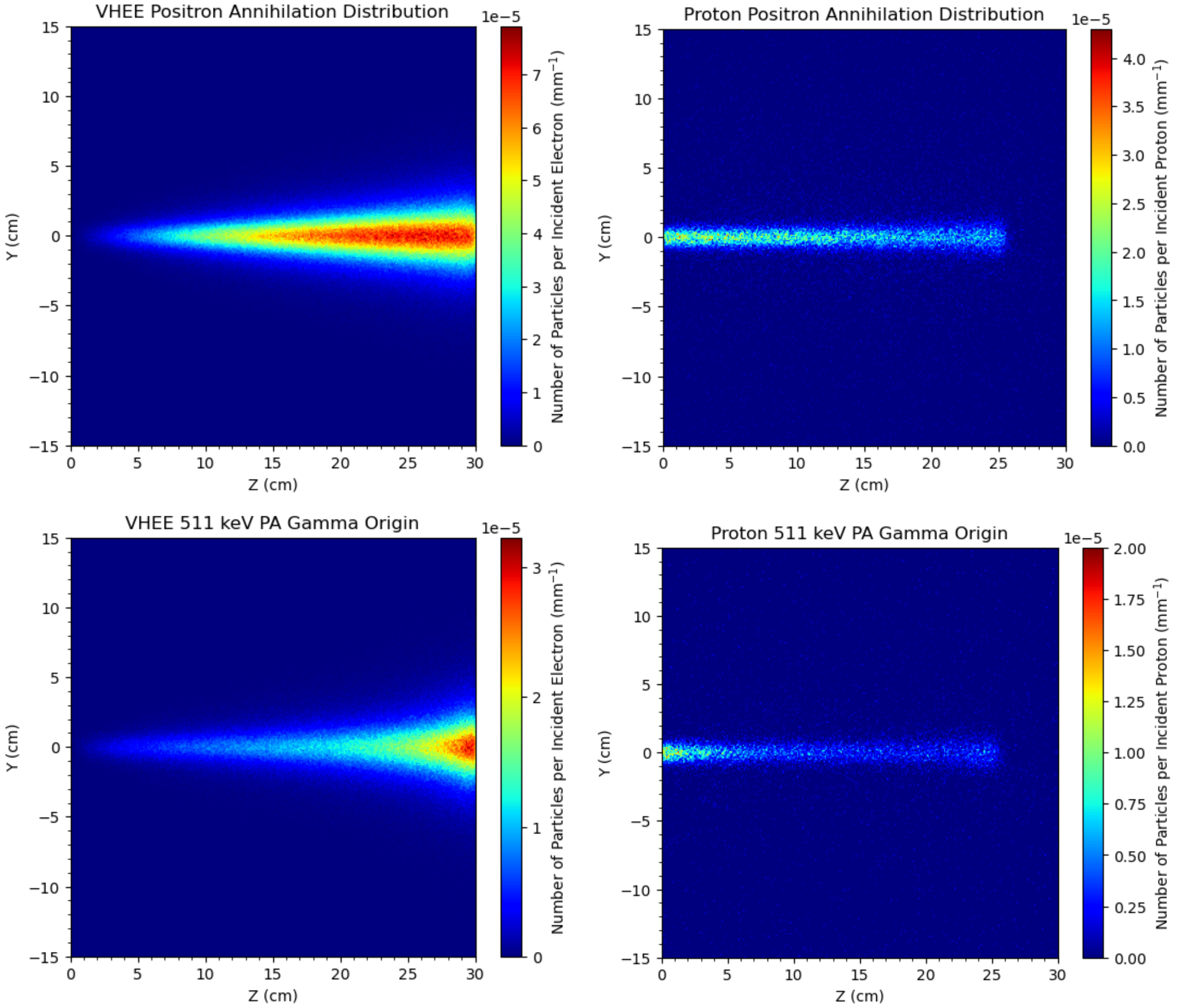

Figure 3.7: The 2D distribution in the z-y plane of the generation of positron annihilation (PA) gamma rays radiation in a water phantom following the irradiation of a 200 MeV VHEE beam (top left) and proton beam, (top right), as well as those with a final energy of 511 keV (bottom left for VHEE and bottom right for protons).

The first distributions shown in Fig. 3.7 are those of the origin of all PA γ-rays resulting from the initial irradiation of the primary beam. The distribution resulting from the proton irradiation shows a range similar to that of the dose distribution in Fig. 3.2. Whereas the distribution resulting from the VHEE beam irradiation varies significantly from the VHEE dose distribution, with the peak of PA emission occurring at the end of the beam range, at a significantly larger depth than that of the maximum dose deposition. The second distributions shown in Fig. 3.7 are filtered so that only PA gammas within the energy range of 510 keV to 512 keV are scored, since PET detectors specifically filter the signal for this energy range. Once again the distribution of PA γ-ray origin following proton irradiation shows a range in close agreement to that of the dose distribution whereas the resulting distribution following the irradiation of the VHEE beam differs still. This time the peak in the distribution of the origin of PA γ-rays occurs even deeper. The two distributions shown in Fig. 3.8 are the β^+-activation distributions within the water phantom. From these distributions it can be seen that for the VHEE irradiation the signal is noticeably lower, albeit still with a similar shape to the distribution of PA γ-ray origin. The proton β^+ emitter distribution remains almost identical to that of the PA γ-ray origin distribution.

From the simulations, it can be determined that the main contribution to the PA γ-ray signal from the VHEE beam irradiation is in fact not from β^+ emitters. The bar plot shown in Fig 3.8, comparing the contribution of β^+ emitters to the total PA γ-ray signal from the VHEE and proton beam irradiation of a water and PMMA phantom, confirms this. Here, only around 0.1% of the total PA γ-ray signal originates from a β^+ decay, as opposed to approximately 40% from the proton irradiation. The biggest contributor to the PA γ-ray signal from VHEE beams is therefore from the annihilation of positrons that have been generated from pair, or triplet, production mechanisms from the interactions of the bremsstrahlung photons with the medium of the target. This means these PA photons will be emitted almost instantaneously, and is hence possible to temporally separate the signal originating from pair and triplet production from that originating from β^+ decay. However the signal from β^+ decay following VHEE irradiation is between 5% to 9% (for water and PMMA phantoms respectively) of that of the β^+ emitter signal from a proton beam irradiation, where the low signal yield is already a challenge. Furthermore, additional considerations of the PET detectors would be necessary, particularly for UHDR VHEE irradiations, where there would be an extremely high instantaneous flux of PA γ-rays and bremsstrahlung photons that could either saturate the electronics or cause radiation damage to the detector system. Another important consideration when comparing between the resulting PA γ-ray from VHEE and proton beams is that the β^+-activation

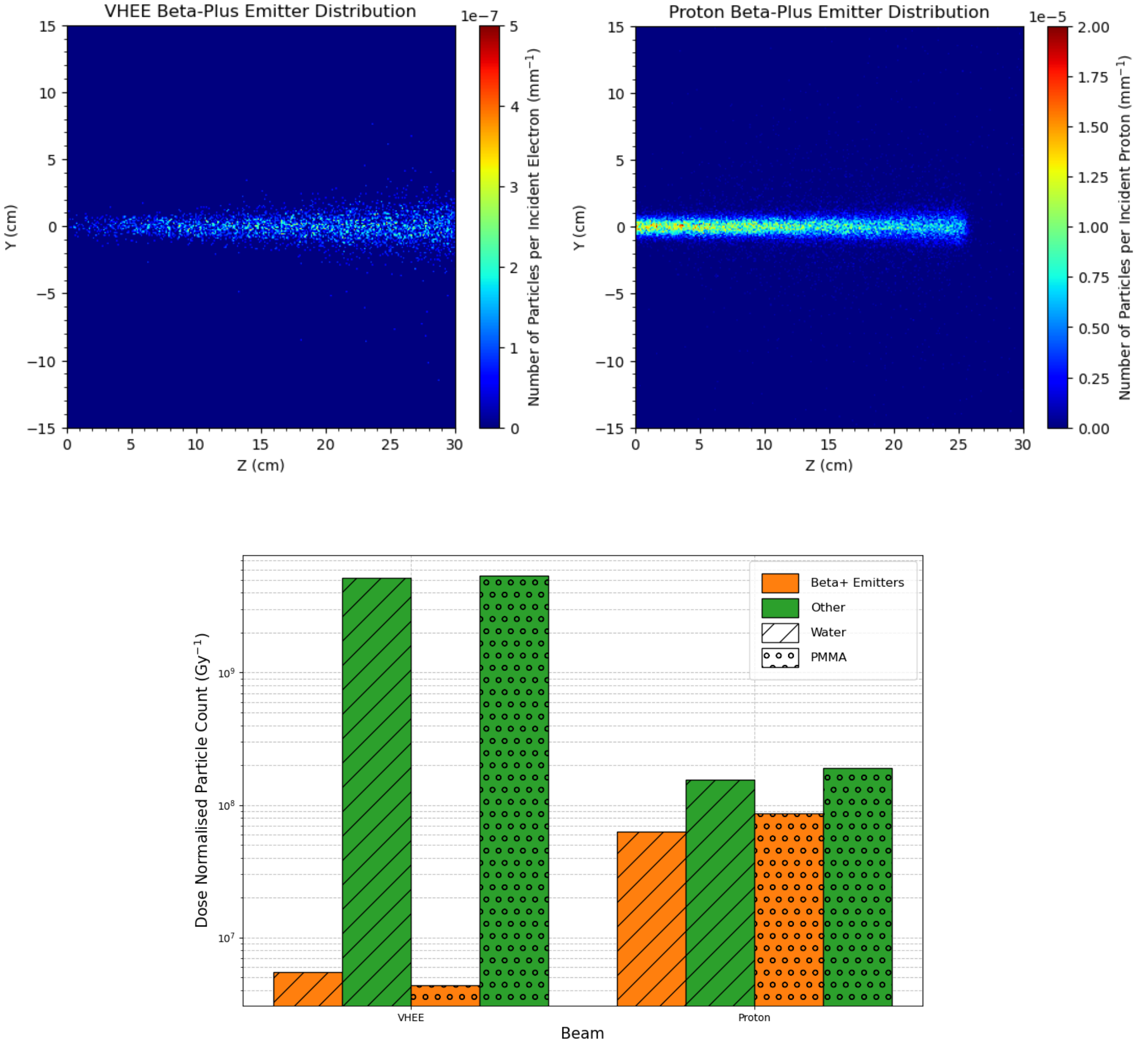

Figure 3.8: The 2D distribution in the z-y plane of the β^+ activity in a water phantom following the irradiation of a 200 MeV VHEE beam (top left) and proton beam (top right), along with a bar plot showing the contributions of PA gamma rays resulting from β^+ emitters to the total signal of PA gamma rays resulting from both the VHEE and proton beam irradiation (bottom).

resulting from the proton beam irradiation is caused primarily by direct inelastic Coulomb interactions between the primary proton beam and the medium. For VHEE beams the β^+-activation is instead induced primarily by photonuclear interactions between the high energy bremsstrahlung photons and the medium. For example, in the water phantom, interactions of the bremsstrahlung with ^{16}O, leads to the leads to the generation of ^{15}O isotopes through the (γ,n) interaction which dominates in the giant dipole resonance region and has a threshold energy of 15.7 MeV [197]. Generation of ^{11}C radioisotopes originate from interactions of higher photon energies that are within the quasi-deuteron region such as (γ, p), (γ, pn) reactions [127]. This means that using in-beam PET imaging for reconstructing the dose distributions of VHEE beams would require a much more complex mathematical analysis to relate the dose distribution to the β^+ activity distribution compared to that for proton beams, since the activity distributions more closely related to the dose deposited by the bremsstrahlung photons for which only account for a small proportion of the overall VHEE dose distribution.

3.7 Cherenkov Radiation

Cherenkov optical imaging dosimetry is a technique used to measure and track the dose distribution in real-time during RT treatment. The method exploits the emission of Cherenkov light, which has been introduced in Section. 2.2.6, and uses time-gated cameras, focused on the irradiation area of the patient surface, to detect the light during the radiation pulses which allows the rejection of the background ambient light [239]. Cherenkov light is emitted over a broad spectrum of wavelengths from UV to near-infrared (NIR) with an inverse square relation, but self-attenuation in the medium which the Cherenkov is emitted leads to a resulting spectrum primarily in the UV-A to NIR [240]. Following patient irradiation, the lower wavelengths of Cherenkov light is preferentially absorbed by the haemoglobin, with mostly red and NIR wavelengths make it to the tissue surface and avoid self-attenuation [241]. Cherenkov optical imaging dosimetry has primarily been used for *in vivo* verification of surface dose distributions during RT treatments with low energy electrons and MV photons, since the Cherenkov light travels less than a centimetre before total absorption [242]. UHDR RT favours Cherenkov imaging dosimetry techniques due to the increase in instantaneous dose rates which result in a significantly more intense emission of Cherenkov radiation [171, 243]. One such study by Rahman *et al* [244] demonstrated the ability of Cherenkov optical imaging of individual pulses from an UHDR 10 MeV electron beam using a gated CMOS camera. The study showed the Cherenkov emission was linear with dose and independent of dose rate up to 300 Gy/s, as well as close agreement with radiochromic film for surface beam profile measurements. Furthermore, in this study lateral depth dose profiles were performed from imaging the water phantom which also agreed closely with radiochromic film measurements. This means that such this dosimetry technique could also be a potential alternative for linac QA measurements at UHDR, which are currently performed using ionisation chambers for conventional RT [243]. Due to the mechanism through which Cherenkov radiation is emitted, Cherenkov optical dosimetry is not a suitable technique for proton therapy, since only the secondary electrons produced emit Cherenkov radiation, which is not closely correlated with the proton range in water. Alternatively other radioluminescence mechanisms have been shown to be viable for proton surface and volume measurements [245]. Therefore the results presented below are a comparison of the Cherenkov emission distribution and dose distribution for the VHEE beam only.

The first distribution presented in Fig. 3.9 is the relative distribution in z-y plane of the emission of Cherenkov radiation from the water phantom following the irradiation of the 200 MeV VHEE beam. This distribution can be seen to be very similar to the percentage dose distribution for the VHEE beam in the water phantom shown in Fig. 3.2. To investigate the similarities between the VHEE dose distribution and the Cherenkov emission more thoroughly, the relative depth dose profiles (averaged over different transverse lengths) and the relative transverse profiles at different depths are also presented in Fig. 3.9. The percentage depth dose (PDD) and percentage depth light (PDL) curves were compared for three different transverse bin widths, 0.4 cm, 2 cm, and 30 cm (the entire distribution). The plot in Fig. 3.2 shows that for the smallest transverse bin width the PDD and PDL are in very close agreement throughout the entire water phantom. For the 2 cm transverse bin width, the Cherenkov PDL is than the PDD for the first 10 cm, then there is close agreement for the remaining distribution. When averaging over the entire transverse width, the Cherenkov PDL is significantly higher than the PDD up until 20 cm depth, then the PDD is higher for the remain-

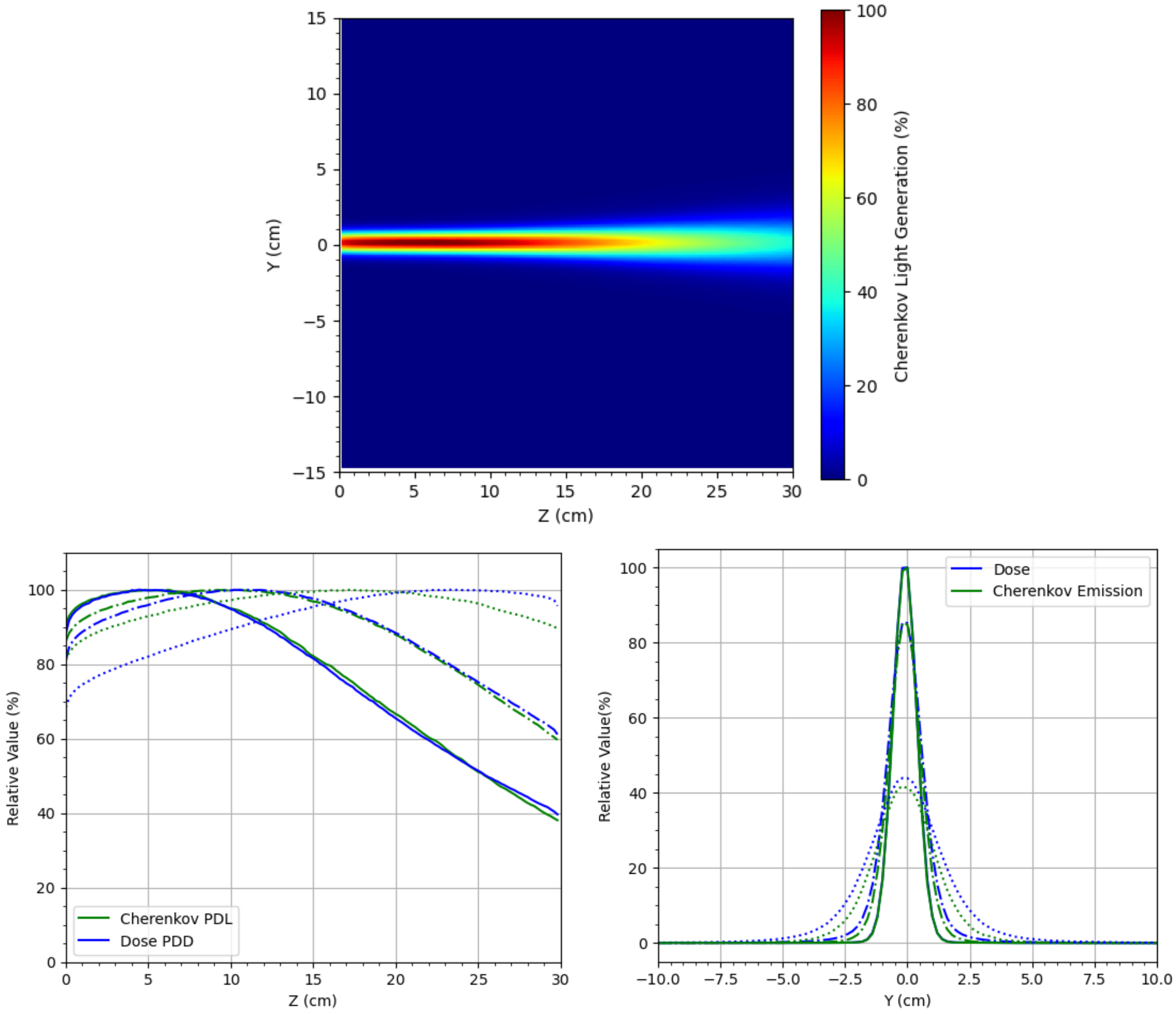

Figure 3.9: The 2D distribution in the z-y plane of the relative Cherenkov radiation emission in a water phantom following the irradiation of a 200 MeV VHEE beam (top), along with the direct comparisons between the relative percentage depth light (PDL) emission from the Cherenkov and percentage depth dose (PDD) from the VHEE beam (bottom left) by averaging over transverse widths of 0.4 cm (solid line), 2 cm (dashed line) and 30 cm (dotted line), and a comparison between the relative dose and Cherenkov emission transverse profiles (bottom right) at depths of 1 cm (solid line), 15 cm (dashed line) and 29 cm (dotted line).

der of the distribution. The comparisons of the transverse profiles of the relative dose distribution and the relative Cherenkov emission distributions were performed at depths of 1 cm, 15 cm, and 29 cm. A Gaussian fit was then applied to each of the distributions, and the σ of the Gaussian fit was obtained. The resulting values are shown in Table 3.1, where it can be seen that the transverse profile sizes are within close agreement at a depth of 1 cm, albeit the transverse dose distribution has a slightly larger beam size. With increasing depth in the water phantom, the discrepancy between the transverse dose and Cherenkov distribution increases, with the dose distribution having a larger size. A similar study by Glaser *et al* [179] compared the Cherenkov and dose distributions for MV photons. Here the distributions showed the opposite trend where the relative Cherenkov emission was lower than the relative dose at shallower depths and was larger at greater depths as well as the Cherenkov transverse distributions having a larger size than the dose distributions at greater depths also. The reason for difference in the distributions between the VHEE beam and MV photons is due to the differences in the mechanisms through which the dose is deposited. For VHEE beams, discrepancies between dose deposition and Cherenkov radiation arise particularly at the edges of the longitudinal distribution and at greater depths in the transverse profiles. In these regions, a significant portion of the deposited dose is due to lower-energy scattered electrons and photon interactions from bremsstrahlung. These secondary particles emit fewer Cherenkov photons compared to the primary high-energy electrons of the VHEE beam. The difference in energy between the primary VHEE beam and these secondary particles leads to a discrepancy between the dose deposited and the Cherenkov radiation emitted, with the Cherenkov signal being lower where the dose from secondary particles is significant. On the other hand, the discrepancies reported for with MV photon are due to the fact that as the photon beam penetrates deeper into the medium, secondary electrons generated by photon interactions play a significant role in dose deposition. These secondary electrons can still be above the Cherenkov threshold and produce Cherenkov radiation. However, due to the scattering of these electrons, the transverse profile of the Cherenkov radiation becomes broader at depth. Additionally, the interactions involving bremsstrahlung photons and their subsequent electron generation contribute more to the dose deposition than to the Cherenkov radiation. This results in a larger relative Cherenkov signal compared to the relative dose at greater depths, as the radiation continues to be generated by high-energy secondary electrons even as the primary photon beam attenuates.

Depth (cm)	Transverse Dose Distribution σ (mm)	Transverse Cherenkov Distribution σ (mm)
1	4.732 ± 0.003	4.689 ± 0.005
15	6.999 ± 0.032	6.304 ± 0.017
29	14.25 ± 0.098	11.87 ± 0.048

Table 3.1: Measurements of the transverse dose and Cherenkov emission distribution measurements obtained from the standard deviation Gaussian fit applied to the vertical projection of the beam profile. The uncertainty of the beam size measurement is expressed as the error on the standard deviation of the 1D Gaussian fit.

The results from this initial investigation show that Cherenkov optical imaging is a promising modality for both surface dosimetry for real-time beam monitoring during patient treatment, as well as for volumetric imaging of a phantom for QA measurements, particularly as an alternative for UHDR QA measurements. Whilst some discrepancies are present, additional calibration can be performed to mitigate the effect of these on the measurements. Furthermore, the significant exit dose of the VHEE beam means it could be possible to perform Cherenkov surface imaging on both the entrance and exit surface of the beam to provide more comprehensive dose monitoring. This method could also be used in parallel with EPID dosimetry measurements, using a similar setup to that developed by Bruza *et al* [246] to work towards a full 3D dose reconstruction.

3.8 Concluding Remarks and Future Considerations

The purpose of this chapter was to use MC simulations of a VHEE beam irradiation of a water and PMMA phantom to characterise the dosimetric properties and those of the secondary radiation produced in order to provide an insight into potential *in vivo* dosimetry and dose monitoring technologies that could be employed for VHEE beams. From the results presented in this chapter, the main techniques that should be considered going forward for VHEE RT are EPID-based transit dosimetry, in-beam PET and Cherenkov optical imaging dosimetry.

EPID-based transit dosimetry is already a well-established IVD technique for conventional MV photon beams so it is a natural choice for it to be considered for VHEE beams. Given the dose distributions of VHEE beams and the likeness to those from MV photons, namely a significant exit dose, means that EPID-based transit dosimetry will likely be applicable to VHEE beams also. Although this does depend on the energy and field size of the VHEE beam, since this determines the magnitude of the exit dose. Furthermore, the well-reported property of VHEE beams being less sensitive to inhomogeneous media to other RT modalities is also favourable for EPID dosimetry since this infers there would be less perturbations of the beam as it passes through the patient. However, since VHEE beams have a larger lateral spread as they pass through the patient, particularly those at the lower end of the VHEE energy range, this will have to be taken into consideration. Furthermore, the composition of the VHEE beam as it leaves the patient will be a mixture of electrons and bremsstrahlung, both with a large energy spread. Therefore, a detector which does not exhibit significant energy dependence across this range would be required, unlike those that are currently employed in conventional photon RT. Finally, if EPID-based transit dosimetry is to be employed for UHDR beams, further considerations are required for the detector since the flat-pannel detectors currently employed are primarily for imaging purposes and hence are not suitable for such large instantaneous doses [247].

Whilst VHEE beams produce a significantly larger yield of PA γ-rays compared to protons. Further investigation determined that the majority of these were produced following the annihilation of positrons generated from pair, or triplet, production mechanisms of the high energy bremsstrahlung photons. This meant that only around 0.1% of the PA γ-rays were produced from β^+-activation within the target, and had a lower yield of PA γ-rays from this mechanism for VHEE beams than for proton beams. It is however possible to separate the two signals temporally since the pair production PA photons are produced instantaneously, whereas those from β^+ emitters are produced following the half life of the emitter. Such a method would hence benefit from VHEE beams at UHDR as opposed to CONV dose rates since this would result in a larger and quicker signal, as well as mitigate the effects of biological washout [237]. A further consideration for this method of *in vivo* dose monitoring is that for the VHEE beam the β^+ activation is induced primarily from photonuclear interactions of the bremsstrahlung photons, as opposed to from the primary beam as is the case for the proton beam. This means the measured β^+ activity follows a closer distribution to the bremsstrahlung dose distribution and is more forward peaked. Therefore, more complex algorithms would be required to reconstruct the dose distribution from the measured β^+ activity, as opposed to those being researched for the same purpose from protons. Other considerations for in-beam PET imaging for dose monitoring with VHEE beams are those for the detector geometry and positioning. Since the simulations show the height of the β^+ activity is towards the end of the phantom and a lot of the PA photons are emitted out of the exit of the phantom, a standard ring-shaped PET detector geometry would likely not be suitable. A setup consisting of two planar arrays could potentially be more feasible, however further simulations and investigations should be carried out to determine the optimal design for such a detector.

Finally, Cherenkov optical imaging appears to be the most promising option for *in vivo* dose monitoring with VHEE beams, particularly for delivery at UHDR. The primary reason being Cherenkov radiation is produced in abundance with high energy relativistic electrons. Since this method has already been well established for clinical MV photons and low energy electrons, as well as low energy electrons at UHDR, it has the potential to be used for surface dosimetry for patient dose monitoring with VHEE beams as well as volumetric imaging for QA measurements. The simulations presented above demonstrated the close agreement between the VHEE dose distributions and the Cherenkov emission distributions, with the closest agreements being for transverse beam profile measurements at the entrance surface of the phantom. Whilst some discrepancies between the dose distribution and Chernekov distribution were apparent where secondary radiation contributes to the dose, i.e. on the edge of the distribution and at greater depths, such effects can easily be characterised and hence accounted for through a calibration procedure. Furthermore, this method can be employed for surface imaging on both the entrance and exit surfaces. Volumetric imaging of Cherenkov radiation in a water or PMMA phantom could also be a promising option for UHDR QA measurements of the lateral longitudinal profiles for VHEE beams. It would be possible to measure the distributions pulse-by-pulse without any concerns for detector saturation as is the case for ionisation chambers which are currently used for machine QA measurements, as measurements have shown so far that for low energy electrons such measurements are dose rate independent up to 300 Gy/s [244].

4 Very High Energy Electron Ultrahigh Dose Rate Radiotherapy Dosimetry Studies at the CERN Linear Electron Accelerator for Research (CLEAR)

4.1 Introduction

The CERN Linear Electron Accelerator for Research (CLEAR), shown in Fig. 4.1, is a user facility at CERN that is currently in a unique position to provide the beam parameters necessary to investigating the delivery of VHEE beams at the intensities necessary for UHDR pre-clinical studies in order to investigate FLASH effect. The work in this chapter outlines the developments and optimisations of a relative dosimetry protocol at CLEAR using radiochromic film. This radiochromic film dosimetry protocol has since been used for a wide variety of VHEE-UHDR experiments at the CLEAR facility such as: investigating the radiobiological and physico-chemical mechanisms and parameter space for the FLASH effect with VHEE beams, determination of the radiobiological effectiveness (RBE) of VHEE beams, dosimetric characterisation of novel dosimeters and detectors for VHEE beams at UHDR, and well as for novel VHEE dose delivery methods. A lot of these experiments involve delivering the same dose of radiation to the sample at UHDR and CONV dose rates. At the CLEAR facility a UHDR irradiation is delivered using one train of many bunches, and a CONV irradiation is delivered with one bunch per pulse with multiple pulses delivered either at 0.833 Hz or 10 Hz. The radiochromic film dosimetry methods outlined in this chapter are used for the dosimetric characterisation of a novel beam monitor described in Chapter 5.

The work in this chapter first describes the CLEAR Facility itself and then proceeds to outline the development of the radiochromic film dosimetry protocol, that involves the preparation, calibration, dose measurement, and beam size determination from the radiochromic films. Following this, the use of this radiochromic film in combination with some of the existing beam instrumentation at the CLEAR facility, integrating current transformers (ICTs) and scintillating YAG screens, to target the dose delivered to samples at a reference depth in water is described. Finally, a comparative study of the radiochromic film dosimetry measurements compared to that made by alanine and TLD passive dosimeters is presented.

4.2 The CLEAR Facility

The CLEAR Facility is a linear accelerator that independent from the main CERN accelerator complex, shown in Fig. 4.2, and has been operational since 2017. The electrons are produced from a Cs_2Te photocathode and are accelerated to energies between 30 and 220 MeV along a 20 m long linear accelerator. The radio-frequency (RF) accelerating structures consist of a RF photo-injector which is then followed by three S-band cavity accelerating structures which have an accelerating gradient of $\approx$ 20 MeV/m. The parameters of electron beams produced are described in Table 4.1 ,

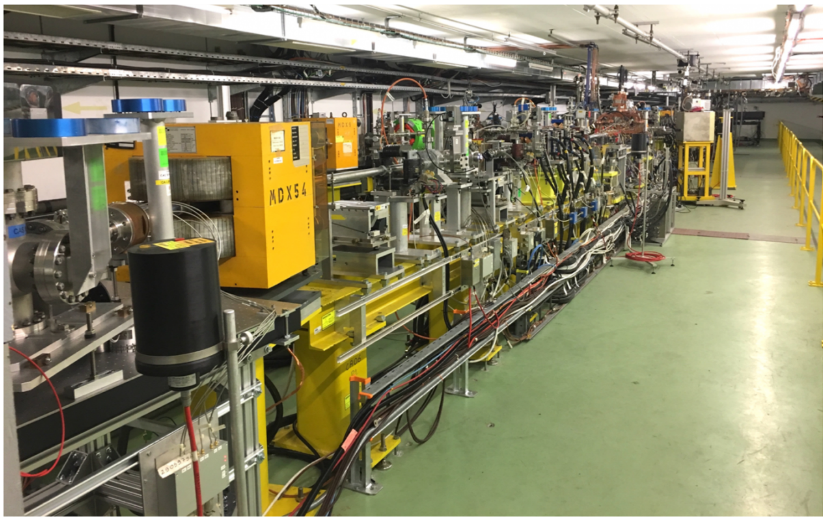

Figure 4.1: Photo of the CLEAR facility beam line.

Parameter	Value
Beam Energy	30 - 200 MeV
Beam Energy Spread	< 0.2% rms (< 1 MeV FWHM)
Bunch Length rms	0.1 - 10 ps
Bunch Frequency	1.5 or 3 GHz
Bunch Charge	0.005 - 1.6 nC
Norm. Emittance	1 - 20 µm
Bunches per Pulse	1 - 200
Max. Pulse Charge	87 nC
Repetition Rate	0.8333 - 10 Hz

Table 4.1: List of CLEAR Beam Parameters as per 2023 [249]

and the time structure of the electron pulses is shown in Fig. 4.3. The nominal operational parameters for the CLEAR facility is at an energy of 200 MeV at a pulse repetition frequency (p.r.f) of 0.833 Hz.

The CLEAR facility was formed from reusing and upgrading the key accelerating components from the probe beam injector, CALIFES, that was part of the CLIC Test Facility (CTF3). The key purpose of CTF3 was to demonstrate the feasibility of the key concepts of the proposed Compact

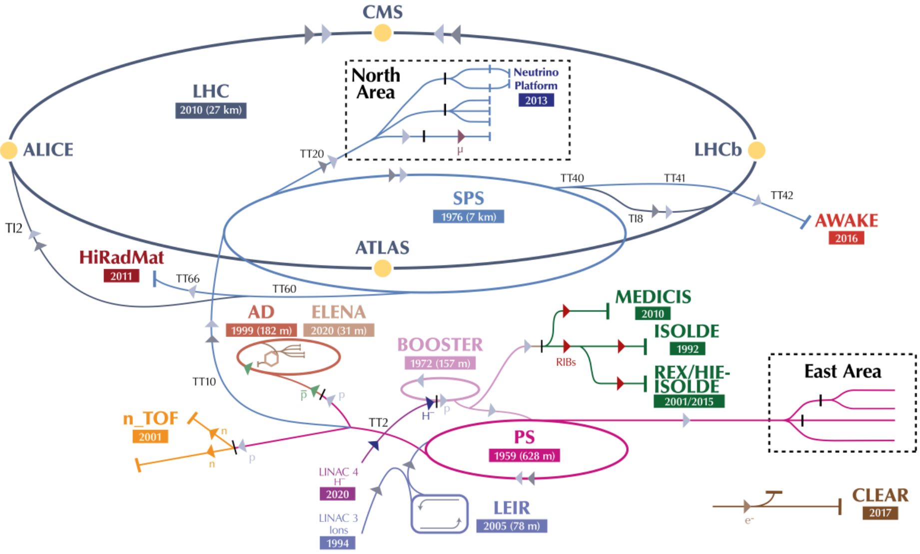

Figure 4.2: The CERN Accelerator Complex, from [248]

Linear Collider (CLIC), and consisted of two electron beam lines - the drive beam and the probe beam. The drive beam consisted of a high current electron beam that was decelerated to provide an accelerating voltage for the probe beam.

The main focus of the CLEAR facility is to provide a large range of electron beam parameters for the purpose of general accelerator research and development and component studies for existing and possible future accelerator applications - including high-gradient acceleration method studies, prototyping and validation of accelerator components for beam diagnostics, irradiations of electronics, and medical applications. The layout of the CLEAR accelerator, as shown in Fig. 4.4. The facility has two dedicated in-air experimental areas: VESPER (Very energetic Electron facility for Space Planetary Exploration missions in harsh Radiative environments), used predominantly for radiation hardness test with electronic components; and the In-Air stand, which has a wider flexibility and hence used for more general testing purposes, including those for medical applications. The facility also hosts a number of in-vacuum test areas for specific beam instrumentation (BI) experiments. Research for medical application at CLEAR has gained significant interest in recent years due to the test facility's unique position to be able to deliver beam parameters in the range that is required to study the feasibility of VHEE and VHEE UHDR RT [250], i.e. electrons of energies of between 50 to 200 MeV, and being able to deliver total doses of above 10 Gy at mean dose rates of above 40 Gy/s. To facilitate VHEE UHDR studies which often involve irradiating a large number of samples within limited time periods, the C-robot was constructed and installed in the In-Air test

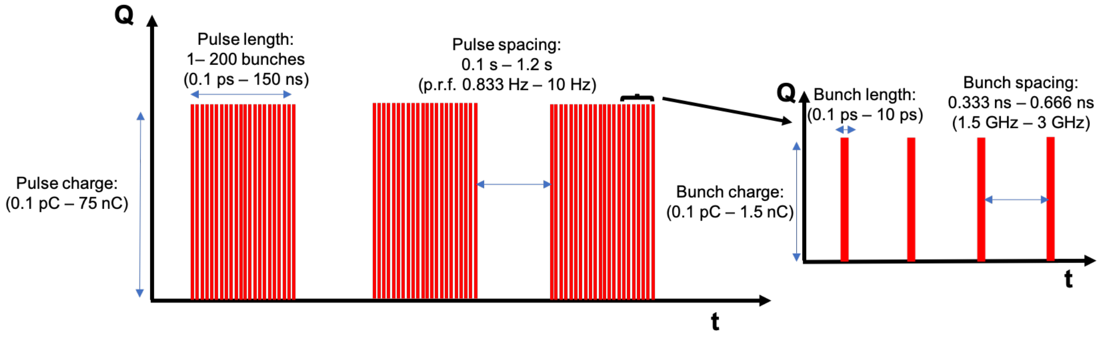

Figure 4.3: The time structure of the electron pulses at CLEAR, adapted from [249].

stand. The C-robot consists of three linear stages for all three axes, a grabber which has a mounted-camera system with a moving filter, and has two tanks (one for storage and another in the electron beam, that is filled with water to be used as a phantom, which can vertically maneuvered out of the electron beam). It is capable of handling more than 30 samples, such as biological samples or dosimeters, which are held in 3D printed holders. Currently, numerous studies have been conducted, with many still ongoing, to research the possible mechanisms behind the FLASH effect as well as to test the feasibility of novel technologies for the delivery, characterisation, dosimetry and monitoring of these unconventional beams. The experiments and results for dosimetry and real-time beam monitoring are the main topic of this chapter and the subsequent chapter in this thesis.

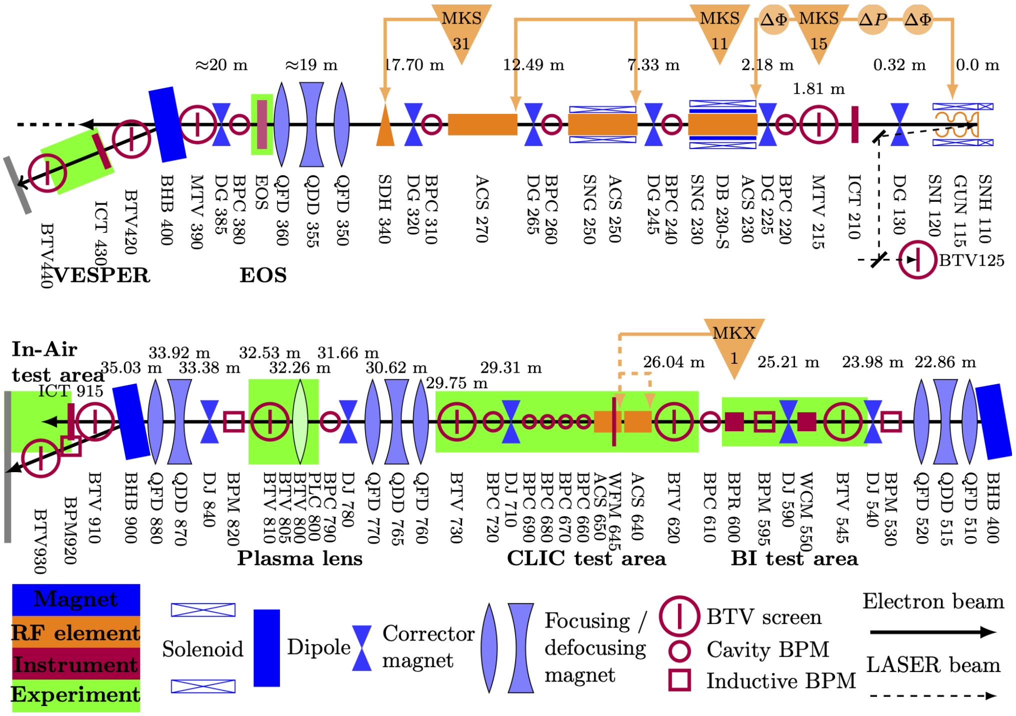

Figure 4.4: Layout of the CLEAR experimental beam line (the electron beam runs from right to left) [251].

4.2.1 Beam Position and Profile Monitors

The C-robot uses a dedicated holder which contains a scintillating YAG:Ce screen and a reflecting mirror, which is read out by a CMOS camera attached to the grabber. This is used for providing beam position, profile and intensity measurements both in air and in the water phantom at the end of the beam line. Further to this, a number of beam position monitors (BPMs) are positioned along the beam line for beam transport optimisation. In addition to the BPMs, several YAG screens and optical transition radiation (OTR) screens are positioned along the linear accelerator, which can be inserted and retracted, for measuring the beam profile in addition to the position - these are also used for the optimisation of the beam transport along the line, as well as for some user experiments.

4.2.2 Charge Measurements

Charge measurements at the CLEAR facility are performed using Integrating Current Transformers, which are positioned in-vacuum shortly after the RF gun at the start of the beam line, as well as in air at both the VESPER and In-Air test stands - which allows also for the measurement of the beam transport along the linear accelerator. An ICT is a type of beam current transformer (BCT). BCTs work on the principle that the arrangement of an ideal iron core around the beam acts as transformer with the particle beam being the equivalent primary winding and the inductive coil is the equivalent secondary winding of the transformer. The electron pulse acts as a single turn in the transformer and induce a proportional current in the windings, the integral of such current over time is equal to the charge of the electron pulse. However, for very short electron bunches (typically < 1 ns) it is difficult to measure the charge using conventional beam current transformers since the output voltage is only proportional to the beam current for long bunches, for short bunches the output voltage duration is much longer than that of the beam current itself [252]. Therefore, ICTs can be used to be provide accurate measurements of the bunch charge by sacrificing almost all longitudinal information about the bunch [253]. This method works on the principle that the pulse's time integral value is present in the lower end of its frequency spectrum. Therefore, the longitudinal bunch shape data, which resides in the high-frequency part of the spectrum, can be ignored. Consequently, its bandwidth can be much narrower than the pulse spectrum. By examining the Fourier transform of a current pulse $i(t)$:

$$I(f) = \int_{-\infty}^{+\infty} i(t)\exp(-i2\pi ft)dt \tag{4.1}$$

$$I(0) = \int_{-\infty}^{+\infty} i(t)dt = q \tag{4.2}$$

The ICT leverages the principle that the value of the time integral of a current pulse $i(t)$, which is its charge q (from Eq. 4.2), is represented by the DC component of the pulse spectrum [254].

4.2.3 Energy Measurements

The energy of the electrons at the CLEAR facility is measured using a magnetic spectrometer line, at either the VESPER test stand or at the In-Air test stand. At both of these locations there is a dipole magnet which can deflect the electrons, and a fluorescent screen which can measure the position of the electrons. The path of the electrons is bent due to the Lorentz force of the dipole's magnetic field, and for a given magnetic field strength, B: the radius of the curvature of the electron path, rho, depends on the momentum, and hence the energy (in MeV):

$$E[MeV] = \frac{B[T]\rho[mm]}{3.3356} \tag{4.3}$$

where 3.3356 is a scaling factor, and $B\rho$ can be described as the magnetic rigidity of the beam. From this, the horizontal displacement of the electrons measured on the fluorescent screen at the end of the spectrometer can be correlated to energy of the electron beam.

4.3 Radiochromic Film Dosimetry at the CLEAR Facility

At the CLEAR facility, for the majority of VHEE UHDR studies, radiochromic film dosimetry is used for relative dosimetry, using Gafchromic EBT3 films for doses up to 10 Gy, EBT-XD films for doses between 0.1 - 40 Gy, MD-V3 films for doses between 10 - 100 Gy. The radiochromic film dosimetry protocol at CLEAR was established based upon the single channel dosimetry protocol outlined in work by Micke *et al.* (2011) [255], and is similar to that used for other UHDR studies using radiochromic film dosimetry [158].

4.3.1 Film and Scanner Preparation

The radiochromic film are cut to dimensions of 35 mm x 45 mm using a laser-cutter, with an alphanumerical code etched on the top-left of the film - both for identification purposes and to control the orientation of the film for both irradiation and scanning. This is because radiochromic films have an orientation-dependent response due to the nature of the monomers and polymers in the active layer [256]. Radiochromic films used at the CLEAR facility are scanned using an Epson Perfection V800 Photo scanner (Epson, Long Beach, US) at least 24 hours after irradiation. Before any films are scanned, the scanner is run in "Preview" mode at least 5 times to warm-up the scanner and reduce any scanner-dependent response artifacts in acquiring the film TIFF image. All films are scanned in the central region of the scanner, delineated by a template to ensure the film is scanned in a reproducible position, in order to further mitigate any scanner-dependent response artefacts [257].

4.3.2 Film Calibration

After being scanned, either the pixel value (PV) or optical density (OD), or net optical density (netOD) is obtained for each of the red, green, and blue colour channels from the scanned image. Therefore, in order obtain the dosimetric information from these values a calibration function relating either the PV or OD to the absorbed dose to water measured by the radiochromic film. Films are calibrated by irradiating the entire area of the film with a uniform dose, either calculated from the monitor units (MU) delivered by the linac or directly measured using a reference dosimeter such as an ionisation chamber directly behind the film. The calibration films for the radiochromic films used at CLEAR were irradiated using a 5.5 MeV electron beam at a dose rate of 0.05 Gy/s, at a depth of 10 mm in solid water phantom with an SSD of 100 cm on the Oriatron eRT6 at CHUV

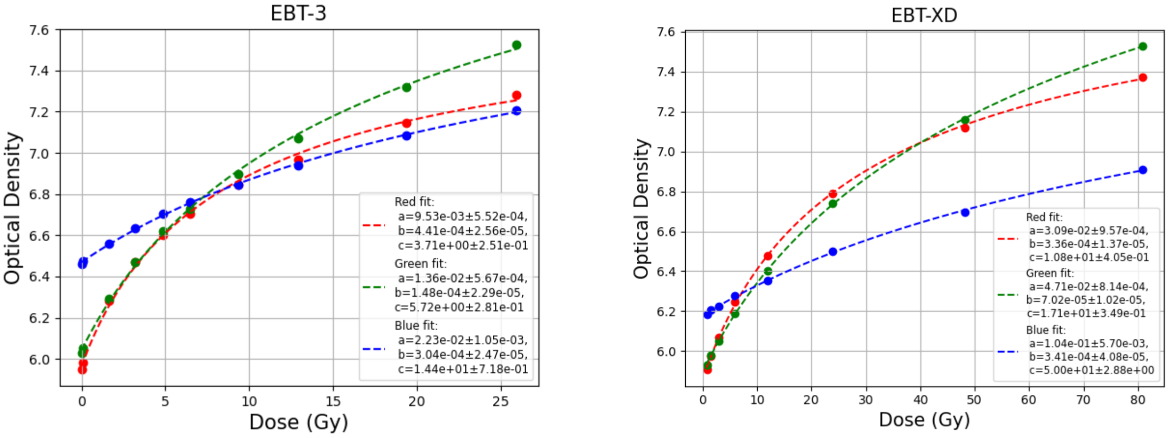

Figure 4.5: Calibration curve for EBT3 (left) and EBT-XD (right) radiochromic film irradiated to 5.5 MeV electrons at the eRT6 machine at CHUV, Lausanne.

Hospital, Lausanne, Switzerland [258]. For each point on the calibration curve, the dose was measured using a PTW Advanced Markus Ionisation Chamber (PTW, Freiburg, Germany). Calibrations were performed with low energy electron beams as opposed to VHEE beams. This is because no reference beam or standardised procedure for radiotherapy dosimetry currently exists for VHEE beams. A number of studies have demonstrated the agreement between radiochromic film measurements alongside Monte Carlo simulations at 165 MeV for radiochromic films calibrated to clinical 20 MeV electron beams [115], as well as for 156 MeV electron beams at CLEAR calibrated to clinical 15 MeV electron beams [100, 104]. Following the irradiation, the calibration films are stored in a black envelope for at least 24 hours before being scanned. Once the films are scanned, the mean pixel value from an area of 50 x 50 pixels over the central region of each calibration film is calculated and converted to optical density using:

$$OD_x = -log\left(\frac{PV_x}{65535}\right) \tag{4.4}$$

where PV_x is the pixel value for each of the colour channels (red, green or blue) and the denominator is the maximum pixel value for the 16-bit scanner. Quite often the netOD is used within radiochromic film analysis, whereby an unexposed film is scanned before irradiation, and the mean

PV is subtracted from the exposed film image. This practise has shown to sometimes reduce the impact of the spatial heterogeneities within the film. However, when employing this method, it is necessary to perfectly match the alignment of the unexposed and exposed film images in order to improve the accuracy of the dose determination. furthermore, using this method introduces larger uncertainties in the determination of the dose and involves an increased workload which may not be necessary [152, 259, 260]. Therefore, in this work only the OD is used. The optical density values are then plotted against the doses they were irradiated to (measured with a PTW Advanced Markus chamber), and fitted according to the Beer-Lambert law:

$$OD = -log\left(\frac{a + bD}{c + D}\right) \tag{4.5}$$

where a, b, and c are the fitting parameters and D is the dose (in Gy). The fitting parameters and their associated uncertainties are calculated using a custom python script. A calibration curve for EBT-XD film with the corresponding fitting parameters is shown in Fig. 4.5.

4.3.3 Radiochromic Film Dosimetric Analysis

As with the calibration films, the films used for relative dosimetry are also left for at least 24 hours before being scanned. The time after irradiation at which the films are actually scanned is kept as close as possible to that which is carried out for the calibration films. The scanned TIFF image pixel map is then converted from RGB pixel values to dose using equations 4.4 and 4.5, rearranging Eq. 4.5 for dose, D using a custom python script. An example film image and the resulting dose distribution is shown in Fig. 4.6. Film dosimetry at CLEAR is performed with green colour channel, since studies have shown that for single channel radiochromic film analysis, this channel provides improved sensitivity for the doses typically used for experiments at the CLEAR facility (typically between 8 Gy and 40 Gy) as well as exhibiting lower noise and improved reproducibility compared to other colour channels within this dose range [146, 260, 261, 262].

For sample irradiations at the CLEAR facility, samples are generally irradiated inside eppendorf

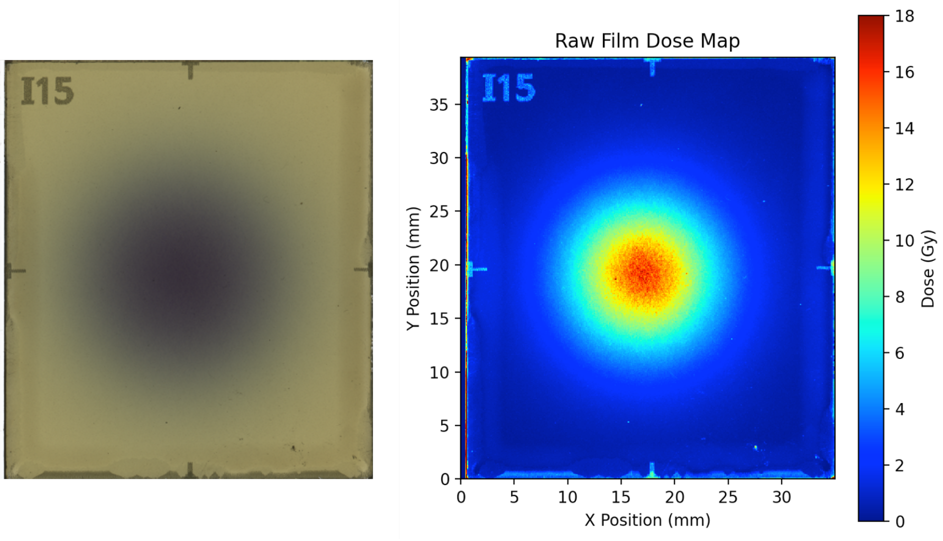

Figure 4.6: Scanned TIFF image of an irradiated EBT3 radiochromic film (left) and processed dose map in the green channel (right)

tubes - these tubes are held in a 3D printed holder with two radiochromic films postponed equidistant in front and behind the sample. The volume that the target sample occupies within the eppendorf tube (located between two radiochromic films) varies. Therefore, a lead pellet of similar size to the target sample is placed inside an additional eppendorf tube holder with a radiochromic film located behind the eppendorf tube in order to know the area of interest and to be able to extract the dose information from the film. This then creates a resulting shadow on the dose distribution on the dose distribution of this radiochromic film, from which an area of interest can be delineated and applied to the radiochromic films used for dosimetry of the irradiated samples. For measurements where there are no samples involved, the dose is determined from averaging the film dose in a circle of diameter 5 mm from the mean of the Gaussian fit on the beam distribution. The dose delivered to the sample or device that is being irradiated is calculated by averaging the dose values of the defined area of interest for both the film in front and behind the sample, and then the mean of these two values is calculated. The standard deviation of the dose over the sample is also calculated across both areas of interested and is then averaged.

4.3.4 Gaussian Beam Dose Targeting

4.3.4.1 Gaussian Beam Size Determination

Determination of the Gaussian beam size from the dose distributions on the radiochromic films is important for two main reasons, the first is to ensure that a large enough area of the beam is covering the sample that is being irradiated. The second reason is for dose targeting purposes. Since the transverse distribution of the VHEE beam at CLEAR in general can be well approximated by a Gaussian distribution, the dose delivered over a region of interest not only depends on the charge per pulse, but also on the spread of the Gaussian distribution. Therefore, to target a specific dose at the centre of the Gaussian dose distribution on the centre of the film, both the pulse charge and the beam size need to be known. From these parameters the dose-area-product (DAP) can be utilised:

$$\text{DAP} = 2\pi A\sigma_x\sigma_y \tag{4.6}$$

where A is the amplitude of the Gaussian fit, or the maximum dose at the centre of the distribution and σ_x and σ_y are the horizontal and vertical beam sizes determined from the standard deviation of the Gaussian fit. Therefore, from a given previous film irradiation where the DAP has been calculated and the delivered charge is known, the target charge to achieve a specific dose on the sample can be determined by measuring the beam size using a scintillating YAG screen held and positioned by the C-robot [250], and use Eq. 4.6 to scale the charge as necessary.

The work presented in this subsection compares three different methods for determining the beam size of the Gaussian distribution:

- a 2D Gaussian fit applied to the entire distribution using:
  $f(x,y) = A\exp\left(-\left(\frac{(x-x_0)^2}{2\sigma_x^2}\right)+\left(\frac{(y-y_0)^2}{2\sigma_y^2}\right)\right)$
- a 1D Gaussian fit applied to x and y strips of 2 mm width using:
  $f(x) = A\exp\left(-\frac{(x-\mu)^2}{2\sigma^2}\right)$

- a 1D Gaussian fit of the projection of the beam distribution along the x and y axes using: $f(x) = A\exp\left(-\frac{(x-\mu)^2}{2\sigma^2}\right)$

The beam size is then determined by obtaining σ from the Gaussian fits. The x and y strips for the 1D Gaussian fit are positioned using the mean of the 2D Gaussian fit y_0 and x_0, respectively. These fits are applied to measurements of both the radiochromic film and scintillating YAG screen for an 8 Gy and 10 Gy electron pulse delivered at UHDR and CONV with film and YAG screen positioned at depth of 150 mm in the water tank. The YAG screen CONV measurement is for a single pulse of 300 pC since the CONV measurements are multiple pulses of 300 pC. Both the film scan images and screen images were cropped to a size of 30 mm by 30 mm ensuring the centre of the film and YAG screen images were aligned. Before applying the Gaussian fits, post-processing is performed to remove the background noise from the images.

The resulting profiles and the corresponding Gaussian fits on the EBT3 radiochromic film for a UHDR single pulse targeting 10 Gy are shown in Fig. 4.7. All of the Gaussian fitting methods can be seen to under-fit the peak of the Gaussian distribution, which could suggest that dose distribution itself is not perfectly Gaussian. It is for this reason that when determining the dose to the samples, an average of the dose from the direct distribution is taken across the area of interest; as opposed to obtaining this information from the Gaussian fit. The corresponding beam profiles and Gaussian fits from the scintillating YAG screen are shown in Fig. 4.8, where the under-fitting of the Gaussian seems to be much less prominent on the 1D Gaussian fits. However it seems to be more significant when applying the 2D Gaussian fit, where the fit also appears to under-estimate the tails of the distribution. The likely cause of this is that the background signal is much stronger on YAG screen, possibly due to the YAG screen being more sensitive to secondary radiation produced by the beam as it passes through the water. The 1D Gaussian fit to the projection of the profiles can be seen to be different between x and y for the YAG screen measurement. This discrepancy can either be attributed to non-symmetric beam pulse, or that the background signal is contributing to a larger summed signal for the projection of the vertical profile.

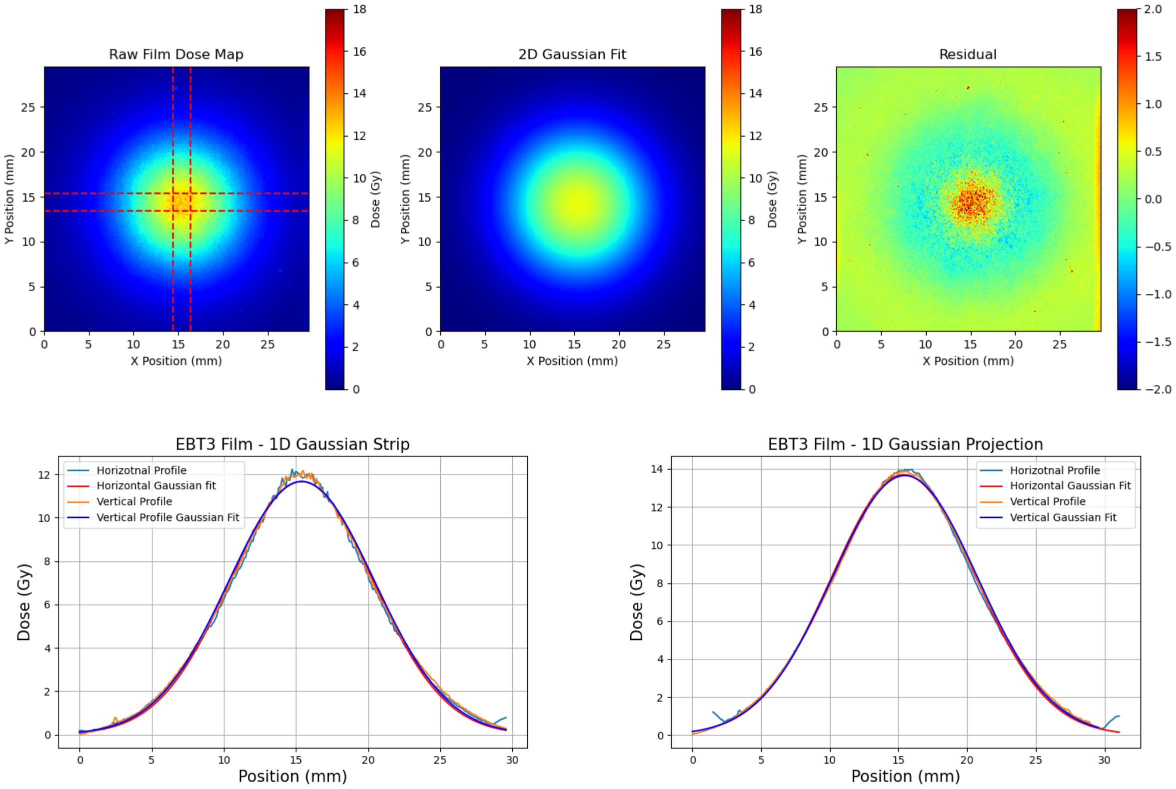

Figure 4.7: EBT3 Film Beam Size measurements of a 10 Gy target VHEE pulse, showing the raw film dose map (top left), 2D Gaussian fit (top centre), 2D Gaussian fit residuals (top right), 1D Gaussian fit to 2 mm wide strips in x and y (bottom left) and 1D Gaussian fit to the x and y projection of the profile (bottom right).

The beam sizes obtained from both the EBT3 radiochromic films and the scintillating YAG screen for both 8 Gy and 10 Gy at UHDR and CONV for all fitting methods are shown in Fig. 4.9. A very clear systematic pattern can be observed for all of the measurements; that the 1D Gaussian fit applied to the strips produces the smallest beam size measurement, the 1D Gaussian fit applied to the projection of the profiles produces the largest beam size measurement, and the 2D Gaussian fit has the largest uncertainty on the beam size measurement. The reasons for this are that projection of the profiles takes in to account all of the signal in the distribution and therefore is strongly dependent on background signal, whilst this effect is minimised the most when taking strips along the centre of the beam distribution. The 2D Gaussian fit is also affected by any background noise, and hence the

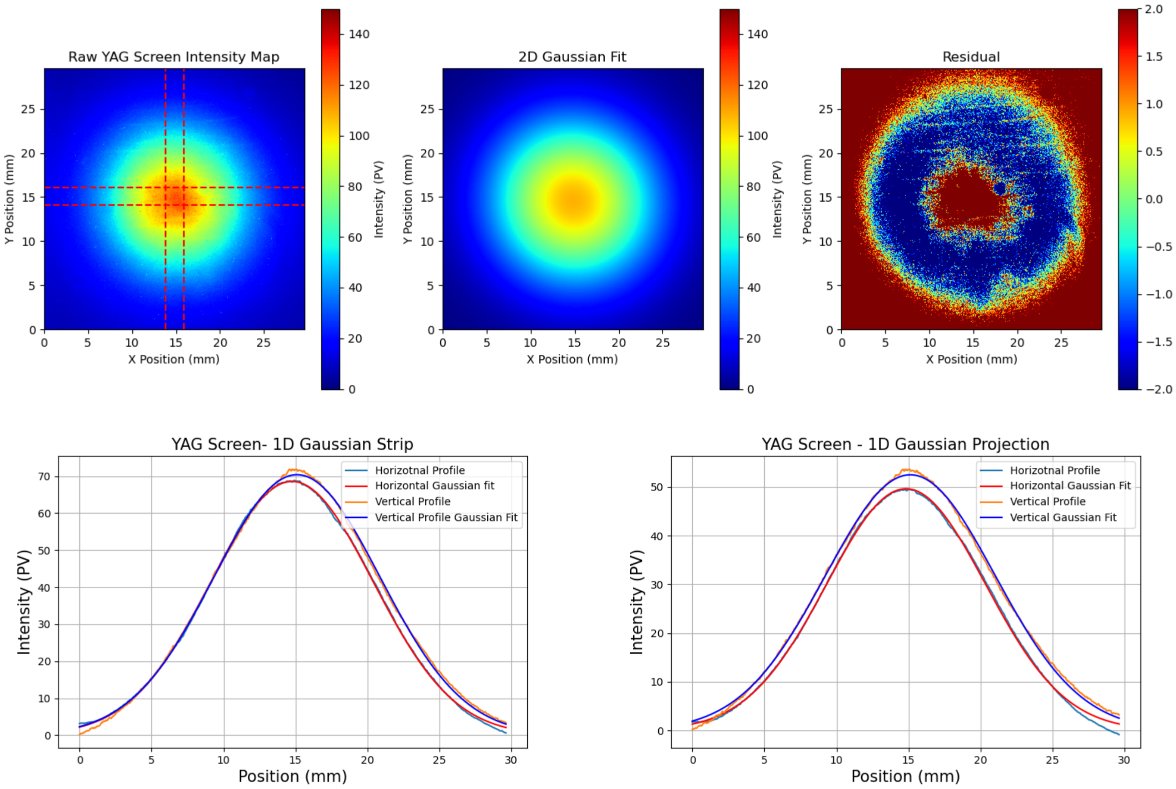

Figure 4.8: YAG Screen Beam Size measurements of an 10 Gy target VHEE pulse, showing the raw YAG screen intensity map (top left), 2D Gaussian fit (top centre), 2D Gaussian fit residuals (top right), 1D Gaussian fit to 2 mm wide strips in x and y (bottom left) and 1D Gaussian fit to the x and y projection of the profile (bottom right).

reason why the difference between the 1D fit to profile strips and the other two methods is notably larger for the YAG screen measurement. The measurement of the beam size using the 1D Gaussian fit applied to horizontal and vertical strips depends very strongly on both the length of the strips, since this determines how much background signal contributes to the beam distribution on the tails, as well as the width of the strips, since this determines how much signal contributes to the value of each point. Therefore, when using this method it is extremely important to ensure these two factors remain constant. Another clear pattern that can be seen from the plots in Fig. 4.9, is that the YAG screen beam size measurements are consistently larger than those obtained from the radiochromic film. The main reason for this can be explained by the fact that the holder with the YAG screen and reflective mirror are positioned in the water tank, whereas the CMOS camera reading out the signal is located out of the water; meaning that the imaged scintillation light signal could be distorted as it passes through of the water.

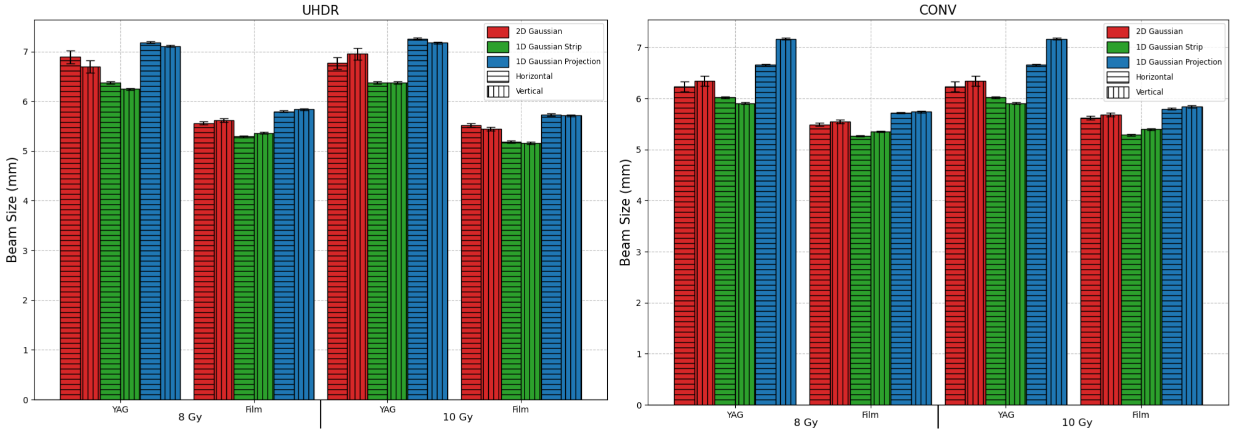

Figure 4.9: Beam size measurements on EBT3 radiochromic film and a scintillating YAG screen for 8 Gy and 10 Gy and UHDR (left) and CONV (right) dose rates. Beam sizes are calculated from σ of the Gaussian fit for three different methods: 2D Gaussian fit, 1D Gaussian fit applied to x and y strips of 2 mm width, and 1D Gaussian fit of the projection of the beam distribution along the x and y axes.

4.3.5 Correlating Charge Measurements to Dose

The CLEAR facility has a number of beam current transformers installed, one in-vacuum after the RF photo-injector, and one in air at the end of each beam pipe, to provide measurements of the charge per electron pulse. Due to the ability of a BCT to provide accurate charge-per-pulse measurements, they have become an increasingly popular form of beam instrumentation on medical research and pre-clinical electron accelerators [75] BCTs have additionally been shown to be traceable back to primary standards [263]. BCTs are becoming more widely used on pre-clinical low energy electron linacs due to their large dynamic range, and the fact that they are non-destructive to the beam [264, 265, 266]. Due to the nature of the dose delivery for these electrons, the beams are flat and collimated to a pre-defined size, which means the BCT reading can be calibrated to monitor the dose delivered at a reference position in water, much like how a transmission ionisation chamber is used in conventional radiotherapy.

As previously mentioned, BCTs do not perform well for ultra-short electron bunches [252, 253], instead ICTs can be used to accurately measure the charge but sacrifice the temporal information of the beam pulse. Therefore, the ICTs installed at the CLEAR facility are only able to measure the charge of the pulse and not the temporal pulse width. Furthermore, due to the Gaussian distribution of the unmodified electron beams at CLEAR, it is not possible to use an ICT to correlate the charge to the dose measurements from these beams. This is because the beam size can vary over time, for different experiments, or even from shot-to-shot and hence for a measured charge the maximum dose is not constant. Instead measurements of the dose-area-product can be calculated from dose distribution measured on a radiochromic film using Eq. 4.6. Measurements were performed correlating the charge measured by the ICT after the exit of the CLEAR beam pipe and correlated to the dose area product determined from the dose distribution on radiochromic films, calculated using the beam sizes from a 2D Gaussian fit over the distribution, and the associated uncertainties are those propagated from the calibration function, beam size measurement and variation in the mean dose across the central area from which the maximum dose, A, is calculated from. The films are positioned at a reference depth in the water tank and the irradiations were performed for both UHDR delivery (i.e. a range of charges-per-pulse and hence pulse width), as well as two different modes of CONV delivery. The first mode consists of the beam parameters for CONV delivery already discussed, involving one or two bunches per pulse delivered per pulse of approximately 400 pC per pulse delivered at 0.833 Hz. More recently, the CONV dose delivery was altered to keep the same mean dose rate but decrease the instantaneous dose rate using a smaller charge per bunch, approximately 10 pC per pulse and delivered at a p.r.f of 10 Hz. Both modes of CONV delivery are described below. In order to evaluate the linear correlation between the measured charge on the ICT and the DAP measured on the film, the coefficient of determination, R^2, is calculated for the linear fit for each of the measurements, using the equation:

$$R^2 = 1 - \frac{\Sigma(y_i - \hat{y}_i)^2}{\Sigma(y_i - \bar{y})^2} \tag{4.7}$$

where y_i are the measured values in the dataset, $\hat{y}_i$ are the fitted values in the dataset and $\bar{y}$ is the mean of the measured values in the dataset. The first measurements shown in Fig. 4.10, were for film irradiations targeting central doses of between 20 Gy and 60 Gy, with the film holders positioned at a depth of 145 mm in water. The charge per bunch was kept the same for UHDR and CONV at 400 pC. The delivered dose was modified by increasing the train length in a single pulse for UHDR irradiations and by delivering more pulses for CONV irradiations. The plot shows that the ICT measurement correlates linearly measured DAP from the radiochromic for both UHDR, with $R^2 = 0.992$ and CONV, with $R^2 = 0.996$. The response between the UHDR and CONV mode is also very similar with corresponding gradients for the linear regression fit of 2.730±0.091 Gy$\cdot$cm^2/nC for UHDR and 2.726±0.059 Gy$\cdot$cm^2/nC for CONV. The other plot shown in Fig. 4.10 shows the measurements targeting central doses of between 10 Gy and 40 Gy with the film holders positioned at a depth of 195 mm in water. For these measurements the UHDR conditions remained the same but the CONV irradiations were delivered with a lower charge per pulse of 10 pC at a p.r.f of 10 Hz. Once again the measured charge on the ICT can be seen to be linear with the measured DAP on the radiochromic films with $R^2 = 0.992$ and $R^2 = 0.999$ for the UHDR and CONV

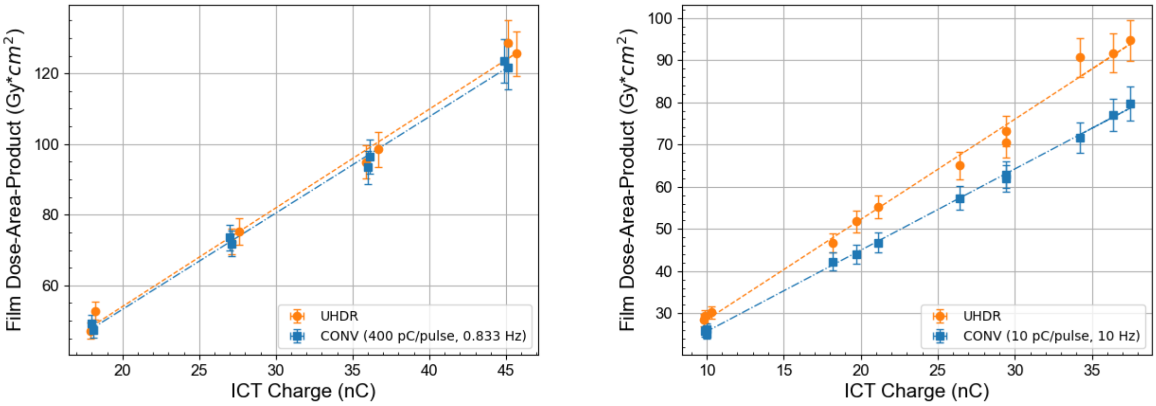

Figure 4.10: Correlation between the ICT charge measurement and the dose-area product measured on MDV3 radiochromic film with a CONV delivery of 300pC/pulse at 0.833 Hz (left). Correlation between the ICT charge measurement and the dose-area product measured on EBT-XD radiochromic film with a CONV delivery of 10pC/pulse 10 Hz (right).

measurements, respectively. The gradients of the linear regression vary much more for this irradiation setup however, with 2.367±0.061 $\mathrm{Gy \cdot cm^2/nC}$ for UHDR and 1.9266±0.018 $\mathrm{Gy \cdot cm^2/nC}$ for CONV. The reason for this is because the much lower charge per pulse for the CONV measurements means the ICT charge readings are more affected by the noise level of the transformer. Since the CONV measurements are determined by accumulating the charge-per-pulse, this noise contribution is also summed, meaning that for the same reading on the ICT as a UHDR reading results in lower measured dose or DAP on the radiochromic film. However, this is not an issue since the linearity between the two modes is still maintained. Furthermore, the noise contribution can be easily evaluated and subtracted. On other pre-clinical machines that use BCTs this is also the case and the BCT is often operated in two separate modes for UHDR and CONV deliveries to improve the sensitivity for CONV measurements [264, 265]. These results, therefore, confirm that it is possible to monitor the DAP of the VHEE beam at both UHDR and CONV delivery modes using an ICT. Furthermore, this demonstrates the ability to predict and target specific doses at a reference for both delivery modes through the use of monitoring the charge per pulse with the ICT, and measuring the beam size using a scintillating YAG screen prior to delivering the dose to the sample, to predict the dose delivered.

4.4 VHEE Radiochromic Film and Passive Dosimetry Comparisons

The work in this section describes the experiments performed at the CLEAR facility to compare the dosimetry measurements obtained by the radiochromic film dosimetry protocol described above at the CLEAR facility, to measurements obtained by two passive dosimetry methods which have been provided by two metrological laboratories in Europe. The first describes a comparison between EBT-XD radiochromic film and alanine pellets provided by national metrological lab of Germany, Physikalisch-Technische Bundesanstalt (PTB) in Braunschweig. The second describes comparisons made between EBT3, EBT-XD and MD-V3 films to small phantoms containing three TLD dosimeters and three radiochromic film cutouts, provided by the Insitiut de Radiophysique, CHUV, Lausanne, Switzerland. In both cases the dosimeters were delivered to the CLEAR facility where they were irradiated simultaneously with the radiochromic films. They were then sent back to the respective institutions for the dose measurements to be made there.

4.4.1 Alanine

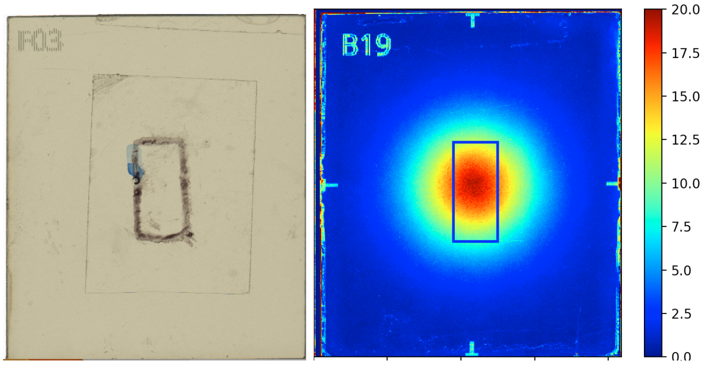

Figure 4.11: TIFF image of example radiochromic film, with area of alanine pellets outlined to define the AOI for determining corresponding dose to the pellets (left), dose map of one of EBT-XD films irradiated targeting 20 Gy showing the AOI overlaid (right).

Measurements were performed with four alanine pellets stacked on top of each other per sample holder, which were attached to the front of a radiochromic EBT-XD film, as shown in Fig 4.11. All measurements were performed at CONV dose rates using one bunch per pulse with 400 pC/bunch delivered at 0.833 Hz, targeting doses of 10 Gy, 15 Gy, and 20 Gy, using VHEE beam energies of 50 MeV, 100 MeV, 150 MeV, and 200 MeV. The beam size was kept constant at approximately $\sigma_{x,y} = 5.5$ mm, as measured on the scintillating YAG screen, to ensure all samples received the same dose distribution. To keep this constant for all electron beam energies, different depths were used for each as shown in Table 4.2. The dose delivered was determined by calculating the mean dose, and corresponding standard deviation, over the AOI shown in Fig. 4.11. The dose to the alanine is determined by PTB through the use of electron spin resonance (ESR) spectroscopy, whereby the concentration of the free radicals created during exposure to the beam are measured. The absorbed dose to water measured by the alanine, $D_{Al,w}$, is calculated by PTB from Equation The dose

Energy (MeV)	Depth in Water (mm)
50	60
100	110
150	145
200	180

Table 4.2: The depth in water each alanine pellet and radiochromic film was irradiated at for each energy.

is determined based on measuring the concentration of these radicals through recording an ESR spectrum of the alanine pellets - which is proportional to the delivered dose. The absorbed dose to water measured by the alanine, $D_{Al,w}$, is calculated with the equation:

$$D_{Al,w} = \left(\frac{A_{det} \cdot k_{env}(T)}{m_{det} \cdot \mathcal{A}_{D,w}^{^{60}\text{Co}}} \right) k_{Al,E} \cdot k_{\text{field}} \tag{4.8}$$

where A_{det} is the signal amplitude measured from the alanine pellet during ESR spectroscopy, m_{det} is mass of the alanine pellet, $k_{env}(T)$ is the temperature correction factor, $k_{Al,E}$ is the beam quality conversion factor and k_{field} is to correct for the non-uniformity of the irradiation field. Finally, $\mathcal{A}_{D,w}^{^{60}\text{Co}}$ is the dose-normalised amplitude which is obtained by measuring the amplitude of the alanine pellets irradiated in a reference ^{60}Co field, where the result is compared to the known result which can be traced back to the primary standard absolute dosimetry measurement [161]. The dose normalised amplitude, $\mathcal{A}_{D,w}^{^{60}\text{Co}}$, can be traced back to the PTB primary standard water calorimeter [161, 267]. To compare the alanine response to the film, the mean dose for the four pellets in each sample holder and the corresponding standard deviation were calculated.

The measured doses on the AOI of the EBT-XD compared to those obtained from the alanine pellets for each irradiation are shown in Fig. 4.12. The first observation that can be made from the data is that the dose values between the EBT-XD films and the alanine agree within the standard deviations of the measurements from each dosimeter, with mean percentage agreements of between 7.16% for 200 MeV and 11.32% for 50 MeV. However, despite this the mean doses recorded on

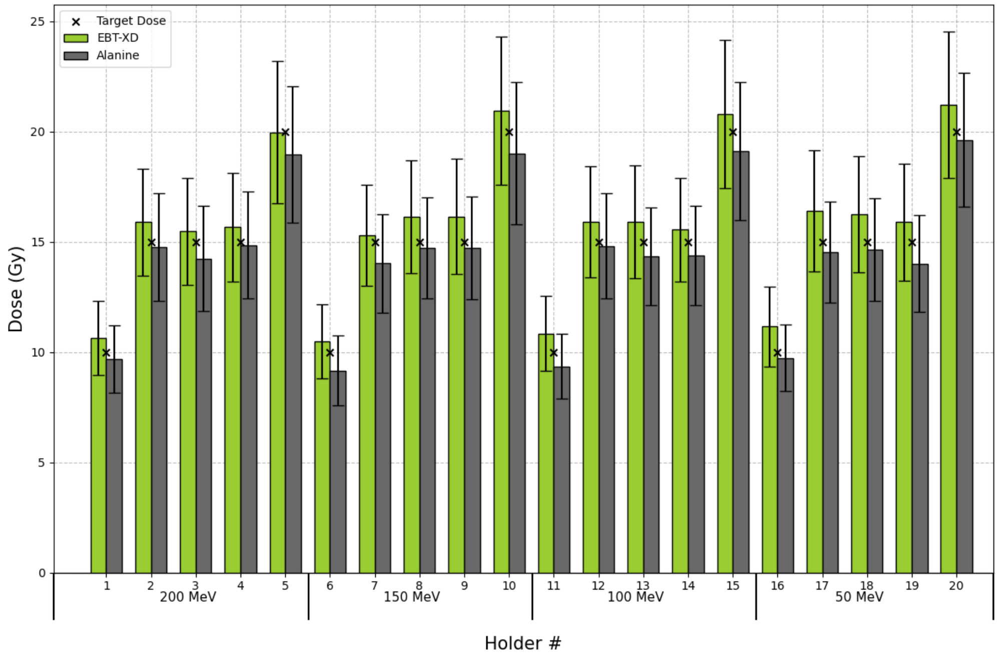

Figure 4.12: Alanine and EBT-XD Radiochromic Film Dose Measurement Comparisons for 50, 100, 150 and 200 MeV VHEE beams at target doses of between 10 and 20 Gy delivered at CONV dose rates.

the radiochromic film and the upper end of the uncertainty range are consistently larger than that for the alanine dose measurements. This could either be due to the radiochromic film dosimetry over-estimating the dose by a small amount or due to the additional uncertainties around the large variation in the beam distribution over the alanine pellets. It can also clearly be seen that the standard deviation for each measurement is significantly larger, with an average of 15.9% for the EBT-XD film and 16.1% for the alanine. These values are much larger than that of the individual uncertainties associated with dose determination from radiochromic films and alanine, which is 5% and 1% respectively. This is mostly because of the large area occupied by the alanine pellets and the Gaussian transverse distribution of the beam meaning each alanine pellet receives a varying dose distribution, whereas their intended use is for use with constant uniform dose distributions. Additionally, the dose determined across the radiochromic film assumed a perfect alignment of the alanine pellets on the film, which may not have been the case; and hence contributes to the uncertainty on the dose determined. For a better validation of these measurements, they should be repeated with a more uniform beam to remove as many of the uncertainties with regards to the dose distribution as possible.

4.4.2 TLD and Radiochromic Film Phantom

These measurements were based on the multi-centre cross validation of the dosimeteric comparison scheme for UHDR irradiation at CHUV, Lausanne and Stanford University, CA, USA, which used a cuboid phantom filled with TLDs, alanine and radiochromic film to compare the measurements of 8 MeV UHDR electron beams [268]. The experimental design was adapted so that the smaller phantoms were used which can be held in the 3D printed holders for the C-Robot and be irradiated in the water tank. The phantoms have an interior cylindrical volume with a diameter of 5 mm and a length of 6 mm and were filled with three LiF-100H TLDs ($3.2\times 3.2\times 0.9\,\mathrm{mm}^3$) and up to ten EBT3 radiochromic films cut to diamter of 5 mm. These phantoms were then positioned inside a 3D printed holder for the C-robot (as shown in Fig 4.13) positioned between an upstream radiochromic film (1 mm in front of the phantom) and a downstream radiochromic film (positioned 4 mm behind the phantom). All of the measurements were targeting a dose of 10 Gy using 200 MeV electrons, delivered both at UHDR dose rates (i.e., one single train of 10 Gy) or CONV dose rates (i.e., one bunch per pulse and multiple pulses delivered at 0.833 Hz). The holders were positioned in the water phantom such that the longitudinal centre of the phantom was at approximately 210 mm in water. The dose was calculated from the film by averaging the film dose over a circle of diameter 6 mm, as shown in Fig 4.13 on the upstream and downstream films, and calculating the corresponding mean and standard deviation both across the AOI and between the two films. The doses from phantoms were determined by the Institut de Radiophysique (IRA), CHUV, Lausanne, whereby the films were analysed according to their own radiochromic film dosimetry protocol. The TLDs were calibrated for absorbed dose to water measurments using a ^{60}Co unit at the IRA, which can be traced back to the primary standard of the absolute dose measurements using a water calorimeter at METAS (Swiss primary standards laboratory) [158, 268]. The calibration of the TLDs and films along with their output reproducibility an uncertainty contribution of 5%. The measured doses across the AOI

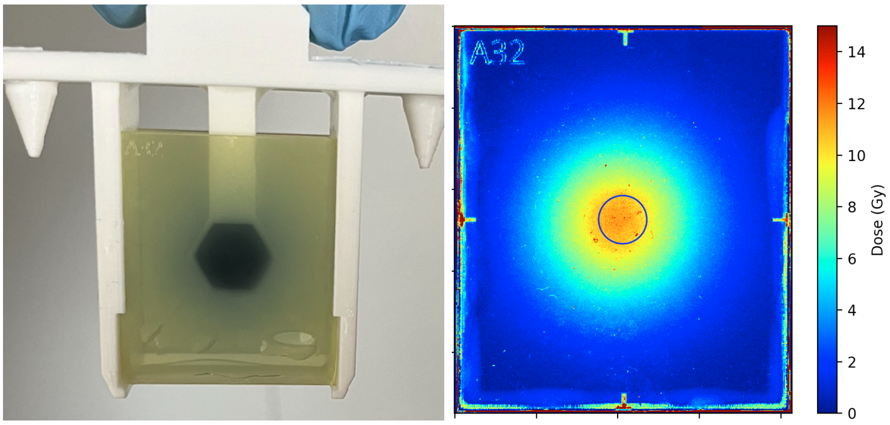

Figure 4.13: Photo of radiochromic film holder, with area of TLD phantom visible behind the film (left), dose map of one of EBT-XD films irradiated targeting 10 Gy showing the AOI overlaid (right).

of the upstream film, downstream film and the mean of the two radiochromic films compared to that from the TLD and film phantom are shown in Fig. 4.14. For most of the measurements the dose obtained from the phantom is within the uncertainty range of the mean film response, with an agreement between the radiochromic film measurements and the phantom dose measurements of 7.86% for EBT3 film, 6.29% for EBT-XD film and 13.2% for MDV3 film. However it can be seen that the phantom dose measurements are within much closer agreement to the downstream film measurements. The separation of the two films was 20 mm, and this large separation is the reason for the notable differences in the doses measured by the upstream and downstream films, and potentially one of the reasons for discrepancies in the doses determined by the films and the phantoms. One suggestion for future work would be to further investigate the longitudinal distribution of the dose between the upstream and downstream films for calculating the dose to sample rather than simply the averaging the doses across the two AOI's since it is likely the dose fall-off is not linear, particularly for separations this large. It can also be seen from Fig. 4.14 that the difference in dose between the upstream and downstream radiochromic films is not constant, suggesting that the beam divergence varies between the irradiation of each phantom holder, further contributing to the uncertainty of the measurements. Likewise with the alanine, the Gaussian beam distribution means that the samples received a large transverse variation in dose. Therefore, future experiments investigating this should aim to minimise the transverse variation of the beam as well as better characterise the longitudinal variation of the dose.

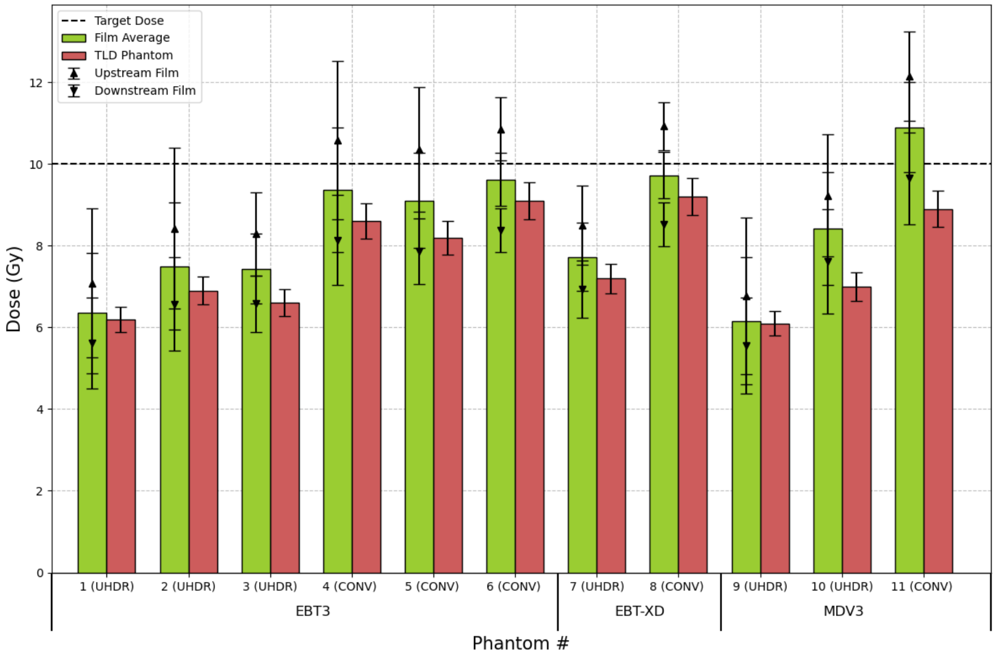

Figure 4.14: TLD/Film Phantom and Radiochromic Film Dose Measurement Comparisons for 200 MeV VHEE beams with a target dose of 10 Gy delivered at UHDR and CONV dose rates.

4.5 Concluding Remarks

The work presented in this chapter describes the radiochromic film dosimetry protocol that has been developed for sample irradiations and detector characterisation for VHEE UHDR irradiations at the CLEAR facility. Additionally it aimed to address the challenge of UHDR dosimetry and dose targeting using Gaussian beam distributions. The first part of the investigation into the determination of beam size using Gaussian fits applied to dose distribution on radiochromic films and YAG screen measurements showed consistent sizes and discrepancies across different fitting methods. The 1D Gaussian fits using horizontal and vertical strips yielded the smallest beam sizes, whereas fits to the

1D projection of profiles resulted in the largest sizes, and finally the 2D Gaussian fits presented the highest uncertainty of the three methods. These variations stem from the sensitivity of the fitting methods to background noise and the influence of signal distribution. The YAG screen, in particular, showed larger beam sizes compared to the EBT3 radiochromic film, likely due to signal distortion as light passes through water. Overall, these results highlight the importance of using a consistent Gaussian fitting method at all stages of the dosimetric analysis in order to achieve an accurate beam size measurement. Furthermore, a protocol was established to target the central dose deposited on the film thorough correlating the charge measurements made with the ICTs to the DAP measured on radiochromic film in water. A strong linear correlation was shown between the charge readings with the DAP of the dose distribution on the radiochromic film for both UHDR and CONV deliveries. Therefore, through the determination the beam size before a sample irradiation using the YAG screen, it is possible to accurately target the dose to the sample just by knowing the charge delivered using the ICT (for a given beam size). For the CONV deliveries using a lower instantaneous dose rate, the correlation between the ICT charge measurement and DAP does vary meaning that separate calibration factors for the two delivery modes are required. Further work is currently being done by members of the CLEAR team to fully characterise this effect and provide a precise correlation between the beam sizes measured on the scintillating YAG screen and the radiochromic films using the 1D strip method, with the eventual goal of being able to perform real-time dosimetry of the VHEE beams at UHDR using the YAG screen.

Finally, a comparison of the doses measured by radiochromic films to that of two other passive dosimetry methods: alanine and TLDs, was performed. The purpose of these measurements was to assess the agreement between the dose determination of all three of these passive dosimetry methods to VHEE beams, since they are all commonly employed for pre-clinical UHDR irradiations. The study showed that the doses measured by both the alanine and the TLD phantoms were in agreement to the doses measured by the radiochromic film, within the uncertainty range. However, there were notably large uncertainties in the measured dose for both the radiochromic film as well as the alanine and TLD phantoms. The main reason for this was largely due to the Gaussian beam distribution and the passive dosimeters being large in size relative to the beam size, meaning that the passive dosimeters received a variation of doses. Additionally, the longitudinal variation between the upstream and downstream films was assumed to be constant, however this likely not the case which caused additional uncertainty in correlating the dose measured by the radiochromic film and the comparative passive dosimeter. Whilst agreement between the dosimetry methods was demonstrated, further measurements either using a larger beam size or fewer dosimeters per sample (so that they occupy a smaller area relative to the beam size) should be performed in order to attempt to reduce the uncertainty in the dose measurements. Recently, a dual scattering foil has been installed inside the beam line to produce uniform collimated beams with a radius of 1 cm [269]. This should allow for a more reproducible and accurate dosimetric comparison of different methods using VHEE beams at UHDR since the dose across the transverse area of the samples is almost uniform. Furthermore, a more comprehensive investigation into the reference depth at which these dosimeters are irradiated at should be investigated in order to accurately correlate the dose on the sample if two radiochromic films are used upstream and downstream of the sample.

5 A Novel Fibre Optic Monitor for Beam Profile and Dose Monitoring at Ultrahigh Dose Rates

5.1 Introduction

In conventional radiotherapy, large-area parallel plate transmission ionisation chambers are a permanently installed fixture within the treatment head or nozzle that are used to monitor the beam fluence as well as other key parameters such as the flatness and symmetry (additionally, in the case of proton PBS - the pencil beam position). These ionisation chambers face the same issue of response saturation at UHDR as those used for reference dosimetry. An additional requirement for monitor chambers at UHDR is speed of the feedback signal to be able to monitor the beam at these dose rates. Currently this is not possible given that the timing response of existing built-in monitor chambers is up to 300 µs [75]. Some studies have been performed on the response of the built-in monitor chamber on a modified ELEKTA Precise linac to a UHDR electron beam. A pulsed 10 MeV electron beam at UHDR, with a 3.5 µs pulse width delivered a pulse repetition frequency of 200 Hz, was used and results showed that standard operating voltage of −320 V the ion collection efficiency of 0.1 at a dose-per-pulse (DPP) of 0.98 Gy/pulse [77]. A logistic fit was used to calculate the correction factors through operating the monitor chamber at an increased voltage of −960 V in order to compensate for the recombination effect. However, such a method introduces large uncertainties on the calculated values. Further work by this research group was performed on re-configuring the built-in monitor chamber on the modified clinical linac for pulsed UHDR electron beams. The modification involved reducing the electrode separation from 1 mm to 0.6 mm, and operating at a further increased voltage of −1200 V. A charge collection efficiency of of $\geq 98\%$ was achieved at a DPP of 0.88 Gy/pulse (70 Gy/s) [78], as shown in Fig. 5.1. For beam monitoring with proton and carbon

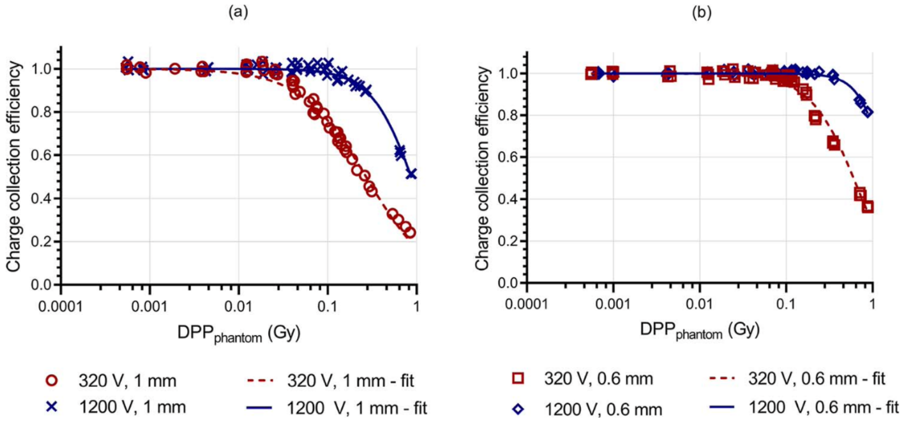

Figure 5.1: Signal per pulse of built-in transmission ionisation monitor chamber, 1 mm electrode separation (a) and 0.6 mm (b) at operating voltages of −320 V and −1200 V, plotted against the DPP for a 10 MeV electron beam with a 3.5 µs pulse width delivered a pulse repetition frequency of 200 Hz. Reproduced from [78], ©2025 Radiation Research Society.

ion UHDR beams for FLASH, the recombination effect within transmission ionisation chambers is lower since the delivery is quasi-continuous rather than pulsed. Therefore applying correction factors or making small modifications to this device to correct the response is more feasible [270]. One approach investigated for UHDR carbon beams was to replace the $Ar - CO_2$ gas within the electrode gap with helium, which causes a smaller number of electron-ion pairs, as well as faster drift time to the electrodes. This resulted in a linear response at a voltage of 1000 V, and an agreement between monitored dose values at UHDR and CONV dose rates of $\pm 1\%$ [67]. Another potential solution is using an ionisation chamber which consists two or three parallel plate chambers, each with independent electrodes that are separated by gaps of varying thickness. This means that each section experiences different recombination effects and hence charge collection efficiencies, which can then be more easily modelled and corrected for [271]. Furthermore, a novel prototype high-resolution position sensing transmission ionisation chamber was developed for FLASH with proton PBS beams from cyclotrons with an air gap of 1 mm (compared to 5 - 10 mm air gaps used in conventional proton beam monitor chambers), along with strip electrodes to provide a beam position resolution of up to 100 µm. This monitor was shown to significantly reduce the ion recombination effect at proton beam dose rates within the UHDR regime [272].

Whilst using a modified or novel built-in transmission ionisation monitor chamber seems like a feasible alternative for UHDR beams which have relatively low instantaneous dose rates i.e., those that are delivered quasi-continuously, or those from modified MV clinical linear accelerator, it is apparent that alternative technology is required for beam monitoring of pulsed novel modalities. This is because the high instantaneous dose rates (which are required due to the low pulse repetition frequency from linear accelerators) cause more severe recombination effects within these ionisation chambers. The ideal characteristics one should aim to achieve when investigating new technologies for online beam monitoring for UHDR RT beams are [75]:

- a large dynamic intensity range in order to deal with beam intensities from conventional RT dose rates up to the UHDR regime;
- a high temporal resolution in order to resolve pulses to determine instantaneous dose rate as well as provide feedback signal for accelerator's safety interlock;
- a high spatial resolution to provide beam position and profile measurements;
- a large sensitive area to be able to monitor the beam over the maximal extent of the clinical treatment fields, that can vary from less than a centimetres up to tens of centimetre;
- a high radiation tolerance since these detectors are a permanent fixture in the machine;
- a high level of beam transparency in order to minimise perturbations to the beam characteristics.

A recently published paper from the European Society for Radiotherapy and Oncology (ESTRO) Physics Workshop outlined what the minimal and optimal requirements are for UHDR beam monitoring [270]. The report stated that the optimal requirements for such a device would be to provide real-time 2D monitoring of the field size and characteristics for a collimated broad beam, and the real-time 2D monitoring of the beam size per spot on segmented detectors for PBS. There are currently number of research groups have been investigating the feasibility novel technologies beam monitoring at UHDR that are required for FLASH-RT. These include beam current transformers (BCTs) [264, 265, 266], an air fluorescence monitor [273], silicon carbide (SiC) detectors [169, 170], and scintillating screens [274, 275].

The use of fibre-based methods, i.e., scintillator-coupled optical fibres and fibre optic Cherenkov sensors, for real-time dosimetry at UHDR has been of particular interest due to its favourable properties such as dose-rate linearity, and high spatial and temporal resolution, with numerous works demonstrating its applicability to real-time dosimetry and pulse monitoring for FLASH with electrons [172, 276, 277, 278], protons [279], kV X-rays [280], and VHEE beams [281]. Orthogonal arrays of scintillating fibres are used for beam profile and intensity measurements of the CERN secondary beam lines [282, 283, 284]. Similar devices have also been developed in recent years for beam fluence and profile monitoring for hadron therapy centres [285, 286, 287], however these devices have only been tested and optimised for the low intensities required for pencil beam scanning dose rates. In radiation therapy scintillation fibre dosimetry, Cherenkov radiation is often considered a source of contamination to the scintillation signal. However, direct detection of Cherenkov signal using optical fibres could be particularly beneficial within UHDR dosimetry since the increased beam intensity associated with this modality favours the detection of the optical photons produced in Cherenkov radiation [172]. Furthermore, Cherenkov light is produced instantaneously, on a timescale of 10^{-12} s, following the interaction between the charged particle and the dielectric medium, hence making it an ideal method for radiation detection at the fast time scales required for UHDR RT. Since the electrons in VHEE beams are ultra-relativistic, the relative variation of the angle of emission of Cherenkov radiation is minimal within the VHEE energy range (50 - 250 MeV) - shown in Fig 2.8 - and therefore a Cherenkov based detector could be more suitable for VHEE dosimetry and real-time beam monitoring.

The work in this chapter presents a novel technology proposed for UHDR online monitoring of the beam profile and dose, particularly for use with VHEE beams, called the Fibre Optic FLASH Monitor (FOFM). This beam monitor consists of an array of optical fibre-based Cherenkov sensors which are readout using a CMOS camera. This chapter first describes the development of the fibre array monitor is outlined along with the initial modifications made to the FOFM to optimise its performance. Since the clinical translation of VHEE-FLASH is likely to either be delivered through pencil beam scanning (PBS) or using collimated broad beams, the FOFM was tested using both beam types. This chapter first describes the initial tests performed at the CLEAR facility with 200 MeV electrons using a single optical fibre in order to evaluate the performance of different photodetectors. Then the first set of measurements taken with the FOFM reported in this chapter are beam profile measurements and DPP response linearity measurements with 160 MeV and 200 MeV electron Gaussian pencil beams at the CLEAR facility, covering the entire DPP range that is used at CLEAR for VHEE UHDR experiments. A further set of measurements of the DPP response linearity, beam profile measurements, in addition to real-time dose monitoring and beam perturbation measurements at CLEAR using uniform flat beams generated from a newly installed dual-scattering system are then described. Finally, a comparison between the FOFM's performance characteristics with other UHDR beam monitors currently under development is evaluated and the next steps in the detector's development towards eventual clinical implementation are outlined.

5.2 Single Fibre Photodetector Evaluation Measurements

A technique utilising scintillating fibres has been implemented by CERN Beam Instrumentation group on the secondary beamlines of the East Area in the experimental area at CERN for beam intensity and profile monitoring of low intensity hadrons for fixed-target experiments. The device consists of an array of scintillating plastic fibres that are read-out using multi-channel silicon photomultipliers (SiPMs) [283]. The group are currently undertaking research to develop an alternative type of fibre array monitor for the CERN North Area which uses higher intensity beams, and therefore an alternative to plastic scintillating fibres is required [284]. Three types of fibre detectors are under investigation:

- Solid-core silica fibre-based Cherenkov sensors
- Liquid scintillator-filled capillaries
- Scintillating gas-filled hollow-core fibres

Due to the abundance of Cherenkov radiation produced by electron beams in the VHEE energy regime, as well as the favorable temporal properties of Cherenkov radiation, the solid-core silica fiber-based Cherenkov sensors were chosen for investigation at the CLEAR facility. The goal was to assess the characteristics of such a detector for potential applications in monitoring the dose and profile of VHEE beams at UHDR for FLASH. Measurements were conducted at the CLEAR facility at CERN using a single silica Fibre Optic Radiation Sensor (FORS), which was readout using a range of different photodetectors: a SiPM, a PMT and a CCD camera. These initial measurements were performed as proof-of-principle tests in order to determine the dynamic range of each photodetector setup, and hence to evaluate the feasibility of each photodetector for the application of a potential fibre optic beam monitor for VHEE UHDR beams. All of the measurements with a

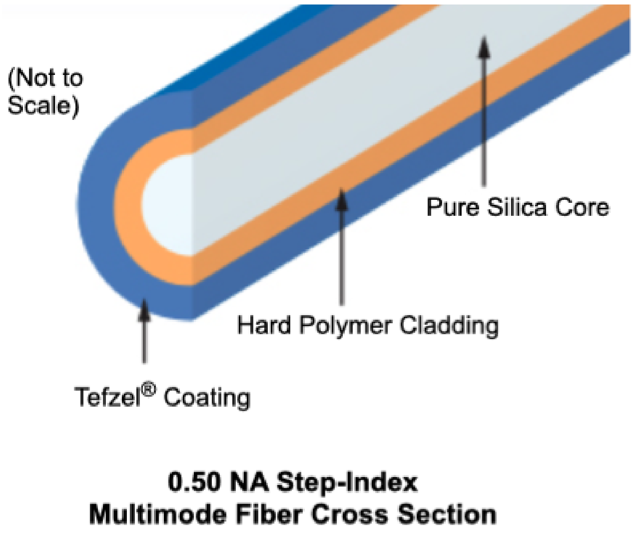

Figure 5.2: Cross-section of the 0.50 NA Step-Index Multi-modal Fibre from ThorLabs.

single optical fibre used a 200 µm core diameter, 0.5 Numerical Aperture (NA) step mult-imodal silica optical fibre (Thorlabs GmbH, Munich, Germany), shown in Fig. 5.2. A sensitive region of 20 cm in length of the silica optical fibre was mounted on a holder positioned within the beam path. However the connection between the sensitive region for each of the photodetector setups varied slightly, as is described below.

5.2.1 SiPM and PMT Photodetectors

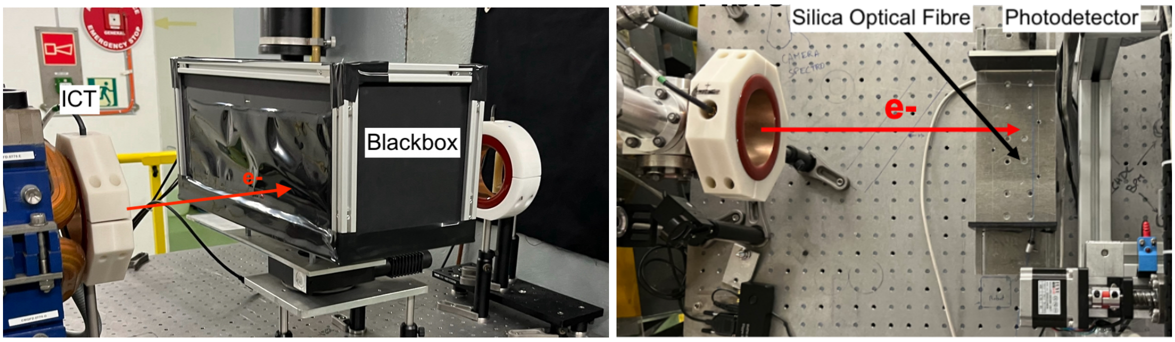

Figure 5.3: Photographs of the single optical fibre measurements setup in the CLEAR in-air test stand, with black box which houses the silica fibre and SiPM/PMT photodetector (left) and the setup showing the alignment of the optical fibre in the beam path (right).

The first measurements involved using a setup with SiPM and PMT photodetectors. For these measurements the sensitive region of the silica optical fibre was directly connected, using optical gel, to a SiPM (Hamamatsu Photonics, Shizouka, Japan) which was in turn connected to a digitiser, shown in Fig. 5.3. For the PMT measurements this was attached instead to a fast photomultiplier tube (PMT) with a Neutral Density (ND) = 6.0 optical filter (10^{-4} % transmission) (Thorlabs GmbH, Munich, Germany) which was readout using a Teledyne LeCroy Oscilloscope. This entire setup was then mounted inside a blackbox, as shown in Fig. 5.3, which used Mylar foil on the beam entrance and exit windows to reduce ambient light picked up as background noise on the photodetector. Measurements were taken for 100 consecutive pulses and the mean amplitude of the signal, recorded on the digitiser or oscilloscope was computed. From this the response of the optical fibre and photodetector at each pulse charge was obtained by integrating the mean signal in a time window of 100 ns for single bunch measurements and 400 ns multi-bunch measurements. To evaluate the linearity of the detector, the response was measured first as a function of the charge per bunch for a single bunch per pulse, by modulating the intensity of the laser power. Then for multiple bunches per pulse the increase of charge per pulse was achieved by operating at a fixed bunch charge and then increasing the pulse width by incrementing the number of bunches. Due to the size of the single fibre setup using the SiPM and PMT photodetectors, it was not possible to simultaneously measure the fibre response with dose measurements on radiochromic films. Furthermore, due to the increase in transverse beam size following the increase in charge per-pulse and pulse width, due to dispersion and beam loading effects in the accelerator, applying a simple dose-charge ratio calibration factor would not be sufficient. Therefore, the response of the solid core silica fibre connected to the SiPM and PMT photodetectors is presented as a function of the charge per pulse, with an approximate conversion to DPP for the highest pulse charge, calculated from the irradiation of an MDV3 radiochromic film to 19.5 nC pulse at a depth of 190 mm in water. A linear regression fit is then performed to describe the behaviour of the response of the fibre as function of charge per pulse. The R^2 value was computed using Eq. 4.7, as a metric to evaluate the linearity of the fibre and photodetector response. Uncertainties in the fibre output were calculated from the standard deviation of the repeated measurements for each charge per pulse.

5.2.1.1 SiPM Measurements

Single Bunch The first measurements using the silica fibre and SiPM photodetector setup were to investigate the response to a single bunch per pulse, with a bunch length of approximately 3 ps. Measurements were taken at a number of bunch charges between 20 pC/bunch and 150 pC/bunch, and the resulting signal traces and response plot are shown in Fig. 5.4, where the R^2 value for the linear fit was 0.973. The response plot appears to show a non-linear increase in the response of the SiPM and silica fibre to an increasing charge per bunch. This is likely due to the non-linearity of SiPMs when exposed to a high intensity of optical photons, such as that associated with the Cherenkov production resulting from the narrow pulse width when using one bunch. This is due to

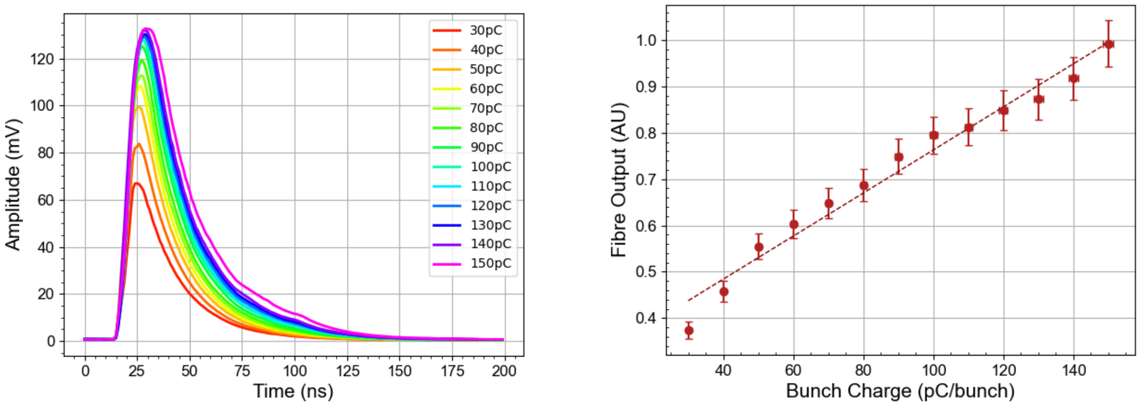

Figure 5.4: Digitiser signal trace for the silica fibre and SiPM photodetector response to a single bunch for charges of between 30 pC and 150 pC (left) and the corresponding response plot of the integrated area under the signal for each bunch charge ($R^2 = 0.973$) (right).

the fact that if two more more photons hit the same pixel within a short amount of time, they are counted by the detector as one.

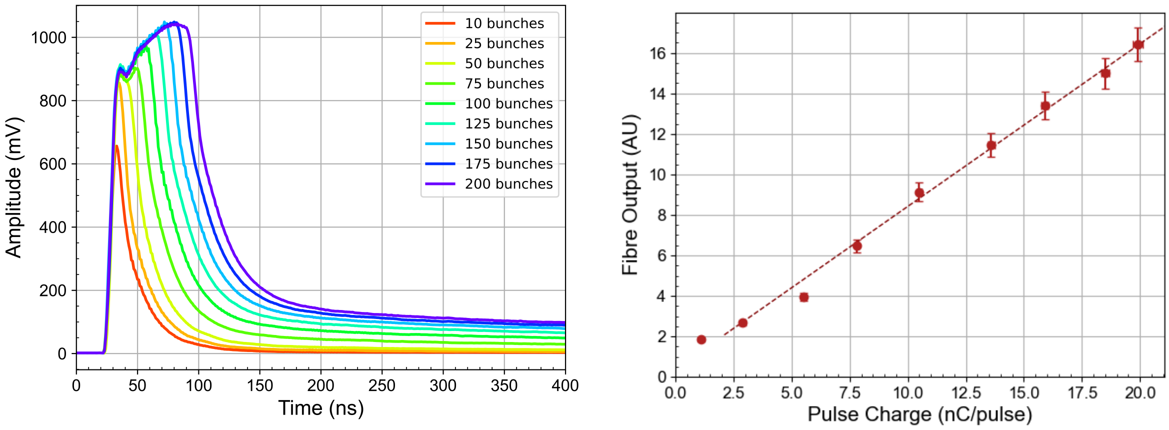

Figure 5.5: Digitiser signal trace for the silica fibre and SiPM photodetector response to each charge per pulse, for pulse widths of between 10 and 200 bunches (left) and the corresponding response plot of the integrated area under the signal for each pulse charge ($R^2 = 0.994$) (right).

Multiple Bunches The following measurements using the SiPM setup, shown in Fig. 5.5 were conducted using trains of multiple bunches with 110 pC/bunch that covered a range of pulse widths between 6.7 and 67 ns, corresponding to between 10 and 200 bunches at 1.5 GHz and charges of between 1.1 nC/pulse and 19.9 nC/pulse. The R^2 value for the linear fit to the SiPM response was 0.994. The response of the optical fibre connected to the SiPM appears to be linear up to charge per pulse of 19.9 nC/pulse, which corresponds to an equivalent dose per pulse of 23.9 Gy/pulse. However, when looking at digitiser signal, the amplitude of the response of the SiPM appears to reach saturation above 50 bunches. Therefore, the apparent linearity is likely to be from an increase in the area under the trace caused by the increase in pulse length and hence signal duration rather than from an increase in the signal amplitude.

5.2.1.2 PMT Measurements

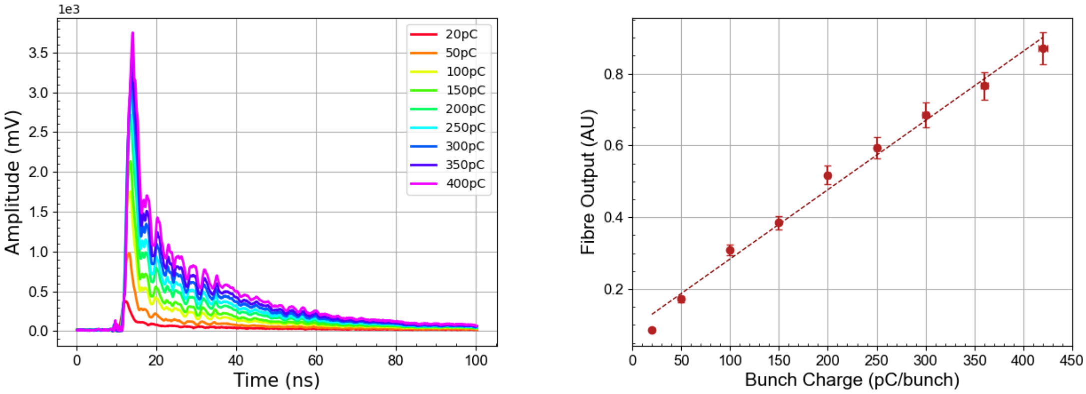

Figure 5.6: Analogue signal trace for the silica fibre and PMT photodetector response to a single bunch for charges of between 20 pC and 400 pC (left) and the corresponding response plot of the integrated area under the signal for each bunch charge ($R^2 = 0.989$) (right).

Single Bunch The first set of response linearity measurements for silica fibre and PMT photodetector were also carried out with a single bunch per pulse beam structure whilst varying the charge per bunch. For the measurements with the PMT the charge per bunch were varied between 20 pC/bunch and 400 pC/bunch. The results from this set of measurements can be seen in Fig. 5.6, where R^2 for the linear fit was 0.989. Therefore, the response of the PMT photodetector shows a better response linearity across the range of bunch charges for a single bunch as compared to the

SiPM, additionally the PMT shows no response saturation for the single bunch measurements.

Multiple Bunches The results obtained using the PMT as photodetector to measure the response of the fibre to pulses of multiple bunches are shown in Fig. 5.7. In these measurements a range of pulse of between 1 - 100 bunches with widths of between 0.7 and 67 ns were used, which corresponds to charges per pulse of between 0.4 nC/pulse and 18.2 nC. The linear fit of the response plot had an R^2 value of 0.984. As was the case for using the SiPM measurements, the signal amplitude saturates when the number of bunches is greater than 30. The integrated response of PMT photodetector exhibits only approximate linearity up to a maximum achievable charge per pulse of 18.2 nC/pulse, which is an equivalent dose per pulse of 24.8 Gy/pulse. Several factors might contribute to the observed deviations from linearity. Saturation of the PMT is the likely cause of the onset of this deviation at about 30 bunches per pulse and above, which has caused the PMT to have a worst response linearity for multiple bunches than was measured for the SiPM. Subsequently, at longer pulse widths, the relation between the DPP and pulse width changes due to increased beam losses. This then decreases the instantaneous dose rate within the pulse and it appears as a larger integrated signal, since the dose is delivered over a longer duration. In this case as well, like with the SiPM, the apparent linearity of the response to increasing DPP's will be from a greater integrated signal from the widening of the pulse duration.

5.2.2 CCD Camera Photodetector

The setup of the experiment was modified when using the optical fibre and a CCD camera as photodetector. Firstly, due to the lower sensitivity of the CCD camera compared to the SiPM and PMT detectors, the sensitive region of the silica optical fibre had to be positioned at 46° to the direction of the electron beam, shown in Fig. 5.8, in order for the CCD camera to detect the Cherenkov signal. Secondly, a longer optical fibre - with a 20 cm sensitive region, 1.2 m transport region) was used and a Retiga R6 6 MP CCD camera (Teledyne Photometrics, Thousand Oaks. US) was positioned in a light-tight blackbox behind the beam dump, as shown in Fig. 5.8. This was because the CCD

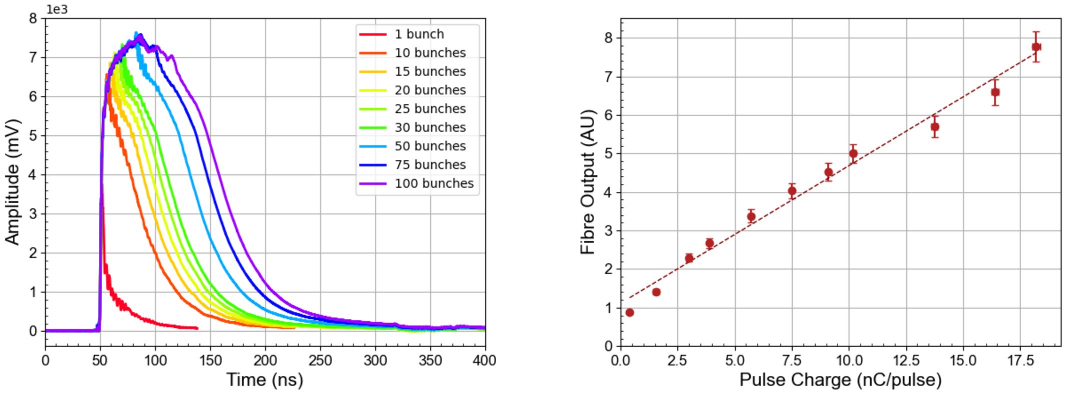

Figure 5.7: Analogue signal trace for the silica fibre and SiPM photodetector response to each charge per pulse, for pulse widths of between 1 and 100 bunches (left) and the corresponding response plot of the integrated area under the signal for each pulse charge ($R^2 = 0.984$) (right).

camera was potentially a lot more susceptible to radiation damage, and so positioned further away from the path of the electron beam to avoid any damage. Since the photodetector was no longer

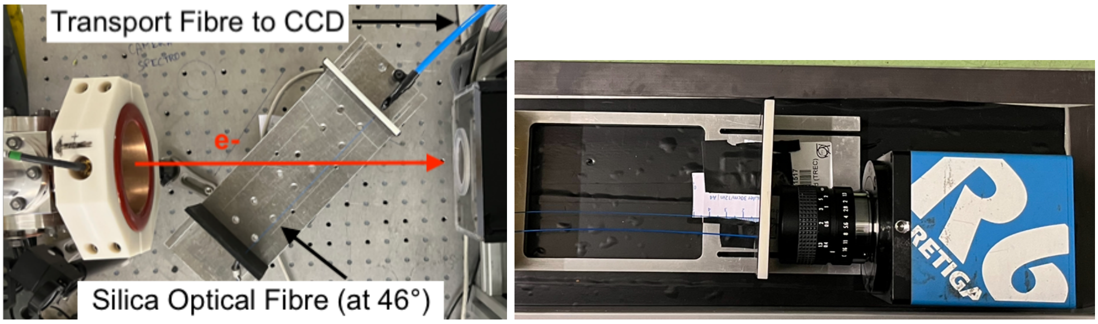

Figure 5.8: Photographs of the single optical fibre measurements setup in the CLEAR in-air test stand, with the sensitive region of the fibre oriented at 46° (left). The setup with the transport fibre and CCD photodetector which was positioned behind the beam dump and hence not visible in this image (right).

in the beam contrary to the SiPM and PMT cases, there was space to mount the single fibre on a motorised stage with vertical movement and this made possible a measurement of the transverse profile of the beam. Measurements were taken for 20 consecutive pulses, at each vertical position. The mean response was then plotted against the vertical position to reconstruct the beam profile and calculate the overall intensity response for each charge-per-pulse. In order to evaluate the linearity of the detector, the response of silica fibre measured by the CCD Camera was obtained as a function of charge per pulse for multiple bunches per pulse, where the increase in charge per-pulse of was achieved by operating at a fixed bunch charge and then increasing the pulse width by incrementing the number of bunches. Furthermore, since the setup in the in-air stand occupied less space, the silica fibre was installed in front of the C-robot water phantom which meant that absorbed dose to water calibrations using radiochromic film were obtained for a 4.7 nC, 9.7 nC and 19.9 nC pulse at a depth of 190 mm in water, and the corresponding dose to charge ratios for the entire range were determined from these three measurements. Therefore, the response linearity measurements for the CCD camera measurements are presented as a function of dose-per-pulse (DPP) as opposed to charge per pulse, with an associated 5% error in the dose determination from the radiochromic film measurement.

5.2.2.1 Profile Measurements

For each value of the beam charge (corresponding to a specific dose-per-pulse value) the optical fibre was moved vertically over the beam position at intervals of 1 mm between -5 & +5 mm with respect to the nominal centre ($y = 0$). For each pulse the mean value of the pixels over the area of the optical fibre on the CCD camera image was taken. 20 measurements of consecutive pulses were acquired at each vertical position. The average of these 20 measurements (with an uncertainty equal to the standard deviation between the repeat measurements) was taken as the response of the detector at the particular vertical position. The response as function of the vertical position of the fibre is shown in Fig. 5.9 for both a 1 nC and 10 nC pulse charge and 200 MeV electrons, as an example. This procedure allowed a reconstruction of the vertical profile of the beam. A Gaussian fit was then performed to the vertical profile of the beam for each value of the beam charge, from which the vertical beam size could obtained, and compared to that measured on the C-robot YAG scintillating YAG screen in air behind the fibre. The vertical beam sizes for the 1 nC pulse, and 10 nC pulse made by moving the single optical fibre, along with the corresponding values of the vertical beam size measured on the scintillating YAG screen are shown in Table 5.1. The vertical

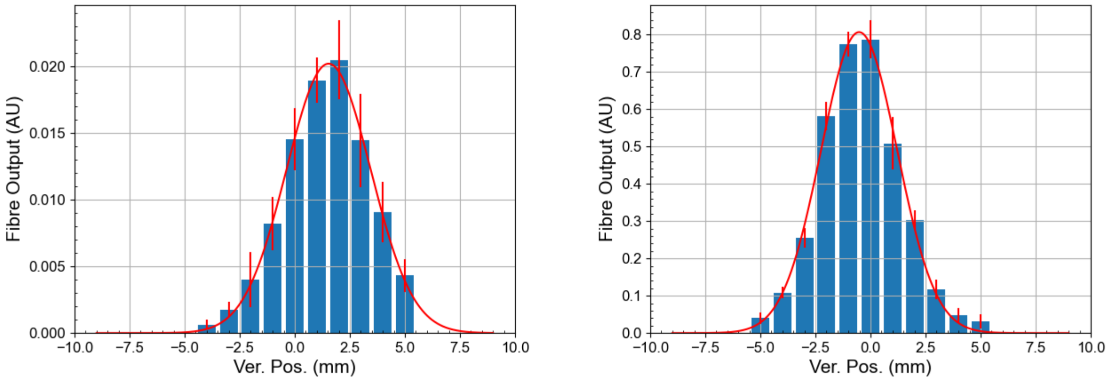

Figure 5.9: Vertical beam profile measurement of 200 MeV electron pulses with a Gaussian fit applied (red line), and with the vertical error bars corresponding to 1σ of the mean value measured from the 20 repeated measurements for each position for a 1 nC pulse (left) and a 10 nC pulse (right).

beam size measurements for the 10 nC can be seen to be in close agreement between the fibre and YAG screen. Whereas the fibre measured profile for the 1 nC is significantly smaller than that from the YAG screen. One likely cause is the lower sensitivity of the CCD camera at the lower charges per pulse, meaning the tails of the Gaussian beam did not generate sufficient Cherenkov light to be measured by the CCD camera.

Pulse Charge (nC)	Fibre beam size (mm)	YAG beam size (mm)
1	1.91 ± 0.09	2.20 ± 0.07
10	1.73 ± 0.03	1.83 ± 0.06

Table 5.1: Vertical beam size measurements made with the single fibre and CCD camera photodetector, and scintillating YAG screen obtained from the standard deviation Gaussian fit applied to the vertical projection of the beam profile. The uncertainty of the beam size measurement is expressed as the error on the standard deviation of the 1D Gaussian fit.

5.2.2.2 Response Linearity

In order to obtain the optical fibre response at a given pulse charge, two different methods were adopted and compared. The first consisted in summing the responses of the detector at each vertical position and the other involved taking the integral of the Gaussian fit over the vertical profile for each dose per pulse. The resulting response linearity plots for both of these methods are shown in Fig. 5.10. Pulse widths in the range of 0.7 to 57 ns were used, corresponding to between 1 and 86 bunches at 200 pC/bunch and charges per pulse of between 0.2 and 25.0 nC/pulse. The response of the detector can be seen to be linear up to a dose per pulse of 39 Gy/pulse, with an R^2 value of 0.985 and 0.998 for the summed response plot and the integral of the Gaussian plot, respectively. The response at DPP's of less than 5 Gy/pulse suffered from having a low signal-to-noise ratio (SNR). A better linear behaviour seems to be observed when using the integral of the Gaussian fit to the vertical profile for each DPP as detector response, however this method has larger error bars for each point due to uncertainties on the Gaussian fit therefore making it a less accurate method for determining the response of the fibre optic monitor. The differences between the two methods could be perhaps explained by the fact that the low intensity outer tails of the Gaussian beam are not efficiently detected due to the low SNR of the CCD camera. This under-response however, is compensated for when using the integral of the Gaussian fit.

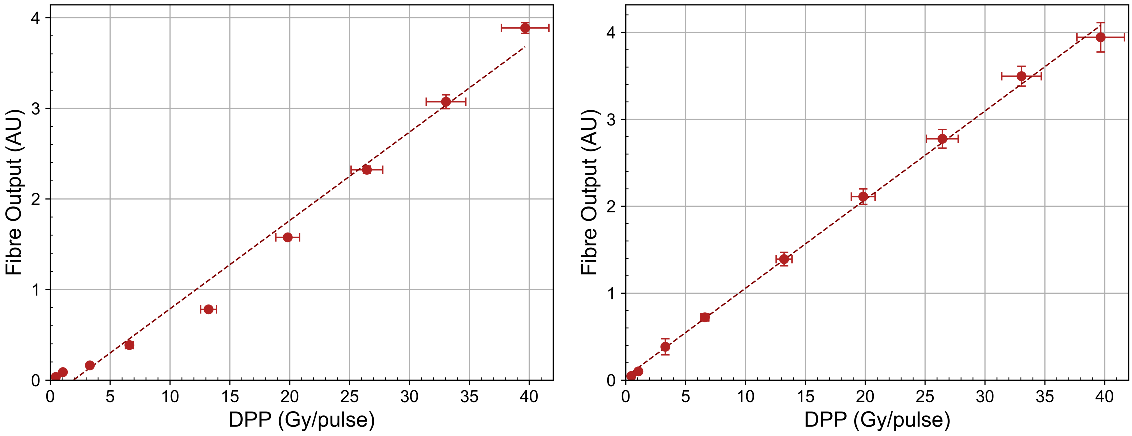

Figure 5.10: The response of the single optical fibre and CCD camera photodetector by summing the pixel value at each vertical position ($R^2 = 0.985$) (left), and where the response is calculated from the integral of the Gaussian fit ($R^2 = 0.998$) (right).

5.2.3 Single Fibre Measurement Conclusions

The purpose of the measurements with a single optical fibre was to determine which of the photodetectors used exhibited the most suitable characteristics. The SiPM and PMT showed a relatively linear response with increasing charge per pulse (and hence corresponding DPP) with R^2= 0.994 and 0.984, respectively. However, the signal amplitude showed saturation and the apparent linearity could likely be attributed to the widening of the pulse width. Alternatively, this demonstrates that these photodetectors have the advantage of a high time resolution that could be able to resolve the pulse width, even when operated under saturation conditions. Therefore the information could be used to monitor the instantaneous dose rate of the beam and a possible final prototype of the FOFM could incorporate a SiPM or a PMT attached to one of the fibres with the purpose of providing temporal information. The CCD camera showed poor linearity (R^2 = 0.985) when summing the fibre response at each vertical position measurement, but conversely showed excellent linearity (R^2 = 0.998) when using the integral of the Gaussian fit applied to the profile for each DPP. This can likely be attributed to the Gaussian fit compensating for the under-response at intermediate DPP's due to the low SNR of the CCD camera, meaning the low intensity tails of the beam are not accurately measured. Furthermore, the relatively low SNR of the CCD camera meant that the optical fibre had to be positioned at an angle in order for a large enough Cherenkov signal to reach the CCD. Therefore, the results from the above section showed that the SiPM and PMT photodetectors were too sensitive to be able to measure the entire range of DPPs used at the CLEAR facility due to saturation of their response. Whilst the CCD camera photodetector setup was able to provide an unsaturated response across this entire range of DPPs, it showed a low SNR ratio at the lower DPPs. This could either have been due to the CCD camera response itself, or from a potentially reduced transmission of Cherenkov light signal due to optical absorption within the cladding and coating of the fibre. The results from the above section showed that whilst the SiPM and PMT photodetectors had an excellent temporal resolution, they were too sensitive to be able to measure the upper range of DPPs used at the CLEAR facility due to saturation of the amplitude of their response. However, these photodetectors could be considered for use within a future detector for the measurement of the pulse width, and hence instantaneous dose rate, as this could be possible even when the response saturates. On the other hand the CCD Camera photodetector setup was able to provide an unsaturated response across this entire range of DPPs, but showed a low SNR ratio at the lower DPPs, and therefore was unable to measure the tails of the Gaussian beam distribution. Furthermore, using a camera-based detector setup would allow to image an entire array rather than requiring a photodetector array.

Taking into consideration the characteristics of the photodetectors used for the single fibre experiments, it was decided that instead a CMOS camera photodetector would be used for detecting the signal for the fibre array measurements for the following reasons: such a detector has mostly the same characteristics as a CCD camera in addition to a larger dynamic range, increased frame rate and increased tolerance to radiation. Additionally, a number of CMOS cameras were already installed in the CLEAR IN-Air test stand experimental area for use with the scintillating YAG screens, which therefore made installation much easier.

5.3 Fibre Array Monitor Assembly

5.3.1 Initial Design

5.3.1.1 Silica Fibres

Ahead of constructing a fibre array, an investigation into the to type of fibre to be used was carried out since there was potentially a reduced transmission of Cherenkov light signal due to optical absorption within the cladding and coating of the fibre. To investigate this, a range of Monte Carlo simulations using different single optical fibre setups with TOPAS were performed.

The TOPAS MC simulation used a 200 MeV electron beam source, with the optical fibre positioned 50 cm away from the beam source. The standard TOPAS GEANT4 physics list was used in addition to the $g4optical$ physics list to enable the creation and transportation of optical photons [218]. The number of optical photons leaving the $x-$ surface of the fibre were scored. The simulation was performed with 1×10^6 histories, and the resulting number of scored optical photons was scaled to provide a value per nanocoulomb.

The first setups that were simulated were those for SiPM and PMT photodetectors and the CCD camera were simulated using a 0.2 mm diameter core multi-modal fibre of 20 cm length oriented at 0° (Setup **1.**) and with 120 cm oriented at 0° (Setup **2.**), and at 45° (Setup **3.**). The remaining two simulation setups involved simulating 30 cm long, bare silica fibres with no coating or cladding, with diameters of 0.2 mm (Setup **4.**), and 0.4 mm (Setup **5.**). The lack of coating and cladding (which had a similar refractive index to the silica core) permitted a larger transmission of the Cherenkov signal to the end of the fibres due to a larger trapping angle because of the larger difference between the refractive index of silica and air. The results shown in Fig. 5.11, show that Setup **5.** has by far

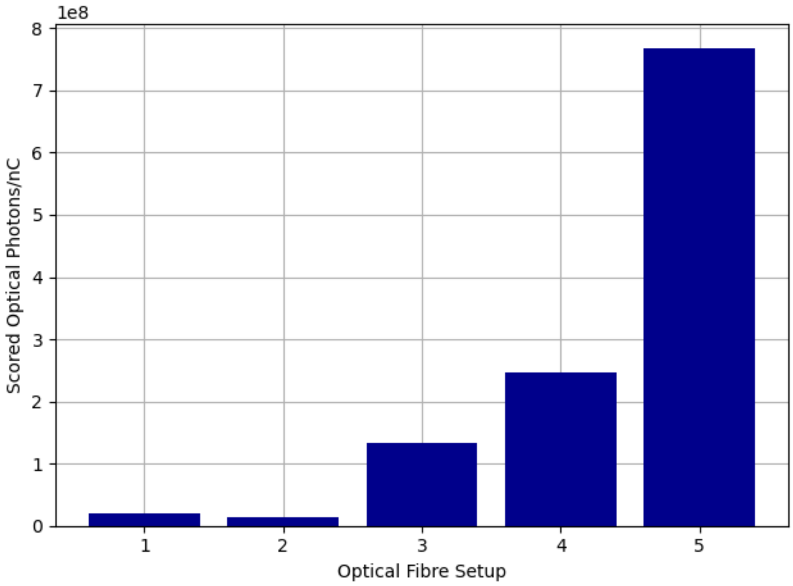

Figure 5.11: A chart showing the scored optical photons from different TOPAS MC simulations of 5 different fibre setups, following the irradiation of a 200 MeV electron beam. **1.** 0.2 mm diameter core multi-modal fibre (0°) 20 cm length, **2.** 0.2 mm diameter core multi-modal fibre (0°) 120 cm length, **3.** 0.2 mm diameter core multi-modal fibre (45°) 120 cm length, **4.** 0.2 mm diameter core fused silica fibre (0°) 30 cm length, **5.** 0.4 mm diameter core fused silica fibre (0°) 30 cm length.

th largest transmission of optical photons to the end of the silica fibre, and hence were chosen for the first prototype of the fibre array monitor.

The first prototype of the Fibre Optic FLASH Monitor (FOFM), consisted of a single vertical array of 24 fused silica fibres, 0.4 mm in diameter and 30 cm in length (Hilgenberg GmbH, Malsfeld, Germany). The bare fused silica fibres were chosen for the FOFM due to the much larger transmission of ligh to the end. Furthermore, using an uncoated silica fibre meant a larger core diameter could be used to achieve the same spatial resolution that is possible with a coated fibre, therefore more Cherenkov light is produced through interactions in a larger volume of silica.

The silica fibres were held in place using two 3D printed supports, as shown in Fig. 5.13. In order to achieve the best possible spatial resolution, the fibre support consisted of three columns of holes - within each row the vertical separation was 0.5 mm, and the vertical separation between rows was 1.0 mm.

5.3.1.2 CMOS Camera

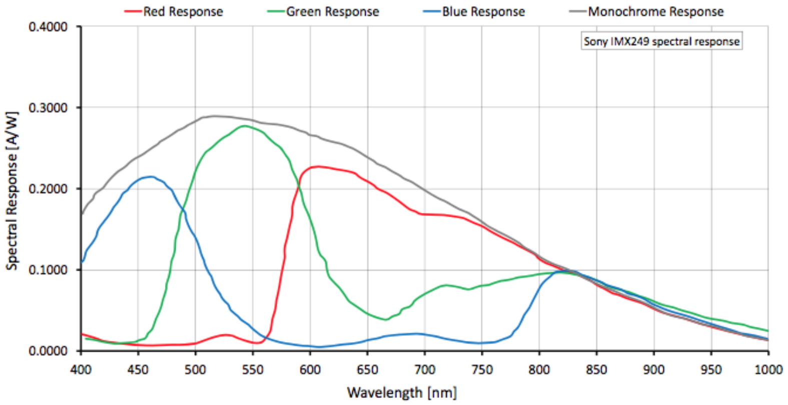

Figure 5.12: Spectral response of the SONY IMX249 CMOS chip, used within the 2.3 MP Basler ace CMOS camera that reads out the signal from the fibres in the FOFM. From [288].

The entire array was readout using a 2.3 MP Basler ace complementary-metal-oxide- semiconductor (CMOS) camera (Basler AG, Ahrensburg, Germany), with a SONY IMX249 CMOS chip. The spectral response of which shown in Fig. 5.12. To focus the light of all the fibres onto the

CMOS camera, a Fujinon H525HA-1B 1:1.4/25 mm lens (Fujifilm Corporation, Tokyo, Japan) was used. The camera was installed such that working distance (WD) between the edge of the lens and the fibres is 105 mm, whereby all fibres in the array were in frame and in focus. The CMOS camera was operated at 8-bit pixel depth at an acquisition rate of 42 frames/s and 0.034 ms exposure time. A black box with a Mylar foil window on the front and back was used to keep the ambient light detected by the CMOS camera to a minimum.

The CMOS camera was chosen in this case instead of a CCD camera since it has all the advantageous properties of the latter with the addition of a larger dynamic range and a faster frame rate. Since the maximum pulse repetition frequency (p.r.f) at CLEAR is 10 Hz, a CMOS camera with a frame rate of 42 frame/s was adequate for the measurements performed, a larger frame rate being not necessary at the CLEAR repetition frequency. However, proposed clinical VHEE linacs are likely to have a p.r.f of at least 100 Hz in order to deliver the prescribed dose over multiple pulses within FLASH timescales. There are commercially available cameras from the same manufacturer with the same properties and resolution but with a frame rate of 168 frame/s, or at frame rates >500 frames/s with a reduced resolution. A CMOS camera has the additional advantage over SiPM and PMT of being able to image multiple fibres simultaneously, compared to requiring one photodetector per fibre sensor.

5.3.2 Improved Design

One of the outcomes of the first set of measurements using the initial FOFM design was that the relative response between the individual fibres within the array varied significantly. The reason for this was believed to be twofold. The first was because of the large variation in the diameters of the fibres provided by he manufacturer ($\pm 25\%$), and secondly because of the quality of the surface of the ends of the fibres. To attempt to improve these issues, the fibres were cleaved from 30 cm to 10 cm at the University of Oxford Department of Physics Crystal Growth Laboratory. This was to ensure a cleaner cut and more uniform cut on the end of the fibres. Secondly, the fibre diameters

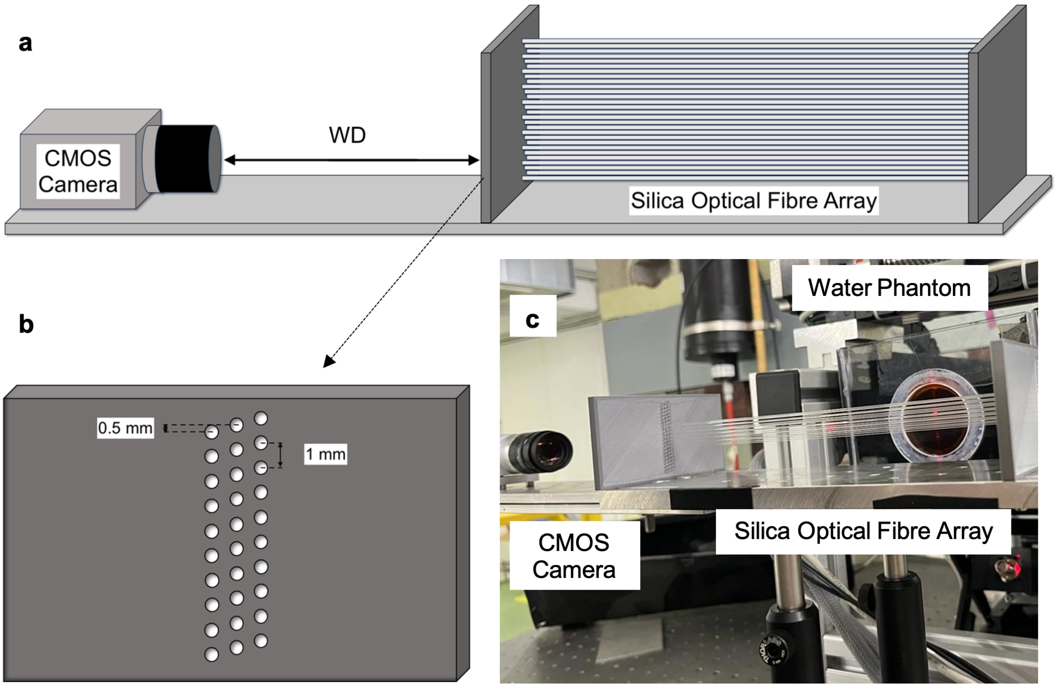

Figure 5.13: a) Schematic of the FOFM assembly with the CMOS cameras and silica fibre array, where the working distance (WD) between the edge of the lens and the fibres is 105 mm. b) Schematic of 3D printed fibre support displaying the vertical arrangement of the silica fibres. c) Photograph of the fibre array of the FOFM, consisting of 24 fused silica fibres, installed in the in-air test stand at the CLEAR facility.

were measured and only those within a tolerance of $\pm 0.05\,\mathrm{mm}$ of each other were chosen. Finally, the ends of the silica fibres were polished using fine sandpaper. Furthermore, a more robust, 3D printed cover was manufactured to cover the fibres which was sealed light-tight with Mylar foil on the front and back. The improved design is shown in 5.14. Due to limitations on the resolution of 3D printing the fibre-end supports, the initial design had an uneven vertical separation between the fibres within each row, and between each row. Therefore an improved fibre-end support was manufactured with four columns instead of three to ensure a uniform spatial resolution of 0.5 mm was achieved.

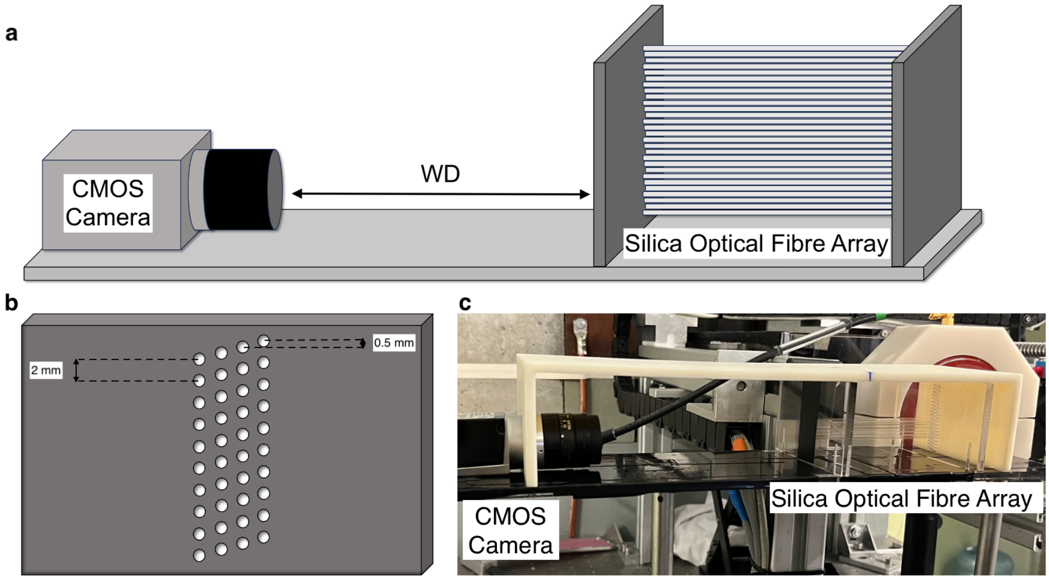

Figure 5.14: a) Schematic of the FOFM assembly with the CMOS cameras and silica fibre array, where the working distance (WD) between the edge of the lens and the fibres is 105 mm. b) Schematic of 3D printed fibre support displaying the vertical arrangement of the silica fibres. c) Photograph of the fibre array of the FOFM, consisting of 24 fused silica fibres, installed in the in-air test stand at the CLEAR facility.

5.4 Experiment Setup

The fibre array monitor was installed on the in-air test stand at the CLEAR facility, the schematic shown in Fig. 5.15 depicts the setup for the initial FOFM measurements. The ICT, positioned in front of the FOFM is used to measure the charge of each electron pulse. The C-Robot, positioned behind the FOFM is used to pick up both radiochromic films and the scintillating yttrium aluminium garnet (YAG) screen in order to position them at different longitudinal positions in the beam path, either in air or in a water phantom. The setup for the following FOFM measurements is shown in Fig. 5.16, which was adapted slightly from the initial setup. The main adaptation was the introduction of the collimator and second ICT, which were used for the uniform beam measurements. Due to limitations on space within the in-air test stand at CLEAR, the second ICT had to be installed behind the FOFM, and the water phantom was moved backwards. An additional scintillating YAG

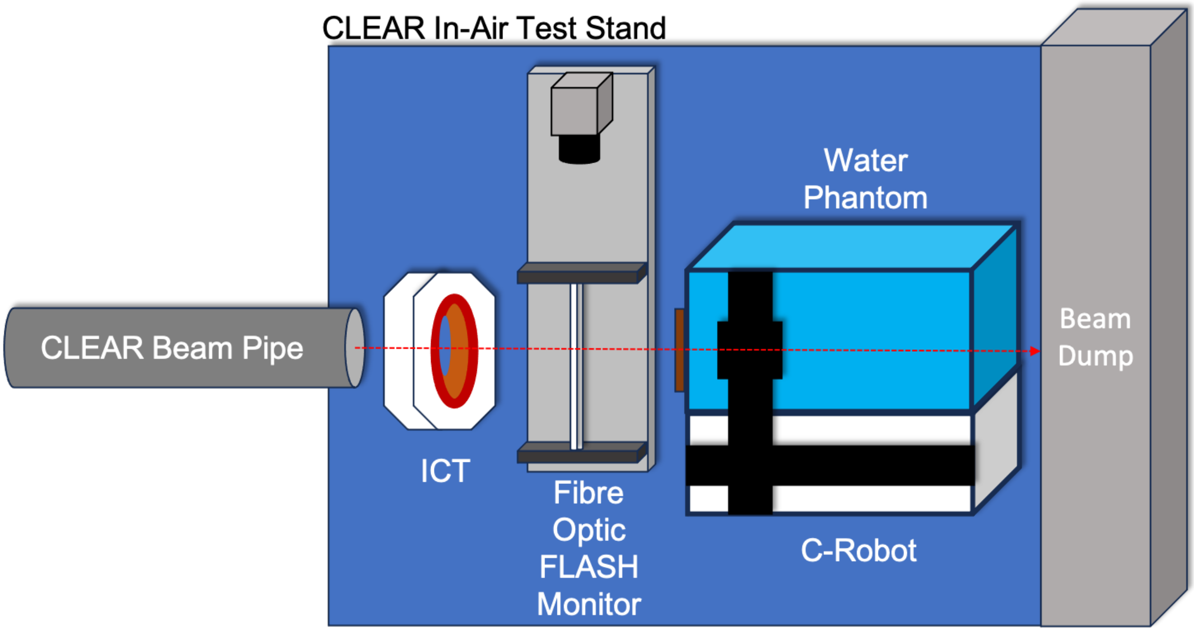

Figure 5.15: Schematic of the plan view of the experimental setup of the first FOFM prototype installed in the in-air test stand at the CLEAR facility.

screen was positioned 80 mm in front of the FOFM for the uniform beam measurements to provide an additional source of beam profile measurements for comparison. The setup described was used both for dose-to-water calibrations for radiochromic films, and for beam profile measurement comparisons in air using both radiochromic films and the scintillating YAG screen. Direct dose-to-water calibrations for the response of the FOFM fibre array were performed using EBT-XD films, while the FOFM beam profile measurement comparisons in air were conducted using HD-V2 and MD-V3 films. To obtain the dose-to-water measurements, the radiochromic film was positioned at a depth of 150 mm and 100 mm (for Gaussian beams) or 25 mm (for uniform flat beams) in a water phantom using the CLEAR C-robot. For the measurements using Gaussian pencil beams, the film analysis involved applying a a 2D Gaussian fit to the dose distribution on the film and the dose was obtained by averaging the values within a circle of radius 5 mm centred on the mean of the Gaussian fit for the green channel. For measurements using a uniform flat beam, this 5 mm radius was positioned at the centre of the circular dose distribution. For the FOFM fibre array profile comparisons with Gaussian

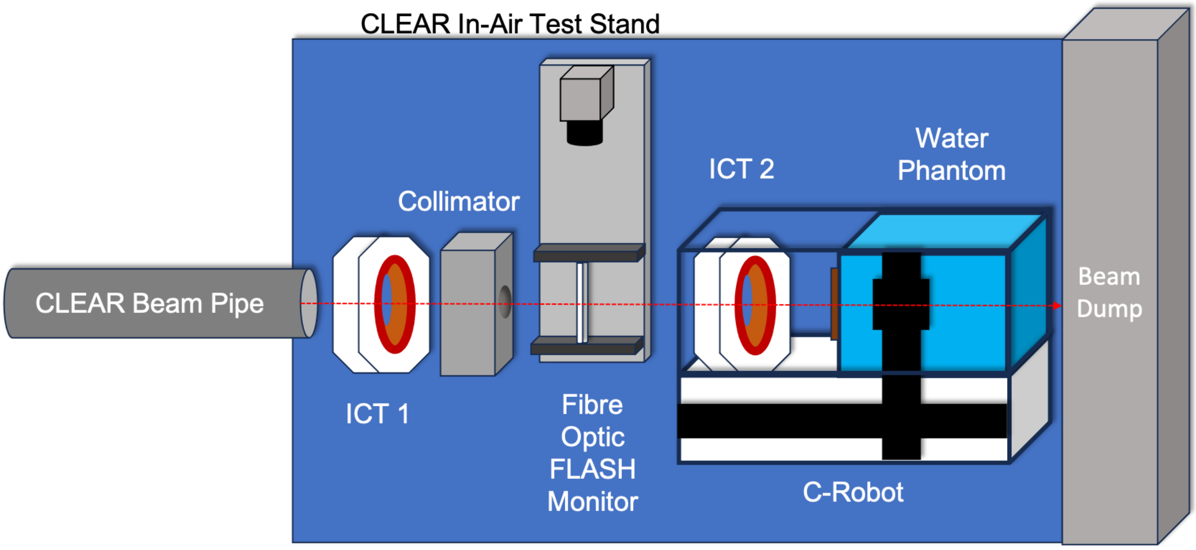

Figure 5.16: Schematic of the plan view of the experimental setup of the second FOFM prototype installed in the in-air test stand at the CLEAR facility.

beams, the projection of the y-axis profile is plotted, and a 1D Gaussian fit is applied whereby the standard deviation of this Gaussian fit is obtained and compared to the standard deviation of the Gaussian fit applied to the FOFM beam profile measurements. Similarly, the profile comparisons with uniform beams also plotted the projection of the y-axis profile, however no fit was applied and the FWHM of each of the y-projection profiles was compared.

5.4.1 Signal Processing

Background subtraction was performed before any of the data analysis was carried out. A background image averaged over 10 frames with the beam off was subtracted from each CMOS camera measurement. A significant proportion of the noise recorded on the CMOS camera was also due to secondary particles and stray radiation from interactions of the beam with materials in the in-air test stand such as the collimator and YAG screen that strike the CMOS camera directly. Therefore, further noise removal were applied to the background subtracted images by removing outliers with a threshold pixel value of at least 20, within a radius of 4 pixels, using ImageJ image processing software. The resulting image that is then processed for both beam intensity and beam profile measurements is shown in Fig. 5.17. Measurements of the intensity of each pulse were obtained from the post-processed CMOS camera image by calculating the mean pixel value from a circle around the area of each fibre, which is then summed. The measurements for the beam profile are also obtained by calculating the mean pixel value from a circle around the area of each fibre but are then plotted against their relative vertical position.

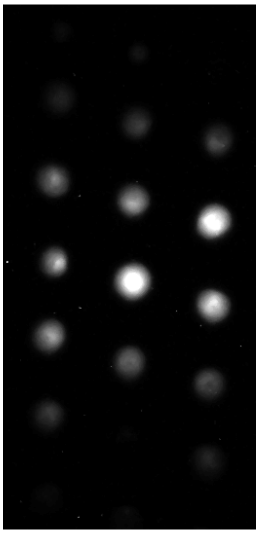

Figure 5.17: An example image of the fibre signal measured by the CMOS camera (after noise removal) following a 30 nC pulse.

5.4.2 Fibre Response Variation and Calibration

The relative response of each individual fibre within the array is going to inherently differ due to slight variations in the diameter of the fibre, the quality of the polish of the end of the fibre, as well as other factors such any other differences in the manufacturing or assembly of the fibres. Therefore, it is important to calibrate the relative response of the individual fibres to ensure that these variations do not affect the beam dose and profile measurements. In order to apply calibrations to the response of the individual fibres, a small Gaussian beam of approximately ($\sigma = 1\,\mathrm{mm}$) and a charge of 1 nC was scanned vertically over the fibre array (with a scintillating YAG screen behind for beam position and size reference measurements). The response of each of the fibres was recorded when the mean of the Gaussian beam was positioned over that particular fibre. The results of the normalised output for the initial prototype are shown in Fig. 5.18. For these measurements the mean normalised fibre output was 42.14 and the standard deviation was 25.86. The response of the fibres was then normalised to the mean response of all the fibres, the correction factors fibre are then obtained from these values. This large variation in the response of the fibres is the main reason as to why the design was upgraded, since having to employ such large correction factors impacts the accuracy of the profile measurements and introduces uncertainties in the fibre output. As stated previously, in an attempt to improve the homogeneity of the relative fibre response, the FOFM design was optimised by cleaving and polishing the fibres. Furthermore, to also ensure that the beam used for obtaining the calibration functions retained a constant size and distribution, the calibration procedure was altered by keeping the beam position constant and installing the FOFM on a vertical moving stage. The responses of the normalised output for the updated prototype are shown in Fig. 5.19. The mean normalised response of the upgraded prototype was 72.97 and the standard deviation was 14.61. This therefore shows that by cleaving and polishing the fibres, as well as excluding fibres with

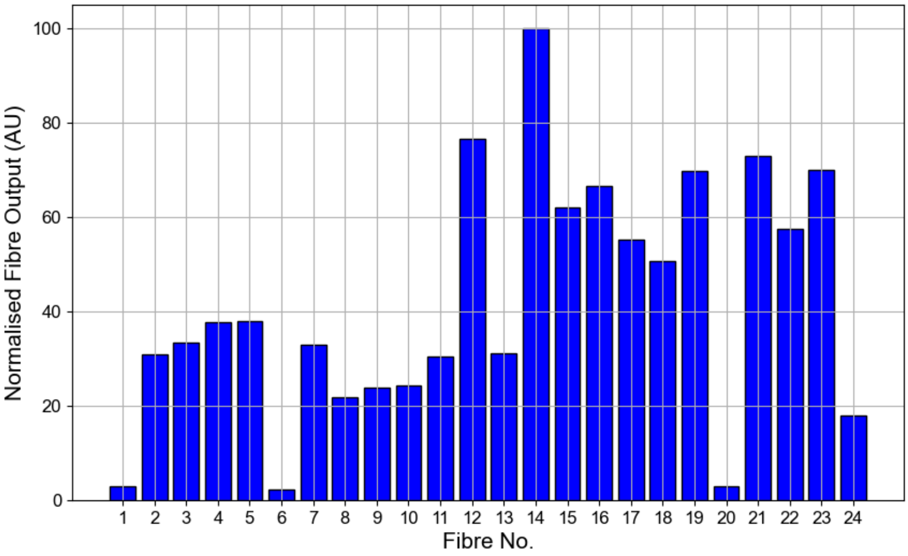

Figure 5.18: Relative normalised response of each of the fibres in the first FOFM prototype.

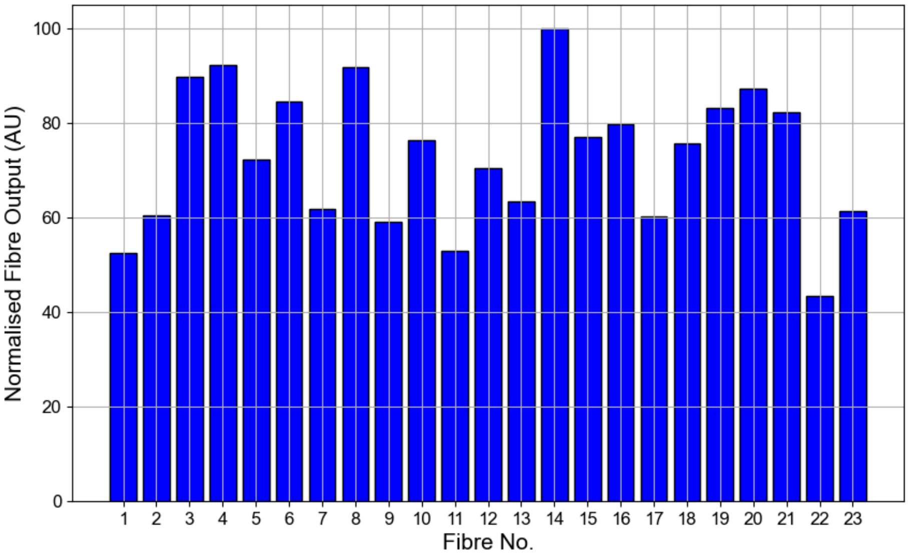

Figure 5.19: Relative normalised response of each of the fibres in the updated FOFM prototype.

diameters that were outside of a given tolerance did indeed improve the homogeneity of the fibre responses and reduce the spread of the relative fibre responses. However, future iterations to the FOFM should aim to improve this homogeneity further, either through a more reliable installation of the fibres, or through an improved polishing process.

5.5 VHEE Gaussian Pencil Beam Measurements

The standard beam provided at the CLEAR facility is a Gaussian pencil beam with $\sigma \approx 1\,\mathrm{mm}$, therefore the majority of the measurements and characterisations of the FOFM were performed with these beam parameters. Furthermore, one of the potential benefits of VHEE beams is the potential for pencil beam scanning and is one of the potential methods being considered for the delivery of VHEE beams at UHDR for FLASH-RT. Hence, if the FOFM were to be employed as a detector for real-time beam monitoring for this particular modality of VHEE delivery, its requirements would be to exhibit a linear response throughout the ultrahigh dose per pulse conditions and provide real-time pulse-by-pulse measurements of the beam spot size and spot position. The results in this section describe the measurements performed to evaluate the response linearity across the entire range of DPPs used for UHDR experiments at the CLEAR facility as well beam profile and size measurements that characterised by the σ of the Gaussian fit applied to the beam profile in comparison to that on radiochromic film and a scintillating YAG screen.

5.5.1 Response Linearity

Measurements of the response linearity of the FOFM were performed by calculating the response of the fibre array monitor across the entire range of DPPs possible at the CLEAR facility. This response was then correlated to the dose measured on a radiochromic film at a reference depth in the water phantom. For each response linearity measurement, the DPP, and hence the charge per pulse is increased by widening the width of the electron pulse by incrementing the number of bunches per pulse from 1 to the maximum achievable ($\approx$ 150 - 175), where the charge per bunch remains the same and therefore the dose rate within the pulse remains the same. The nominal operation of the CLEAR beam is the maximum charge per bunch, in this case 400 pC, since this is when the photocathode laser is operated at full power and hence beam is at its most stable. Three measurements of the DPP were taken with the FOFM for each value of the DPP, and then a radiochromic film irradiation is performed. The mean value of the three FOFM measurements is then plotted against the dose obtained from the radiochromic film. An error bar of $\pm 5\%$ was determined for the EBT-XD DPP dose-to-water measurements, and the standard deviation between the three consecutive shots for the FOFM measurements are plotted as the error in the fibre output. A linear regression is then applied to the response linearity measurements from which the R^2 value is calculated. The first response linearity measurement with 200 MeV electrons was performed with pulse charges between 3.2 and 50.7 nC/pulse, with corresponding pulse widths in the range of 9 – 105 ns. The results of which are shown in Fig. 5.20. For these measurements, the DPP varied from 4.3 to 39.0 Gy/pulse and the whole range was covered using the same CMOS camera settings, using a normalised gain of 0.7. The data show that the FOFM exhibits a linear response over the entire range of DPP's, with the linear fit having an R^2 value of 0.996.

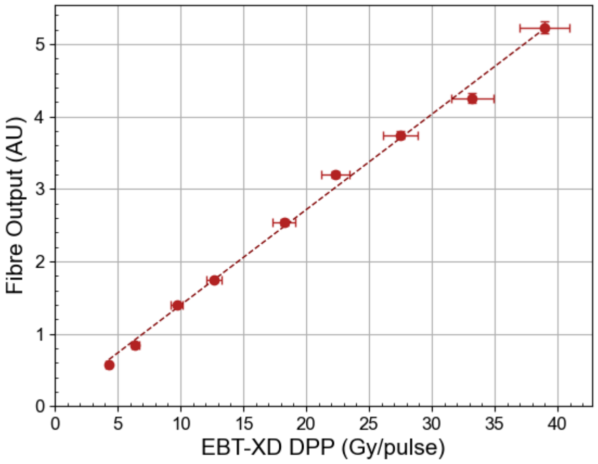

Figure 5.20: The dose-per-pulse (DPP) response of the first FOFM prototype between 4.3 and 39.0 Gy/pulse, with the same gain settings on the CMOS camera for all measurements ($R^2 = 0.996$).

In order to extend the range of DPP's to values below 5 Gy/pulse, two separate CMOS data acquisition (DAQ) settings were used for the low intensity and high intensity measurements. For the low intensity DAQ Mode a normalised camera gain of 1 was used while, for high intensity DAQ Mode, this gain was set to 0.7, the same as shown in Fig. 5.20. The response of the FOFM when operated in these two modes is shown in Fig. 5.21 for 200 MeV electrons with 400 pC/bunch. In low intensity DAQ Mode, DPP's between 0.9 and 6.1 Gy/pulse were covered with corresponding pulse widths of 0.7 to 9 ns and showed a clear linear response with an R^2 value of 0.996. In the high intensity DAQ Mode, DPP values between 6.1 and 57.4 Gy/pulse were used, corresponding to pulse widths of 9 - 130 ns. Once more this showed a linear response across the measured range of DPPs , with an R^2 value of 0.999. In order to show the linearity of the FOFM response across the entire dynamic range, all measurements in which the two DAQ modes were used, the same DPP for the final measurement in low intensity DAQ Mode as the first measurement in high intensity DAQ Mode, and the low intensity DAQ Mode values were scaled accordingly. Fig. 5.21 shows this, where the low intensity DAQ Mode data points from Fig. 5.21 have been scaled by the ratio of responses from the 6.1 Gy/pulse DPP in the high intensity DAQ and low intensity DAQ modes. The response can still be seen to be linear across this entire range of DPP's, and has an R^2 value of 0.999. For the remainder of the DPP response linearity measurements in this section, this scaling has been applied to all of the low intensity DAQ Mode data points.

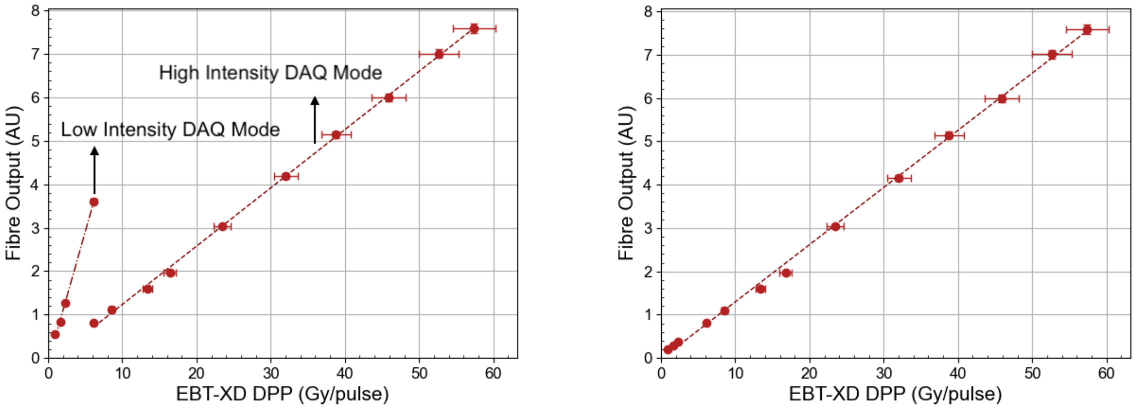

Figure 5.21: Plot showing the dose-per-pulse (DPP) response of the first FOFM prototype between 0.9 Gy/pulse and 6.1 Gy/pulse in low intensity DAQ Mode ($R^2 = 0.996$) and 3.1 Gy/pulse and 57.4 Gy/pulse in high intensity DAQ ($R^2 = 0.999$) mode (left). The same plots but with the low intensity DAQ Mode values scaled by the ratio between the 3.1 Gy/pulse measurements made with low intensity and high intensity DAQ mode ($R^2 = 0.999$) (right).

5.5.1.1 Energy Dependence

The DPP response linearity of the FOFM array was investigated for two different energies, the nominal energy at CLEAR of 200 MeV, and 160 MeV, to investigate the energy dependence of the response within the VHEE energy range. A comparison of the response of the fibre monitor to the two energies was performed with DPP's between 0.9 and 38.8 Gy/pulse (with 400 pC/bunch and pulse widths of 0.7 – 76 ns is shown in Fig. 5.22. The response for 200 MeV, and 160 MeV can be seen to be linear, and of the similar gradient, the values for which are displayed in Table 5.2. The R^2 value is 0.997 for the 200 MeV measurement and 0.999 for the 160 MeV measurement. In these measurements a constant offset between the 200 MeV and 160 MeV responses can be seen. This disparity can be attributed to the difference in the percentage depth dose distribution for the two

VHEE energies, and the constant position of the EBT-XD film, since the 160 MeV VHEE beam has an earlier fall-off, hence for the same pulse charge (and therefore the same fibre output), a smaller dose is deposited at the depth of the EBT-XD film (150 mm in water).

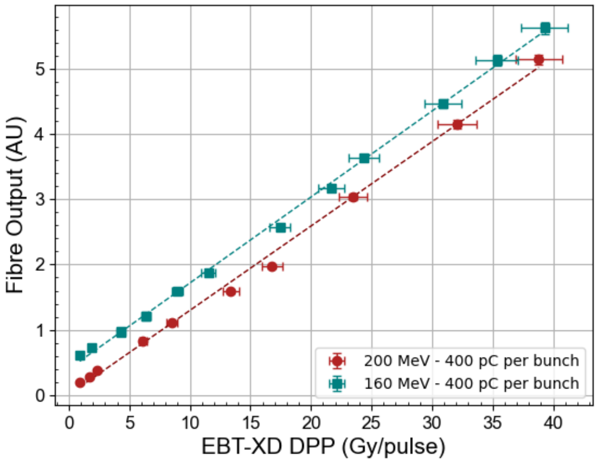

Figure 5.22: The dose-per-pulse (DPP) response of the first FOFM prototype between 0.9 Gy/pulse and 38.8 Gy/pulse for a 200 MeV electron beam ($R^2 = 0.997$) and a 160 MeV ($R^2 = 0.999$) electron beam at 400 pC/bunch.

5.5.1.2 Instantaneous Dose Rate Dependence

Recent research suggests that the instantaneous dose rate, i.e. the dose rate within each pulse of radiation, could be an important parameter in eliciting the FLASH effect. Therefore, it is important to rule out that variations of this parameter do not affect the response of the FOFM for the same DPP. Therefore, the DPP response linearity measurements at 200 MeV and 160 MeV were repeated with two different pulse structures. It should be observed, however, that even with the same pulse width and charge, the dose rate within the pulse can vary. This variation is due to beam loading effects which are present for longer pulse widths and decrease the intensity of the later bunches on these longer trains. Since the charge per bunch is only measured for a single bunch per pulse, a range of instantaneous dose rates are given for each pulse structure. The first structure used was the same as for the results presented so far, i.e. the nominal and maximum charge per bunch of 400 pC, corresponding to an instantaneous dose rate range of 0.3 - 1 × 10^9 Gy/s. The second bunch structure had a significantly lower charge per bunch, 75 pC, hence a longer pulse width for the same DPP, which corresponds to an instantaneous dose rate of 0.9 - 2.6 × 10^8 Gy/s. The results obtained with this second bunch structure are shown in 5.23 for both 200 MeV and 160 MeV, with corresponding pulse widths of 5 – 130 ns. For comparison, the straight lines which are the results of the fit to the linear dependence of the response, obtained from the data with nominal charge per bunch shown in Fig. 5.23, are superimposed. The data displayed in Fig. 5.24, show that the linearity of the response with DPP is similar for both 200 MeV and 160 MeV energies, and for 400 pC/bunch and 75 pC/bunch pulse structures. The values for the gradients and the standard error of the gradient for these measurements are shown in Table 5.2, where all gradients are in agreement within their respective standard errors.

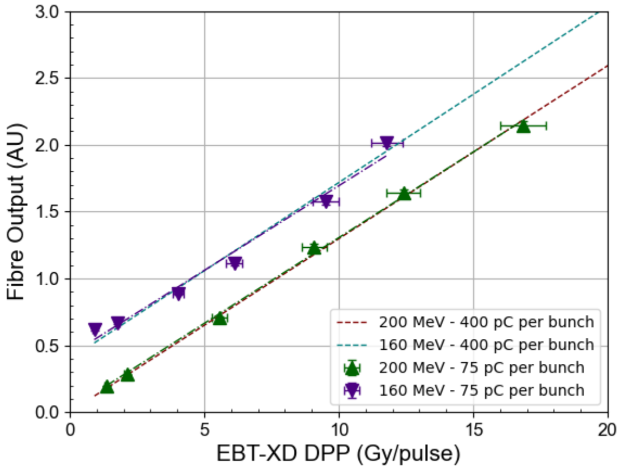

Figure 5.23: The DPP response of the first FOFM prototype for a 200 MeV ($R^2 = 0.998$) and a 200 MeV ($R^2 = 0.981$) electron beam at 75 pC/bunch (with the fits from the 400 pC/bunch measurements shown for comparison).

5.5.1.3 Response Linearity of Upgraded Prototype

All of the measurements of the DPP response linearity of the FOFM presented in this section thus-far were performed with the initial prototype consisting of 30 cm length silica fibres. The main

Energy (MeV)	Charge per bunch (pC)	Gradient of linear fit	Standard error of gradient
200	400	0.130	0.002
200	75	0.128	0.002
160	400	0.132	0.001
160	75	0.127	0.007

Table 5.2: The gradient values of the linear fit and their corresponding standard error for the measurements shown in Fig. 5.22 and 5.23.

purpose of optimising the design of the monitor was for the improvement of the beam profile measurements, due to the large variation in the individual relative fibre response. Further measurements of the DPP response linearity to Gaussian pencil beams were performed with the modified prototype as well. Repeat measurements were performed with 200 MeV and 160 MeV electron beams at 400 pC/bunch. Another modification to this new setup was the alteration of the reference depth in water at which the EBT-XD films were positioned for reference dose-to-water measurements. This depth was changed from 150 mm to 100 mm. The reason for this being that a shallower depth is more realistic for a VHEE reference dose measurement for beam monitor calibration. Therefore, it must be noted that the dose-to-charge ratio for the DPP response linearity figure for these measurements is greater due to the reference dose measurement being taken at a higher position in the PDD curve. The DPP measurements were taken with pulse charges of between 0.4 nC/pulse (5 ps pulse width) to 38.1 nC/pulse (105 ns pulse width) for 200 MeV electrons and between 0.4 nC/pulse (5 ps pulse width) to 19.8 nC/pulse (40 ns pulse width) for 160 MeV electrons. Subsequently, two DAQ modes were used again to allow the CMOS camera photodetector to cover the entire range of DPPs. The results are shown in Fig. 5.24, where both energies have a linear response across the entire range of DPPs measured (up to 76.2 Gy/pulse and 46.6 Gy/pulse for 200 MeV and 160 MeV energies, respectively) with $R^2 = 0.999$. Both measurements show an improved R^2 value compared to the initial prototype measurements, likely due to the improved uniformity between the relative fibre response. Larger uncertainties in the measurement of the Fibre Output on this occasion are observed, especially towards the upper-end of the DPPs and are due to higher fluctuation in the recorded charge per pulse for this particular experimental run. Furthermore, the values for the gradient of the linear regression fit and the standard error of the gradients are shown in Table 5.3. Once again it can be seen that the gradients are within close agreement with each other, further confirming the response is not dependent on the electron beam energy within this range. Also, from Fig. 5.24 it can be seen that the offset between the 200 MeV and 160 MeV energies is significantly reduced as opposed to that seen in Fig. 5.22. This can be attributed to the change in the reference depth of the EBT-XD dose measurements. The shallower depth of the radiochromic film means that the difference in the dose deposited is reduced at this reference position. However, for more systematic measurements in future, a reference depth for each VHEE beam energy should be established.

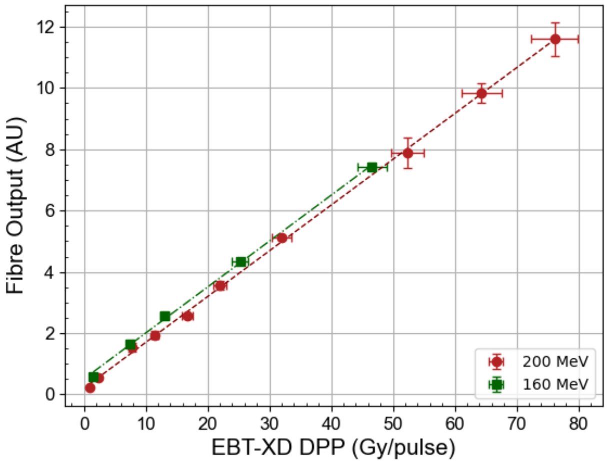

Figure 5.24: The dose-per-pulse (DPP) response of the upgraded FOFM prototype between 0.9 Gy/pulse and 76.2 Gy/pulse for a 200 MeV electron beam (with $R^2 = 0.999$) and a 160 MeV electron beam (with $R^2 = 0.999$), both at 400 pC/bunch.

Energy (MeV)	Charge per bunch (pC)	Gradient of linear fit	Standard error of gradient
200	400	0.149	0.001
160	400	0.150	0.002

Table 5.3: The gradient values of the linear fit and their corresponding standard error for the measurements shown in Fig. 5.24.

5.5.2 Profile Measurements

Fibre array monitors have been widely used for the measurement of beam profiles for mostly small, Gaussian, and approximately radially symmetric beams. This is because the measured profile on each of the horizontal and vertical fibre arrays is the projection of the profile in that axis. In other words the output signal from the fibre array is a Radon transform of the 2D transverse distribution of the beam impinging on the fibres, in whichever axis the array is oriented. The Radon transform of a function $R(\rho,\theta)[f(x,y)]$ is the integral of $f(x,y)$ along a lines that are defined by $\rho = xcos\theta + ysin\theta$ from the origin. The equation for a Radon transform is:

$$R(\rho,\theta)[f(x,y)] = \int_{-\infty}^{\infty}\int_{-\infty}^{\infty} f(x,y)\delta(\rho - xcos\theta + ysin\theta)dxdy \tag{5.1}$$

where δ is the Dirac delta function [289]. For a 2D Gaussian distribution given by:,

$$f(x,y) = \frac{1}{2\pi\sigma_x\sigma_y}\text{exp}\left(-\frac{x^2}{2\sigma_x^2} - \frac{y^2}{2\sigma_y^2}\right) \tag{5.2}$$

the Radon transform projecting this 2D Gaussian distribution onto the y axis where $\rho = y, \theta = \frac{\pi}{2}$, i.e. what is measured by the single vertical FOFM array, is:

$$R(y,\theta = \frac{\pi}{2})[f(x,y)] = \int_a^b \frac{1}{2\pi\sigma_x\sigma_y}\text{exp}\left(-\frac{x^2}{2\sigma_x^2} - \frac{y^2}{2\sigma_y^2}\right)dx \tag{5.3}$$

using the identity of the error function erf$(v) = \frac{2}{\sqrt{\pi}}\int_0^v \text{exp}(-u^2)du$ and then by letting $u = \frac{x}{\sqrt{2}\sigma_x}$ and hence $du = \frac{dx}{\sqrt{2}\sigma_x}$. This eventually gives a resulting distribution of:

$$R(y,\theta = \frac{\pi}{2})[f(x,y)] = \frac{1}{2\sqrt{2\pi\sigma_y^2}}\text{exp}\left(-\frac{y^2}{2\sigma_y^2}\right)\left[\text{erf}\left(\frac{b}{\sqrt{2}\sigma_x}\right) - \text{erf}\left(\frac{a}{\sqrt{2}\sigma_x}\right)\right] \tag{5.4}$$

Which shows that the Radon transform of a 2D Gaussian distribution into 1D on the y axis is still a Gaussian distribution with amplitude scaled by a factor relating to the standard deviation of the Gaussian distribution in the x axis.

In order to reconstruct the profile of the beam measured by the FOFM, the pixel value of each of the individual fibres recorded by the CMOS camera was plotted against their corresponding vertical position. For the purpose of comparison and validation, in-air profile measurements were also made using radiochromic film (EBT-XD, MD-V3 and HD-V2) and on a scintillating YAG screen - both positioned at 300 mm behind the FOFM. A Gaussian fit was applied to the vertical projection of the profile from both the radiochromic film and the scintillating YAG screen, and compared to the profile reconstructed from the FOFM. The profile measurements performed with the initial design show a 0.5 mm separation between the three fibres in each row, but there is a vertical separation of 1 mm between each row. An example of the non-calibrated profile measurements (i.e. before the correction factors obtained from calibration of the relative fibre response are applied) are shown for a 1 nC and 10 nC pulse in Fig. 5.25. The nominal electron beam parameters at CLEAR were used for all of the beam profile measurements, namely 200 MeV energy and charge of 400 pC/bunch. Two different measurements were done on a single pulse, one at 1 nC/pulse, corresponding to 2.1 Gy/pulse, and another at 10 nC/pulse, corresponding to 17.0 Gy/pulse.

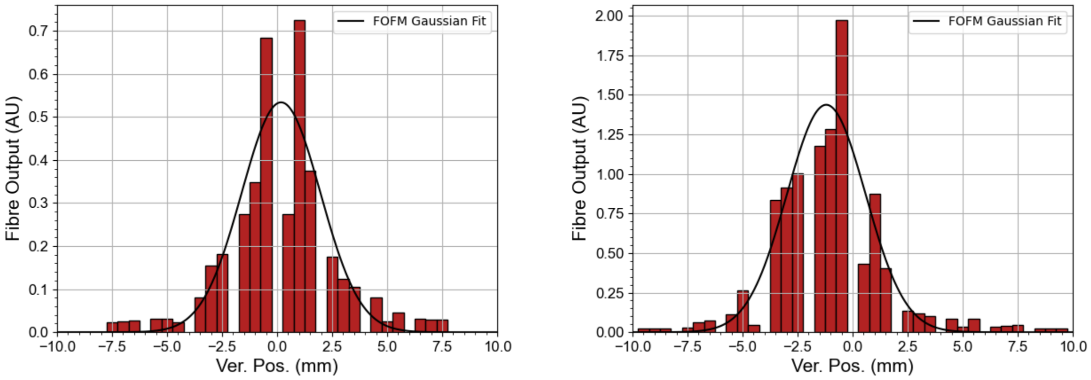

Figure 5.25: Pre-calibration vertical profile measurements made by the first FOFM prototype for a 1 nC (left); and a 10 nC (right) electron pulse at 200 MeV with a Gaussian fit applied (black line).

The vertical beam profile measured by the first FOFM prototype with 30 cm length fibres for a 1 nC pulse and a 10 nC pulse are shown in Fig.5.26. Whereby the low intensity DAQ mode was used for 1 nC and the high intensity DAQ mode was used for 10 nC. The beam size, computed

Pulse Charge (nC)	FOFM beam size (mm)	Film beam size (mm)	YAG beam size (mm)
1	2.02 ± 0.15	2.08 ± 0.03 (MD-V3)	1.98 ± 0.02
10	1.71 ± 0.09	1.66 ± 0.01 (HD-V2)	1.87 ± 0.01

Table 5.4: Vertical beam size measurements made with the FOFM, radiochromic film (with the type of film stated in brackets), and scintillating YAG screen obtained from the standard deviation Gaussian fit applied to the vertical projection of the beam profile. The uncertainty of the beam size measurement is expressed as the error on the standard deviation of the 1D Gaussian fit.

from the standard deviation of the Gaussian fit applied to the vertical profiles, was estimated to be 2.02 ± 0.15mm for the 1 nC pulse and 1.71 ± 0.09mm for the 10 nC. The uncertainty is calculated from the error on the Gaussian fit. A comparison between these values and those obtained from the vertical profile projection from radiochromic films and a scintillating YAG screen is shown in Table 5.4. The beam profile measurements made with the FOFM are consistent with those obtained using different techniques, with the exception of the YAG screen measurement for the 10 nC pulse. The gaps present in the plots of these beam profiles are due to the manufacturing of the initial fibre-end support meaning that the fibres were not uniformly spaced by 0.5 mm, but had a 1 mm separation between each row.

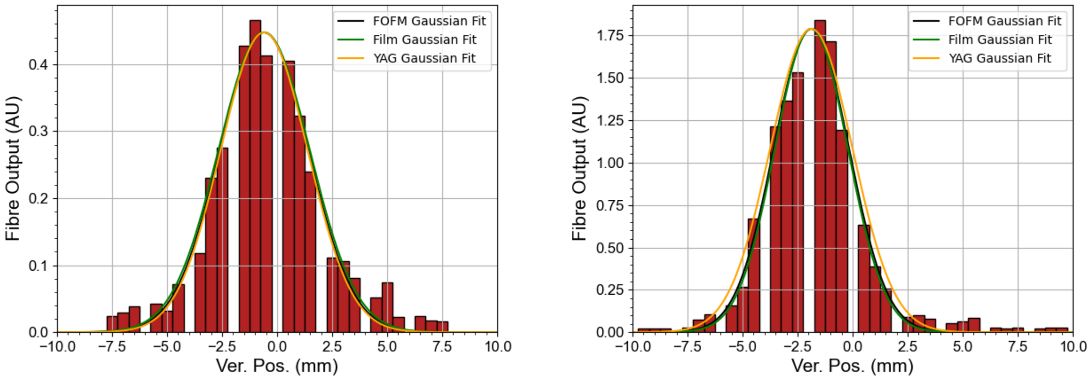

Figure 5.26: Post-calibration vertical profile measurements made by the first FOFM prototype for a 1 nC (left); and a 10 nC (right) electron pulse at 200 MeV with a Gaussian fit applied (black line), comparing the Gaussian fits from the radiochromic film measurement (green line), and YAG screen measurement (yellow line).

In addition to the updated design of the FOFM including shortened and polished fibre ends, in an attempt to improve the homogeneity of the relative response of each of the fibres and hence achieve a better accuracy of the beam profile. This improved design also included adding an additional column of staggered holes on the fibre end support in order to achieve a 0.5 mm spatial resolution. The vertical beam profile measurements from this updated FOFM design following calibration of the individual fibre relative response is shown in Fig. 5.27, as well the corresponding Gaussian fits, for 200 MeV electrons with pulse charges of between 0.5 nC and 40 nC. The first two vertical profile measurements were performed using the low intensity DAQ mode for 0.5 nC and 1 nC, and the remaining used the high intensity DAQ mode. A larger tail can be observed at vertical positions of below 0 mm or the 0.5 nC and 1 nC measurements, due to the higher gain setting being used, along with the beam being positioned on the upper part of the fibre array, therefore amplifying the noise level on these fibres, even after background subtraction. Comparative vertical profile measurements were performed using radiochromic film and the scintillating YAG screen for pulse charges of 1 nC and 10 nC with 200 MeV electrons and for 1 nC with 160 MeV electrons. The Gaussian fits from the FOFM vertical profile measurement, the radiochromic film measurement and the YAG screen measurement are overlaid on top of the FOFM vertical profile in Fig. 5.28. The corresponding beam size determined from the standard deviation (σ) of these applied Gaussian fits are shown in Table 5.5. Firstly, it is evident from the FOFM beam sizes that the precision of the beam profile measurements was improved through optimising the FOFM design since the uncertainty of the Gaussian fits is lower than the first measurements from Table 5.4. The close agreement (within the uncertainty of the Gaussian fit) between the FOFM and radiochromic film measurements is also retained, and the values reported in Table 5.5 are closer in agreement than those in Table 5.4. The YAG screen beam profile measurement for the 1 nC pulse with 200 MeV electrons is within the uncertainty range of the FOFM measurement. Once again, this is not the case for the 10 nC pulse. This vertical beam size measurement is also not within the uncertainty range for the 1 nC pulse profile measurement with 160 MeV electrons. Some potential reasons for these variations are likely to be due to the noise and background levels on the YAG screen as well as potential inconsistencies

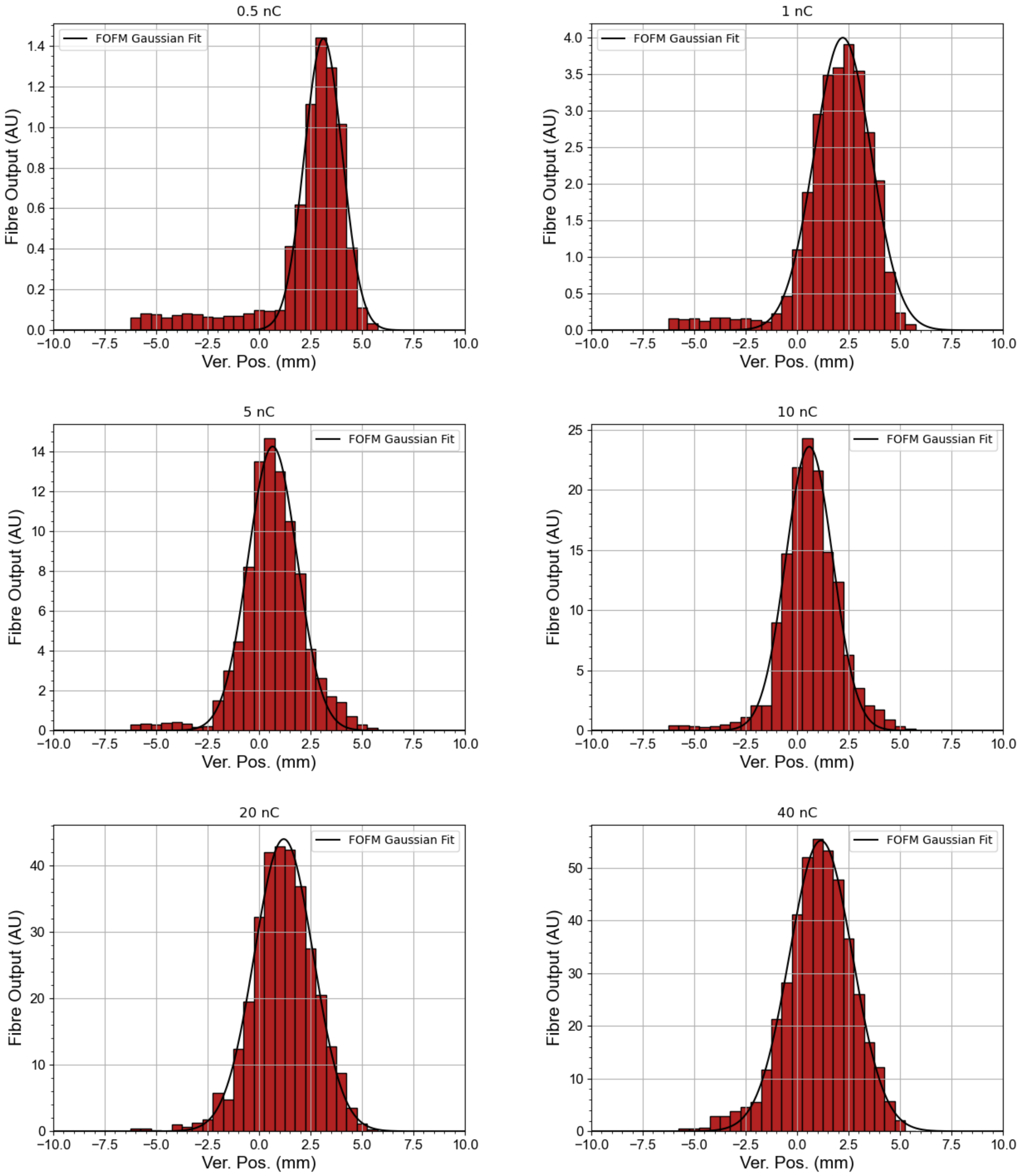

Figure 5.27: Vertical beam profile measurements using the upgraded FOFM prototype of a uniform dual-scattered 200 MeV electron beam for a 0.5 nC (top left), 1 nC (top right) (using a CMOS camera normalised gain of 1), 5 nC (centre left), 10 nC (centre right), 20 nC (bottom left) and 40 nC (bottom right) (using a CMOS camera normalised gain of 0.3) pulses. The applied Gaussian fit is shown with the black line.

in the camera gain used for measuring the beam profile on the YAG screen.

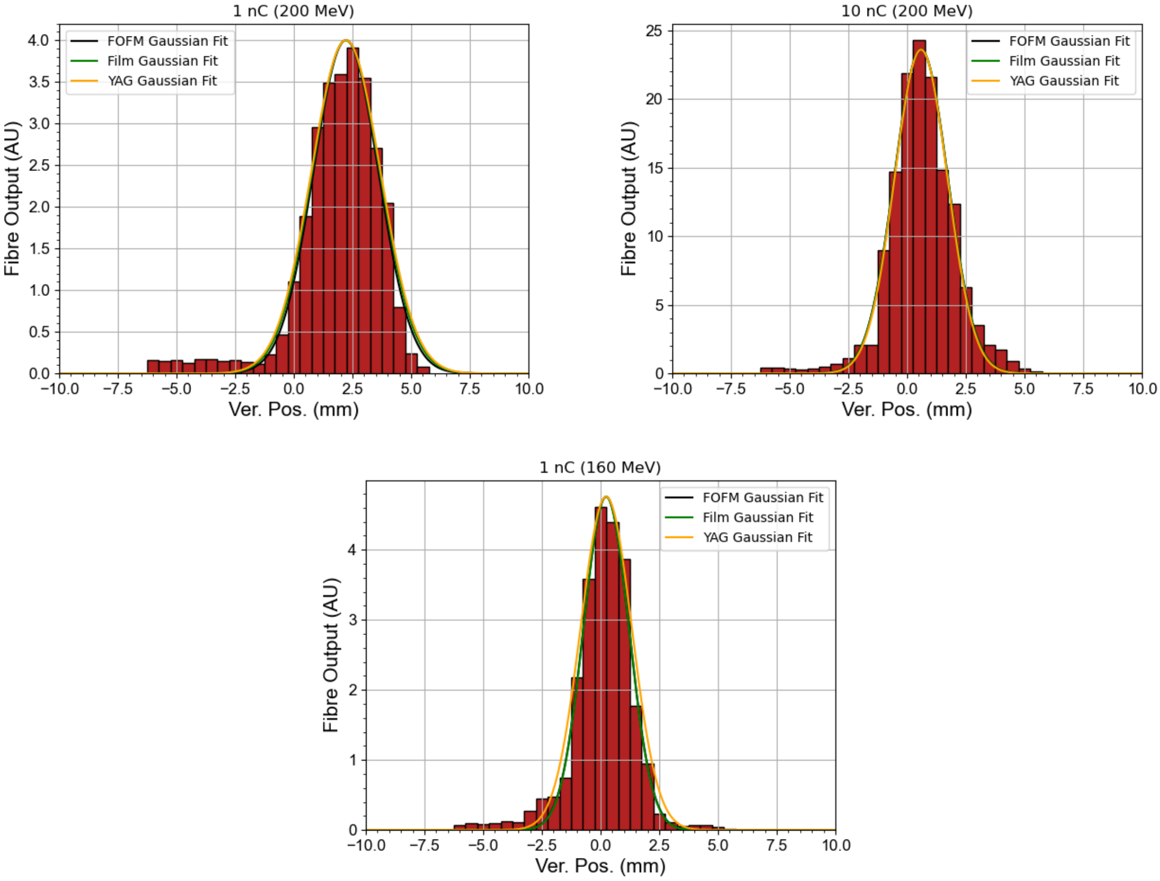

Figure 5.28: Gaussian beam profile measurements for the upgraded FOFM prototype 200 MeV electrons with a 1 nC pulse (top left) and 10 nC (top right) and for 160 MeV electrons with a 1 nC pulse (bottom) with a Gaussian fit applied (black line), comparing the Gaussian fits from the radiochromic film measurement (green line), and YAG screen measurement (yellow line).

5.6 VHEE Uniform Beam Measurements

Current research suggests that the upper limit on the total time of delivery for the treatment dose for FLASH is 100 ms [48]. This therefore puts strict requirements on the technological aspects of delivering VHEE beams that can achieve conformal dose distributions for deep-seated tumours. Subsequently, if pencil beam scanning is used, it needs to be performed very quickly in order to

Pulse Charge (nC)	FOFM beam size (mm)	Film beam size (mm)	YAG beam size (mm)
1 (200 MeV)	1.39 ± 0.08	1.44 ± 0.13 (EBT-XD)	1.47 ± 0.01
10 (200 MeV)	1.14 ± 0.07	1.14 ± 0.01 (HD-V2)	1.12 ± 0.01
1 (160 MeV)	0.97 ± 0.05	0.97 ± 0.01 (EBT-XD)	1.09 ± 0.01

Table 5.5: Vertical beam size measurements made with the updated FOFM prototype with an improved spatial resolution, radiochromic film (with the type of film stated in brackets), and scintillating YAG screen obtained from the standard deviation Gaussian fit applied to the vertical projection of the beam profile. The uncertainty of the beam size measurement is expressed as the error on the standard deviation of the 1D Gaussian fit.

meet these constraints on the treatment time. Thus, current technology may not permit the use of pencil beam scanning given the temporal dose-delivery requirements for eliciting FLASH effect with a UHDR VHEE device [108]. Alternatively, a more simple and feasible treatment technique to deliver conformal dose distributions on such time scales is the use of a small number of fixed beam lines to deliver collimated broad VHEE beams using 3D-conformal RT (3D-CRT). This is the most likely method of dose delivery for the first clinically implemented VHEE-FLASH machines. Therefore, this next section presents the results of the measurements of the FOFM response and vertical profile measurements of a collimated broad VHEE beam. Very recently, an in-vacuum dual-scattering system was installed at the CLEAR facility by Robertson *et al* [269] to produce uniform collimated VHEE beams (with an energy of 200 MeV) up to ultrahigh doses per pulse with a diameter of approximately 1 cm. The dual-scattering system works by utilising two scatterers: the first to magnify the beam through Coulomb scattering, and the second is shaped such that it matches the beams distribution at a set location so that it produces further magnification along with a uniform transverse profile. Finally the beam is collimated to ensure only the uniform transverse profile is transmitted. Whilst clinically used broad VHEE beams will likely have to be a larger diameter in order to deliver 3D-CRT, the dual-scattered beams at CLEAR provide sufficient beam parameters to evaluate the feasibility of FOFM to measure the beam for this method of dose delivery. Fibre array detectors are typically only used for the measurement of small pencil beams, therefore the work in this section is important for determining the feasibility of using such a detector for the field size and characteristics measurements of broad beams for RT. The results below shows DPP response linearity, dose monitoring, beam vertical profile measurements and beam perturbation measurements to the uniform dual-scattered 200 MeV electron beams. These were performed using the setups shown in Figs. 5.14 and 5.16 with upgraded FOFM design with 10 cm length silica fibres.

5.6.1 Response Linearity

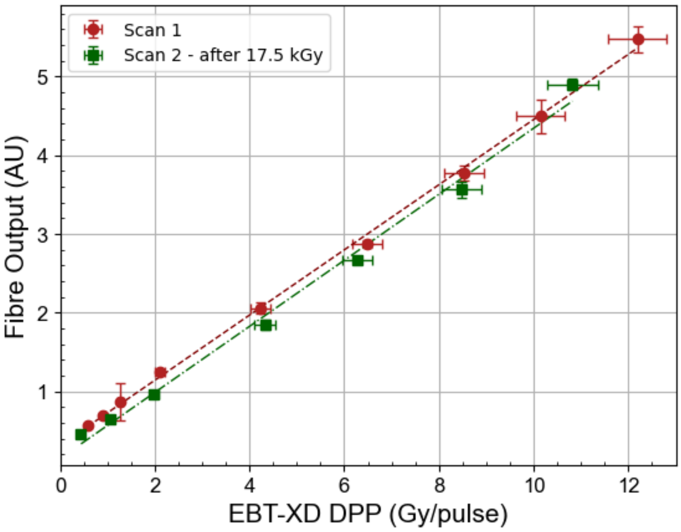

Figure 5.29: The dose-per-pulse (DPP) response of the upgraded FOFM prototype between 0.6 Gy/pulse and 12.2 Gy/pulse for a 200 MeV dual-scattered electron beam at 66.6 pC/bunch performed before, (with $R^2 = 0.999$), and after, (with $R^2 = 0.994$), accumulating a total dose of approximately 17.5 kGy in 24 hours.

The response linearity measurements of the FOFM to uniform VHEE beams was performed similarly to that with Gaussian beams. The exception being that the reference depth of the EBT-XD film was shallower (25 mm in water), since this depth was chosen in order to retain the flatness of the beam. Furthermore, a smaller range of DPPs were investigated since the dual-scattering and collimation system limits the maximum achievable charge per pulse and hence DPP. Consequently, the CMOS camera for the FOFM was operated in the low intensity DAQ mode (normalised gain of 1) for all measurements due to the reduced charge density of the dual-scattered VHEE beam. The uniform beam DPP response linearity measurement was performed with a charge per bunch pre-collimation of 400 pC/bunch, which was reduced to 66.7 pC/bunch after collimation. The range of pulse charges used was between 0.28 nC/pulse (corresponding to 4 bunches per pulse and a pulse width of 3 ns) and 5.77 nC/pulse (corresponding to 85 bunches per pulse with a pulse width of 57 ns). Two DPP response linearity scans were performed, the second of which was 24 hours after the first scan, and after the FOFM had accumulated a total charge of approximately 17.5 kGy from repeat radiation from a Gaussian pencil beam. The purpose of these two measurements was to evaluate the stability and reproducibility of the response of the FOFM. The results of these two DPP response linearity measurements are shown in Fig. 5.29. Once more, the response of the monitor can be seen to be linear across the entire range of DPPs measured (between 0.6 Gy/pulse and 12.2 Gy/pulse) with R^2 values of 0.999 and 0.994 for the first and second scans, respectively. The response can also be seem to be stable between the two measurements, with gradients of 0.414 ± 0.005 and 0.420 ± 0.013, which are within the uncertainty range of each other.

5.6.2 Dose Monitoring

One of the primary functions of an RT beam monitor to provide a measurements of the beam fluence in monitor units (MU), which correspond to the dose deposited by the beam at reference depth in water (for MV photons it is defined as 1 MU = 0.01 Gy at D_{max} for a 10 cm × 10 cm beam). However, for pencil beams the definition of monitor units is not as well defined, and definitions vary. The pulse-by-pulse variability of the beam size and intensity of the CLEAR electron beam makes it difficult to define such a system for measuring Gaussian pencil beams with the FOFM for these feasibility measurements. However, the addition of the dual-scattering system at the CLEAR facility means that the feasibility of the FOFM to provide DPP dose monitoring can be evaluated due to the constant collimated beam size and uniform transverse distribution of the dose. In order to investigate this, the equation of the linear regression fit applied to Scan 2 from Fig. 5.29 was obtained and rearranged as:

$$\text{DPP}_{\text{FOFM}}[\text{Gy/pulse}] = \frac{(\text{Fibre Output [AU]} - \text{Scan 2 Intercept})}{\text{Scan 2 Gradient}} \tag{5.5}$$

This equation was then applied to the Fibre Output measurements from ’Scan 1’ in 5.29, and plotted against the EBT-XD radiochromic film dose-to-water measurements, shown in Fig. 5.29. It can be seen from the figure that FOFM predicted DPP agrees extremely closely with that measured with the EBT-XD film, particularly with the 0% residual line falling within the uncertainty of all the measurements. The percent RMS deviation between $\mathrm{DPP_{FOFM}}$ and $\mathrm{DPP_{EBT\text{-}XD}}$ was 3.17%. Therefore demonstrating that the response linearity and short-term stability of the FOFM at the ultrahigh dose-per-pulses measured is promising for the potential use of the FOFM as a beam dose monitor for VHEE FLASH RT.

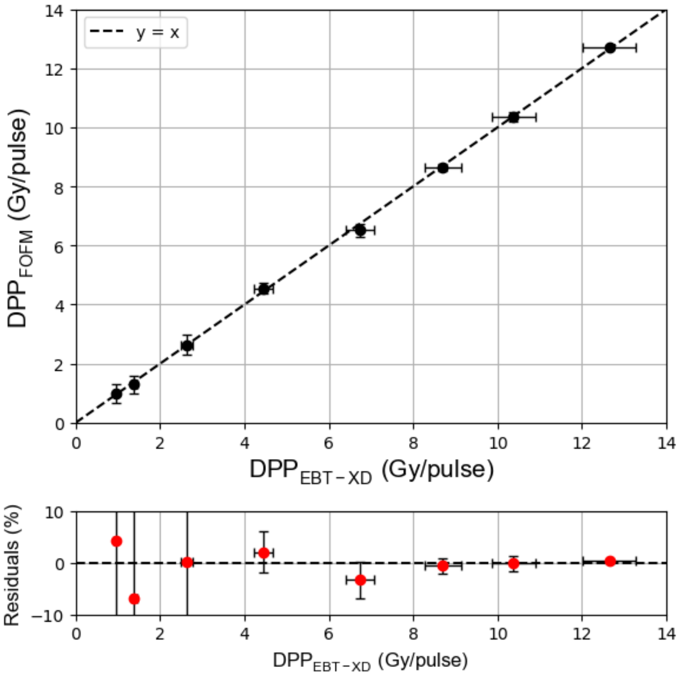

Figure 5.30: The predicted DPP determined from the FOFM output using Eq. 5.5 plotted against the measured DPP with EBT-XD films at 25 mm depth in water. The dashed line with slope 1 is plotted to evaluate the deviation from linearity of the FOFM response. The percentage residual from this slope is plotted below.

5.6.3 Profile Measurements

The broad collimated uniform VHEE beam produced by the dual-scattering system at the CLEAR facility has 2D circular distribution (with a slight penumbra due to lateral scattering), with a diameter of approximately 1 cm. A 2D circular distribution centred at the origin with radius, R can be defined as:

$$f(x,y) = \begin{cases} A & \text{if } x^2+y^2 \leq R^2 \\ 0 & \text{otherwise} \end{cases} \tag{5.6}$$

Where A is the amplitude of the intensity of the circular distribution. The Radon transform, previously defined in Eq. 5.1, of a circular distribution (assumed to be circularly symmetric) projected onto the y axis, where $\rho = y, \theta = \frac{\pi}{2}$, can be expressed as:

$$R(y)[f(x,y)] = 2\sqrt{R^2 - y^2}, |y| \leq R \tag{5.7}$$

Hence, it can be seen that the measured distribution of circularly collimated uniform broad beam by the vertical FOFM array is a semi-ellipse which is centered at the origin and has endpoints at $y = \pm R$. Consequently for two orthogonal arrays, the 2D beam profile can be determined using either inverse Radon transformations with filtered back-projection, or through the use of reconstruction algorithms. However, for the case of vertical profile measurements made with the FOFM prototype, reconstructing the full 2D transverse distribution from from this vertical projection measurement alone is not trivial.

For the purpose of this section, the full-width half maximum (FWHM) of the semi-ellipse is calculated for each of the uniform beam profile measurements. This is likewise calculated for the vertical projections of the profiles from the YAG screens and radiochromic film. Fig. 5.31 shows the calibrated vertical beam profiles measured on the FOFM for pulse charges of between 0.5 nC and 5 nC to the dual-scattered 200 MeV electrons. As for the uniform beam response linearity measurements, the low intensity DAQ mode was used for all measurements. The asymmetric tail observed

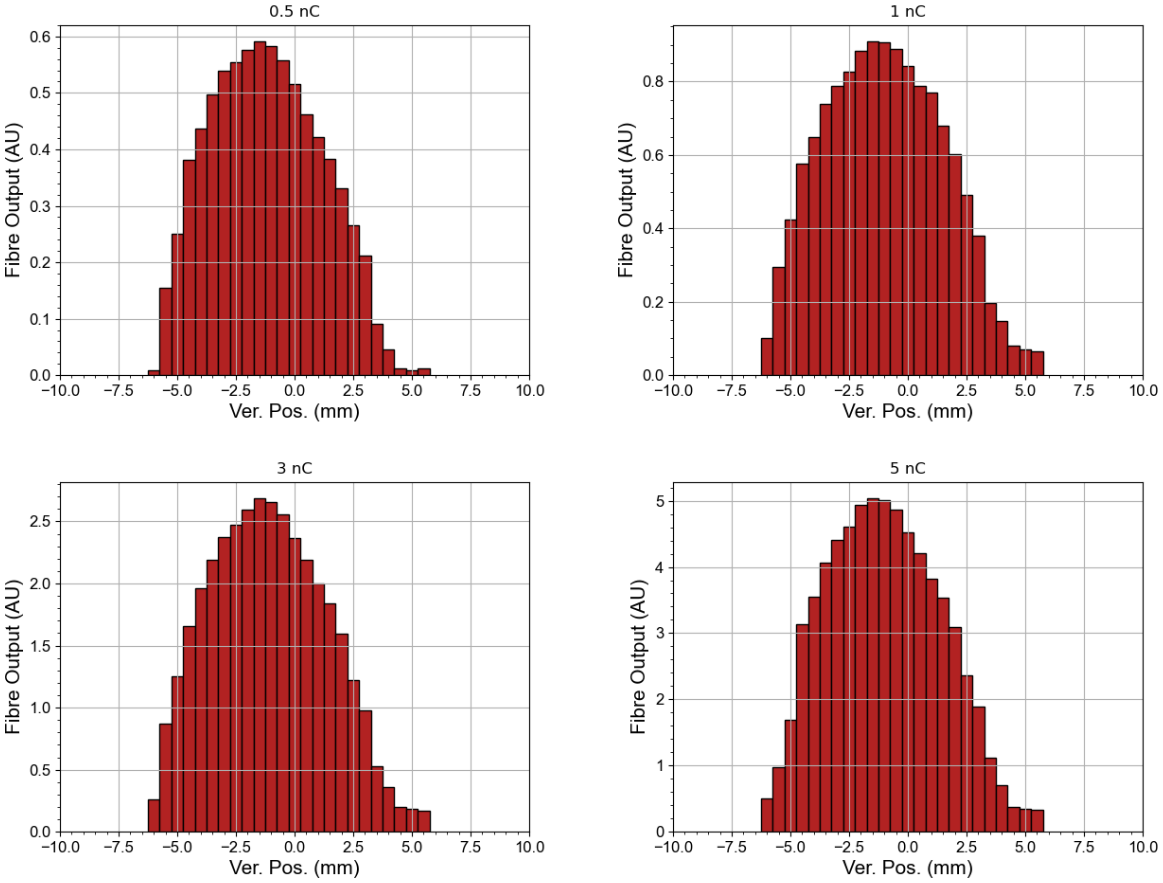

Figure 5.31: Vertical beam profile measurements using the upgraded FOFM prototype of a uniform dual-scattered 200 MeV electron beam for a 0.5 nC (top left), 1 nC (top right), 3 nC (bottom left) and 5 nC (bottom right) pulse.

between the vertical positions of 4.5 - 5.5 mm on all of the profiles in the figure is due to the noise that is still present on the fibre readings following background removal methods, with scatter radiation from the collimator potentially also contributing to this background reading. The shape of all of the profiles is clearly semi-elliptical however the profiles are not perfectly shaped, and this is likely due to some uncertainties accumulated through the calibration procedure. Such uncertainties are more prominent for uniform beam measurements since the fibres receive a more homogeneous dose and therefore magnify any discrepancies in the relative fibre response. The normalised intensity vertical beam profile measurements for a 1 nC pulse obtained using the FOFM in comparison to the made on a YAG screen 80 mm in front of the FOFM (YAG 1), and on radiochromic film and another scintillating YAG screen both 140 mm downstream of the FOFM are shown in Fig. 5.32, with the corresponding FWHM measurements shown along with those for a 5 nC pulse in Table 5.6. A good agreement between all the vertical profile FWHM measurements can be seen. The closest agreement is between the upstream YAG screen and the FOFM. A wider profile with larger tails is observed on the radiochromic film and downstream YAG screens, and can likely be attributed to increased lateral scattering in VHEE beam both from the upstream YAG screen and from the beam having to travel further in air before the being measured by the second YAG screen or radiochromic film. This effect is much more pronounced with a dual-scattered uniform beam as opposed to a small Gaussian pencil beam. The noticeably large FWHM value for the 5 nC pulse obtained for the HD-V2 radiochromic film is most likely due to the high background level and poor signal achieved on this film measurement since the dose was at the lower end of the optimal range of that for this specific film type. The tails present above the beam profile of the fibre array is signal that is still present after the background and noise removal methods prior to irradiation and could therefore be attributed the signal in the fibres from secondaries produced by the collimator. A further contribution to this signal could also be from the calibration factor for the fibres.

Pulse Charge (nC)	FWHM (mm)			
	FOFM	Film	YAG 1	YAG 2
1	7.56	7.70 (EBT-XD)	7.50	8.12
5	7.11	8.10 (HD-V2)	7.42	/

Table 5.6: Vertical uniform beam size measurements made withthe upgraded FOFM prototype, radiochromic film (with the type of film stated in brackets), and scintillating YAG screen obtained from the full-width half maximum (FWHM) of the vertical projection of the beam profile.

Despite the beam profile determination for circular uniform beams from a vertical fibre array being more difficult than that for a small Gaussian pencil beam, the FOFM demonstrated relatively good agreement for the FWHM measurements between the different modalities. This therefore demonstrates that it is promising modality for measuring the 2D beam profile for 3D-CRT beams

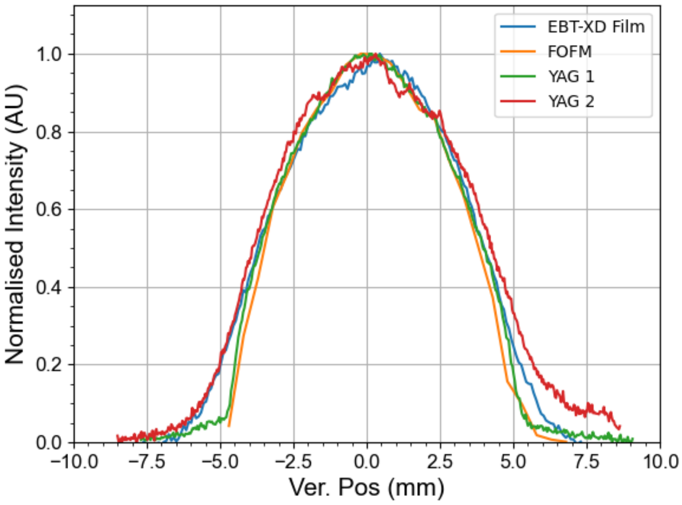

Figure 5.32: Plot showing the comparison of the normalised vertical beam profile measurements for a 1 nC pulse using the FOFM (orange), EBT-XD film (blue), and YAG screens positioned before (green) and after (red) the FOFM for a uniform dual-scattered 200 MeV electron beam.

using two orthogonal arrays which will be able to reconstruct the 2D transverse distribution and hence monitor it pulse-by-pulse in real-time.

Two key parameters that transmission ionisation chambers monitor for broad beams is the flatness and symmetry of the beam. For a fully realised FOFM beam monitor system, the measurement of the beam symmetry could be easily implemented using the fibre arrays by comparing the responses of the two fibres at equal distance from the centre of the array. On the other hand, the flatness measurement is more challenging for circular uniform beams, since such a measurement would need to be performed on the reconstructed 2D profile. Thus this flatness measurement is then also susceptible to any potential errors introduced by the reconstruction algorithm as well as being restricted by the computation time. Consequently, providing such a measurement could be difficult to do real-time on a pulse-by-pulse basis for the purpose of providing any necessary alterations to consequent pulses within FLASH timescales. If the FOFM is used to measure a square collimated beam, similar to the dose distribution of MV photon beams following the jaw collimators but prior to the MLCs (or other component for transverse beam shaping), this makes the profile measurements, along with the flatness and symmetry measurements much simpler since the Radon transform of a 2D square distribution is a top-hat function in the horizontal and vertical axes, from which the necessary beam profile characteristics can be obtained and analysed much more easily.

5.7 Beam Perturbation Measurements

One of the key requirements of an RT beam monitor that sets it apart from standard detectors for dosimetry is the need for it to have a minimal perturbation on the beam since it is a permanent installation in the beam path. To investigate the impact of a single fibre array on the VHEE beam, radiochromic film measurements were performed with Gaussian and uniform beams both in air, 200 mm behind the FOFM and in a water phantom, 200 mm behind the FOFM (100 mm and 25 mm depth for Gaussian and uniform beams, respectively, with the FOFM inserted and removed from the path of the beam. Measurements were performed to assess the impact on the size of the beam and the maximum dose deposited on the film by the beam. To measure the effect on the beam size, a vertical beam profile was taken using 2 mm wide vertical strip was taken through the centre of the beam distribution from which the FWHM was calculated. To measure the dose, the maximum dose for each distribution was calculated. The first measurements with a 1 nC Gaussian beam pulse are

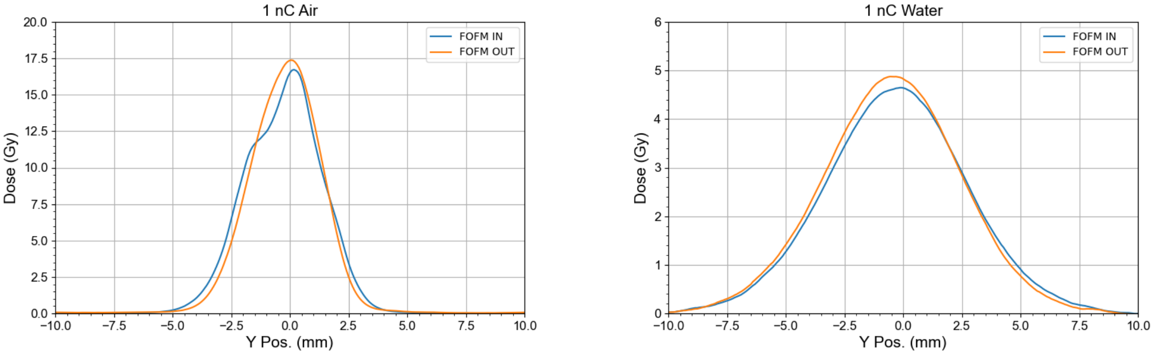

Figure 5.33: Vertical profiles taken with a 2 mm strip width of 200 MeV VHEE Gaussian pencil beams with a pulse charge of 1 nC both in air (200 mm behind the FOFM) (left), and at a depth of 100 mm in a water phantom (positioned 200 mm behind the FOFM) (right) with the FOFM inserted and extracted from the beam path.

Beam Distribution	Pulse Charge (nC)	In Air or Water	Maximum Dose (Gy)		Beam FWHM (mm)	
			Fibres In	Fibres Out	Fibres In	Fibres Out
Gaussian	1	Air	16.72	17.38	3.80	3.47
Gaussian	1	Water	4.65	4.88	6.77	6.68
Flat	1	Air	2.62	2.61	9.24	9.21
Flat	5	Water	10.22	10.19	9.83	9.18

Table 5.7: Measurements in air (25 mm behind the FOFM) and in water (25 mm depth for uniform beams and 100 mm depth for Gaussian beams) of the beam profile and maximum dose using radiochromic film for both uniform and Gaussian 200 MeV electron beams with the FOFM inserted and removed in the beam path.

shown in Fig 5.33, with the corresponding beam size and maximum dose measurements shown in Table 5.7. It can be seen that the maximum dose is reduced by 3.4% in air and by 4.7% in water. However, the smaller reduction in air is more likely to be due to a more prominent shadowing effect on the fibres, whereas this effect is smeared out by further scattering in water. An increase in the FWHM of the beam profile of 9.5% in air and increase of 1.3% in water can also be seen. Once again, the smaller difference in water can be attributed to the beam distribution being smoothed out by the additional scattering in water. Furthermore, it can be seen that when the FOFM is inserted, the Gaussian profile is retained, with the monitor causing the profile to widen; whereas the in air measurement shows shadows where the beam scatters off the fibres.

The profile measurements using a dual-scattered uniform beam are shown in Fig. 5.34, where a 1 nC pulse is used for the in air measurement and a 5 nC pulse is used for the in water measurement. Again, the corresponding beam size and maximum dose measurements shown in Table 5.7. Counter-intuitively, the maximum dose measured is higher for both the in air and in water measurements when the FOFM is inserted (by 0.38% and 0.29%, respectively). However, from looking at Fig. 5.34 it can be seen that this increase is from the shadowing of the FOFM, likely due to an increase in charge density in the small gaps between the fibres from electrons scattering off the fibres causing an increase in the dose in these regions. Furthermore, the shadowing is more evident on the water measurements for the uniform beam compared to the Gaussian beam because the radiochromic film is at a shallower depth of 25 mm as compared to 100 mm for the Gaussian beam. The FWHM can be seen to increase by 3.3% in air and 7.1% in water when the FOFM is inserted. The larger increase in the FWHM seen in water could also be due to the larger pulse charge of 5 nC being used.

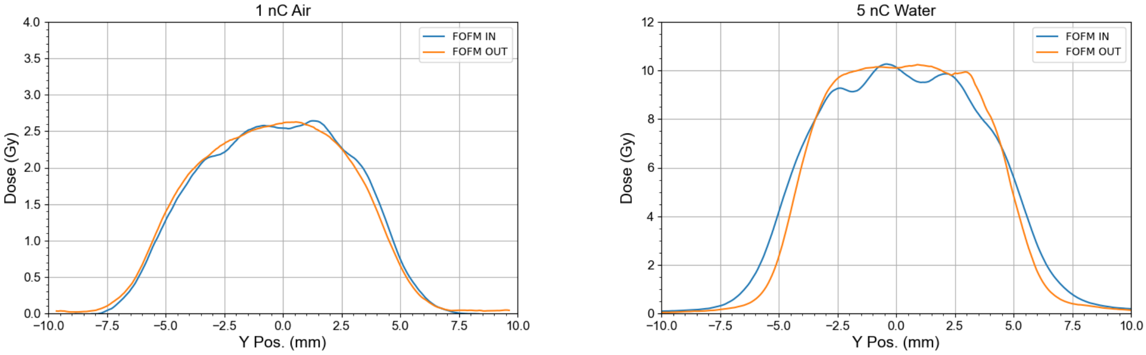

Figure 5.34: Vertical profiles taken with a 2 mm strip width of 200 MeV VHEE uniform beams with a pulse charge of 1 nC in air (200 mm behind the FOFM) (left), and 5 nC at a depth of 25 mm in a water phantom (positioned 200 mm behind the FOFM) (right) with the FOFM inserted and extracted from the beam line.

From these results it can be seen that the Gaussian beam measured in water was the least impacted by the FOFM being inserted, and that all other measurements showed some level of shadowing and hence loss of uniformity from the FOFM. This is then clearly something that would need to be considered if looking to implement such a detector on a clinical FLASH-RT machine. One point to bare in mind is that the source-to-surface distance (SSD) in these measurements was only 200 mm, which is much shorter than typical clinically used SSDs (usually around 100 cm). Having a larger SSD for such measurements would likely reduce the prominent shadows caused by the FOFM due to increased scattering in air by the VHEE beam. Another reason for the presence of these shadows from the fibre could be due to the small vertical separation between the fibres (since the vertical distance between the centres of the fibres is 0.5 mm, yet the fibre diameter is 0.4 mm), as well as the horizontal staggering of the fibres. This effect could potentially be mitigated through constructing the arrays using one column of fibres and ensuring no gaps between the fibres.

Furthermore, silica fibres with a square cross-section, instead of circular, could also minimise this effect.

5.8 Temporal Resolution

Some of the key minimum requirements for UHDR beam monitors stated in the report from the ESTRO FLASH Physics Workshop were based on the temporal requirements of such a detector - namely being to be able to monitor the number of pulses, the pulse width, pulse repetition frequency and pulse structure [270] The frame rate of the CMOS used for the FOFM measurements presented here was 42 frames/s. The reason for this being that the maximum p.r.f achievable at CLEAR is 10 Hz. However, as already stated the same model of CMOS camera is available with a frame rate of >500 frames/s which could be used to monitor the beam dose and profile at a higher p.r.f of up to 500 Hz. At this frame rate it is still only possible to achieve the requirements of monitoring the p.r.f and number of pulses. Given that typically the pulse width is on the order of μs or ns; in order to monitor the pulse width and pulse structure (e.g. number of bunches), a much higher temporal resolution would be required. One such possibility could be to use either an SiPM or PMT detector, as shown in the previous chapter. A possible final prototype of the FOFM could incorporate a SiPM or a PMT attached to one of the fibres either in the centre or on the outside of the array with the purpose of providing temporal information. Since these photodetectors have the advantage of a high temporal resolution that could resolve the pulse width, even when operated under saturation conditions. A configuration similar to the one described in the paper by García Díez *et al* [290] where the principle has been demonstrated using a plastic scintillator coupled to a SiPM via a fibre for monitoring the pulse structure in high dose rate proton therapy.

5.9 Comparison to VHEE-FLASH Treatment Planning Dose Rate Requirements

A significant amount work has been published on the treatment plans proposed for VHEE, suggesting minimum beam intensities of 9.375×10^{11} electrons/s for >90% of the PTV, to receive a dose-averaged dose rate in excess of 40 Gy/s [291]. Assuming similar beam parameters and size at which the FOFM was tested with at the CLEAR facility, the above intensity requirement translates into a minimum DPP of 23 Gy/pulse at 10 Hz p.r.f, or 2.3 Gy/pulse at 100 Hz p.r.f. Therefore, the measurements described in this chapter demonstrate that indeed the FOFM exhibits the response linearity required for dose monitoring for VHEE into - and possibly beyond - the UHDR regime necessary for inducing the FLASH effect. It is more likely that a VHEE-FLASH treatment machine will deliver the prescribed dose with a p.r.f 100 Hz or more, since this allows for the delivery of multiple pulses, and hence the ability to alter the pulses, within the time constraints of the FLASH effect. Hence DPPs within the lower range of what was explored within this study are more likely to be implemented clinically.

5.10 Performance Comparison to Other UHDR Beam Monitors Under Development

A number of novel UHDR beam monitors are under development for the purpose of online beam monitoring for FLASH-RT. Table 5.8 shows a comparison of the characteristics of these, compared to that demonstrated by the FOFM. In terms of response linearity, the FOFM appears to be performing best along with BCTs and the SiC detectors. However, the reported numbers for many of the detectors is limited by the maximum achievable DPP or dose rate of the treatment machine, this is the case for the Ce-doped YAG [275] and FLASHDC [273] detectors. The FLASH Beam Scintillator Monitor (FBSM) was tested up to 8 Gy/pulse (237 Gy/s) however, the measurement at 8 Gy/pulse

Detector	Linear Response Up To:	2D Profile Measurements?	Spatial Resolution (mm)	Temporal Resolution (μs)
FOFM	76.2 Gy/pulse (max 10 Hz p.r.f)	✓	0.5	2000 (with 500 frames/s CMOS)
FBSM [274]	4 Gy/pulse < DPP < 8 Gy/pulse (30 Hz p.r.f)	✓	0.37	50
SiCs [170]	21 Gy/pulse (245 Hz p.r.f)	✓	1	< 1
Ce-doped YAG [275]	2 Gy/pulse (300 Hz p.r.f)	✓	< 1	2000 (with 500 frames/s CMOS)
FLASHDC [273]	20 Gy/pulse (300 Hz p.r.f)	×	NA	/
BCT [264, 265]	>15 Gy/pulse	×	NA	0.35
Modified Transmission IC [78]	0.88 Gy/pulse (200 Hz p.r.f)	(Flatness and Symmetry)	NA	300

Table 5.8: Comparison of the characteristics of current UHDR beam monitors that are under development.

fell below linearity by approximately 6% [274]. For beam profile measurement accuracy, the beam profile measurements made by the FBSM for UHDR beam monitoring were reported to have fits that agree with those made with Gafchromic EBT-XD films within 1.4%, and those made by the Ce-doped YAG were between 0.05% for a 120 mm sized applicator and 3.6% for a 18 mm applicator [275]. The FOFM profile measurements had a varying degree of agreement with radiochromic film measurements - ranging between $0\% - 3.4\%$ discrepancies for Gaussian beams and between 1.9% and 12% for uniform beams. However, the larger discrepancy on the FOFM measurements for the uniform circular beams also includes the accumulated errors in the projection of the profile. The CMOS camera currently used by the FOFM (with a frame rate of 42 frames/s) has the lowest temporal resolution of all the detectors discussed here, however it is possible to use an alternative CMOS camera model that has a 500 frames/s frame rate (similar to that used with the Ce-doped YAG which was able to provide pulse-by-pulse profile measurements at a 300 Hz p.r.f [275]. Furthermore, using the FOFM with an additional SiPM or PMT coupled to one of the fibres in the array, or in parallel with a BCT would allow the FOFM detector arrangement to have a sub-microsecond resolution to achieve pulse-width measurements.

5.11 Concluding Remarks and Future Directions Towards the Next Generation FOFM and Clinical Implementation

The results presented in this chapter demonstrate the successful development and characterisation of a novel detector technology for UHDR online beam dose and profile monitoring with VHEE beams. The use of an array of silica fibres to measure VHEE beams via Cherenkov radiation, with CMOS Camera readout, has shown considerable promise as a monitoring solution. This work represents the first comprehensive development and characterisation of a detector specifically designed for monitoring VHEE UHDR beams. As such, the results of the development and testing of the first prototype have already been published [292], and a further second publication outlining the rest of the results in this chapter is under preparation. The initial results with this first FOFM prototype, obtained with 200 MeV and 160 MeV electron Gaussian pencil beams at the CLEAR facility at CERN. These results showed that the FOFM exhibited excellent response linearity across a large dynamic range with DPP's from 0.9 to 57.4 Gy/pulse (with reference dose-to-water measurements performed with EBT-XD films at 150 mm in water), i.e. over the entire range of DPPs possible at the CLEAR facility. It was also demonstrated that the response of the fibre array did not depend on energy and instantaneous dose rate, both important factors for monitoring the delivery of the VHEE dose at UHDR. Furthermore, the FOFM was able to perform accurate pulse-by-pulse measurements of the vertical beam profile following calibration of the fibres, showing agreement with profile measurements performed using radiochromic film and a scintillating YAG screen. The FOFM design was optimised by cleaving the fibres, polishing the ends of the silica fibres, and improving the spatial resolution of the FOFM. This resulted in an improved homogeneity between the response of the individual fibres, as well as improved accuracy in the vertical beam profile measurements when compared to those made on radiochromic films and improved response linearity. The installation of a dual-scattering system at the CLEAR facility also meant it was possible to characterise the FOFM to collimated uniform beams, whereby it was demonstrated that the detector could predict the dose deposited on EBT-XD film at a reference depth in water to within less that 5%, as demonstrated in Fig. 5.30. The vertical beam profile measurements were less trivial with a uniform circularly collimated beam than for a Gaussian pencil beam due to the Radon transform of this distribution. Albeit, comparisons between the vertical projection of the uniform beam profile measured on the FOFM, radiochromic film and YAG screens showed some level of agreement, although further work is required to develop an accurate way of reconstructing and monitoring the profile for this type of transverse beam distribution. Whilst measurements of the beam profile on radiochromic with and without the FOFM array inserted in the beam path showed only some perturbation of the dose distribution on the film measurement. Shadows from the silica fibres were particularly noticeable on the in air profile measurements. To avoid this in future, the fibre array should be constructed to further minimise any gaps between the fibres in the array to mitigate this effect. Although, the profile measurements were made at a much shorter distance from the fibre detector than the distance between the head of the treatment machine and the patient. This larger distance in the clinical setup could mean that the scattering in air could negate the effect of the shadowing on the beam distribution. Overall, the silica fibre array detector shows a lot of promise as a potential option for an UHDR beam monitor for VHEE beam since it has shown to have the largest dynamic range compared to other detectors under development, and has the ability to accurately measure the beam profile.

The next steps in the development of the FOFM would be to construct and characterise a second array to perform horizontal profile measurements simultaneously, and develop a back-end readout system to provide real-time beam intensity and profile reconstruction. Whilst it is still unsure what the exact beam parameters on a clinical VHEE-FLASH treatment machine will be, it is likely that the pulse repetition frequency will be above 100 Hz, and hence a CMOS camera with a higher frame rate will be required. Since Vanreusel *et al* [275] was able to perform pulse-by-pulse measurements of a 300 Hz electron beam with a 500 frames/s CMOS camera, a CMOS with a similar frame rate should be considered for the next iteration of the FOFM. Furthermore, commensurate with a higher p.r.f is a lower DPP range, and it is likely that DPPs towards the lower range of those tested at CLEAR will be more realistic in the clinic. Therefore, the readout detector should aim to improve and optimise the accuracy, precision and reliability of monitoring such DPPs. The UHDR beam monitoring requirements which the FOFM are currently not able to meet are the measurement of the pulse width and structure for instantaneous dose rate measurements, due to the temporal resolution limit of CMOS cameras. A solution to this limitation could be to connect a SiPM or PMT photodetector to one of the fibres within the FOFM array to provide measurements of the pulse width and structure. Whilst some measurements in this chapter verifies the short-term stability of the response of the FOFM, further measurements are necessary to ensure that such a monitor would be feasible for use on a clinical VHEE machine. The characterisation of any ageing or deterioration of the response of the fibres following irradiations with doses in the range of that expected throughout the lifetime of a typical monitor chamber should be performed in order to meet the requirement of radiation hardness, as described by Romano *et al* [75], particularly since the beam monitor will be a a permanent fixture inside the machine head. Radiation hardness tests of the silica fibres used in the experiment described in this paper are currently being carried out at the IRRAD facility at CERN, with 24 GeV protons up to doses on the order of MGy's with both the Cherenkov signal from the beam and light transmission from a bulb are being measured [284]. Similar tests will be carried out at the CLEAR facility investigating the stability of the response and of its linearity, following irradiations of large doses. Furthermore, it is envisaged to investigate the use of square-shaped silica rods as an alternative to the fibres, since this shape is likely to produce a more homogeneous signal.

5.11.1 A Hybrid Detector

One alternative proposed method of implementing the FOFM clinically could be in the form of a hybrid detector paired with another form of instrumentation that performs optimally in areas where the FOFM response has a higher uncertainty. A beam monitoring system of this sort was suggested within the ESTRO FLASH Physics workshop report on the requirements of a UHDR beam monitor [270]. For example, whilst the results in this chapter showed the FOFM provided excellent response linearity and accurate profile measurements further work is required to determine the long term response stability of the fibres and precision of their dose monitoring. However, BCT's have already been show to excel in their response stability and can monitor the dose at UHDR (as shown in the previous chapter in Fig. 4.10) and do so within clinically acceptable uncertainties, with the addition of providing temporal information about the pulse width and structure. [264, 265, 266]. Therefore, a hybrid detector consisting of the FOFM and a BCT would be a robust option where the BCT can provide temporal information and monitor the fluence of the beam with its proven response stability, and the FOFM can also provide an additional measurement of the beam fluence as well as spatial information such the beam spot size and position for pencil beams, and the field size and uniformity for broad beams.

6 Conclusions and Future Work

6.1 Discussion and Conclusions

The delivery of Very High Energy Electron (VHEE) beams at ultrahigh dose rates (UHDR) for FLASH radiotherapy of deep-seated tumours has the potential to revolutionise the field of radiation oncology through the possibility of widening the therapeutic window. This is achieved by the apparent reduced toxicity to healthy tissue whilst maintaining the same level of tumour control. Delivering the radiation dose at UHDR comes with the additional benefits of reducing treatment time and lowering the intra-fraction uncertainties by effectively freezing the organ motion within the patient. Furthermore, VHEE beams have shown to posses favourable characteristics such as an increased range, compared to clinical electron beams energies, reduced sensitivity to inhomogeneities and the ability to be electromagnetically scanned and/or focused. Additionally, VHEE beams offer a favourable radiation modality for the delivery of UHDR radiotherapy to elicit the FLASH effect in deep-seated tumours; with the additional benefit of being technologically easier to deliver these beams than it is for other modalities such as photons and hadrons. However, one of the main technological challenges that needs addressing before bringing FLASH radiotherapy to the clinic is that of real-time dosimetry, since ionisation chambers - the gold standard for reference dosimetry, relative dosimetry and beam monitoring for radiotherapy - experience significant recombination effects under these conditions and hence exhibit a non-linear response in the UHDR regime. The pulsed nature of the delivery of VHEE beams, along with their ultrashort pulse lengths (typically on the order of tens to hundreds of nanoseconds), means that in order to meet the mean dose rate requirements of the FLASH effect, VHEE beams have an ultrahigh dose-per-pulse (UHDPP) along with an extremely high instantaneous dose rate. This further exacerbates the recombination effect in ionisation chambers, and means that providing correction factors - as has been done for other UHDR radiation modalities - is unlikely to be sufficient for VHEE UHDR radiotherapy dosimetry. Based on this, the goals of this thesis were to investigate dosimetry and real-time beam monitoring at UHDR with VHEE beams in three main areas: firstly characterising the interactions of VHEE beams with a water and PMMA phantom to evaluate the feasibility of using the secondary radiation generation as a means of *in vivo* dose verification; secondly through the development, refinement and characterisation of relative dosimetry protocols at the CLEAR facility using radiochromic film for use in VHEE-UHDR experiments; and finally through the development of a novel optical fibre array monitor for real-time beam profile and dose monitoring.

Monte Carlo Characterisation of VHEE Interactions for Dose Monitoring The first investigation was to characterise the interactions of VHEE beams in a water and PMMA phantom using TOPAS Monte Carlo simulation software and evaluate the dose distributions and secondary particle generation for the feasibility of using different *in vivo* dose verification methods. *In vivo* dosimetry and dose monitoring plays a key role in strive towards online adaptive radiation therapy whereby any deviations to the delivered dose or patient anatomy can be detected and accounted for in real-time. Furthermore, such methods would be vital in facilitating the clinical translation of FLASH radiotherapy using VHEE beams at UHDR in order to verify the correct dose has been delivered to the tumour volume, as well as ensuring the correct beam parameters have been delivered in order to elicit the FLASH effect. The first evaluation performed using the MC simulations was that of the yield resulting secondary particles scored leaving the water or PMMA phantom following the irradiation of a 200 MeV VHEE beam and proton beam. The measurements showed that the VHEE beam produced the highest amounts of bremsstrahlung radiation, positron annihilation (PA) gamma rays and Cherenkov radiation, per Gray of dose deposited. The proton beam irradiation produced a higher yield of secondary neutrons and prompt gamma (PG) rays. The characteristics of the VHEE dose distributions demonstrate that electronic portal imaging device (EPID)-based transit dosimetry would likely be a feasible method for *in vivo* dose verification methods for VHEE beams. Although considerations of the large energy spread of both electrons and bremsstrahlung radiation that will be present in the signal needs to be taken, as well as the fact that VHEE beams show a greater lateral spread at the exit of the patient or the phantom. Furthermore, if such a method is to be used for UHDR treatments, the dynamic range of the detector needs to be large enough to deal with such a high intensity of radiation. The use of prompt PA gamma rays for the dose verification for VHEE FLASH RT had been proposed in the literature and the signal from the VHEE beam irradiation was noticeably higher than that for protons. However further investigation showed that only 0.1% of these PA gamma rays following VHEE beam irradiation were from β^+ activity, and the remainder were from positrons produced from pair, or triplet, production from the bremsstrahlung radiation. However, it is still possible to separate the signal temporally and the delivery of VHEE beams at UHDR would provide a stronger and faster signal. The induced β^+ activity is induced primarily through photonuclear interactions of the bremsstrahlung with the target, therefore meaning any algorithms correlating the activity with the dose would likely have to be more complex than those currently being developed for proton therapy purposes. Cherenkov radiation was by far the largest form of secondary radiation emitted, especially for VHEE beams. The Monte Carlo simulations showed that the distribution of the emitted Cherenkov radiation closely matched that of the VHEE dose distribution. Slight variations were present in regions where lower energy electrons or bremsstrahlung radiation contributed largely to the dose however such variations can be calibrated for. Cherenkov optical imaging dosimetry has already been successfully demonstrated for UHDR RT with 10 MeV electrons, and therefore is a promising method for monitoring the surface dose pulse by pulse VHEE UHDR irradiations. Volumetric Cherenkov imaging could also be a promising modality for quality assurance measurements of the longitudinal and lateral dose profile measurements in phantom for VHEE UHDR beams given the proven dose rate linearity of such a method along with the speed of detection.

Very High Energy Electron Ultrahigh Dose Rate Radiotherapy Dosimetry Studies at the CERN Linear Electron Accelerator for Research (CLEAR) The second research contribution was the development and refinement of a radiochromic film dosimetry protocol at the CLEAR Facility. The CLEAR Facility is currently in a unique position to be able to provide the relevant parameters necessary for pre-clinical radiobiological and dosimetry measurements of VHEE beams at UHDR. It is therefore necessary to ensure that accurate dosimetry protocols are in place so that any observable difference in the effects of either the samples or of the detectors between the UHDR and conventional dose rate (CONV) irradiations is due to differences in the dose rate as opposed to differences in the total delivered dose. The development work of the radiochromic film dosimetry protocol was first outlined and then methods for beam size measurements were investigated. Since the VHEE beam at the CLEAR facility is Gaussian, beam size determination is important both for ensuring a sufficient dose is delivered over a large enough area to cover the sample and secondly for targeting the dose in the sample. The dose-area-product is used for these purposes. Beam size determination were performed and compared using three types of Gaussian fits: 1D Gaussian fits to horizontal and vertical strips of the profile, 2D Gaussian fits, and 1D Gaussian fits to horizontal and vertical projection of the profile. One-dimensional Gaussian fits to horizontal and vertical strips produced the smallest beam size, while fits to the projection of profiles resulted in the largest sizes, with 2D Gaussian fits displaying the highest uncertainty. These variations stem from the sensitivity of the fitting methods to background noise and the influence of signal distribution. Notably, the YAG screen showed systematically larger beam sizes compared to those made with EBT3 radiochromic film, likely due to signal distortion as light passes through water. These results highlighted the importance of which method to use for accurate beam size measurement. Charge measurements made with ICTs along with the the dose-area-product obtained from radiochromic film measurements at a reference position in water verified that it is possible to correlate the charge readings with the DAP for both UHDR and CONV deliveries, and hence use these measurements to target the central maximum dose on the sample being irradiated. For CONV irradiations using a lower charge per bunch and hence a lower instantaneous dose rate, the correlation between the ICT charge measurement and DAP varied due to the CONV charge per pulse being close to the noise level of the ICT reading. Therefore, this means that separate calibration factors are required for the two delivery modes. Finally, dose measurements made with the radiochromic film were compared to those from the alanine and TLD methods: comparing dose measurements for CONV irradiations at a range of VHEE energies with alanine pellets and comparing UHDR and CONV measurements with 200 MeV phantoms containing TLDs and small cutouts of radiochromic films. The results of these comparisons showed agreement within the uncertainty range between radiochromic film dose measurements and that of the passive dosimeters. However, there were notably large uncertainties from dose measurements across all dosimeters. This is primarily due to the Gaussian beam distribution, resulting in a variation of doses received by passive dosimeters.

A Novel Fibre Optic Monitor for Beam Profile and Dose Monitoring at Ultrahigh Dose Rates
The final contribution was the design, development and dosimetric characterisation of a novel optical fibre beam monitor for real-time beam profile and dose monitoring of UHDPP VHEE beams, as an alternative to the currently used transmission ionisation chamber which saturates at these dose rates. The basis of the detector is an array of silica fibre-based Cherenkov radiation sensors, which generate Cherenkov radiation as the relativistic electron beam passes through the fibres which is then read out using a photodetector. Initial single fibre measurements were performed at the CLEAR facility using 200 MeV electrons with a multi-modal silica optical fibre to evaluate the performance of different photodetectors; SiPM, PMT, and CCD camera. Both the SiPM and PMT demonstrated relatively linear responses but signal amplitude saturation was observed at the larger charges per pulse. However, the high temporal resolution of these photodetectors meant that the width of the electron pulses could be observed. Measurements with the CCD camera photodetector utilised a vertical moving stage to perform vertical profile measurements as well as taking the integral measurements as the beam intensity. The CCD camera exhibited a better linearity when using the integral of the Gaussian fit applied to the profile for each dose-per-pulse (DPP) as opposed to when summing the fibre response at each vertical position. this was likely due to the Gaussian fit compensating for the under-response at intermediate DPPs due to the CCD camera's low signal-to-noise ratio, which is unable to accurately measure the low-intensity tails of the beam. Following these measurements

it was decided to construct the fibre array monitor using bare fused silica fibres, to increase the transmission of the Cherenkov light, and use a CMOS camera as the photodetector since it has a larger dynamic range and a faster frame rate than a CCD camera, as well as being capable of reading out the entire array, the detector was coined the Fibre Optic FLASH Monitor (FOFM). Initial results with the first FOFM prototype, using 200 MeV and 160 MeV electron Gaussian pencil beams at the CLEAR facility, demonstrated a linear response with DPP across the entire range of DPP's used. The response was shown to have minimal dependence across the energies and instantaneous dose rates used. Pulse-by-pulse measurements of the vertical beam profile, following fibre calibration, agreed with measurements using radiochromic film. Improvements in fibre cleaving, polishing, and spatial resolution optimisation improved the homogeneity of the relative response between each of the individual fibres response and hence improved the accuracy in vertical beam profile measurements. The installation of a dual-scattering system at the CLEAR facility enabled FOFM characterisation with collimated uniform beams, These measurements demonstrated that the FOFM could predict dose deposition on EBT-XD film at a reference depth in water within 5%, for DPPs up to the maximum producible DPP of 12 Gy/pulse. Vertical beam profile measurements with uniform circularly collimated beams were more challenging than with Gaussian pencil beams due to the Radon transform of this distribution. Despite this, comparisons between the vertical projection of the uniform beam profile measured on the FOFM, radiochromic film, and YAG screens showed some agreement. However, further work is required to develop accurate reconstruction and monitoring methods for this type of transverse beam distribution. Additionally, measurements of beam profiles with and without the FOFM array inserted showed some perturbation of the dose distribution on film, with fibre shadows being noticeably present in air profile measurements. This effect can likely be mitigated by further minimising gaps between fibres in the array. These measurements demonstrated that the FOFM is promising technology for real-time monitoring of the beam profile and dose for VHEE beams at UHDR.

6.2 Future Work

***In vivo* Dose Verification** The work presented on the characterisations of VHEE beam interactions in water and PMMA phantoms was intended to evaluate the feasibility of potential methods for *in vivo* dose verification methods. The outcome of the study pointed towards EPID-based transit dosimetry, in-beam PET and Cherenkov optical imaging as the most promising methods. However, much more in-depth simulations of more realistic beams and detector setups would be required to verify this. For both EPID and in-beam PET methods, simulations of detector geometries and locations need to be carried out. Whilst for Cherenkov optical imaging, the simulations have already shown that the distributions are closely correlated. This method has also been verified for clinical energy UHDR electron beams [244], therefore similar measurements using a time-gated CMOS camera and radiochromic films should be carried out with VHEE UHDR beams.

Relative Dosimetry Procedures at the CLEAR Facility Further work is currently being undertaken by members of the CLEAR team in order to fully characterize the observed discrepancies and establish a precise correlation between beam sizes measured on the scintillating YAG screen and the radiochromic films . The ultimate goal is to enable real-time dosimetry of VHEE beams at UHDR using the YAG screen. The recent installation of a dual-scattering foil system for uniform VHEE beams at the CLEAR facility means that the uncertainties and variation of the dose over the samples targeted is now significantly reduced. This also means that dose targeting and prediction is much simpler, since a direct correlation between the dose deposited at a reference position, can be directly correlated to the charge reading of a BCT positioned after the collimator, as has already been established in a number of pre-clinical UHDR electron facilities [264, 265, 266]. This development should also allow for a more comprehensive and accurate dosimetric comparison of different methods using VHEE beams at UHDR, given the uniform dose across the transverse area of the samples. Additionally, a thorough investigation into the reference depth at which these dosimeters are irradiated should be conducted to accurately interpolate the dose on the sample when using two radiochromic films upstream and downstream of the sample. An increasing number of detectors designed specifically for UHDR irradiations are becoming increasingly available, such as the modified geometry ionisation chambers [80, 81, 82], flashDiamond detector [168], and SiC detectors [170, 293]. Such detectors should also be tested and characterised with the VHEE UHDR beams at the CLEAR facility, with the goal of being used to provide real-time dose measurements at the reference depth potions in water, either for calibration measurements for ICT or for real-time dosimetry during sample irradiations.

Fibre Optic FLASH Monitor Future steps in the development of the FOFM first include the construction and characterisation of a second silica fibre array for simultaneous horizontal profile measurements. and developing a back-end readout system for real-time beam intensity and profile reconstruction. The current iteration of the FOFM prototype was optimised to suit the range of beam parameters at the CLEAR facility. However, looking further into the future for potential clinical implementation, future clinical VHEE-FLASH treatment machines will likely have a pulse repetition frequency above 100 Hz in order to facilitate the delivery of multiple pulses within FLASH timescales. Therefore, a CMOS camera with a higher frame rate will be necessary. Successful pulse-by-pulse measurements of a 300 Hz electron beam with a 500 frames/s CMOS camera performed by Vanreusel *et al* [275] suggest that a similar frame rate should be considered for the next FOFM iteration. Furthermore, higher p.r.f. will likely be associated with a lower DPP range, therefore requiring further optimisation of the readout detector's accuracy, precision, and reliability for monitoring such DPPs. While the current FOFM cannot measure pulse width and structure for instantaneous dose rate measurements due to the temporal resolution limits of CMOS cameras, connecting a SiPM or PMT photodetector to one of the FOFM array fibres could potentially provide these measurements. Alternatively, a hybrid detector, as suggested in the ESTRO FLASH Physics workshop report [270], could be employed. For example, a BCT could offer additional intensity measurements and temporal information about pulse width and structure, alongside the FOFM's beam profile and position measurements. Further measurements are needed to verify the long-term stability of the FOFM response, ensuring its feasibility for clinical VHEE machines. Characterising any ageing or deterioration of the fibres' response following irradiations with doses expected over the monitor's lifetime is essential. Ongoing radiation hardness tests at CERN's IRRAD facility with 24 GeV protons up to MGy doses, measuring both the Cherenkov signal from the beam and light transmission from a bulb. Similar tests at the CLEAR facility will further investigate the stability and linearity of the FOFM's response after large dose irradiations.

6.3 Final Concluding Remarks

The overall aim of this thesis was to address the current challenge of dosimetry and real-time beam monitoring at UHDR, for VHEE FLASH-RT. Such research is extremely relevant since at present, the very first clinical VHEE FLASH-RT treatment machine is currently under construction at Centre Hospitalier Universitaire Vaudois (CHUV), Lausanne, Switzerland and due to be complete in 2025 [110], and a number of other facilities are proposed also. The work in this thesis provides valuable contributions to address the knowledge gaps within this field of research in order to overcome the technological challenge of dosimetry and beam monitoring at UHDR and allow for the clinical translation of VHEE FLASH RT. The work in **Chapter 3** concluded that EPID-based dosimetry and Cherenkov optical imaging could prove to be promising options for *in vivo* dose verification methods for VHEE radiotherapy. Being able to monitor and verify the dose delivered to the patient would be extremely important for new RT modalities, especially for FLASH, where the delivery of the dose in short timescales adds additional uncertainties. The radiochromic film dosimetry protocol established in **Chapter 4** has already been used for numerous pre-clinical radiobiological studies investigating the FLASH effect with VHEE beams, and therefore the work in this chapter is playing a crucial role in advancing the understanding of the FLASH effect, which is necessary to enable its clinical translation. Finally, the work in **Chapter 5** proposed a novel silica fibre array detector for the real-time beam monitoring of VHEE beams at UHDR. Currently no other technology exists at present that has been demonstrated to monitor both the dose and the profile of the beam at the dose rates required for VHEE FLASH. Therefore, demonstrating that the work presented in this chapter has the potential to used on a clinical machine.

Bibliography

[1] J Ferlay et al. *Global Cancer Observatory: Cancer Today (version 1.1)*. 2024. URL: `https://gco.iarc.fr/today` (visited on 01/31/2024).

[2] J Ferlay et al. *Global Cancer Observatory: Cancer Tomorrow (version 1.1)*. 2024. URL: `https://gco.iarc.fr/tomorrow` (visited on 01/31/2024).

[3] J. Maddams, M. Utley, and H. Møller. "Projections of cancer prevalence in the United Kingdom, 2010-2040". *British Journal of Cancer* 107 (2012). ISSN: 00070920. DOI: `10.1038/bjc.2012.366`.

[4] Office for National Statistics. *Cancer registration statistics, England Statistical bulletins - Office for National Statistics*. 2021. URL: `https://www.ons.gov.uk/` (visited on 02/10/2024).

[5] Josep M. Borras et al. "The impact of cancer incidence and stage on optimal utilization of radiotherapy: Methodology of a population based analysis by the ESTRO-HERO project". *Radiotherapy and Oncology* 116 (2015). ISSN: 18790887. DOI: `10.1016/j.radonc.2015.04.021`.

[6] Ajay Aggarwal et al. "The future of cancer care in the UK-time for a radical and sustainable National Cancer Plan". *The lancet oncology* 25 (2024), e6–e17. ISSN: 1470-2045. DOI: `10.1016/S1470-2045(23)00511-9`.

[7] Katie Spencer et al. "Variable and fixed costs in NHS radiotherapy; consequences for increasing hypo fractionation". *Radiotherapy and Oncology* 166 (2022). ISSN: 18790887. DOI: `10.1016/j.radonc.2021.11.035`.

[8] W. C. Röntgen. "Ueber eine neue Art von Strahlen". eng. *Annalen der Physik* 300.1 (1898), pp. 1–11. ISSN: 0003-3804.

[9] Manuel Lederman. “The early history of radiotherapy: 1895-1939”. *International Journal of Radiation Oncology, Biology, Physics* 7 (1981). ISSN: 03603016. DOI: `10.1016/0360-3016(81)90379-5`.

[10] S. Birkenhake and R. Sauer. “Historical essentials influencing the development of radiooncology in the past 100 years”. *Experientia* 51 (1995). ISSN: 00144754. DOI: `10.1007/BF01941265`.

[11] Andrzej Kułakowski. “The contribution of Marie Skłodowska-Curie to the development of modern oncology”. *Analytical and Bioanalytical Chemistry* 400 (2011). ISSN: 16182650. DOI: `10.1007/s00216-011-4712-1`.

[12] Gösta Forssell and A. Renander. “Second International Congress of Radiology, Stockholm, July 23–27, 1928”. *Radiology* 10 (1928). ISSN: 0033-8419. DOI: `10.1148/10.5.450a`.

[13] Dylan Y. Breitkreutz, Michael D. Weil, and Magdalena Bazalova-Carter. “External beam radiation therapy with kilovoltage x-rays”. *Physica Medica* 79 (2020). ISSN: 1724191X. DOI: `10.1016/j.ejmp.2020.11.001`.

[14] B. J. Healy et al. “Cobalt-60 Machines and Medical Linear Accelerators: Competing Technologies for External Beam Radiotherapy”. *Clinical Oncology* 29 (2017). ISSN: 14332981. DOI: `10.1016/j.clon.2016.11.002`.

[15] E.B. Podgorsak. “Radiation Oncology Physics: A Handbook for Teachers and Students. Chapter 6: External Photon Beams: Physical Aspects.” *Radiation Oncology Physics: A Handbook for Teachers and Students* (2005).

[16] Philip Mayles, Alan Nahum, and Jean Claude Rosenwald. *Handbook of radiotherapy physics: Theory and practice, second edition, two volume set*. Vol. 1. 2021. DOI: `10.1201/9780429201493`.

[17] David I. Thwaites and John B. Tuohy. “Back to the future: The history and development of the clinical linear accelerator”. *Physics in Medicine and Biology* 51 (2006). ISSN: 00319155. DOI: `10.1088/0031-9155/51/13/R20`.

[18] M. Weissbluth et al. “The Stanford Medical Linear Accelerator”. *Radiology* 72 (1959). ISSN: 0033-8419. DOI: `10.1148/72.2.242`.

[19] Adam Konefał et al. “Energy spectra in water for the 6 MV X-ray therapeutic beam generated by Clinac-2300 linac”. *Radiation Measurements* 72 (2015). ISSN: 13504487. DOI: `10.1016/j.radmeas.2014.11.008`.

[20] Bruce J. Gerbi et al. “Recommendations for clinical electron beam dosimetry: Supplement to the recommendations of Task Group 25”. *Medical Physics* 36 (2009). ISSN: 00942405. DOI: `10.1118/1.3125820`.

[21] Kenneth R. Hogstrom and Peter R. Almond. “Review of electron beam therapy physics”. *Physics in Medicine and Biology* 51 (2006). ISSN: 13616560. DOI: `10.1088/0031-9155/51/13/R25`.

[22] Avinash Pilar et al. “Intraoperative radiotherapy: Review of techniques and results”. *ecancermedicalscience* 11 (2017). ISSN: 17546605. DOI: `10.3332/ecancer.2017.750`.

[23] Igor S. Chumachenko, Roman A. Murashko, and Arthur A. Keshabyan. “Intraoperative radiation therapy in the treatment of breast cancer. From the past to the future”. *Innovative Medicine of Kuban* (2022). ISSN: 25419897. DOI: `10.35401/2500-0268-2022-25-1-77-82`.

[24] R. R. WILSON. “Radiological use of fast protons.” *Radiology* 47 (1946). ISSN: 00338419. DOI: `10.1148/47.5.487`.

[25] John H. Lawrence. “Proton irradiation of the pituitary”. *Cancer* 10 (1957). ISSN: 10970142. DOI: `10.1002/1097-0142(195707/08)10:4<795::AID-CNCR2820100426>3.0.CO;2-B`.

[26] Administrator. *PTCOG - Facilities in Operation — ptcog.site*. `https://www.ptcog.site/index.php/facilities-in-operation-public`. [Accessed 29-03-2024].

[27] Wayne D. Newhauser and Rui Zhang. “The physics of proton therapy”. *Physics in Medicine and Biology* 60 (2015). ISSN: 13616560. DOI: `10.1088/0031-9155/60/8/R155`.

[28] Harald Paganetti, ed. *Proton Therapy Physics*. CRC Press, 2016.

[29] William F. Morgan and Marianne B. Sowa. "Effects of ionizing radiation in nonirradiated cells". *Proceedings of the National Academy of Sciences of the United States of America* 102 (2005). ISSN: 00278424. DOI: `10.1073/pnas.0507119102`.

[30] Julie A. Reisz et al. "Effects of ionizing radiation on biological molecules - mechanisms of damage and emerging methods of detection". *Antioxidants and Redox Signaling* 21 (2014). ISSN: 15577716. DOI: `10.1089/ars.2013.5489`.

[31] K. H. Chadwick and H. P. Leenhouts. "A molecular theory of cell survival". *Physics in Medicine and Biology* 18 (1973). ISSN: 00319155. DOI: `10.1088/0031-9155/18/1/007`.

[32] Jian Z. Wang et al. "A generalized linear-quadratic model for radiosurgery, stereotactic body radiation therapy, and high-dose rate brachytherapy". *Science Translational Medicine* 2 (2010). ISSN: 19466234. DOI: `10.1126/scitranslmed.3000864`.

[33] A. Dawson and T. Hillen. "Derivation of the tumour control probability (TCP) from a cell cycle model". *Computational and Mathematical Methods in Medicine* 7 (2006). ISSN: 17486718. DOI: `10.1080/10273660600968937`.

[34] Michael Baumann and Cordula Petersen. "TCP and NTCP: A basic introduction". *Rays - International Journal of Radiological Sciences* 30 (2005). ISSN: 03907740.

[35] H Holthusen. "Erfahrungen über die Verträglichkeitsgrenze für Röntgenstrahlen und deren Nutzanwendung zur Verhütung von Schäden". *Strahlentherapie* 57 (1936).

[36] J. A. del Regato. "Henri Coutard." *International journal of radiation oncology, biology, physics* 13 (1987). ISSN: 03603016. DOI: `10.1016/0360-3016(87)90017-4`.

[37] John E. Moulder and Colin Seymour. "Radiation fractionation: the search for isoeffect relationships and mechanisms". *International Journal of Radiation Biology* 94 (2018). ISSN: 13623095. DOI: `10.1080/09553002.2017.1376764`.

[38] Alan E. Nahum. "The Radiobiology of Hypofractionation". *Clinical Oncology* 27 (2015). ISSN: 14332981. DOI: `10.1016/j.clon.2015.02.001`.

[39] Craig Elith et al. “An introduction to the intensity-modulated radiation therapy (IMRT) techniques, tomotherapy, and VMAT”. *Journal of Medical Imaging and Radiation Sciences* 42 (2011). ISSN: 19398654. DOI: 10.1016/j.jmir.2010.11.005.

[40] Fenny Gozal et al. “Dosimetric analysis of three-dimensional conformal radiotherapy, intensity-modulated radiotherapy-step and shoot, helical tomotherapy, and volumetric modulated arc therapy in prostate cancer radiotherapy”. *Journal of Cancer Research and Therapeutics* 17 (2021). ISSN: 19984138. DOI: 10.4103/jcrt.JCRT_57_19.

[41] Tania De La Herman et al. “Dosimetric comparison between IMRT delivery modes: Step-and-shoot, sliding window, and volumetric modulated arc therapy - For whole pelvis radiation therapy of intermediate-to-high risk prostate adenocarcinoma”. *Journal of Medical Physics* 38 (2013). ISSN: 09716203. DOI: 10.4103/0971-6203.121193.

[42] May Teoh et al. “Volumetric modulated arc therapy: A review of current literature and clinical use in practice”. *British Journal of Radiology* 84 (2011). ISSN: 00071285. DOI: 10.1259/bjr/22373346.

[43] Rémy Kinj and Jean Bourhis. “How Stereotactic Radiotherapy Changed the Landscape in Cancer Care”. *Cancers* 15 (2023). ISSN: 20726694. DOI: 10.3390/cancers15061734.

[44] C. D. Town. “Effect of high dose rates on survival of mammalian cells [9]”. *Nature* 215 (1967). ISSN: 00280836. DOI: 10.1038/215847a0.

[45] R. J. Berry et al. “Survival of mammalian cells exposed to x rays at ultra-high dose-rates.” *The British journal of radiology* 42 (1969). ISSN: 00071285. DOI: 10.1259/0007-1285-42-494-102.

[46] Nolan Esplen, Marc S. Mendonca, and Magdalena Bazalova-Carter. “Physics and biology of ultrahigh dose-rate (FLASH) radiotherapy: A topical review”. *Physics in Medicine and Biology* 65 (2020). ISSN: 13616560. DOI: 10.1088/1361-6560/abaa28.

[47] Vincent Favaudon et al. “Ultrahigh dose-rate FLASH irradiation increases the differential response between normal and tumor tissue in mice”. *Science Translational Medicine* 6 (2014). ISSN: 19466242. DOI: 10.1126/scitranslmed.3008973.

[48] Marie Catherine Vozenin, Jean Bourhis, and Marco Durante. “Towards clinical translation of FLASH radiotherapy”. *Nature Reviews Clinical Oncology* 19 (2022). ISSN: 17594782. DOI: 10.1038/s41571-022-00697-z.

[49] Pierre Montay-Gruel et al. “Irradiation in a flash: Unique sparing of memory in mice after whole brain irradiation with dose rates above 100 Gy/s”. *Radiotherapy and Oncology* 124 (2017). ISSN: 18790887. DOI: 10.1016/j.radonc.2017.05.003.

[50] Marie Catherine Vozenin et al. “The Advantage of FLASH Radiotherapy Confirmed in Mini-pig and Cat-cancer Patients”. *Clinical Cancer Research* 25 (2019). ISSN: 15573265. DOI: 10.1158/1078-0432.CCR-17-3375.

[51] Carla Rohrer Bley et al. “Dose- And Volume-Limiting Late Toxicity of FLASH Radiotherapy in Cats with Squamous Cell Carcinoma of the Nasal Planum and in Mini Pigs”. *Clinical Cancer Research* 28 (2022). ISSN: 15573265. DOI: 10.1158/1078-0432.CCR-22-0262.

[52] Jean Bourhis et al. “Treatment of a first patient with FLASH-radiotherapy”. *Radiotherapy and Oncology* 139 (2019). ISSN: 18790887. DOI: 10.1016/j.radonc.2019.06.019.

[53] Anthony E. Mascia et al. “Proton FLASH Radiotherapy for the Treatment of Symptomatic Bone Metastases: The FAST-01 Nonrandomized Trial”. *JAMA Oncology* 9 (2023). ISSN: 23742445. DOI: 10.1001/jamaoncol.2022.5843.

[54] Pierre Montay-Gruel et al. “Hypofractionated FLASH-RT as an effective treatment against glioblastoma that reduces neurocognitive side effects in mice”. *Clinical Cancer Research* 27 (2021). ISSN: 15573265. DOI: 10.1158/1078-0432.CCR-20-0894.

[55] B. C. Rothwell et al. “Determining the parameter space for effective oxygen depletion for FLASH radiation therapy”. *Physics in Medicine and Biology* 66 (2021). ISSN: 13616560. DOI: 10.1088/1361-6560/abe2ea.

[56] Joseph D. Wilson et al. “Ultra-High Dose Rate (FLASH) Radiotherapy: Silver Bullet or Fool’s Gold?” *Frontiers in Oncology* 9 (2020). ISSN: 2234943X. DOI: `10.3389/fonc.2019.01563`.

[57] Simon Jolly et al. “Technical challenges for FLASH proton therapy”. *Physica Medica* 78 (2020). ISSN: 1724191X. DOI: `10.1016/j.ejmp.2020.08.005`.

[58] Anna Vignati et al. “Beam Monitors for Tomorrow: The Challenges of Electron and Photon FLASH RT”. *Frontiers in Physics* 8 (2020). ISSN: 2296424X. DOI: `10.3389/fphy.2020.00375`.

[59] Jia Ling Ruan et al. “Irradiation at Ultra-High (FLASH) Dose Rates Reduces Acute Normal Tissue Toxicity in the Mouse Gastrointestinal System”. *International Journal of Radiation Oncology Biology Physics* 111 (2021). ISSN: 1879355X. DOI: `10.1016/j.ijrobp.2021.08.004`.

[60] Jeannette Jansen et al. “Changes in Radical Levels as a Cause for the FLASH effect: Impact of beam structure parameters at ultra-high dose rates on oxygen depletion in water”. *Radiotherapy and Oncology* 175 (2022). ISSN: 18790887. DOI: `10.1016/j.radonc.2022.08.024`.

[61] Leonhard Karsch et al. “Beam pulse structure and dose rate as determinants for the flash effect observed in zebrafish embryo”. *Radiotherapy and Oncology* 173 (2022). ISSN: 18790887. DOI: `10.1016/j.radonc.2022.05.025`.

[62] Vincent Favaudon, Rudi Labarbe, and Charles L. Limoli. “Model studies of the role of oxygen in the FLASH effect”. *Medical Physics* 49 (2022). ISSN: 24734209. DOI: `10.1002/mp.15129`.

[63] Eui Jung Moon, Kristoffer Petersson, and Monica M. Olcina. “The importance of hypoxia in radiotherapy for the immune response, metastatic potential and FLASH-RT”. *International Journal of Radiation Biology* 98 (2022). ISSN: 13623095. DOI: `10.1080/09553002.2021.1988178`.

[64] Jeannette Jansen et al. “Does FLASH deplete oxygen? Experimental evaluation for photons, protons, and carbon ions”. *Medical Physics* 48 (2021). ISSN: 24734209. DOI: `10.1002/mp.14917`.

[65] Xu Cao et al. “Quantification of Oxygen Depletion During FLASH Irradiation In Vitro and In Vivo”. *International Journal of Radiation Oncology Biology Physics* 111 (2021). ISSN: 1879355X. DOI: `10.1016/j.ijrobp.2021.03.056`.

[66] Pierre Montay-Gruel et al. “Long-term neurocognitive benefits of FLASH radiotherapy driven by reduced reactive oxygen species”. *Proceedings of the National Academy of Sciences of the United States of America* 166 (2019). ISSN: 10916490. DOI: `10.1073/pnas.1901777116`.

[67] Walter Tinganelli et al. “Ultra-High Dose Rate (FLASH) Carbon Ion Irradiation: Dosimetry and First Cell Experiments”. *International Journal of Radiation Oncology Biology Physics* 112 (2022). ISSN: 1879355X. DOI: `10.1016/j.ijrobp.2021.11.020`.

[68] Jian Yue Jin et al. “Ultra-high dose rate effect on circulating immune cells: A potential mechanism for FLASH effect?” *Radiotherapy and Oncology* 149 (2020). ISSN: 18790887. DOI: `10.1016/j.radonc.2020.04.054`.

[69] Antje Galts and Abdelkhalek Hammi. “FLASH radiotherapy sparing effect on the circulating lymphocytes in pencil beam scanning proton therapy: impact of hypofractionation and dose rate”. *Physics in Medicine and Biology* 69 (2024). ISSN: 13616560. DOI: `10.1088/1361-6560/ad144e`.

[70] Ankang Hu et al. “Radical recombination and antioxidants: a hypothesis on the FLASH effect mechanism”. *International Journal of Radiation Biology* 99 (2023). ISSN: 13623095. DOI: `10.1080/09553002.2022.2110307`.

[71] Kristoffer Petersson et al. “High dose-per-pulse electron beam dosimetry -A model to correct for the ion recombination in the advanced markus ionization chamber”. *Medical Physics* 44 (2017). ISSN: 24734209. DOI: `10.1002/mp.12111`.

[72] M. McManus et al. “The challenge of ionisation chamber dosimetry in ultra-short pulsed high dose-rate Very High Energy Electron beams”. *Scientific Reports* 10 (2020). ISSN: 20452322. DOI: `10.1038/s41598-020-65819-y`.

[73] Daniela Poppinga et al. “VHEE beam dosimetry at CERN Linear Electron Accelerator for Research under ultra-high dose rate conditions”. *Biomedical Physics and Engineering Express* 7 (2020). ISSN: 20571976. DOI: `10.1088/2057-1976/abcae5`.

[74] Rafael Kranzer et al. “Ion collection efficiency of ionization chambers in ultra-high dose-per-pulse electron beams”. *Medical Physics* 48 (2021). ISSN: 24734209. DOI: `10.1002/mp.14620`.

[75] Francesco Romano et al. “Ultra-high dose rate dosimetry: Challenges and opportunities for FLASH radiation therapy”. *Medical Physics* 49 (2022). ISSN: 24734209. DOI: `10.1002/mp.15649`.

[76] Kevin Liu et al. “Evaluation of ion chamber response for applications in electron FLASH radiotherapy”. *Medical Physics* 51 (2024). ISSN: 24734209. DOI: `10.1002/mp.16726`.

[77] Elise Konradsson et al. “Correction for Ion Recombination in a Built-in Monitor Chamber of a Clinical Linear Accelerator at Ultra-High Dose Rates”. *Radiation Research* 194 (2020). ISSN: 19385404. DOI: `10.1667/RADE-19-00012`.

[78] Elise Konradsson et al. “Reconfiguring a Plane-Parallel Transmission Ionization Chamber to Extend the Operating Range into the Ultra-High Dose-per-pulse Regime”. *Radiation Research* 201 (2024). ISSN: 19385404. DOI: `10.1667/RADE-23-00177.1`.

[79] M. Gotz, L. Karsch, and J. Pawelke. “A new model for volume recombination in plane-parallel chambers in pulsed fields of high dose-per-pulse”. *Physics in Medicine and Biology* 62 (2017). ISSN: 13616560. DOI: `10.1088/1361-6560/aa8985`.

[80] Faustino Gómez et al. “Development of an ultra-thin parallel plate ionization chamber for dosimetry in FLASH radiotherapy”. *Medical Physics* 49 (2022). ISSN: 24734209. DOI: `10.1002/mp.15668`.

[81] Kevin Liu et al. *Development of novel ionization chambers for reference dosimetry in electron FLASH radiotherapy*. 2024.

[82] Fabio Di Martino et al. “A new solution for UHDP and UHDR (Flash) measurements: Theory and conceptual design of ALLS chamber”. *Physica Medica* 102 (2022). ISSN: 1724191X. DOI: 10.1016/j.ejmp.2022.08.010.

[83] Emil Schüler et al. “Experimental Platform for Ultra-high Dose Rate FLASH Irradiation of Small Animals Using a Clinical Linear Accelerator”. *International Journal of Radiation Oncology Biology Physics* 97 (2017). ISSN: 1879355X. DOI: 10.1016/j.ijrobp.2016.09.018.

[84] Michael Lempart et al. “Modifying a clinical linear accelerator for delivery of ultra-high dose rate irradiation”. *Radiotherapy and Oncology* 139 (2019). ISSN: 18790887. DOI: 10.1016/j.radonc.2019.01.031.

[85] De Huan Xie et al. “Electron ultra-high dose rate FLASH irradiation study using a clinical linac: Linac modification, dosimetry, and radiobiological outcome”. *Medical Physics* 49 (2022). ISSN: 24734209. DOI: 10.1002/mp.15920.

[86] Pierre Montay-Gruel et al. “FLASH radiotherapy with photon beams”. Vol. 49. 2022. DOI: 10.1002/mp.15222.

[87] Nolan Esplen et al. “Design optimization of an electron-to-photon conversion target for ultra-high dose rate x-ray (FLASH) experiments at TRIUMF”. *Physics in Medicine and Biology* 67 (2022). ISSN: 13616560. DOI: 10.1088/1361-6560/ac5ed6.

[88] Stephen E. Sampayan et al. “Megavolt bremsstrahlung measurements from linear induction accelerators demonstrate possible use as a FLASH radiotherapy source to reduce acute toxicity”. *Scientific Reports* 11 (2021). ISSN: 20452322. DOI: 10.1038/s41598-021-95807-9.

[89] Nolan Esplen et al. “Dosimetric characterization of a novel UHDR megavoltage X-ray source for flash radiobiological experiments”. *Scientific Reports* 14.1 (2024). DOI: 10.1038/s41598-023-50412-w.

[90] E. Pedroni et al. “Pencil beam characteristics of the next-generation Proton Scanning Gantry of PSI: Design issues and initial commissioning results”. *The European Physical Journal Plus* 126.7 (2011). DOI: 10.1140/epjp/i2011-11066-0.

[91] Till Tobias Böhlen et al. “Very high-energy electron therapy as light-particle alternative to transmission proton FLASH therapy – An evaluation of dosimetric performances”. *Radiotherapy and Oncology* 194 (2024). ISSN: 18790887. DOI: 10.1016/j.radonc.2024.110177.

[92] Arash Darafsheh et al. “Spread-out Bragg peak proton FLASH irradiation using a clinical synchrocyclotron: Proof of concept and ion chamber characterization”. *Medical Physics* 48 (2021). ISSN: 24734209. DOI: 10.1002/mp.15021.

[93] Ahmed Naceur et al. “Extending deterministic transport capabilities for very-high and ultra-high energy electron beams”. *Scientific reports* 14 (2024). ISSN: 20452322. DOI: 10.1038/s41598-023-51143-8.

[94] C. DesRosiers et al. “150-250 MeV electron beams in radiation therapy”. *Physics in Medicine and Biology* 45 (2000). ISSN: 00319155. DOI: 10.1088/0031-9155/45/7/306.

[95] Lech Papiez, Colleen DesRosiers, and Vadim Moskvin. “Very high energy electrons (50 - 250 MeV) and radiation therapy”. *Technology in Cancer Research and Treatment* 1 (2002). ISSN: 15330346. DOI: 10.1177/153303460200100202.

[96] Hao Zha and Alexej Grudiev. “Design of the Compact Linear Collider main linac accelerating structure made from two halves”. *Physical Review Accelerators and Beams* 20 (2017). ISSN: 24699888. DOI: 10.1103/PhysRevAccelBeams.20.042001.

[97] L. Faillace et al. “Perspectives in linear accelerator for FLASH VHEE: Study of a compact C-band system”. *Physica Medica* 104 (2022). ISSN: 1724191X. DOI: 10.1016/j.ejmp.2022.10.018.

[98] “Radiotherapy with laser-plasma accelerators: Monte Carlo simulation of dose deposited by an experimental quasimonoenergetic electron beam”. *Medical Physics* 33 (2006). ISSN: 00942405. DOI: 10.1118/1.2140115.

[99] Luca Labate et al. “Toward an effective use of laser-driven very high energy electrons for radiotherapy: Feasibility assessment of multi-field and intensity modulation irradiation schemes”. *Scientific Reports* 10 (2020). ISSN: 20452322. DOI: `10.1038/s41598-020-74256-w`.

[100] Till Tobias Böhlen et al. “Characteristics of very high-energy electron beams for the irradiation of deep-seated targets”. *Medical Physics* 48 (2021). ISSN: 24734209. DOI: `10.1002/mp.14891`.

[101] K. Kokurewicz et al. “Focused very high-energy electron beams as a novel radiotherapy modality for producing high-dose volumetric elements”. *Scientific Reports* 9 (2019). ISSN: 20452322. DOI: `10.1038/s41598-019-46630-w`.

[102] Karolina Kokurewicz et al. “An experimental study of focused very high energy electron beams for radiotherapy”. *Communications Physics* 4 (2021). ISSN: 23993650. DOI: `10.1038/s42005-021-00536-0`.

[103] L. Whitmore et al. “Focused VHEE (very high energy electron) beams and dose delivery for radiotherapy applications”. *Scientific Reports* 11 (2021). ISSN: 20452322. DOI: `10.1038/s41598-021-93276-8`.

[104] Agnese Lagzda et al. “Influence of heterogeneous media on Very High Energy Electron (VHEE) dose penetration and a Monte Carlo-based comparison with existing radiotherapy modalities”. *Nuclear Instruments and Methods in Physics Research, Section B: Beam Interactions with Materials and Atoms* 482 (2020). ISSN: 0168583X. DOI: `10.1016/j.nimb.2020.09.008`.

[105] Magdalena Bazalova-Carter et al. “Treatment planning for radiotherapy with very high-energy electron beams and comparison of VHEE and VMAT plans”. *Medical Physics* 42 (2015). ISSN: 24734209. DOI: `10.1118/1.4918923`.

[106] Emil Schuler et al. “Very high-energy electron (VHEE) beams in radiation therapy; Treatment plan comparison between VHEE, VMAT, and PPBS”. *Medical Physics* 44 (2017). ISSN: 00942405. DOI: `10.1002/mp.12233`.

[107] A. Muscato et al. “Treatment planning of intracranial lesions with VHEE: comparing conventional and FLASH irradiation potential with state-of-the-art photon and proton radiotherapy”. *Frontiers in Physics* 11 (2023). ISSN: 2296424X. DOI: 10.3389/fphy.2023.1185598.

[108] Till Tobias Böhlen et al. “3D-conformal very-high energy electron therapy as candidate modality for FLASH-RT: A treatment planning study for glioblastoma and lung cancer”. *Medical Physics* 50 (2023). ISSN: 24734209. DOI: 10.1002/mp.16586.

[109] Maria Grazia Ronga et al. “Back to the future: Very high-energy electrons (vhees) and their potential application in radiation therapy”. *Cancers* 13 (2021). ISSN: 20726694. DOI: 10.3390/cancers13194942.

[110] CHUV press release. *CHUV, CERN and THERYQ joinforces for a world first in cancer radiotherapy*. 2022. URL: https://www.chuv.ch/fr/chuv-home/espace-pro/journalistes/communiques-de-presse/detail/chuv-cern-and-theryq-join-forces-for-a-world-first-in-cancer-radiotherapy (visited on 2024).

[111] Peter G. Maxim, Sami G. Tantawi, and Billy W. Loo. “PHASER: A platform for clinical translation of FLASH cancer radiotherapy”. *Radiotherapy and Oncology* 139 (2019). ISSN: 18790887. DOI: 10.1016/j.radonc.2019.05.005.

[112] O. Lundh et al. “Comparison of measured with calculated dose distribution from a 120-MeV electron beam from a laser-plasma accelerator”. *Medical Physics* 39 (2012). ISSN: 00942405. DOI: 10.1118/1.4719962.

[113] Ashalnd Inc. *Radiotherapy Films*. 2024. URL: https://www.ashland.com/industries/medical/radiotherapy-films (visited on 05/10/2024).

[114] Magdalena Bazalova-Carter et al. “Comparison of film measurements and Monte Carlo simulations of dose delivered with very high-energy electron beams in a polystyrene phantom”. *Medical Physics* 42 (2015). ISSN: 24734209. DOI: 10.1118/1.4914371.

[115] A. Subiel et al. “Dosimetry of very high energy electrons (VHEE) for radiotherapy applications: Using radiochromic film measurements and Monte Carlo simulations”. *Physics in Medicine and Biology* 59 (2014). ISSN: 13616560. DOI: `10.1088/0031-9155/59/19/5811`.

[116] Anna Subiel et al. “Challenges of dosimetry of ultra-short pulsed very high energy electron beams”. *Physica Medica* 42 (2017). ISSN: 1724191X. DOI: `10.1016/j.ejmp.2017.04.029`.

[117] Arash Darafsheh. *Radiation Therapy Dosimetry: A Practical Handbook*. CRC Press, 2021. DOI: `10.1201/9781351005388`.

[118] E. Segrè. *Experimental Nuclear Physics*. Experimental Nuclear Physics v. 1. Wiley, 1953. ISBN: 9780598745040. URL: `https://books.google.co.uk/books?id=m2MGAQAAIAAJ`.

[119] International Atomic Energy Agency and E.B. Podgorsak. *Basic radiation physics*. Vienna: IAEA, 2005, pp. 1–43.

[120] Berger. M.J. et al. *ESTAR, PSTAR, and ASTAR: Computer Programs for Calculating Stopping-Power and Range Tables for Electrons, Protons, and Helium Ions (version 1.2.3)*. 2004. URL: `http://physics.nist.gov/Star` (visited on 2024).

[121] David W. O. Rogers. “Introduction to Radiological Physics and Radiation Dosimetry by F. H. Attix”. *Medical Physics* 14 (1987). DOI: `10.1118/1.596041`.

[122] W. Heitler. *The quantum theory of radiation*. Vol. 5. International Series of Monographs on Physics. Oxford: Oxford University Press, 1936.

[123] O. Klein and Y. Nishina. “On the scattering of radiation by free electrons according to dirac’s new relativistic quantum dynamics”. 2014. DOI: `10.1142/9789814571616_0015`.

[124] H. Bethe and W. Heitler. “On the stopping of fast particles and on the creation of positive electrons”. *Proceedings of the Royal Society of London. Series A, Containing Papers of a Mathematical and Physical Character* 146 (1934). ISSN: 0950-1207. DOI: `10.1098/rspa.1934.0140`.

[125] INTERNATIONAL ATOMIC ENERGY AGENCY. *Handbook on Photonuclear Data for Applications Cross-sections and Spectra*. Vienna, 2000. URL: https://www.iaea.org/publications/6043/handbook-on-photonuclear-data-for-applications-cross-sections-and-spectra.

[126] Xiao-tian Mao, Kenneth R. Kase, and Walter R. Nelson. "Giant dipole resonance neutron yields produced by electrons as a function of target material and thickness". *Health Phys.* 70 (1996), pp. 207–214. DOI: 10.1097/00004032-199602000-00008.

[127] T. Kawano et al. "IAEA Photonuclear Data Library 2019". *Nuclear Data Sheets* 163 (2020). ISSN: 00903752. DOI: 10.1016/j.nds.2019.12.002.

[128] B. L. Berman and S. C. Fultz. "Measurements of the giant dipole resonance with monoenergetic photons". *Rev. Mod. Phys.* 47 (1975), pp. 713–761. DOI: 10.1103/RevModPhys.47.713.

[129] J. S. Levinger. "Nuclear photodisintegration". *Conf. Proc. C* 670207V3 (1967), pp. 411–428.

[130] William P. Swanson. "Calculation of Neutron Yields Released by Electrons Incident on Selected Materials". *Health Phys.* 35 (1978), p. 353. DOI: 10.1097/00004032-197808000-00019.

[131] Colleen DesRosiers. "An evaluation of very high energy electron beams (up to 250 MeV) in radiation therapy". PhD thesis. Purdue University, 2004.

[132] M.M. Barbier. *Induced Radioactivity*. North-Holland Publishing Company, 1969. ISBN: 9780720401455. URL: https://books.google.co.uk/books?id=0VMbAQAAIAAJ.

[133] Thongchai A.M. Masilela, Rachel Delorme, and Yolanda Prezado. "Dosimetry and radioprotection evaluations of very high energy electron beams". *Scientific Reports* 11 (2021). ISSN: 20452322. DOI: 10.1038/s41598-021-99645-7.

[134] Rachel Delorme et al. "First theoretical determination of relative biological effectiveness of very high energy electrons". *Scientific Reports* 11 (2021). ISSN: 20452322. DOI: 10.1038/s41598-021-90805-3.

[135] D. J. Thomas. “International Commission on Radiation Units and Measurements. Report 85: Fundamental quantities and units for ionizing radiation.” *Reports of the International Commission on Radiation Units and Measurements (ICRU)* 150 (2011). ISSN: 0144-8420.

[136] IAEA TRS 398. “Absorbed Dose Determination in External Beam Radiotherapy”. *Atomic Energy* (2000). ISSN: 00179078.

[137] IAEA and WHO. “Calibration of Reference Dosimeters for External Beam Radiotherapy Technical Reports Series No. 469”. *IAEA* (2009). ISSN: 0074-1914.

[138] Pedro Andreo et al. *Fundamentals of ionizing radiation dosimetry*. John Wiley & Sons, 2017.

[139] Carlos Eduardo de Almeida and Camila Salata. “Absolute, Reference, and Relative Dosimetry in Radiotherapy”. *Dosimetry*. Ed. by Thomas J. FitzGerald and Maryann Bishop-Jodoin. Rijeka: IntechOpen, 2022. Chap. 4. DOI: `10.5772/intechopen.101806`. URL: `https://doi.org/10.5772/intechopen.101806`.

[140] International Electrotechnical Comission. *IEC 60601-2-1 Medical Electrical Equipment – Part 2-1: Particular requirements for the basic safety and essential performance of electron accelerators in the range 1 MeV to 50 MeV*. 2020.

[141] Igor Olaciregui-Ruiz et al. “In vivo dosimetry in external beam photon radiotherapy: Requirements and future directions for research, development, and clinical practice”. *Physics and Imaging in Radiation Oncology* 15 (2020). DOI: `10.1016/j.phro.2020.08.003`.

[142] Jessica R. Miller et al. “Polarity effects and apparent ion recombination in microionization chambers”. *Medical Physics* 43 (2016). ISSN: 24734209. DOI: `10.1118/1.4944872`.

[143] J. W. BOAG. “Ionization measurements at very high intensities. Pulsed radiation beams.” *The British journal of radiology* 23 (1950). ISSN: 00071285. DOI: `10.1259/0007-1285-23-274-601`.

[144] J. Böhm. “Saturation corrections for plane-parallel ionisation chambers”. *Physics in Medicine and Biology* 21 (1976). ISSN: 00319155. DOI: `10.1088/0031-9155/21/5/004`.

[145] J. W. Boag, E. Hochhäuser, and O. A. Balk. "The effect of free-electron collection on the recombination correction to ionization measurements of pulsed radiation". *Physics in Medicine and Biology* 41 (1996). ISSN: 00319155. DOI: `10.1088/0031-9155/41/5/005`.

[146] Slobodan Devic, Nada Tomic, and David Lewis. "Reference radiochromic film dosimetry: Review of technical aspects". *Physica Medica* 32 (2016). ISSN: 1724191X. DOI: `10.1016/j.ejmp.2016.02.008`.

[147] Megha Sharma et al. "Beam quality and dose rate dependency of Gafchromic EBT3 film irradiated with therapeutic megavolt photon beams". *Radiation Measurements* 146 (2021). ISSN: 13504487. DOI: `10.1016/j.radmeas.2021.106632`.

[148] L. Karsch et al. "Dose rate dependence for different dosimeters and detectors: TLD, OSL, EBT films, and diamond detectors". *Medical Physics* 39 (2012). ISSN: 00942405. DOI: `10.1118/1.3700400`.

[149] Gholamreza Ataei et al. "Evaluation of dose rate and photon energy dependence of gafchromic EBT3 film irradiating with 6 MV and Co-60 photon beams". *Journal of Medical Signals and Sensors* 9 (2019). ISSN: 22287477. DOI: `10.4103/jmss.JMSS_45_18`.

[150] Krzysztof Chełmiński et al. "Energy dependence of radiochromic dosimetry films for use in radiotherapy verification". *Reports of Practical Oncology and Radiotherapy* 15 (2010). ISSN: 15071367. DOI: `10.1016/j.rpor.2010.02.003`.

[151] Maria F. Chan et al. "Technical note: Energy dependence of the Gafchromic EBT4 film: Dose-response curves for 70 kV, 6 MV, 6 MV FFF, 10 MV FFF, and 15 MV x-ray beams". *Medical Physics* 50 (2023). ISSN: 24734209. DOI: `10.1002/mp.16240`.

[152] Tania Santos, Tiago Ventura, and Maria do Carmo Lopes. "A review on radiochromic film dosimetry for dose verification in high energy photon beams". *Radiation Physics and Chemistry* 179 (2021). ISSN: 18790895. DOI: `10.1016/j.radphyschem.2020.109217`.

[153] Elsa Y. León-Marroquín et al. “Spectral analysis of the EBT3 radiochromic films for clinical photon and electron beams”. *Medical Physics* 46 (2019). ISSN: 24734209. DOI: 10.1002/mp.13330.

[154] E. Yazmin León-Marroquín et al. “Response characterization of EBT-XD radiochromic films in megavoltage photon and electron beams”. *Medical Physics* 46 (2019). ISSN: 24734209. DOI: 10.1002/mp.13708.

[155] Indra J. Das. *Radiochromic film: Role and applications in radiation dosimetry*. 2017. DOI: 10.1201/b20964.

[156] Elsa Y. León Marroquin et al. “Evaluation of the uncertainty in an EBT3 film dosimetry system utilizing net optical density”. *Journal of Applied Clinical Medical Physics* 17 (2016). ISSN: 15269914. DOI: 10.1120/jacmp.v17i5.6262.

[157] J. Sorriaux et al. “Evaluation of Gafchromic® EBT3 films characteristics in therapy photon, electron and proton beams”. *Physica Medica* 29 (2013). ISSN: 11201797. DOI: 10.1016/j.ejmp.2012.10.001.

[158] Maud Jaccard et al. “High dose-per-pulse electron beam dosimetry: Usability and dose-rate independence of EBT3 Gafchromic films: Usability”. *Medical Physics* 44 (2017). ISSN: 24734209. DOI: 10.1002/mp.12066.

[159] Jakob Helt-Hansen et al. “Medical reference dosimetry using EPR measurements of alanine: Development of an improved method for clinical dose levels”. *Acta Oncologica* 48 (2009). ISSN: 1651226X. DOI: 10.1080/02841860802279725.

[160] Oswaldo Baffa and Angela Kinoshita. “Clinical applications of alanine/electron spin resonance dosimetry”. *Radiation and Environmental Biophysics* 53 (2014). ISSN: 0301634X. DOI: 10.1007/s00411-013-0509-2.

[161] Alexandra Bourgouin et al. “Absorbed-dose-to-water measurement using alanine in ultra-high-pulse-dose-rate electron beams”. *Physics in Medicine and Biology* 67 (2022). ISSN: 13616560. DOI: 10.1088/1361-6560/ac950b.

[162] S. W. S. McKeever, M. Moscovitch, and P. D. (Peter David) Townsend. *Thermoluminescence dosimetry materials : properties and uses*. Nuclear Technology Pub, 1995, p. 204. ISBN: 1870965191. URL: `https://inis.iaea.org/search/search.aspx?orig_q=RN:28037727`.

[163] Yigal Horowitz. "A Unified and Comprehensive Theory of the TL Dose Response of Thermoluminescent Systems Applied to LiF: Mg,Ti". 2006. DOI: `10.1016/B978-044451643-5/50014-9`.

[164] E. Tochilin and N. Goldstein. "Dose rate and spectral measurements from pulsed X-ray generators". *Health Physics* 12 (1966). ISSN: 15385159. DOI: `10.1097/00004032-196612000-00007`.

[165] Chester S. Reft. "The energy dependence and dose response of a commercial optically stimulated luminescent detector for kilovoltage photon, megavoltage photon, and electron, proton, and carbon beams". *Medical Physics* 36 (2009). ISSN: 00942405. DOI: `10.1118/1.3097283`.

[166] Jeppe Brage Christensen et al. "Al2O3:C optically stimulated luminescence dosimeters (OSLDs) for ultra-high dose rate proton dosimetry". *Physics in Medicine and Biology* 66 (2021). ISSN: 13616560. DOI: `10.1088/1361-6560/abe554`.

[167] Anatoly B. Rosenfeld et al. "Semiconductor dosimetry in modern external-beam radiation therapy". *Physics in Medicine and Biology* 65 (2020). ISSN: 13616560. DOI: `10.1088/1361-6560/aba163`.

[168] Marco Marinelli et al. "Design, realization, and characterization of a novel diamond detector prototype for FLASH radiotherapy dosimetry". *Medical Physics* 49 (2022). ISSN: 24734209. DOI: `10.1002/mp.15473`.

[169] Francesco Romano et al. "First Characterization of Novel Silicon Carbide Detectors with Ultra-High Dose Rate Electron Beams for FLASH Radiotherapy". *Applied Sciences (Switzerland)* 13 (2023). ISSN: 20763417. DOI: `10.3390/app13052986`.

[170] Giuliana Milluzzo et al. “Comprehensive dosimetric characterization of novel silicon carbide detectors with UHDR electron beams for FLASH radiotherapy”. *Medical Physics* (2024). DOI: `https://doi.org/10.1002/mp.17172`.

[171] Muhammad Ramish Ashraf et al. “Dosimetry for FLASH Radiotherapy: A Review of Tools and the Role of Radioluminescence and Cherenkov Emission”. *Frontiers in Physics* 8 (2020). ISSN: 2296424X. DOI: `10.3389/fphy.2020.00328`.

[172] M. Ramish Ashraf et al. “Individual pulse monitoring and dose control system for preclinical implementation of FLASH-RT”. *Physics in Medicine and Biology* 67 (2022). ISSN: 13616560. DOI: `10.1088/1361-6560/ac5f6f`.

[173] J. B. Birks. “The Theory and Practice of Scintillation Counting: International Series of Monographs on Electronics and Instrumentation”. *Pergamon Press* (1967).

[174] J. B. Birks. “Scintillations from organic crystals: Specific fluorescence and relative response to different radiations”. *Proceedings of the Physical Society. Section A* 64 (1951). ISSN: 03701298. DOI: `10.1088/0370-1298/64/10/303`.

[175] L. L.W. Wang et al. “Determination of the quenching correction factors for plastic scintillation detectors in therapeutic high-energy proton beams”. *Physics in Medicine and Biology* 57 (2012). ISSN: 00319155. DOI: `10.1088/0031-9155/57/23/7767`.

[176] Daniel Robertson et al. “Quenching correction for volumetric scintillation dosimetry of proton beams”. *Physics in Medicine and Biology* 58 (2013). ISSN: 00319155. DOI: `10.1088/0031-9155/58/2/261`.

[177] Cherenkov, P. A. “Visible luminescence of pure liquids under the influence of γ-radiation”. *Dokl. Akad. Nauk SSSR* 2.8 (1934), pp. 451–454. DOI: `10.3367/UFNr.0093.196710n.0385`.

[178] I. M. Frank and I. E. Tamm. “Coherent visible radiation of fast electrons passing through matter”. *Compt. Rend. Acad. Sci. URSS* 14.3 (1937). Ed. by V. L. Ginzburg, B. M. Bolotovsky, and I. M. Dremin, pp. 109–114. DOI: `10.3367/UFNr.0093.196710o.0388`.

[179] Adam K. Glaser et al. “Optical dosimetry of radiotherapy beams using Cherenkov radiation: The relationship between light emission and dose”. *Physics in Medicine and Biology* 59 (2014). ISSN: 13616560. DOI: `10.1088/0031-9155/59/14/3789`.

[180] Joseph Wolfenden et al. “Cherenkov Radiation in Optical Fibres as a Versatile Machine Protection System in Particle Accelerators”. *Sensors* 23 (2023). ISSN: 14248220. DOI: `10.3390/s23042248`.

[181] Yasuhiro Koike. *Fundamentals of Plastic Optical Fibers*. Wiley, 2015. DOI: `10.1002/9783527646500`.

[182] Bahaa E A Saleh and Malvin Carl Teich. *Fundamentals of Photonics , 2nd Edition*. Wiley, 2007.

[183] Stefan Gundacker and Arjan Heering. “The silicon photomultiplier: Fundamentals and applications of a modern solid-state photon detector”. *Physics in Medicine and Biology* 65 (2020). ISSN: 13616560. DOI: `10.1088/1361-6560/ab7b2d`.

[184] Mark L. Maiello. “Physics and Engineering of Radiation Detection”. *Health Physics* 94 (2008). ISSN: 0017-9078. DOI: `10.1097/01.hp.0000295554.27735.22`.

[185] A. S. Beddar et al. “A miniature "scintillator-fiberoptic-PMT" detector system for the dosimetry of small fields in stereotactic radiosurgery”. *IEEE Transactions on Nuclear Science* 48 (2001). ISSN: 00189499. DOI: `10.1109/23.940133`.

[186] W. S. Boyle and G. E. Smith. “Charge Coupled Semiconductor Devices”. *Bell System Technical Journal* 49 (1970). ISSN: 15387305. DOI: `10.1002/j.1538-7305.1970.tb01790.x`.

[187] M. Bigas et al. “Review of CMOS image sensors”. *Microelectronics Journal* 37 (2006). ISSN: 00262692. DOI: `10.1016/j.mejo.2005.07.002`.

[188] E.J.N. Wilson. *An Introduction to Particle Accelerators*. An Introduction to Particle Accelerators. Oxford University Press, 2001. ISBN: 9780198508298. URL: `https://academic.oup.com/book/11694`.

[189] S.Y. Lee. *Accelerator Physics*. G - Reference,Information and Interdisciplinary Subjects Series. World Scientific, 2012. ISBN: 9789814374941. URL: `https://books.google.co.uk/books?id=1ghppwAACAAJ`.

[190] Andrea Latina. *Introduction to Transverse Beam Dynamics*. 2014. URL: `https://indico.cern.ch/event/1149120/contributions/4822271/` (visited on 2024).

[191] V. Kain. "Beam Dynamics and Beam Losses – Circular Machines". en. *CERN Yellow Reports* (2016), Vol 2 (2016): Proceedings of the 2014 Joint International Accelerator School: Beam Loss and Accelerator Protection. DOI: `10.5170/CERN-2016-002.21`. URL: `https://e-publishing.cern.ch/index.php/CYR/article/view/228`.

[192] E. Bravin. *Transverse emittance*. 2020. URL: `https://arxiv.org/abs/2005.05770`.

[193] M Vretenar. *Linear Accelerators*. 2014. DOI: `10.5170/CERN-2014-009.295`. URL: `https://cds.cern.ch/record/1982425`.

[194] David Alesini. *Linac*. 2021. URL: `https://arxiv.org/abs/2103.16500`.

[195] J. Haimson. "Electron bunching in travelling wave linear accelerators". *Nuclear Instruments and Methods* 39 (1966). ISSN: 0029554X. DOI: `10.1016/0029-554X(66)90040-1`.

[196] Agnese Lagzda. "VHEE Radiotherapy Studies at CLARA and CLEAR Facilities". PhD thesis. University of Manchester, 2019.

[197] Anna Subiel. "Feasibility Studies on the Application of Relativistic Electron Beams from a Laser Plasma Wakefield Accelerator in Radiotherapy". PhD thesis. University of Strathclyde, 2014.

[198] Wouter van Elmpt et al. "A literature review of electronic portal imaging for radiotherapy dosimetry". *Radiotherapy and Oncology* 88 (2008). ISSN: 01678140. DOI: `10.1016/j.radonc.2008.07.008`.

[199] Michael G. Herman et al. "Clinical use of electronic portal imaging: Report of AAPM Radiation Therapy Committee Task Group 58". *Medical Physics* 28 (2001). ISSN: 00942405. DOI: `10.1118/1.1368128`.

[200] Sean L. Berry et al. "Implementation of EPID transit dosimetry based on a through-air dosimetry algorithm". *Medical Physics* 39 (2012). ISSN: 00942405. DOI: `10.1118/1.3665249`.

[201] Sean L. Berry et al. "Initial clinical experience performing patient treatment verification with an electronic portal imaging device transit dosimeter". *International Journal of Radiation Oncology Biology Physics* 88 (2014). ISSN: 03603016. DOI: `10.1016/j.ijrobp.2013.09.045`.

[202] Markus Wendling et al. "A simple backprojection algorithm for 3D in vivo EPID dosimetry of IMRT treatments". *Medical Physics* 36 (2009). ISSN: 00942405. DOI: `10.1118/1.3148482`.

[203] B Mijnheer et al. "TU-C-BRE-11: 3D EPID-Based in Vivo Dosimetry: A Major Step Forward Towards Optimal Quality and Safety in Radiation Oncology Practice". *Medical Physics* 41 (2014). ISSN: 0094-2405. DOI: `10.1118/1.4889274`.

[204] Eric Van Uytven et al. "Validation of a method for in vivo 3D dose reconstruction for IMRT and VMAT treatments using on-treatment EPID images and a model-based forward-calculation algorithm". *Medical Physics* 42 (2015). ISSN: 24734209. DOI: `10.1118/1.4935199`.

[205] Katia Parodi and Jerimy C. Polf. "In vivo range verification in particle therapy". *Medical Physics* (2018). DOI: `10.1002/mp.12960`.

[206] Katia Parodi. "Latest developments in in-vivo imaging for proton therapy". *British Journal of Radiology* 93 (2020). ISSN: 1748880X. DOI: `10.1259/bjr.20190787`.

[207] K. Parodi, W. Enghardt, and T. Haberer. "In-beam PET measurements of beta plus radioactivity induced by proton beams". *Physics in Medicine and Biology* 47 (2002). ISSN: 00319155. DOI: `10.1088/0031-9155/47/1/302`.

[208] Paulo Crespo, Georgy Shakirin, and Wolfgang Enghardt. "On the detector arrangement for in-beam PET for hadron therapy monitoring". *Physics in Medicine and Biology* 51 (2006). ISSN: 00319155. DOI: `10.1088/0031-9155/51/9/002`.

[209] P. Dendooven et al. "Short-lived positron emitters in beam-on PET imaging during proton therapy". *Physics in Medicine and Biology* 60 (2015). ISSN: 13616560. DOI: 10.1088/0031-9155/60/23/8923.

[210] Chul Hee Min et al. "Prompt gamma measurements for locating the dose falloff region in the proton therapy". *Applied Physics Letters* 89 (2006). ISSN: 00036951. DOI: 10.1063/1.2378561.

[211] M. Testa et al. "Real-time monitoring of the Bragg-peak position in ion therapy by means of single photon detection". *Radiation and Environmental Biophysics* 49 (2010). ISSN: 0301634X. DOI: 10.1007/s00411-010-0276-2.

[212] Christian Golnik et al. "Range assessment in particle therapy based on prompt gamma-ray timing measurements". *Physics in Medicine and Biology* 59 (2014). ISSN: 13616560. DOI: 10.1088/0031-9155/59/18/5399.

[213] A. Schumann et al. "Simulation and experimental verification of prompt gamma-ray emissions during proton irradiation". *Physics in Medicine and Biology* 60 (2015). ISSN: 13616560. DOI: 10.1088/0031-9155/60/10/4197.

[214] K. C. Jones et al. "Proton beam characterization by proton-induced acoustic emission: Simulation studies". *Physics in Medicine and Biology* 59 (2014). ISSN: 13616560. DOI: 10.1088/0031-9155/59/21/6549.

[215] Moiz Ahmad et al. "Theoretical detection threshold of the proton-acoustic range verification technique". *Medical Physics* 42 (2015). ISSN: 24734209. DOI: 10.1118/1.4929939.

[216] J. Perl et al. "TOPAS: An innovative proton Monte Carlo platform for research and clinical applications". *Medical Physics* 39 (2012). ISSN: 00942405. DOI: 10.1118/1.4758060.

[217] P. Arce et al. "Report on G4-Med, a Geant4 benchmarking system for medical physics applications developed by the Geant4 Medical Simulation Benchmarking Group". *Medical Physics* 48 (2021). ISSN: 24734209. DOI: 10.1002/mp.14226.

[218] Geant4 Collaboration. *Geant4 Physics Reference Manual Release 10.7 (2020)*.

[219] Peter B. Greer and Michael P. Barnes. “Investigation of an amorphous silicon EPID for measurement and quality assurance of enhanced dynamic wedge”. *Physics in Medicine and Biology* 52 (2007). ISSN: 00319155. DOI: 10.1088/0031-9155/52/4/014.

[220] Aya Miyatake, Teiji Nishio, and Takashi Ogino. “Development of activity pencil beam algorithm using measured distribution data of positron emitter nuclei generated by proton irradiation of targets containing 12C, 16O, and 40Ca nuclei in preparation of clinical application”. *Medical Physics* 38 (2011). ISSN: 00942405. DOI: 10.1118/1.3641829.

[221] Marlen Priegnitz et al. “An experiment-based approach for predicting positron emitter distributions produced during therapeutic ion irradiation”. *IEEE Transactions on Nuclear Science* 59 (2012). ISSN: 00189499. DOI: 10.1109/TNS.2011.2172629.

[222] K. Frey et al. “TPSPET - A TPS-based approach for in vivo dose verification with PET in proton therapy”. *Physics in Medicine and Biology* 59 (2014). ISSN: 00319155. DOI: 10.1088/0031-9155/59/1/1.

[223] Falk Pönisch et al. “The modelling of positron emitter production and PET imaging during carbon ion therapy”. *Physics in Medicine and Biology* 49 (2004). ISSN: 00319155. DOI: 10.1088/0031-9155/49/23/002.

[224] K. Parodi et al. “Clinical CT-based calculations of dose and positron emitter distributions in proton therapy using the FLUKA Monte Carlo code”. *Physics in Medicine and Biology* 52 (2007). ISSN: 00319155. DOI: 10.1088/0031-9155/52/12/004.

[225] W. Enghardt et al. “Dose quantification from in-beam positron emission tomography”. *Radiotherapy and Oncology*. Vol. 73. 2004. DOI: 10.1016/S0167-8140(04)80024-0.

[226] W. Enghardt et al. “Charged hadron tumour therapy monitoring by means of PET”. *Nuclear Instruments and Methods in Physics Research, Section A: Accelerators, Spectrometers, Detectors and Associated Equipment*. Vol. 525. 2004. DOI: 10.1016/j.nima.2004.03.128.

[227] E. Fourkal, J. Fan, and I. Veltchev. “Absolute dose reconstruction in proton therapy using PET imaging modality: Feasibility study”. *Physics in Medicine and Biology* 54 (2009). ISSN: 00319155. DOI: `10.1088/0031-9155/54/11/N02`.

[228] Katia Parodi and Thomas Bortfeld. “A filtering approach based on Gaussian-powerlaw convolutions for local PET verification of proton radiotherapy”. *Physics in Medicine and Biology* 51 (2006). ISSN: 00319155. DOI: `10.1088/0031-9155/51/8/003`.

[229] Steffen Remmele et al. “A deconvolution approach for PET-based dose reconstruction in proton radiotherapy”. *Physics in Medicine and Biology* 56 (2011). ISSN: 00319155. DOI: `10.1088/0031-9155/56/23/017`.

[230] D. Möckel et al. “Quantification of beta+ activity generated by hard photons by means of PET”. *Physics in Medicine and Biology* 52 (2007). ISSN: 13616560. DOI: `10.1088/0031-9155/52/9/012`.

[231] Matthew T Studenski. “Proton therapy dosimetry using positron emission tomography”. *World Journal of Radiology* 2 (2010). ISSN: 1949-8470. DOI: `10.4329/wjr.v2.i4.135`.

[232] “The application of PET to quality assurance of heavy-ion tumor therapy”. *Strahlentherapie und Onkologie* 175 (1999). ISSN: 01797158. DOI: `10.1007/bf03038884`.

[233] Francesco Pennazio et al. “Carbon ions beam therapy monitoring with the INSIDE in-beam PET”. *Physics in Medicine and Biology* 63 (2018). ISSN: 13616560. DOI: `10.1088/1361-6560/aacab8`.

[234] A. C. Kraan. “Range verification methods in particle therapy: Underlying physics and Monte Carlo modelling”. *Frontiers in Oncology* 5 (2015). ISSN: 2234943X. DOI: `10.3389/fonc.2015.00150`.

[235] Xuping Zhu et al. “Monitoring proton radiation therapy with in-room PET imaging”. *Physics in Medicine and Biology* 56 (2011). ISSN: 00319155. DOI: `10.1088/0031-9155/56/13/019`.

[236] F. Abouzahr et al. “The first PET glimpse of a proton FLASH beam”. *Physics in Medicine and Biology* 68 (2023). ISSN: 13616560. DOI: 10.1088/1361-6560/acd29e.

[237] F. Abouzahr et al. “The first probe of a FLASH proton beam by PET”. *Physics in Medicine and Biology* 68 (2023). ISSN: 13616560. DOI: 10.1088/1361-6560/ad0901.

[238] Alessio Sarti et al. “Deep Seated Tumour Treatments With Electrons of High Energy Delivered at FLASH Rates: The Example of Prostate Cancer”. *Frontiers in Oncology* 11 (2021). ISSN: 2234943X. DOI: 10.3389/fonc.2021.777852.

[239] Yana Zlateva et al. “Cherenkov emission-based external radiotherapy dosimetry: I. Formalism and feasibility”. *Medical Physics* 46 (2019). ISSN: 24734209. DOI: 10.1002/mp.13414.

[240] Rachael Hachadorian et al. “Correcting Cherenkov light attenuation in tissue using spatial frequency domain imaging for quantitative surface dosimetry during whole breast radiation therapy”. *Journal of Biomedical Optics* 24 (2018). ISSN: 15602281. DOI: 10.1117/1.jbo.24.7.071609.

[241] W. G. Zijlstra, A. Buursma, and W. P. Meeuwsen-Van Der Roest. “Absorption spectra of human fetal and adult oxyhemoglobin, de-oxyhemoglobin, carboxyhemoglobin, and methemoglobin”. *Clinical Chemistry* 37 (1991). ISSN: 00099147. DOI: 10.1093/clinchem/37.9.1633.

[242] Yana Zlateva et al. “Cherenkov emission-based external radiotherapy dosimetry: II. Electron beam quality specification and uncertainties”. *Medical Physics* 46 (2019). ISSN: 24734209. DOI: 10.1002/mp.13413.

[243] M. Ramish Ashraf et al. “Technical Note: Single-pulse beam characterization for FLASH-RT using optical imaging in a water tank”. *Medical Physics* 48 (2021). ISSN: 24734209. DOI: 10.1002/mp.14843.

[244] Mahbubur Rahman et al. “Electron FLASH Delivery at Treatment Room Isocenter for Efficient Reversible Conversion of a Clinical LINAC”. *International Journal of Radiation*

Oncology Biology Physics 110 (2021). ISSN: 1879355X. DOI: 10.1016/j.ijrobp.2021.01.011.

[245] Katsunori Yogo et al. "Luminescence imaging of water irradiated by protons under FLASH radiation therapy conditions". *Physics in Medicine and Biology* 68 (2023). ISSN: 13616560. DOI: 10.1088/1361-6560/ace60b.

[246] Petr Bruza et al. "Online Combination of EPID Cherenkov Imaging for 3-D Dosimetry in a Liquid Phantom". *IEEE Transactions on Medical Imaging* 36 (2017). ISSN: 1558254X. DOI: 10.1109/TMI.2017.2717800.

[247] Agnese Chendi et al. "EPID-based 3D dosimetry for pre-treatment FFF VMAT stereotactic body radiotherapy plan verification using dosimetry CheckTM". *Physica Medica* 81 (2021). ISSN: 1724191X. DOI: 10.1016/j.ejmp.2020.12.014.

[248] Ewa Lopienska. "The CERN accelerator complex, layout in 2022. Complexe des accélérateurs du CERN en janvier 2022". *CERN CDS* (2022). General Photo. URL: https://cds.cern.ch/record/2800984.

[249] P. Korysko et al. "The CLEAR user facility: a review of the experimental methods and future plans". *Proc. 14th International Particle Accelerator Conference*. 14. 2023, pp. 876–879. ISBN: 978-3-95450-231-8. DOI: 10.18429/JACoW-IPAC2023-MOPL141.

[250] P. Korysko et al. "VHEE and ultra high dose rate radiotherapy studies in the CLEAR user facility". *Proc. 14th International Particle Accelerator Conference*. 14. 2023, pp. 5063–5066. ISBN: 978-3-95450-231-8. DOI: 10.18429/JACoW-IPAC2023-THPM078.

[251] K.N. Sjobak et al. "Status of the CLEAR Electron Beam User Facility at CERN". *Proc. 10th International Particle Accelerator Conference (IPAC'19)*. 10. 2019, pp. 983–986. ISBN: 978-3-95450-208-0. DOI: doi:10.18429/JACoW-IPAC2019-MOPTS054.

[252] K. B. Unser. "Design and Preliminary Tests of a Beam Intensity Monitor for LEP". *Proceedings of the IEEE Particle Accelerator Conference, Chicago*. 1989.

[253] Yuchi Wu et al. "A new method to calculate the beam charge for an integrating current transformer". *Review of Scientific Instruments* (2012). DOI: 10.1063/1.4750072.

[254] L. Soby et al. “A New Integrating Current Transformer for the LHC”. *Proc. 3rd International Beam Instrumentation Conference*. 2014.

[255] Andre Micke, David F. Lewis, and Xiang Yu. “Multichannel film dosimetry with nonuniformity correction”. *Medical Physics* 38 (2011). ISSN: 00942405. DOI: 10.1118/1.3576105.

[256] Martin J. Butson, T. Cheung, and P. K.N. Yu. “Scanning orientation effects on Gafchromic EBT film dosimetry”. *Australasian Physical and Engineering Sciences in Medicine* 29 (2006). ISSN: 01589938. DOI: 10.1007/BF03178579.

[257] L. Paelinck, W. De Neve, and C. De Wagter. “Precautions and strategies in using a commercial flatbed scanner for radiochromic film dosimetry”. *Physics in Medicine and Biology* 52 (2007). ISSN: 00319155. DOI: 10.1088/0031-9155/52/1/015.

[258] Maud Jaccard et al. “High dose-per-pulse electron beam dosimetry: Commissioning of the Oriatron eRT6 prototype linear accelerator for preclinical use: Commissioning”. *Medical Physics* 45 (2018). ISSN: 24734209. DOI: 10.1002/mp.12713.

[259] I. Méndez et al. “On multichannel film dosimetry with channel-independent perturbations”. *Medical Physics* 41 (2014). ISSN: 00942405. DOI: 10.1118/1.4845095.

[260] Azam Niroomand-Rad et al. “Report of AAPM Task Group 235 Radiochromic Film Dosimetry: An Update to TG-55”. *Medical Physics* 47 (2020). ISSN: 24734209. DOI: 10.1002/mp.14497.

[261] Elsa Y. León-Marroquín et al. “Spectral analysis of the EBT3 radiochromic films for clinical photon and electron beams”. *Medical Physics* 46 (2019). ISSN: 24734209. DOI: 10.1002/mp.13330.

[262] Antony L. Palmer and David Nash. “Radiochromic film dosimetry in radiotherapy: a survey of current practice in the United Kingdom”. *The British journal of radiology* 97 (2024). ISSN: 1748880X. DOI: 10.1093/bjr/tqae008.

[263] A. Schüller et al. “Traceable charge measurement of the pulses of a 27 MeV electron beam from a linear accelerator”. *Journal of Instrumentation* (2017). ISSN: 17480221. DOI: 10.1088/1748-0221/12/03/P03003.

[264] Roxane Oesterle et al. “Implementation and validation of a beam-current transformer on a medical pulsed electron beam LINAC for FLASH-RT beam monitoring”. *Journal of Applied Clinical Medical Physics* 22 (2021). ISSN: 15269914. DOI: 10.1002/acm2.13433.

[265] Patrik Gonçalves Jorge et al. “Technical note: Validation of an ultrahigh dose rate pulsed electron beam monitoring system using a current transformer for FLASH preclinical studies”. *Medical Physics* 49 (2022). ISSN: 24734209. DOI: 10.1002/mp.15474.

[266] Kevin Liu et al. “Dual beam-current transformer design for monitoring and reporting of electron ultra-high dose rate (FLASH) beam parameters”. *Journal of Applied Clinical Medical Physics* 24 (2023). ISSN: 15269914. DOI: 10.1002/acm2.13891.

[267] Achim Krauss. “The PTB water calorimeter for the absolute determination of absorbed dose to water in 60Co radiation”. *Metrologia* 43 (2006). ISSN: 00261394. DOI: 10.1088/0026-1394/43/3/008.

[268] Patrik Gonçalves Jorge et al. “Design and validation of a dosimetric comparison scheme tailored for ultra-high dose-rate electron beams to support multicenter FLASH preclinical studies”. *Radiotherapy and Oncology* 175 (2022). ISSN: 18790887. DOI: 10.1016/j.radonc.2022.08.023.

[269] C. Robertson et al. “Dual-scattering foil installation at CLEAR”. *Proc. IPAC’23*. 14. 2023, pp. 5059–5062. ISBN: 978-3-95450-231-8. DOI: 10.18429/JACoW-IPAC2023-THPM073.

[270] Cristina Garibaldi et al. “Minimum and optimal requirements for a safe clinical implementation of ultra-high dose rate radiotherapy: A focus on patient’s safety and radiation protection”. *Radiotherapy and Oncology* 196 (2024), p. 110291. ISSN: 0167-8140. DOI: https://doi.org/10.1016/j.radonc.2024.110291. URL: https://www.sciencedirect.com/science/article/pii/S0167814024002135.

[271] Simona Giordanengo and Hugo Palmans. “Dose detectors, sensors, and their applications”. Vol. 45. 2018. DOI: `10.1002/mp.13089`.

[272] Wei Zou et al. “Characterization of a high-resolution 2D transmission ion chamber for independent validation of proton pencil beam scanning of conventional and FLASH dose delivery”. *Medical Physics* 48 (2021). ISSN: 24734209. DOI: `10.1002/mp.14882`.

[273] Antonio Trigilio et al. “The FlashDC project: Development of a beam monitor for FLASH radiotherapy”. *Nuclear Instruments and Methods in Physics Research, Section A: Accelerators, Spectrometers, Detectors and Associated Equipment* 1041 (2022). ISSN: 01689002. DOI: `10.1016/j.nima.2022.167334`.

[274] Daniel S. Levin et al. “A prototype scintillator real-time beam monitor for ultra-high dose rate radiotherapy”. *Medical Physics* (2024). ISSN: 24734209. DOI: `10.1002/mp.17018`.

[275] Verdi Vanreusel et al. “A dose rate independent 2D Ce-doped YAG scintillating dosimetry system for time resolved beam monitoring in ultra-high dose rate electron “FLASH” radiation therapy”. *Sensors and Actuators A: Physical* 371 (2024), p. 115313. ISSN: 0924-4247. DOI: `https://doi.org/10.1016/j.sna.2024.115313`. URL: `https://www.sciencedirect.com/science/article/pii/S0924424724003066`.

[276] Vincent Favaudon et al. “Time-resolved dosimetry of pulsed electron beams in very high dose-rate, FLASH irradiation for radiotherapy preclinical studies”. *Nuclear Instruments and Methods in Physics Research, Section A: Accelerators, Spectrometers, Detectors and Associated Equipment* 944 (2019). ISSN: 01689002. DOI: `10.1016/j.nima.2019.162537`.

[277] Dong Hyeok Jeong et al. “Optical filter-embedded fiber-optic radiation sensor for ultra-high dose rate electron beam dosimetry”. *Sensors* 21 (2021). ISSN: 14248220. DOI: `10.3390/s21175840`.

[278] Verdi Vanreusel et al. “Point scintillator dosimetry in ultra-high dose rate electron “FLASH” radiation therapy: A first characterization”. *Physica Medica* 103 (2022). ISSN: 1724191X. DOI: `10.1016/j.ejmp.2022.10.005`.

[279] Eleni Kanouta et al. "Time-resolved dose rate measurements in pencil beam scanning proton FLASH therapy with a fiber-coupled scintillator detector system". *Medical Physics* 50 (2023). ISSN: 24734209. DOI: 10.1002/mp.16156.

[280] Alexander Hart et al. "Lead-doped scintillator dosimeters for detection of ultrahigh dose-rate x-rays". *Physics in Medicine and Biology* 67 (2022). ISSN: 13616560. DOI: 10.1088/1361-6560/ac69a5.

[281] Alexander Hart et al. "Plastic scintillator dosimetry of ultrahigh dose-rate 200 MeV electrons at CLEAR". *IEEE Sensors Journal* (2024). ISSN: 15581748. DOI: 10.1109/JSEN.2024.3353190.

[282] Iñaki Ortega Ruiz. "Accurate Profile Measurement of the low Intensity Secondary Beams in the CERN Experimental Areas". PhD thesis. Ecole Polytechnique, Lausanne, 2018.

[283] I. Ortega Ruiz et al. "The XBPF, a new multipurpose scintillating fibre monitor for the measurement of secondary beams at CERN". *Nuclear Instruments and Methods in Physics Research, Section A: Accelerators, Spectrometers, Detectors and Associated Equipment* 951 (2020). ISSN: 01689002. DOI: 10.1016/j.nima.2019.162996.

[284] E. Buchanan et al. "Radiation Hard Beam Profile Monitors for the North Experimental Beamlines CERN". *Proc. IBIC'23*. International Beam Instrumentation Conference 12. 2023. ISBN: 978-3-95450-236-3. DOI: 10.18429/JACoW-IBIC2023-WE3C03.

[285] B. D. Leverington et al. "A prototype scintillating fibre beam profile monitor for Ion Therapy beams". *Journal of Instrumentation* 13 (2018). ISSN: 17480221. DOI: 10.1088/1748-0221/13/05/P05030.

[286] O. Allegrini et al. "Characterization of a beam-tagging hodoscope for hadrontherapy monitoring". *Journal of Instrumentation* 16 (2021). ISSN: 17480221. DOI: 10.1088/1748-0221/16/02/P02028.

[287] Paulo Magalhaes Martins et al. "A Single-Particle Trigger for Time-of-Flight Measurements in Prompt-Gamma Imaging". *Frontiers in Physics* 8 (2020). ISSN: 2296424X. DOI: 10.3389/fphy.2020.00169.

[288] Vision Technology Pte Ltd_2020. *Spectral Response of SONY IMX249*. 2020. URL: `https://vitalvisiontechnology.com/gige-cameras/alliedvision-gige-cameras/mako-g-234/spectral-for-sony-imx249/` (visited on 05/22/2024).

[289] Johann Radon. "On the determination of functions from their integral values along certain manifolds". *IEEE Transactions on Medical Imaging* 5.4 (1986), pp. 170–176. DOI: `10.1109/TMI.1986.4307775`.

[290] Miguel García Díez et al. "Technical note: Measurement of the bunch structure of a clinical proton beam using a SiPM coupled to a plastic scintillator with an optical fiber". *Medical Physics* 50 (2023). ISSN: 24734209. DOI: `10.1002/mp.16333`.

[291] Guoliang Zhang et al. "Treatment planning consideration for very high-energy electron FLASH radiotherapy". *Physica Medica* 107 (2023). ISSN: 1724191X. DOI: `10.1016/j.ejmp.2023.102539`.

[292] Joseph J Bateman et al. "Development of a novel fibre optic beam profile and dose monitor for very high energy electron radiotherapy at ultrahigh dose rates". *Physics in Medicine Biology* 69 (2024), p. 085006. ISSN: 0031-9155. DOI: `10.1088/1361-6560/ad33a0`. URL: `https://iopscience.iop.org/article/10.1088/1361-6560/ad33a0`.

[293] Celeste Fleta et al. "State-of-the-art silicon carbide diode dosimeters for ultra-high dose-per-pulse radiation at FLASH radiotherapy". *Physics in Medicine and Biology* 69 (2024), p. 095013. ISSN: 0031-9155. DOI: `10.1088/1361-6560/ad37eb`. URL: `https://iopscience.iop.org/article/10.1088/1361-6560/ad37eb`.